University of Strathclyde

Department of Naval Architecture, Ocean and Marine Engineering

CFD-Based Hydrodynamic Analyses of Ship Manoeuvrability, Course Keeping Control, and Seakeeping

Daejeong Kim

A thesis presented in fulfilment of the requirements for the degree of Doctor of Philosophy

2022

This thesis is the result of the author's original research. It has been composed by the author and has not been previously submitted for examination which has led to the award of a degree.

Signed: Date:

Acknowledgements

The completion of this thesis would not have been possible without the assistance and support of many outstanding individuals. First of all, I would like to express my deepest gratitude and appreciation to my primary supervisor, mentor, and all-around role model, Dr Tahsin Tezdogan, for providing invaluable guidance, continuous support, and encouragement during my PhD study period at the University of Strathclyde. His vast knowledge and plentiful experience, and generosity have encouraged me throughout my academic research and daily life. Furthermore, I am influenced by his optimistic and enthusiastic nature. I continue to admire his professionalism, which will always serve as an example for me. This has undoubtedly broadened my perspective on issues relevant to my research.

In addition, I would like to thank my second supervisor, Dr Byongug Jeong, for always being very helpful and supportive. I am indebted to him for his insight and precious advice. I would like to extend my appreciation to Dr Soonseok Song who passionately instructed me on how to develop the free-running CFD model employed in this thesis.

I would also like to thank my ex-supervisor Professor Jeongbin Yim for his encouragement and careful advice.

Moreover, I am grateful to the Faculty of Engineering at the University of Strathclyde for providing the ARCHIE-WeSt High Performance computing facilities. The CFD results were obtained using the ARCHIE-WeSt High-Performance Computer (www.archie-west.ac.uk) based at the University of Strathclyde.

Finally, I would like to thank my parents for their love and support throughout my studies. I am fortunate to have been raised in a family that always supports my decisions and believes in me, which has surely helped me reach this point. I appreciate your enduring patience.

Contents

List of Figures

List of Tables

Abstract

Ship manoeuvrability is closely related to the safety of ship operation in a real seaway; therefore, predicting a ship's manoeuvring performance is of great importance. However, an accurate prediction of ship manoeuvrability in a real seaway is one of the most challenging problems in ship hydrodynamics, attributed to the complexity of the flow arising from the hydrodynamic interactions between the hull, propeller, rudder, and external disturbances during manoeuvres. To date, theoretical methods have been widely used for the prediction of ship manoeuvring behaviours in real sea states. These approaches rely on assumptions from the potential flow theory. However, the reliability of the potential flow theory is limited due to the lack of physics associated with viscous and turbulent effects and the free surface resolution, which are significant for manoeuvring problems. Hence, such effects which are ignored in the potential flow theory should be incorporated in the numerical codes. In light of this, Reynolds-Averaged Navier-Stokes (RANS) approaches are very attractive alternatives to the theoretical methods since they are capable of directly accounting for viscous effects in their calculations.

Free-running Computational Fluid Dynamics (CFD) simulations are progressively gaining popularity for manoeuvring prediction since they are capable of incorporating viscous and turbulent effects being important on ship manoeuvring as well as do not use any consumables (as opposed to experiments). However, due to its brevity, there are no definite guidelines and recommendations regarding the numerical setup of the free-running CFD simulation in different environmental conditions such as waves, shallow waters, and currents. Given this, in this thesis, the general framework is proposed for the analysis of ship manoeuvrability, course-keeping control, and seakeeping using the unsteady RANS computation coupled with the equations of rigid body motion with full six degrees of freedom (6DOF), with a particular focus on the numerical modelling for a free-running CFD model.

Ships are exposed to various environmental loads such as waves, wind, and currents during their operations at sea. Such external disturbances can lead to substantial changes in the behaviour of a ship during manoeuvring when compared to its inherent behaviour in calm water. Nevertheless, to date, the vast majority of studies in the field of ship manoeuvrability have been devoted to analysing the inherent manoeuvrability of a ship in calm water in conformity with the recommendation of ITTC. Their findings are not able to provide general observations on the relationship between external disturbances and manoeuvring behaviours. This thesis, therefore, aims to systematically carry out hydrodynamic analyses of a ship's manoeuvring performance in different environmental conditions (including deep-unrestricted water, regular waves, irregular waves, shallow water, and ocean currents) in order to provide an in-depth understanding of a ship's manoeuvrability for navigational safety at sea.

Firstly, a literature review of previous publications on all aspects of ship manoeuvrability is performed. The literature survey presents an overview of current standards and guidelines regarding the assessment of ship manoeuvrability, and then outlines a classification of the methods widely applied to manoeuvring problems. The research gaps detected during the literature review are also listed, which are addressed in detail in this PhD. thesis.

Following this, free-running CFD models are developed for the prediction of the ship's

manoeuvring performance by means of an unsteady RANS solver. These models are validated against the available experimental results from a free-running test. The numerical results are found to be in good agreement with available experimental data, which demonstrates that the numerical approach proposed in the present thesis is reliable in estimating ship manoeuvrability in various environmental conditions.

Afterwards, a series of free-running CFD simulations are carried out to analyse the manoeuvrability of the ship characterised by a traditional single rudder / single propeller configuration in different environmental conditions. It is revealed that the environmental conditions applied in this thesis have a strong effect on the manoeuvring performance of the ship, including the hydrodynamic loads, kinematic parameters, turning indices, and trajectories through comparative analyses.

Finally, the main results obtained from each chapter of this thesis are summarised and discussed, and recommendations for future work are made.

It is highly believed that the general framework presented in this thesis could encourage academic researchers to participate in research on manoeuvring problems by performing free-running CFD simulations without much difficulty. It is also expected that the numerical results drawn from the hydrodynamic analyses in this thesis will provide navigators with a deeper insight into the ship manoeuvrability in real sea states as well as support them in proper decision-making for ship handling actions to avoid collision. In addition to this, the high-fidelity CFD model developed in this thesis can easily be combined with a path-following algorithm for maritime autonomous surface ships (MASS), providing a valuable contribution to enhancing the safety of autonomous marine navigation.

1. INTRODUCTION

1.1. Background

With the increasing demand for marine transportation, shipping activities have accounted for more than 80% of global trade (Cepeda et al., 2019). The reliance on water-borne transportation has contributed to the number of maritime accidents causing serious harm to life, property, and ocean environment. According to the Annual Overview of Marine Casualties and Incidents 2020 released by EMSA (2020), the navigation casualties associated with collision, contact and grounding incidents are responsible for more than 44% of all marine incidents. Without a doubt, inadequate manoeuvring actions by Masters and navigation officers, who are in charge of ship handling with a high focus on navigation safety, are recognised as the leading cause of such maritime accidents. Zhang and Li (2017) pointed out that rough sea conditions were closely associated with a great number of marine accidents. In addition, Ventikos et al. (2018) showed a close correlation between safe navigation and adverse weather conditions by carrying out the statistical analysis of navigational accidents related to the failure of manoeuvrability. In this regard, it is imperative to understand ships' manoeuvring behaviours in real sea states to ensure navigational safety at sea.

The Marine Environment Protection Committee (MEPC) of the International Maritime Organization (IMO) adopted the interim guidelines for determining minimum propulsion power to maintain the manoeuvrability of ships in adverse conditions which is specifically concerned with the course keeping capability in waves (IMO, 2014). Following this, a specialist committee responsible for the manoeuvring performance of ships in waves was formed by the 29th International Towing Tank Conference (ITTC, 2017b). Such documents have been recently updated in an effort to enhance navigational safety at sea (IMO, 2021; ITTC, 2021c). As noted, recent trends in ship manoeuvres show an increasing demand for accurately evaluating a ship's manoeuvrability in waves, attracting more attention from academic researchers.

An accurate prediction of ship manoeuvrability in a real seaway is one of the most challenging problems in ship hydrodynamics, attributed to the complexity of the flow arising from the hydrodynamic interactions between the hull, propeller, rudder, and external disturbances during manoeuvres (Broglia et al., 2015). To date, theoretical methods have been widely used for the prediction of ship manoeuvring characteristics in waves; these approaches rely on assumptions from the potential flow theory. However, the reliability of the potential flow theory is limited due to the lack of physics associated with viscous and turbulent effects and the free surface resolution, which are significant for manoeuvring problems. Hence, such effects which are ignored in the potential flow theory should be incorporated in the numerical codes. In light of this, Reynolds-Averaged Navier-Stokes (RANS) approaches are very attractive alternatives to the theoretical methods since they are capable of directly accounting for viscous effects in their calculations (Tezdogan et al., 2015).

Free-running tests in wave basins, as an experimental method, have been perceived to be the most reliable approach in predicting the manoeuvrability of a ship in waves since they are the closest method to mimic real operating conditions. Experimental data, thanks to high reliability,

are usually used as benchmark data sets for comparison with other approaches. However, it is very costly and time-consuming to prepare a ship model equipped with a controllable rudder and propeller and arrange the facilities suited to the experiments. For example, a large wave basin, manoeuvring control units, and other measurement devices should be additionally fitted to test facilities in order to perform free-running tests in waves. Due to these demanding requirements, most research organisations have had to convince themselves for restricting their experiments to calm water cases only. As a result, ship manoeuvring experiments in waves have been limitedly conducted at a few research institutes such as the Iowa Institute of Hydraulic Research (IIHR), Hiroshima University (HR), and Korea Research Institute of Ships and Ocean Engineering (KRISO).

Computational Fluid Dynamics (CFD) techniques, on the other hand, are increasingly gaining popularity as a universal tool applicable to ship hydrodynamic problems as computational capabilities increase more and more. Advances in computational power and numerical algorithms have made it possible to perform fully nonlinear simulations of ship manoeuvres in waves, accounting for viscous and turbulent effects being important on ship manoeuvring. The applications of CFD in manoeuvring problems have remarkable advantages in providing very detailed results including hydrodynamic forces and moments, surface elevations and velocity/pressure fields which lead to a better interpretation of the hydrodynamic phenomena occurring during ship manoeuvres. It is therefore expected that CFD-based techniques will become an indispensable method for the analysis of ship manoeuvrability in waves for the foreseeable future.

This thesis is based on unsteady RANS approaches. The main focus will lie in the CFD-based unsteady RANS simulations of ship manoeuvres and seakeeping performance in waves. This can be tackled by conducting unsteady Reynolds-Averaged Navier-Stokes computations coupled with the equations of rigid body motion with full six degrees of freedom.

To the best of this author's knowledge, this thesis introduces novel research targeting practical aspects of ship manoeuvrability, course keeping control, and seakeeping performance in waves, as discussed in Section 1.2.

1.2. Research Motivations and Novelty

Free-running CFD simulations (based on unsteady RANS approaches) are progressively gaining popularity for manoeuvring prediction since they can directly take into account both viscous and rotational effects in the numerical methods, which is significant in ship manoeuvring. However, due to its brevity, there are no definite guidelines and recommendations regarding the numerical setup of the free-running CFD simulation in different environmental conditions such as waves, shallow waters, and currents. Thus, a general framework is developed for the analysis of ship manoeuvrability, course-keeping control, and seakeeping using the unsteady RANS computation, with a particular focus on the numerical modelling for a free-running CFD model (Chapter 4).

Ships are exposed to various environmental loads such as waves, wind, and currents during their operations at sea. Such external disturbances can lead to substantial changes in the behaviour of a ship during manoeuvring when compared to its inherent behaviour in calm water.

Among these disturbances, waves have been recognised as the most influential factor leading to substantial changes in a ship's performance. Thus, the manoeuvring behaviour of a ship in waves needs to be properly understood and handled in real navigation.

Not surprisingly, the ITTC Manoeuvring Committee (ITTC, 2021c) has focused mainly on the issues of ship manoeuvrability in waves, with particular attention to the state-of-the-art methods for ship manoeuvrability prediction. In addition, the Marine Environment Protection Committee (MEPC) of the IMO has provided the guidelines for determining minimum propulsion power to maintain the manoeuvrability of ships in adverse conditions to ensure its navigational safety at sea (IMO, 2021). Nevertheless, due to its brevity, very few studies managed to discuss the impact of waves on the manoeuvring performance of vessels.

In practice, Masters and navigation officers have limited access to the shipyard data which are generally measured by full-scale sea trials or model-scale experiments in accordance with ITTC (2021b). It should be borne in mind that such data offer limited information on the manoeuvrability of a ship in calm water; they are not equally relevant to the manoeuvrability in real sea states. To date, the vast majority of studies have been devoted to analysing the inherent manoeuvrability of a ship in calm water in conformity with the recommendation of ITTC (2021b), as will be presented in Chapter 3. In addition, several studies on the manoeuvrability of a ship in waves only focused on case-specific analyses with a few specific wave conditions, such that their findings are not able to provide the general observations on the relationship between waves and manoeuvring behaviours.

In this context, the contribution of waves to a ship's manoeuvrability is needed to be comprehensively studied with particular emphasis on various wave conditions covering the whole range of important wave directions, wavelengths, and wave heights. The research presented in this thesis utilised the strengths of URANS simulations to provide a comprehensive description of a ship's manoeuvrability, obtaining reliable and detailed results with much less cost when compared to Experimental Fluid Dynamics (EFD). The motivations and novelty behind the studies provided in the main chapters are as follows:

- **Effects of wave characteristics**: A ship’s performance is highly dependent on sea conditions affected by waves. From a hydrodynamic point of view, sea waves have an influence on ship motions and loads, as well as ship's manoeuvring performance. In other words, the seakeeping and manoeuvrability of a ship can be affected by a combination of wave characteristics such as wave height, period/length, and direction when a ship sails in waves. It has been observed in real operations that a ship can encounter various wave conditions characterised by different wave heights, periods/lengths, and directions. It is therefore critical to understand the contribution of wave characteristics to the manoeuvrability of a ship to ensure navigational safety at sea. A very limited number of studies dedicated to understanding the effects of wave properties on a ship's manoeuvrability exist in the open literature, however, they do not provide a systematic investigation on the course-keeping and turning capabilities of a ship in waves. In this regard, the present thesis will systematically analyse the effects of different wave characteristics on a ship's performance by means of an unsteady RANS solver. Emphasis is placed on course-keeping and turning capabilities

and seakeeping performance in waves (Chapters 5, 6, and 7).

- **Effects of propulsion loss in waves**: The loss of ship propulsion has been reported to be the most frequent cause of accidents at sea over the last few years. The loss of propulsive power has a notable effect on the behaviour of a ship during ship manoeuvring, and hence the manoeuvrability of ships suffering from propulsion loss should be accurately estimated for navigation safety. To date, however, numerous academic studies have only accounted for the manoeuvrability of a ship in normal operating conditions in which all machinery related to the navigation system are working properly. It is an undeniable fact that the past studies have the advantage of being informative in confirming the manoeuvring performance of ships in normal conditions. However, they were not able to offer insight into the understanding of the ship's manoeuvrability under the propulsion failure event in which a rotating propeller should be suddenly in a non-rotating state during manoeuvring. To the best of this author's knowledge, there is no study in the literature addressing the contributions of a propulsion failure to the manoeuvrability of a ship in waves. These points demonstrate that the investigation into the relationship between the propulsion failure and the manoeuvring performance of a ship in a real seaway is necessary (Chapter 8).
- **Ship manoeuvrability in irregular waves**: Ship manoeuvrability studies are usually carried out in calm and regular seas; however, an irregular sea state can better present the real operational conditions at sea, compared to both calm and regular seas. Without a doubt, irregular waves can lead to perceptible changes in the manoeuvring performance of a ship compared to that in calm water, which is closely associated with navigational safety at sea. For this reason, it is of importance to analyse the manoeuvrability of a ship in an irregular seaway. To the best of this author's knowledge, no such study focusing on course-keeping and turning manoeuvres has been published to date, using a fully nonlinear unsteady RANS model (Chapter 9).

In addition to waves, additional factors that can affect the performance of a ship during its operation should be also investigated in detail for navigational safety at sea.

- **Ship manoeuvrability in shallow water**: The manoeuvring performance of a ship in shallow water is substantially different from its performance in deep water, attributed to shallow water effects caused by the presence of a finite water depth. Without a doubt a ship will navigate in areas of shallow water at various times during its operational life (such as when approaching harbours or ports), which underscores the importance of understanding the shallow water effects on ship manoeuvrability. Limited studies exist which include free-running CFD simulations of ship manoeuvrability in shallow water, however, they do not present any discussion about the course keeping and turning capabilities of a ship (Chapter 10).
- **Ship manoeuvrability in currents**: The manoeuvring behaviour of a vessel in currents differs remarkably from its behaviour in water without a current, stemming from hydrodynamic effects caused by the presence of the current. Given that vessels operating in open seas and coastal waters are mostly exposed to ocean currents, it is important to have an understanding of the influence of currents on ship

manoeuvrability. To the best of this author's knowledge, there exist no studies on the influence of currents on ship manoeuvrability due to experimental restrictions. The need to overcome these impediments identified in experimental approaches has encouraged the development of a cost-effective and high-fidelity method for the evaluation of ship manoeuvrability in currents (Chapter 11).

1.3. Thesis Structure

With regard to the structure of this thesis, it consists of 12 chapters.

- Chapter 2 (RESEARCH AIM AND OBJECTIVES) presents the research aim and objectives with a description of specific tasks designed to achieve them.
- Chapter 3 (LITERATURE REVIEW) is devoted to a literature review of previous publications on all aspects of ship manoeuvrability. It first presents an overview of current standards and guidelines regarding the assessment of ship manoeuvrability, and then outlines a classification of the methods widely applied to manoeuvring problems. Finally, an in-depth literature review is provided with a focus on the specific areas that will be addressed in the main chapters of this thesis.
- Chapter 4 (METHODOLOGY) illustrates the general methodology proposed in the present thesis and provides a detailed description of the numerical setup of the free-running CFD model developed.
- Chapter 5 (FREE-RUNNING CFD SIMULATIONS FOR DIFFERENT REGULAR WAVE DIRECTIONS) presents a numerical study of ship manoeuvrability in regular waves of different directions by means of a fully nonlinear unsteady RANS solver. In this chapter, two representative free-running manoeuvres are conducted, namely, course keeping control and standard turning circle manoeuvres in regular waves covering a range of important wave directions. The results obtained are compared with available experimental data and are found to be in good agreement. It is shown that the manoeuvring behaviours of a ship are significantly dependent on the direction of wave propagation.
- Chapter 6 (FREE-RUNNING CFD SIMULATIONS FOR DIFFERENT REGULAR WAVE LENGTHS) presents fully nonlinear unsteady RANS simulations to predict the course-keeping and turning capabilities of the KRISO Container Ship model in regular waves of different wavelengths. The manoeuvring analyses are carried out in bow waves covering a range of important wavelength-to-ship-length ratios for constant wave height. It is demonstrated that the wavelength has a significant influence on the manoeuvring performance.
- Chapter 7 (FREE-RUNNING CFD SIMULATIONS FOR DIFFERENT REGULAR WAVE HEIGHTS) presents details of a numerical study on free-running CFD simulations to estimate the manoeuvrability of the KCS under various wave height conditions. Manoeuvring analyses are carried out in the bow quartering waves of a range of wave heights for constant wavelength. The results clearly reveal that wave

heights have a strong effect on the manoeuvring behaviour of the ship, including ship's speeds, seakeeping behaviour, and critical turning indices through comparative analyses under different wave height conditions.

- Chapter 8 (FREE-RUNNING CFD SIMULATIONS FOR A SHIP WITH PROPULSION SYSTEM FAILURE IN REGULAR WAVES) provides a numerical investigation into the effects of a propulsion failure on the manoeuvrability of the KRISO Container Ship (KCS) using a fully nonlinear URANS model, which is capable of resolving complex fluid-structure interactions with high accuracy. A series of case studies are performed to compare the ship performances of both the normal and propulsion loss condition, especially for the course keeping and turning circle manoeuvres.

- Chapter 9 (FREE-RUNNING CFD SIMULATIONS FOR IRREGULAR WAVES) presents the CFD-based hydrodynamic analyses of ship course keeping control and turning performance in irregular waves. Comparisons with the ship manoeuvrability in both calm and regular seas are also made with a view to identifying the changes in the manoeuvring characteristics of the ship.

- Chapter 10 (FREE-RUNNING CFD SIMULATIONS FOR SHALLOW WATERS) provides an analysis of the shallow water effects on the manoeuvring performance of a container ship. To this purpose, the free-running model for the prediction of ship manoeuvrability in shallow water has been developed by means of an unsteady RANS solver. A series of manoeuvring simulations are performed in shallow waters covering a range of important water depth to draft ratios, and partially validated with the available experimental data from a free-running test.

- Chapter 11 (FREE-RUNNING CFD SIMULATIONS FOR CURRENTS) presents a numerical study of ship manoeuvrability in different currents. Firstly, a model-scale container ship (the KRISO Container Ship) is used to develop the Computational Fluid Dynamics (CFD) model capable of performing a self-propelled free manoeuvre. Then, a validation study is carried out to assess the validity of the CFD model by comparison with the available experimental results from a free-running test. Following this, a series of manoeuvring simulations (i.e., standard turning manoeuvres) in deep waters covering a range of current speed to ship speed ratios are conducted using the present CFD model.

- Chapter 12 (DISCUSSION AND CONCLUSIONS) provides a discussion of the achievement of the research aim and objectives, contributions to the maritime industry, as well as limitations of this research and recommendations for future work. It also summarises the meaningful conclusions drawn from this research work.

2. RESEARCH AIM AND OBJECTIVES

2.1. Aim and Objectives

The overall aim of this thesis is to contribute to enhancing the safety of navigation at sea, providing a comprehensive understanding of the manoeuvring performance of a ship in a real seaway. To this purpose, the main chapters of this thesis will be devoted to hydrodynamic analyses of ship manoeuvrability, course keeping control, and seakeeping performance using CFD.

The specific objectives of this thesis are as follows:

- Objective 1: To examine the shortcomings of the current standards, existing practices, and studies on ship manoeuvrability based on the critical review of the literature and to identify open research questions
- Objective 2: To develop a general framework for the analysis of ship manoeuvrability using CFD, with particular focus on the numerical modelling for free-running CFD model
- Objective 3: To investigate the effects of wave directions on the manoeuvring performance of a ship by means of an unsteady RANS solver
- Objective 4: To evaluate the contributions of wave lengths to the course-keeping and turning capabilities of a ship performing fully nonlinear unsteady RANS simulations
- Objective 5: To examine the correlations between a ship's manoeuvrability and wave heights using a CFD-based RANS solver
- Objective 6: To introduce a CFD-based unsteady RANS simulation model to assess the effects of a propulsion failure on the manoeuvrability of a ship in waves
- Objective 7: To analyse the effects of irregular waves on the course-keeping and turning capabilities of a ship using a fully nonlinear unsteady RANS model
- Objective 8: To predict the shallow water effects on the manoeuvring performance of a ship by employing an unsteady RANS solver
- Objective 9: To evaluate the effects of ocean currents on the manoeuvrability of a ship with particular emphasis on the turning capability, performing free-running CFD simulations
- Objective 10: To recommend future studies to enhance an understanding of the ship manoeuvrability at sea. This research is expected to be used as a guide for exploring extended scopes while investigating limitations identified by this thesis

2.2. Tasks

In this PhD study a series of tasks have been performed as presented in Figure 2.1 with an aim to achieve the research aim and objectives.

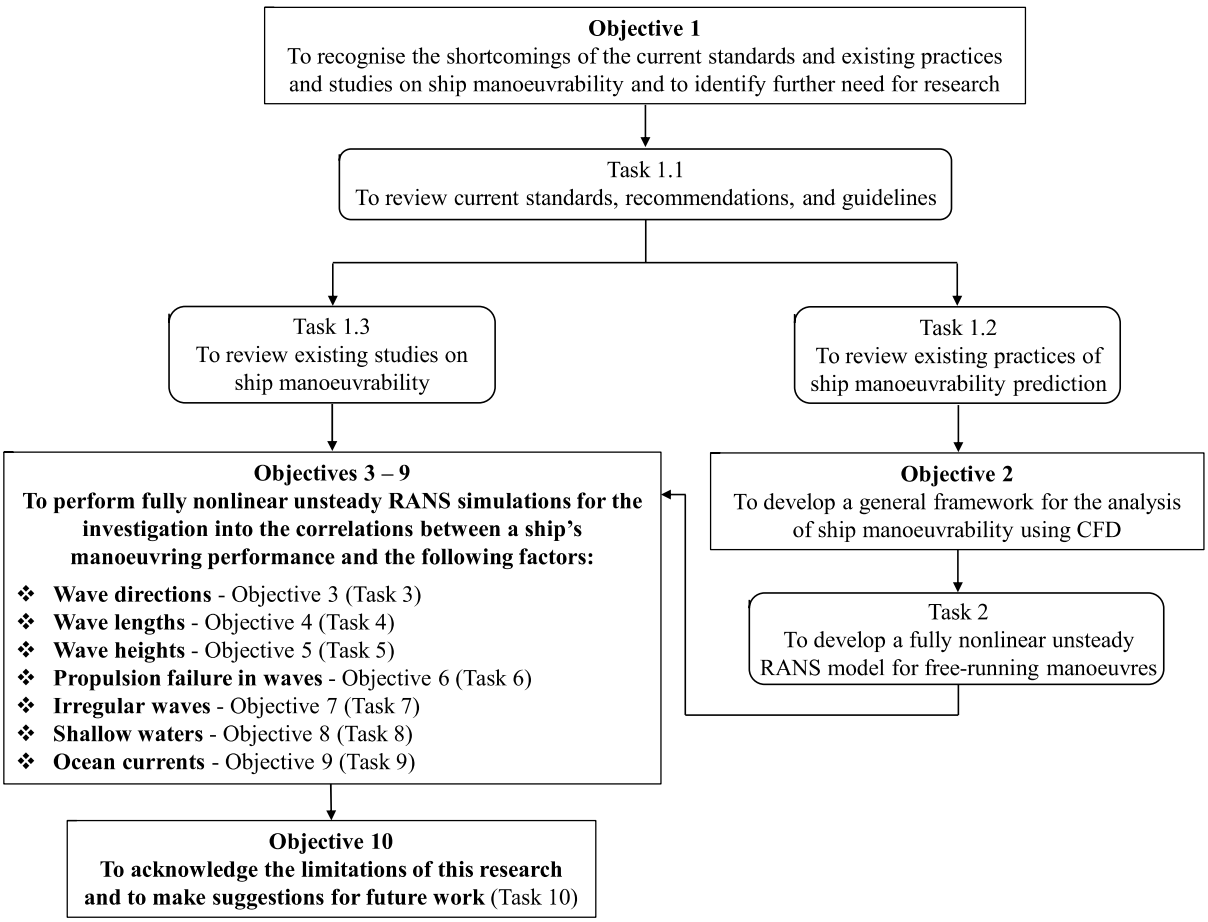

Figure 2.1 Flowchart for the research work presented in this thesis.

Tasks 1.1 - 1.3: Literature review (Chapter 3)

A critical literature review was conducted based on the publications related to ship manoeuvrability to identify what needs to be further studied in this field. In particular, the current standards and practices pertinent to the assessment of the manoeuvring performance of a ship were thoroughly reviewed to recognise their shortcomings.

Task 2: CFD modelling of a free-running ship (Chapter 4)

It was envisaged that a high-fidelity model for ship manoeuvrability prediction would be necessary to obtain reliable numerical results. Hence, it was decided to employ CFD-based techniques which can take into account viscous effects as well as resolve complicated mutual interactions between the hull, propeller, and rudder during manoeuvres. In this task, a numerical modelling framework for free-running CFD simulations was first proposed. Based on the numerical methods presented in the framework, a fully nonlinear unsteady RANS model was developed to perform a self-propelled free manoeuvre in a CFD environment.

Tasks 3 – 9: Hydrodynamic analyses of ship manoeuvrability, course keeping control, and seakeeping (Chapters 5 - 11)

Major tasks to achieve Objectives 3 – 9 are to investigate the following effects on the manoeuvring performance of a ship:

- Different wave directions - Task 3 (Chapter 5);
- Different wave lengths - Task 4 (Chapter 6);
- Different wave heights - Task 5 (Chapter 7);
- Propulsion system failure in waves - Task 6 (Chapter 8);
- Irregular waves - Task 7 (Chapter 9);
- Shallow water – Task 8 (Chapter 10); and
- Ocean currents - Task 9 (Chapter 11).

A series of free-running CFD simulations to estimate the manoeuvrability of a ship in various wave conditions (Tasks 3 - 7) were carried out. In addition to this, additional numerical studies of ship manoeuvrability in shallow water (Task 8) and currents (Task 9) were performed using a URANS solver to identify the effects of finite depths and currents on the manoeuvring characteristics. The results obtained were combined and plotted in form of graphs which could provide a general relationship between the ship's manoeuvring performance and the critical environmental factors.

Task 10: Suggestions for future work (Chapter 12)

The findings obtained from each chapter of the present thesis were reviewed, with an emphasis on the limitation of this research. Further work needed in this field was recognised, and recommendations were made for future research.

3. LITERATURE REVIEW

3.1. Introduction

A preliminary literature review is conducted in this chapter to identify the literature gaps in the field of ship manoeuvrability and to justify the aim and objectives of this PhD thesis. Firstly, an overview of current standards and guidelines concerned with the evaluation of ship manoeuvrability will be described. Then, a classification of the methods that have been still widely adopted for the prediction of ship manoeuvrability will be made. Finally, the chapter will be devoted to a survey of the literature on the specific areas of research relevant to the main chapters of this thesis.

3.2. Current Standards and Guidelines

The prediction of a ship's manoeuvring performance in calm water has practically become an industry norm by the IMO standards for ship manoeuvrability (IMO, 2002; ITTC, 2021b). According to the IMO requirements, manoeuvring tests should be performed in the calmest possible weather conditions as well as in deep water (more than four times the mean draught of a ship). Accordingly, naval architects and marine engineers generally evaluate the inherent manoeuvrability of a ship in deep unrestricted water such as turning, yaw checking, and course keeping abilities during the initial stages of design through model-scale experiments or numerical simulations. As a result, Masters and navigation officers in real navigation have only access to the shipyard data pertinent to the inherent manoeuvrability of a ship in calm water, limiting their understanding of ship handling in a real seaway. It should be borne in mind that environmental loads (i.e., external disturbances) can cause perceptible changes in the manoeuvrability of a ship during operation when compared to its inherent manoeuvrability in calm water.

The introduction of the Energy Efficiency Design Index (EEDI) by the IMO to increase energy efficiency and reduce greenhouse gas (GHG) emissions of shipping has raised interest in ship manoeuvrability in waves. To achieve the stringent requirements of the EEDI regulation, operating ships should reduce carbon dioxide (CO_2) emissions. One way of complying with these demanding EEDI requirements is to reduce the installed main engine power, by which CO_2 emissions and fuel consumption can be decreased. However, vessels with insufficient propulsion power may have poor course-keeping and manoeuvring capabilities especially in rough seas, which can cause a serious ship safety problem. In response, the Marine Environment Protection Committee (MEPC) has adopted the guidelines for determining minimum propulsion power to maintain the manoeuvrability of ships in adverse conditions (IMO, 2021). According to the guidelines, a vessel can move forward with the speed of 2.0 knots through water in wind and wave directions from head to 30 degrees off-bow when operating in adverse weather conditions. Adverse conditions represent sea conditions with the following parameters (Table 3.1):

Table 3.1 The definition of adverse weather conditions, according to IMO (2021).

Significant wave height h_S, m	Peak wave period T_P, s	Mean wind speed V_W, m/s
6.0	7.0 to 15.0	22.6

In the meantime, the ITTC Advisory Council proposed a Technical Committee which is responsible for studying manoeuvring characteristics of a vessel in waves. The technical committee was established by the 28th International Towing Tank Conference (ITTC, 2017b). Following this, the SIMMAN workshop was organised in 2020 to discuss not only ship manoeuvring in calm water but also ship manoeuvring performance in waves (SIMMAN, 2020). In the Final Report and Recommendations to the 29th ITTC of the Manoeuvring Committee (ITTC, 2021c), an unsteady RANS approach has been recommended as a state-of-the-art method for estimating the manoeuvring performance of a ship in waves.

These standards and guidelines above clearly demonstrate the growing awareness of the importance of a ship's manoeuvrability in a real seaway.

3.3. Classification of Ship Manoeuvring Prediction Methods

At present, the prediction of the manoeuvring performance of a vessel has been generally addressed by means of indirect or direct approaches (Hasanvand and Hajivand, 2019).

The indirect methods (known as System-Based (SB) methods) involve performing manoeuvring simulations by solving simplified mathematical models. Two distinctive mathematical models have been mainly used, such as the Abkowitz model (Abkowitz, 1964) and the Manoeuvring Modelling Group (MMG) model (Inoue et al., 1981b; Yasukawa and Yoshimura, 2015). As an example, the MMG model for three degrees of freedom (DOF) is described as follows:

$$\begin{cases} m(\dot{u} - rv) = X \\ m(\dot{v} - ru) = Y \\ I_{ZZ}\dot{r} = N \end{cases} \tag{3.1}$$

in which m is the mass of body, I_{ZZ} is the moment of inertia about z-axis in the body frame

$u, v, \dot{u}, \dot{v}$ are the surge/sway velocities and accelerations

$r, \dot{r}$ are the yaw angular velocity and acceleration

X, Y are the surge and sway resultant forces acting on the ship

N is the yaw resultant moment acting on the ship

The hydrodynamic forces (X, Y) and moment (N) in Equation (3.1) are decomposed into three components in the MMG model: the bare hull, rudder, and propeller.

$$\begin{cases} X = X_{\mathrm{H}} + X_{\mathrm{R}} + X_{\mathrm{P}} \\ Y = Y_{\mathrm{H}} + Y_{\mathrm{R}} \\ N = N_{\mathrm{H}} + N_{\mathrm{R}} \end{cases} \tag{3.2}$$

where the subscripts H, R, P denote hull, rudder, and propeller, respectively. For more details on the MMG model, reference can be made to Yasukawa and Yoshimura (2015).

In the indirect approaches, the complete set of hydrodynamic coefficients (related to the terms on the right-handed side of Equation (3.2)) need to be obtained from experiments or CFD-based simulations (ITTC, 2021a). A major advantage of the indirect methods is that they are not time-consuming in terms of performing the manoeuvring simulation. However, the accuracy of these mathematical models may be limited due to uncertainties in the hydrodynamic coefficients. Moreover, the complex interactions between the hull, rudder, and propeller are very difficult to precisely capture which could diminish the calculation accuracy (Mofidi and Carrica, 2014). It is worth noting that the mathematical models together with the potential flow theory can be used for the prediction of ship manoeuvring characteristics in waves. Given that the potential flow theory neglects the influence of viscosity and thus suffers some limitations due to the lack of physics related to viscous effects, the simplified mathematical models cannot accurately resolve the complex manoeuvring behaviour of a ship in waves.

The direct approaches include conducting free-running model experiments in a manoeuvring basin or simulating free-running manoeuvres by means of Computational Fluid Dynamics (CFD). Free-running tests in wave basins have been recognised as the most robust way to evaluate the manoeuvring performance of ships in waves. This experimental-based research can provide highly reliable information about the manoeuvrability of a ship since it is considered the closest way to mimic real operating conditions. However, it is time-consuming, expensive, and technically demanding as well as requires a large wave basin. As a result, ship manoeuvring experiments in waves have been limitedly conducted at a few research institutes, as also mentioned in Section 1.1.

With the great progress in computer science and technology, the CFD has become a high-fidelity numerical method to perform direct free-running simulations to assess a ship's manoeuvring and seakeeping performance in waves. A CFD method can incorporate both viscous and rotational effects in the flow and free surface waves, and therefore accurately resolve the complex fluid-structure interactions. In other words, CFD can provide manoeuvring results with higher accuracy, compared to the indirect approaches based on simplified mathematical models. Currently, RANS-based CFD simulations of free-running manoeuvres have been highly preferred by researchers thanks to high accuracy and relatively low computational costs. Although it is true that the manoeuvrability of a ship can be more accurately estimated by Large Eddy Simulation (LES) or Direct Numerical Simulation (DNS) than RANS methods, LES/DNS simulations are computationally very expensive; their applications to free-running manoeuvres are not feasible in practice.

The Reynolds-averaged Navier-Stokes equations are time-averaged equations of motion for fluid flow. The equations are based on Reynolds decomposition, whereby a flow variable is decomposed into its time-mean and fluctuating components in a turbulent flow. For unsteady

incompressible flows, the averaged continuity and momentum equations are expressed in tensor notation and Cartesian coordinates as in the following expressions (Ferziger and Peric, 2020):

$$\frac{\partial(\rho\bar{u}_i)}{\partial x_i} = 0 \tag{3.3}$$

$$\frac{\partial(\rho\bar{u}_i)}{\partial t} + \frac{\partial}{\partial x_i}\left(\rho\bar{u}_i\bar{u}_j + \rho\overline{u'_\iota u'_\jmath}\right) = -\frac{\partial\bar{p}}{\partial x_i} + \frac{\partial\bar{\tau}_{ij}}{\partial x_i} \tag{3.4}$$

where ρ is the fluid density, $\bar{u}_i$ is the averaged velocity vector, x_i (i=1, 2, 3) are the Cartesian coordinates, $\rho\overline{u'_\iota u'_\jmath}$ is the Reynolds stresses, $\bar{p}$ is the mean pressure and $\bar{\tau}_{ij}$ are the mean viscous stress tensor components. This stress tensor for a Newtonian fluid can be given in Equation (3.5)

$$\bar{\tau}_{ij} = \mu\left(\frac{\partial\bar{u}_i}{\partial x_j} + \frac{\partial\bar{u}_j}{\partial x_i}\right) \tag{3.5}$$

in which μ is the dynamic viscosity.

A turbulence model is required when performing RANS simulations, to complete the RANS equations (for the closure of the system) and to address the uncertainty of the stress tensor (Ferziger and Peric, 2020).

3.4. Manoeuvring Problems in Deep Unrestricted Water

A set of linear and non-linear hydrodynamic coefficients for the SB method can be determined from captive model experiments such as the Planar Motion Mechanism (PMM) or the Circular Motion Test (CMT), such that the trajectory and kinematic parameters of a ship during manoeuvres can be estimated.

Inoue et al. (1981a) performed a number of captive model experiments to investigate the hydrodynamic forces and moments acting on a ship in even keel and trimmed conditions. They analysed the relations between the forces and loading condition of a ship using a regression method and proposed the semi-empirical formula for the practical estimation of the hydrodynamic derivatives associated with the lateral forces and moments experienced by a ship during manoeuvres in calm water. It is an undeniable fact that using the semi-empirical formula has the advantage of enabling the determination of the hydrodynamic coefficients without performing experiments; however, the validity of such coefficients cannot be guaranteed (Liu et al., 2015).

Son and Nomoto (1981) carried out a numerical study to analyse the yaw-sway-roll coupling motion of the S175 container ship (characterised by a single rudder/ single propeller configuration) during turning manoeuvres in calm water by means of the SB method. They determined the hydrodynamic coefficients of the ship from PMM tests. Skjetne et al. (2004) performed path-following numerical simulations using a complete nonlinear dynamic manoeuvring model of a ship. They presented a methodology for the task of manoeuvring an offshore supply vessel along desired paths in calm water without environmental disturbances. The hydrodynamic parameters of the nonlinear model were identified by carrying out captive

model tests and the results of the free-running experiment using a robust control law demonstrated that the task for accurate manoeuvre along desired paths by the nonlinear mathematical model could be achievable. In Maimun et al. (2011), a numerical investigation on the manoeuvrability of a pusher-barge system in calm water was conducted using the MMG model. They determined the hydrodynamic coefficients of the pusher-barge by means of captive model experiments using a planar motion mechanism and then simulated turning and zigzag manoeuvres in the time domain to evaluate the manoeuvring characteristics. Similar System-Based simulations were presented in Shin and Choi (2011), where a series of captive model tests were carried out to predict the manoeuvring performance of the KCS model in calm water. All hydrodynamic coefficients required for using the MMG model were acquired from PMM and CMT tests. Their simulation results of turning-circle and zigzag manoeuvres were compared with those of other research institutes. The application of PMM experiments to the prediction of the manoeuvrability of manifold models can be found in Guedes et al. (2018); Kleine et al. (2018).

Recently, CFD-based simulations have been used to determine the hydrodynamic coefficients of a ship, virtually performing captive model tests (i.e., PMM and CMT tests) in a CFD environment. Moreover, experimental data, which can be used as benchmark data sets for validation of CFD computations of ship manoeuvres, were reported in the SIMMAN 2008 workshop organised in Copenhagen, Denmark in April 2008 (Stern et al., 2011). In SIMMAN 2008, EFD data for PMM, CMT, and free-running model tests in deep unrestricted water were presented for different types of ships such as a container ship (KCS), a surface combatant (DTMB 5415), very large crude oil carriers (KVLCC1 and KVLCC2). These experimental data have encouraged a number of researchers to study the manoeuvring characteristics of ships in calm water using CFD, currently being employed as a resource to validate their CFD predictions.

In Simonsen et al. (2012), standard 10°/10°, 20°/20° zigzag and 35° turning circle manoeuvres in calm water were simulated using the SB method based on a combination of computed and measured hydrodynamic input data. In their work, they carried out RANS simulations of virtual static PMM tests (i.e., oblique towing tests) to calculate the relevant hydrodynamic coefficients of a ship using the commercial CFD software STAR-CCM+. The overall agreement between the computed and measured forces and moments was found satisfactory. In addition, the manoeuvring results simulated by the SB approach were found in good agreement with available experiments. Hajivand and Mousavizadegan (2015a, 2015b) simulated a series of captive model tests in a CFD platform to obtain the linear and nonlinear velocity dependent damping coefficients of the DTMB 5512 model ship by means of a RANS solver. A satisfactory agreement was found between the simulated results and available experimental data. Similar computations were conducted in Sung and Park (2015), in which the bare hull manoeuvring coefficients of the KCS, KVLCC1 and 2 were determined to predict the manoeuvrability of the ships in calm water by means of RANS-based virtual captive model tests. In addition, several studies presented in He et al. (2016); Guo and Zou (2017); Guo et al. (2018); Liu et al. (2018); Balagopalan et al. (2020); Franceschi et al. (2021) performed the RANS simulations of captive model tests to determine the hydrodynamic derivatives and to simulate ship manoeuvres (SB simulations).

However, as stated previously, the simplified mathematical models for the SB method cannot accurately resolve the interactions between hull, propeller, and rudder during manoeuvring. Another CFD application is the free-running simulations of standard manoeuvres (i.e., direct approaches) with rotating propeller(s) and steering rudders(s). These direct CFD approaches have the capability to account for viscous and turbulent effects being important on ship manoeuvring as well as do not use any consumables (as opposed to experiments). In addition, free-running CFD simulations are advantageous in that they can provide very detailed hydrodynamic results with respect to ship manoeuvres that would be very difficult to measure experimentally. These benefits of CFD simulations have attracted great attention from academic and industrial fields in recent years, being referred to as high-fidelity simulations.

Muscari et al. (2008), as the first researchers in the field of CFD applications for the direct prediction of ship manoeuvrability, implemented free-running CFD simulations using an unsteady Reynolds Averaged Navier-Stokes approach. They evaluated the turning behaviours of a self-propelled twin-screw patrol vessel in calm water, where the flow field interaction between the ship hull and the propeller was taken into account by a simplified propeller model. Similarly, Broglia et al. (2013) carried out free-running manoeuvres using URANS simulations to deeply investigate the turning capability of a twin-screw single-rudder model in deep calm water. In this work, a dynamic overlapping grid method was implemented to handle complex geometries and multiple bodies in relative motion, whilst the rotating propeller effects were modelled based on the actuator disk concept. Then, Mofidi and Carrica (2014) performed free-running zigzag manoeuvres in deep calm water for the fully appended geometry, eliminating the modelling of a rotating propeller to take into account all physics involved in the manoeuvre (utilising CFDShip-Iowa, which is a piece of general-purpose CFD software developed at the University of Iowa). The numerical results obtained from their study consisting of kinematic and dynamic parameters during the manoeuvre were validated against the available measured data, concluding that using CFD to compute standard manoeuvres with moving propeller and rudder is highly feasible. In Broglia et al. (2015), the turning manoeuvres of a self-propelled naval supply vessel were thoroughly analysed by means of an unsteady RANS solver. The vessel considered in this work was characterised by a fully appended single rudder/twin screws configuration. Each propeller was modelled by an actuator disk, well modified to resolve oblique flow effects. They presented the distribution of hydrodynamic forces and moments acting on the hull, rudder, and stern appendages in detail to provide a deeper insight into the dynamic performance of the vessel. The results obtained using the CFD methods were compared to free-running model tests and showed a good agreement in respect of both kinematic and trajectory parameters. The authors further extended their studies to different stern appendages, namely the twin rudder configuration and centreline skeg (Dubbioso et al., 2016). Emphasis was placed on the turning behaviours of the new configuration, compared to the single rudder configuration in terms of the hydrodynamic forces and moments acting on the hull, appendages during manoeuvres. An implementation of the dynamic overset method in OpenFOAM with application to KCS self-propulsion and zigzag manoeuvres in calm water was presented by Shen et al. (2015). Their CFD results for self-propulsion and zigzag simulations were found to be in good agreement with the experimental data, although relatively coarse grids were applied in their CFD simulations. In Wang et al. (2016), URANS simulations for the ONR Tumblehome ship model performing 6DOF self-propulsion and turning circle

manoeuvres in calm water were described. It has to be stated that in this work the propeller were directly discretised, such that the strict requirements for the resolution of the propeller flow should be complied with. By comparison with available experimental results, the validity of the free-running CFD simulations has been proved. The comparison in terms of both trajectory and kinematic parameters showed an overall agreement. Finally, Kim et al. (2021c) investigated the manoeuvrability of the KVLCC2 performing turning and zigzag manoeuvres in calm water. They used the CFD software STAR-CCM+, as a RANS solver to carry out free-running simulations. Their research demonstrated the effectiveness of the free-running CFD simulation to predict the manoeuvrability of a ship, with satisfactory comparisons between the CFD results and experiments.

3.5. Unified Manoeuvring and Seakeeping Analyses in Waves

As can be seen in IMO (2014); ITTC (2017b); IMO (2021); ITTC (2021c), an increasing demand for understanding a ship's manoeuvring performance in waves has drawn more and more attention from academic and industrial audiences. However, to date, current research on the effect of waves on a ship's manoeuvring behaviour has been highly limited in number as well as in scope. An experimental investigation on the manoeuvrability of a vessel in waves was performed within the European funded Project SHOPERA, as presented in Papanikolaou et al. (2015); el Moctar et al. (2016); Papanikolaou et al. (2016); Sprenger et al. (2016). In their research, the manoeuvring characteristics of the KVLCC2 and DTC ship models were comprehensively investigated by carrying out turning and zigzag manoeuvres in different wave conditions (parameters of variation: wave direction, wave period, wave height), contributing to the establishment of a benchmark and validation database regarding manoeuvring problems in waves. Sanada et al. (2019) performed free-running tests of the ONR Tumblehome model in regular waves at the Iowa Institute of Hydraulic Research (IIHR) wave basin. In their experiments, course keeping, turning, and zigzag manoeuvres were carried out for three different wavelengths to identify the effect of wavelengths on the manoeuvrability of the ship. Extensive experimental data consisting of ship trajectories and 6DOF motions/velocities for all tests were presented, confirming that the ONR Tumblehome ship has higher manoeuvrability than that of S-175 and Very Large Crude Carrier (VLCC) due to its slender hull characterised by the twin-rudder twin-screw configuration. Hasnan et al. (2019) analysed the turning performance of ships in short-crested irregular waves by means of free-running tests; two types of ship were considered: the KVLCC2 and the KCS. The free-running tests were carried out in five head waves with different patterns based on the same wave conditions (significant wave height, mean wave period, and main wave direction). In Kim et al. (2019), an experimental study on the manoeuvrability of a well-known benchmarking ship (the KVLCC2) was conducted performing free-running model tests in different regular waves (with the variations of directions, lengths, and heights). They highlighted the contributions of wave parameters such as directions, lengths, and heights to the turning performance of the ship, with particular emphasis on its trajectories. The authors extended their previous study to the experimental analysis of the course-keeping and turning behaviours of the KVLCC2 in long-crested irregular waves (representing sea states 5 and 6), performing free-running model tests (Kim et al., 2022). Yasukawa et al. (2021) discussed the turning capabilities of the KCS ship model in regular waves in regular waves with a wave height of 3.6m in full scale (the ratio of wavelength to ship

length was 1.0), carrying out free-running model tests in a square tank at the National Research Institute of Fisheries Engineering, Hiroshima University. A detailed analysis in terms of ship trajectories, seakeeping performance, and kinematic parameters during turning manoeuvres in waves are reported in this work. It has to be mentioned that the experimental data produced from the free-running tests in their research can be available in SIMMAN (2020) and were used as benchmark data for validation in the later chapters of this thesis.

Apart from experiments, numerical models have been employed for the prediction of ship manoeuvring characteristics in waves. Over years of research, mathematical models combined with the potential flow theory have been used for these manoeuvring analyses. Fossen (2005) developed a unified state-space model for ship manoeuvring, station-keeping, and control in a seaway. However, this unified model has the underlying limitation that only some of the nonlinear wave effects are taken into account. Skejic and Faltinsen (2008) adopted a two-time scale model to combine the high-frequency seakeeping motion and the low-frequency manoeuvring motion in regular waves. The ship manoeuvring analysis was based on the nonlinear slender-body theory, while the mean second-order wave loads in incident waves were predicted by the potential flow theory. Seo and Kim (2011) used a 4 degrees of freedom MMG model along with a time-domain ship motion code to solve the wave-body interaction problem, in which the mean drift forces and moments were considered by using a direct pressure integration method. Their results showed similar trends with the experiments but with some discrepancies. In Subramanian and Beck (2015), a time-domain body exact strip theory was proposed to evaluate the manoeuvrability of a ship in a seaway. They used semi-empirical methods with an aim to estimate propeller characteristics, calm water resistance, viscous forces and rudder lift forces. In addition, the governing equations of rigid body motion were coupled to the hydrodynamic model to determine ship responses, using linearized free surface boundary conditions for stability and computational efficiency. The results obtained from turning circle simulations for the S-175 were compared against available experimental data, demonstrating their model is capable of capturing general qualitative aspects of the problem. Subsequently, a series of past research applied similar approaches to predict the behaviour of a ship during manoeuvres in waves (Zhang and Zou, 2016; Paroka et al., 2017). As pointed out in Wang and Wan (2018), however, those studies have revealed that analysis results obtained by the theoretical methods are highly likely to bring out some discrepancies with experimental data available. This underscores that the simplified mathematical models are not able to accurately capture the complex fluid-structure interactions between the hull, rudder, propeller, and waves.

As stated previously in Section 3.4, the studies devoted to free-running CFD simulations in calm water demonstrated the excellence of the CFD simulations with free-running ship models by showing good agreement between CFD results and the experimental data available. More recently, several researchers have started to focus on the ship's manoeuvrability in various wave conditions by applying the Stokes wave models. Wang et al. (2017) carried out RANS simulations to study the course keeping capability of the ONR Tumblehome ship in regular waves of different directions (i.e., head, bow quartering, and beam waves). They used naoe-FOAM-SJTU which is a CFD solver developed on the open-source platform OpenFOAM. In their study, a dynamical overlapping grid approach was used to handle large ship motions and rudder movement during free-running manoeuvres in waves. In addition, a course keeping

control module was developed with the aim of achieving course keeping demand. The simulation results were validated against the benchmark data from the Tokyo 2015 CFD Workshop on ship hydrodynamics. Good agreements were obtained for course keeping manoeuvres. Following this, free-running simulations of the ONR Tumblehome ship model in regular waves were further carried out for zigzag manoeuvres in waves of three different wavelengths(Wang et al., 2018), standard turning circle manoeuvres in head waves (Wang and Wan, 2018). Their CFD results agreed well with the available experimental data in terms of both ship trajectories and kinematic parameters, indicating free-running CFD simulations are reliable in predicting the manoeuvrability of a ship in waves.

3.6. Ship Manoeuvrability in Shallow Water

Toxopeus et al. (2013) presented a numerical investigation on shallow water effects on the hydrodynamic forces and moments of the KVLCC2, performing RANS simulations for a selected set of manoeuvring conditions and water depths. A series of captive model tests for steady drift motion and oscillatory yaw motion were carried out for different water depths at INSEAN (Rome Towing Tank). Their study demonstrated that when the ratio of water depth to draft is less than 1.5, limited water depth has a significant influence on ship resistance, forces and moments, and the local flow field around the ship. In Carrica et al. (2016), an experimental and numerical study on the manoeuvrability of the KCS in shallow water was performed. They conducted a 20/5 modified zigzag manoeuvre in which the approach conditions are Fr (Froude number) = 0.095 and h/D (depth to draft ratio) = 1.2. Free-running tests were carried out in the shallow water towing tank at Flanders Hydraulics Research and free-running CFD simulations were performed with the ship hydrodynamics code REX, a merge of the codes CFDShip-Iowa v4.5. In their work, the comparison in terms of kinematic and dynamic parameters confirmed the satisfactory agreement between available experimental free-running tests and their CFD predictions. In addition, the principal properties of the flow field were described, with particular attention to the strong mutual interactions between the hull, the propeller, the rudder, and the tank bottom (the sea bed). Lee and Hong (2017) carried out numerical simulations to analyse the hydrodynamic forces and moments acting on the KVLCC2 and DTC in different shallow waters by means of a RANS solver. It was revealed that the hydrodynamic forces moments experienced by the ship remarkably increased as the ratio of water depth to draft decreased. Liu et al. (2019) performed the virtual pure sway tests of the DTC model in shallow water to determine hydrodynamic derivatives by means of a RANS solver. The agreement between their CFD results and experimental data available was satisfactory in terms of the hydrodynamic forces and the resultant hydrodynamic derivatives.

3.7. Concluding Remarks

In this chapter, a broad survey of the literature was made on the previous studies in the field of ship manoeuvrability, together with the investigation of related existing standards and prediction methods. This literature review suggested that numerous past studies in this field have been devoted to the prediction of ship manoeuvrability in calm water. In addition, several previous studies which aimed to estimate the manoeuvring performance of a ship in waves only focused on case-specific analyses with a few specific wave conditions.

During this literature survey, the following aspects for further research in this field have been detected:

- There exist no CFD studies in the literature analysing the effects of wave directions, periods/lengths, and heights on the course keeping and turning capabilities of a ship.
- To date, no study has investigated the effects of a propulsion failure on the manoeuvrability of a ship in waves using a CFD-based unsteady RANS method.
- No study has been performed on the prediction of ship manoeuvrability in an irregular sea state using a fully nonlinear unsteady RANS model.
- The CFD studies performed to date have not predicted the course keeping and turning behaviours of a ship in shallow water.
- No study has looked into the effects of ocean currents on the manoeuvring behaviour of a ship using CFD.

The main chapters of this thesis (Chapters 5 - 11) are designed to fill the research gaps listed above by means of a state-of-the-art RANS approach.

4. Methodology

4.1. Introduction

This chapter will provide the general methodology used in this PhD thesis, with a detailed description of the numerical setup of the CFD model in the included sub-sections.

4.2. Research Methodology

As shown in Figure 4.1, the research methodology applied in this thesis comprises four main stages to assess the manoeuvring performance of a ship: 1) goal and scope, 2) numerical modelling, 3) execution of free-running simulations, and 4) results of analysis.

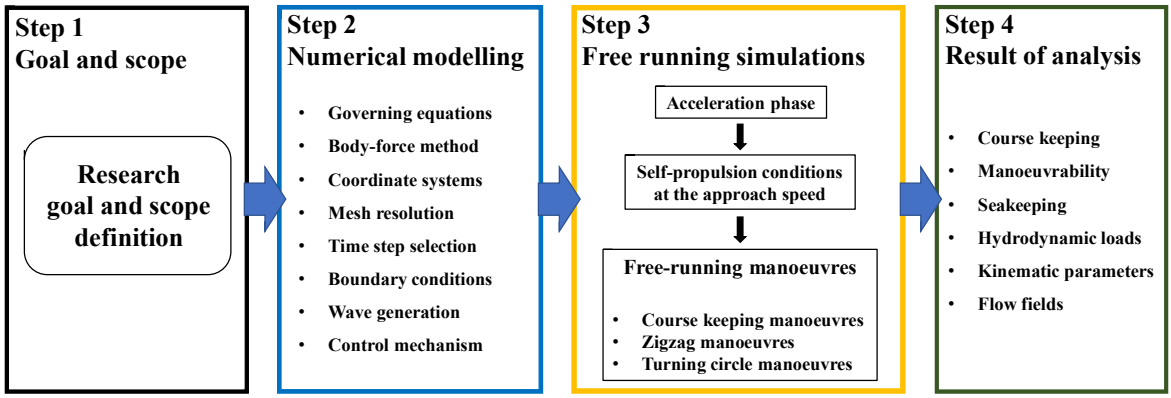

Figure 4.1 General methodology followed in the thesis.

The first step deals with the overall research goal and the selection of the analysis scope. The scope of numerical simulations should be sufficiently well defined to represent the general patterns or observations on the relation between the variable factors selected and the manoeuvring performance of a ship. The scope includes the following items:

- A CFD solver for free-running simulations.
- Ship types and geometries to be studied.
- Approach conditions including the target speed of a ship.
- Environmental conditions such as deep unrestricted water, regular waves, irregular waves, shallow water, and ocean currents.
- Assumptions to be applied.

Given the scope of the analysis, the numerical setup of a free-running CFD model is performed in the second step. Special care is needed when carrying out numerical modelling tasks, and in this regard, the following features should be taken into consideration:

- Governing equations to be solved.
- Body-force propeller model.

- Coordinate systems to solve 6DOF motions.
- Mesh resolution.
- Determination of the time step.
- Computational domain and boundary conditions.
- Wave generation.
- Control mechanism for free-running manoeuvres.

In the third step, the self-propulsion computation in a given environmental condition should be first carried out to reach the target surge speed. Then, several representative free-running manoeuvres are performed, namely, course-keeping, zigzag, and turning circle manoeuvres to identify the manoeuvring behaviours of a ship. In the fourth step, all of the results from this research including the important hydrodynamic features, the critical manoeuvring indices, and relevant flow fields are demonstrated and discussed in detail.

4.3. Numerical Modelling

The commercial CFD software STAR-CCM+ (version 15.04), developed by Siemens, was utilised to implement the numerical simulations in this thesis. The detailed features of the numerical schemes adopted in this research are described in the following sub-sections.

4.3.1. Ship geometry

In this thesis, all the free-running simulations were carried out for the KRISO Container Ship (KCS) model with a scale factor of 75.24, which is one of the benchmark hull forms. The overview of the ship geometry characterised by a traditional single rudder / single propeller configuration is depicted in Figure 4.2, and the principal characteristics of the model are listed in

Table **4.1**.

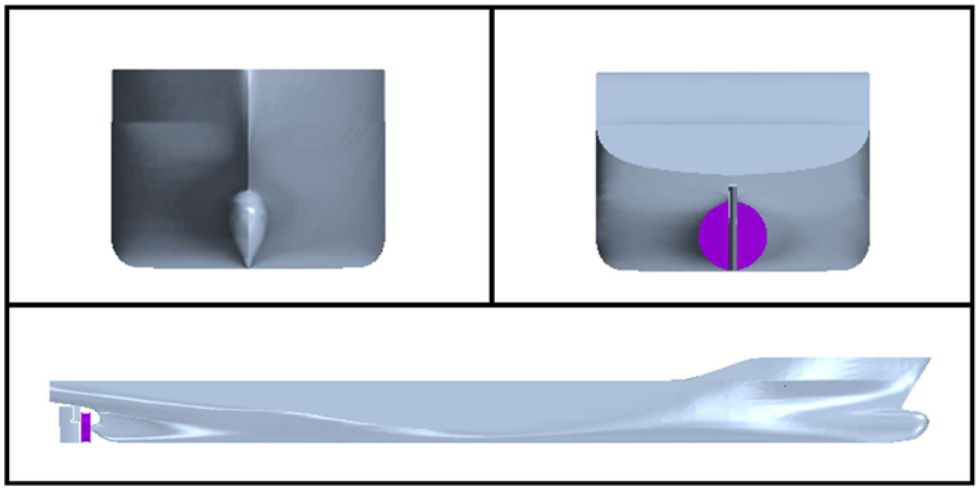

Figure 4.2 KCS geometry with a semi balanced rudder and an actuator disk.

Table 4.1 The main particulars of the KCS model used in this thesis.

Main particulars	Symbols	Model scale (1:75.24)
Length between the perpendiculars	$L_{BP}(m)$	3.057
Length of waterline	$L_{WL}(m)$	3.0901
Beam at waterline	$B_{WL}(m)$	0.4280
Draft	$\mathrm{D}(m)$	0.1435
Displacement	$\Delta(m^3)$	0.1222
Block coefficient	C_B	0.651
Ship wetted area with rudder	S (m^2)	1.6834
Longitudinal centre of buoyancy	$\%L_{BP}$, fwd+	-1.48
The metacentric height	$\mathrm{GM}(m)$	0.008
Radius of gyration	K_{xx}/B	0.49
Radius of gyration	$K_{yy}/L_{BP}, K_{zz}/L_{BP}$	0.25
Propeller diameter	$D_P(m)$	0.105
Propeller rotation direction (view from stern)		Right hand side
Rudder turn rate	(deg./s)	20.1

4.3.2. Governing equations

Turbulent flows around the ship were computed by the numerical solution of the unsteady Reynolds Averaged Navier-Stokes (URANS) equations, under the assumption of Newtonian, incompressible, and viscous fluid. Without considering the body forces, the continuity and momentum equations for the flow can be expressed in vectorial form as follows:

$$\nabla \cdot \mathbf{U} = 0 \tag{4.1}$$

$$\frac{\partial(\rho \mathbf{U})}{\partial t} + \nabla \cdot \left[\rho\left(\mathbf{U} - \mathbf{U_g}\right)\mathbf{U}\right] = -\nabla p + \nabla \cdot (\mu_{\mathrm{eff}} \nabla \mathbf{U}) + \nabla \mathbf{U} \cdot \nabla \mu_{\mathrm{eff}} + q_i \tag{4.2}$$

where $\nabla \cdot(\cdot)$ and $\nabla(\cdot)$ indicate the divergence and gradient operators, respectively. $\mathbf{U}$ is the

fluid velocity and $\mathbf{U}_g$ is the grid velocity; p is the static pressure; ρ is the fluid density; $\mu_{\text{eff}} = \rho(\nu + \nu_t)$ stands for the effective dynamic viscosity, where ν and ν_t represent the kinematic and eddy viscosity, respectively (ν_t is obtained from the turbulence model); q_i is a user-defined source term.

The Menter's Shear Stress Transport (SST) model (Menter, 1994) was adopted in this thesis to complete the URANS equations (for the closure of the system). The SST turbulence model is a two-equation eddy viscosity turbulence model which blends the merits of the k−ω turbulence model in the inner region of the boundary and the k-ε turbulence model in the far-field through blending functions depending on the turbulence length scale. This turbulence model has been widely adopted in the literature for free-running CFD models (Mofidi and Carrica, 2014; Carrica et al., 2016; Wang and Wan, 2018; Wang et al., 2018; Kim et al., 2021b). The first closure equation is the transport equation for the turbulent kinetic energy k, while the second one is the transport equation for the specific dissipation rate ω. The two closure equations can be given as follows:

$$\frac{\partial(\rho k)}{\partial t} + \nabla\cdot(\rho k\mathbf{U}) = \left[\mu_t\left(\nabla\mathbf{U} + (\nabla\mathbf{U})^{\mathrm{T}} - \frac{2}{3}\nabla\cdot\mathbf{U}\right) - \frac{2}{3}\rho k\delta_{i,j}\right]\nabla\mathbf{U} \tag{4.3}$$
$$-\beta^*\rho\omega k + \nabla\cdot[(\mu + \sigma_k\mu_t)\nabla k]$$

$$\frac{\partial(\rho\omega)}{\partial t} + \nabla\cdot(\rho\omega\mathbf{U}) = \frac{\gamma}{\nu_t}\left[\mu_t\left(\nabla\mathbf{U} + (\nabla\mathbf{U})^{\mathrm{T}} - \frac{2}{3}\nabla\cdot\mathbf{U}\right) - \frac{2}{3}\rho k\delta_{i,j}\right]\nabla\mathbf{U} - \beta\rho\omega^2 \tag{4.4}$$
$$+\nabla\cdot[(\mu + \sigma_\omega\mu_t)\nabla\omega] + 2\rho(1 - F_1)\frac{\sigma_{\omega 2}}{\omega}\nabla k\cdot\nabla\omega$$

in which,

the first blending function F_1 is defined as $F_1 = \tanh\left\{\left[\min\left(\max\left(\frac{\sqrt{k}}{0.09\omega y}; \frac{500\nu}{y^2\omega}\right); \frac{4\rho\sigma_{\omega 2}k}{CD_{k\omega}y^2}\right)\right]^4\right\}$ with $CD_{k\omega} = \max\left(\frac{2\rho\sigma_{\omega 2}}{\omega}\nabla k\cdot\nabla\omega; 10^{-20}\right)$. y represents the distance from the nearest wall. The eddy-viscosity coefficient in the SST model is defined as $\mu_t(=\rho\nu_t) = \frac{\rho a_1 k}{\max(a_1\omega; \Omega F_2)}$ where Ω is the absolute value of the vorticity and F_2 is the second blending function defined by $F_2 = \tanh\left\{\left[\max\left(2\frac{\sqrt{k}}{0.09\omega y}; \frac{500\nu}{y^2\omega}\right)\right]^2\right\}$. The constants Φ (β^*, β, σ_k, σ_ω, ⋯) of the turbulence model are calculated from the constants, Φ_1, Φ_2, as follows: $\Phi = F_1\Phi_1 + (1 - F_1)\Phi_2$. The constants of the formulas can be found in Menter (1994) for details.

The Volume of Fluid (VOF) method was adopted to model three-dimensional free-surface flows and the transport equation can be written as (SIMMAN, 2020):

$$\frac{\partial\alpha_i}{\partial t} + \nabla\cdot\left[\alpha_i(\mathbf{U} - \mathbf{U_g})\right] = S_{\alpha_i} - \frac{\alpha_i}{\rho_i}\frac{D\rho_i}{Dt} - \frac{1}{\rho_i}\nabla\cdot(\alpha_i\rho_i\mathbf{v}_{d,i}) \tag{4.5}$$

where α_i denotes the volume fraction of phase i and its value varies from 0 to 1 to describe the relative proportion of fluid in each cell ($\alpha = 0$: non-wetting phase (air), $0 < \alpha < 1$: two-phase interface (free surface), $\alpha = 1$: wetting phase (water)). In the two-phase interface, its density and viscosity are expressed as a smooth function of the volume fraction. As the

simulation evolves in time, the volume fraction function defined in the whole computational domain is advected by the underlying fluid motion. S_{α_i} is a user-defined source term of phase i; $\frac{D\rho_i}{Dt}$ is the Lagrangian derivative of the phase densities ρ_i; $\mathbf{v}_{d,i}$ is the diffusion velocity. As stated in Di Mascio et al. (2007), the VOF method can be advantageous in treating complex interface evolutions, even breaking and reconnecting surfaces, and in its mass conservation properties. It is worth noting that source terms for the momentum equation (q_i) and the VOF transport equation (S_{α_i}) can be employed to satisfactorily reduce the accumulation errors due to undesired wave reflections occurring at domain boundaries (Perić and Abdel-Maksoud, 2018). The VOF approach has been used in many other studies performed by means of CFD simulations to position the free surface, such as Tezdogan et al. (2016), Kavli et al. (2017), Terziev et al. (2019), and Terziev et al. (2020).

The computations in this thesis are all based on the URANS solver which uses a finite volume method that discretises the Navier-Stokes equations. The spatial discretisation of the convection and diffusive terms of the governing transport equations was achieved through a second-order upwind scheme and a second-order centred scheme, respectively. The temporal terms in the governing equations were discretised with a second-order implicit backward Euler scheme. For pressure-velocity coupling, the SIMPLE (Semi-Implicit Method for Pressure-Linked Equations) algorithm was used with under-relaxation factors of 0.7 for velocities and 0.4 for pressure as a segregated approach.

4.3.3. Body-force propeller model

A ship propeller was modelled through an actuator disk of finite thickness based on the body force method, in which both axial and tangential body forces are distributed in the flow field within the disk to simulate propeller effects. The ship model used in this thesis is equipped with a right-handed propeller of which rotation direction is clockwise when propelling the vessel forward as viewed from the ship's stern. Throughout all simulations, the direction in which thrust is produced by the disk model was determined in accordance with the characteristic of the right-handed propeller. The thrust and torque generated by the actuator disk is dependent on the thrust and torque coefficients K_T and K_Q selected from the propeller performance curve as a function of the advance ratio J ($J = V_{ship} / nD$, where V_{ship} represents the velocity at the propeller location, n is the rotation rate, D is the propeller diameter). V_{ship} was calculated in this thesis as the volume-averaged velocity over the inflow velocity plane which is located upstream of the actuator disk to consider the actual velocity field at the propeller position (Figure 4.3).

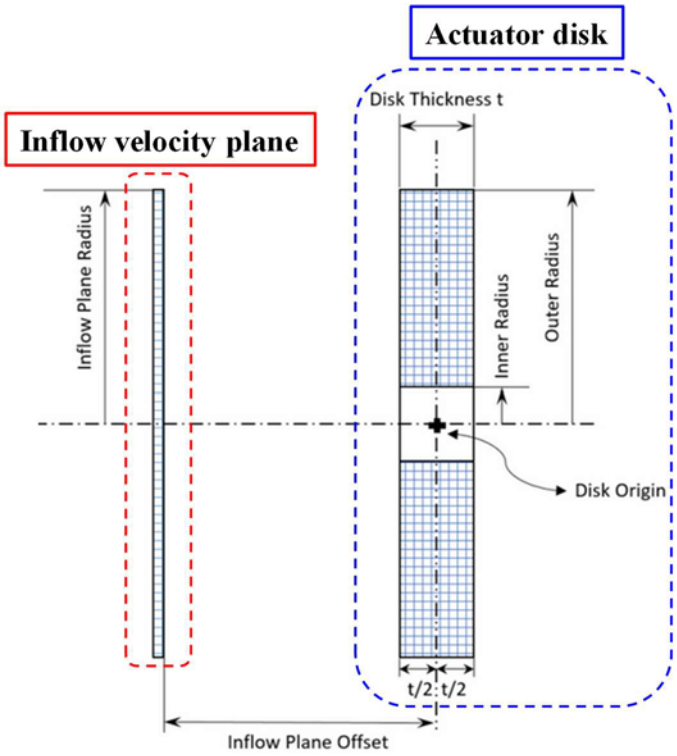

Figure 4.3 The schematic view of the actuator disk model and inflow velocity plane, adapted from Siemens (2020).

Once the thrust and torque are determined for the operating advance ratio, a uniform volume forces $\mathbf{f_b}$ distribution over the cylindrical actuator disk is prescribed as follows:

$$f_{bx} = A_x r^* \sqrt{1 - r^*} \tag{4.6}$$

$$f_{b\theta} = A_\theta \frac{r^* \sqrt{1 - r^*}}{r^*(1 - r"_h) + r"_h} \tag{4.7}$$

$$r^* = \frac{r" - r"_h}{1 - r"_h},\ r"_h = \frac{R_H}{R_P} \text{ and } r" = \frac{r}{R_P} \tag{4.8}$$

in which f_{bx} denotes the body force component in axial direction, $f_{b\theta}$ denotes the body force component in tangential direction, r is the radial coordinate, R_H is the hub radius and R_P is the propeller radius. The constants A_x and A_θ are computed in the following equations, with T, Q, and t_{disk} representing the thrust, the torque, and the actuator disk thickness, respectively.

$$A_x = \frac{105}{8} \cdot \frac{T}{\pi t_{disk}(3R_H + 4R_P)(R_P - R_H)} \tag{4.9}$$

$$A_\theta = \frac{105}{8} \cdot \frac{Q}{\pi t_{disk} R_P (3R_H + 4R_P)(R_P - R_H)} \tag{4.10}$$

4.3.4. Coordinate systems to solve 6DOF motions

For the solution of the fluid flow and ship motions, four right-hand coordinate frames were

defined as indicated in Figure 4.4: (1) Earth-fixed frame ($o_o - x_o y_o z_o$), (2) Ship-fixed frame ($o_s - x_s y_s z_s$), 3) Propeller-fixed frame ($o_p - x_p y_p z_p$), and (4) Rudder-fixed frame ($o_r - x_r y_r z_r$).

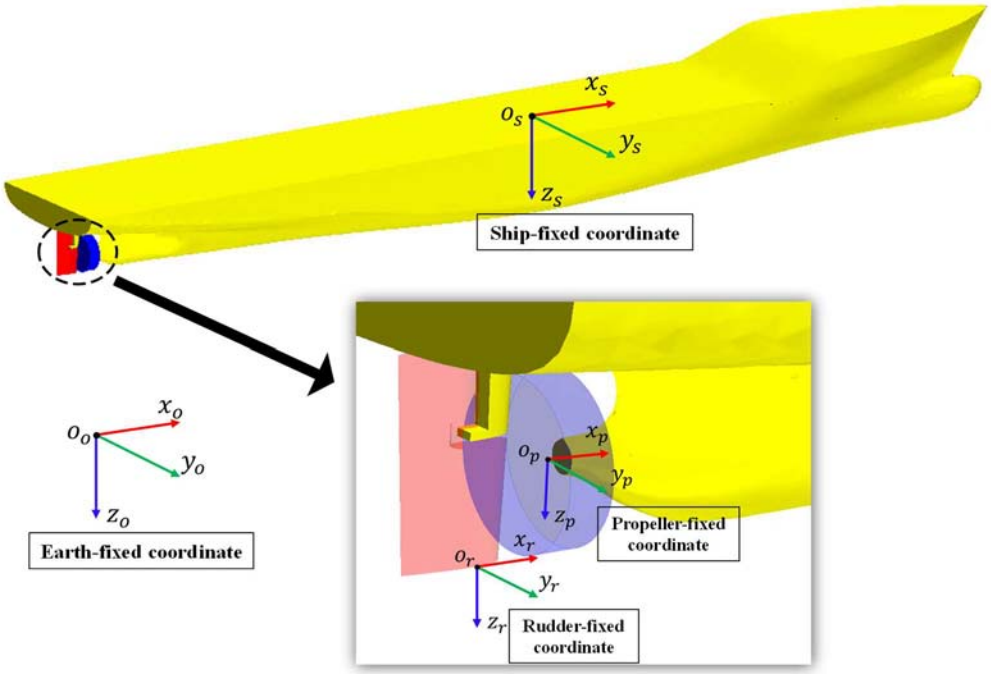

Figure 4.4 The Coordinate systems of the ship manoeuvring simulation used in this thesis.

● Earth-fixed coordinate frame ($o_o - x_o y_o z_o$): An inertial coordinate frame with its origin at the pivot point (o_o) of the computational domain. When the solution is initialised, the axis $o_o x_o$ is parallel to the ship's longitudinal axis (positive forward), the axis $o_o y_o$ is parallel to the ship's transverse axis (positive starboard side), and the axis $o_o z_o$ completes a right-handed orthogonal frame (positive downwards).

● Ship-fixed coordinate frame ($o_s - x_s y_s z_s$): a moving reference frame fixed to the hull with the origin fixed at the centre of mass of the ship. The axis $o_s x_s$ is aligned with the ship's longitudinal axis (directed towards the bow), the axis $o_s y_s$ is orthogonal to the vertical plane of symmetry (directed towards the starboard), and the $o_s z_s$ is directed towards downward direction as a right-handed orthogonal frame.

● Propeller-fixed coordinate frame ($o_p - x_p y_p z_p$): a moving reference frame fixed to the hull with the origin located at the centre of the propeller. The axis $o_p x_p$ indicates the direction in which thrust force is produced by the actuator disk.

● Rudder-fixed coordinate frame ($o_r - x_r y_r z_r$): a moving reference frame fixed to the hull with the origin taken at the bottom of the rudder on the Aft Perpendicular (AP). The axis $o_r z_r$ is the axis about which the rudder blade rotates (the positive sign of the rudder angle: deflection to the port side).

In this thesis, the dynamic behaviour of the ship during free-running manoeuvres was simulated with the use of the Dynamic Fluid Body Interaction (DFBI) approach (Siemens, 2020). The flow field was solved in the Earth-fixed inertial coordinate system so that the hydrodynamic

forces and moments acting on the ship were computed. The forces and moments in the Earth-fixed frame were then projected into the non-inertial ship-fixed coordinate system to solve the motion equations of the rigid body which is given as follows:

$$\begin{cases} X = m[\dot{u} + qw - rv] \\ Y = m[\dot{v} + ru - pw] \\ Z = m[\dot{w} + pv - qu] \end{cases} \tag{4.11}$$

$$\begin{cases} K = I_{xx}\dot{p} + (I_{zz} - I_{yy})rq \\ M = I_{yy}\dot{q} + (I_{xx} - I_{zz})pr \\ N = I_{zz}\dot{r} + (I_{yy} - I_{xx})pq \end{cases} \tag{4.12}$$

in which m is the mass of body

u, v, w are the surge/sway/heave velocities

p, q, r are the roll/pitch/yaw angular velocities

X, Y, Z are the surge/sway/heave resultant forces acting on the ship

K, M, N are the roll/pitch/yaw resultant moments acting on the ship

I_{xx}, I_{yy}, I_{zz} are the moments of inertia about the principal axes in the body frame

The velocities of the ship can be calculated by solving Equations (4.11) and (4.12) and the new position and attitude of the ship can be obtained by integrating these kinematic parameters over time.

4.3.5. Mesh resolution

In this sub-section, the general mesh generation techniques adopted within this thesis will be presented. It has to be mentioned that the resulting mesh configuration in each chapter (Chapters 5 - 11) varied depending on the characteristics of the problem considered. The specific details of the resulting mesh generated in each chapter will be described in the following chapters of this thesis.

The computational domain meshes were generated by applying the automatic meshing facility in STAR-CCM+, which automatically generates the surface or volume grids suitable for the finite volume method. A surface remesher tool was used to enhance the overall quality of part surfaces and optimise the mesh quality for the volume grids. A trimmed cell mesher was used for the volume meshes. The resulting mesh was made up mainly of hexahedral cells with trimmed cells neighbouring the surface. The prism layer mesh model was adopted to provide orthogonal prismatic cells adjacent to the wall surfaces or boundaries, which is required to resolve near-wall flow accurately. Prism layers refer to the region of closely packed cells near solid surfaces to capture the boundary layer. Local grid refinements were made in the vicinity of the bow, the stern, the tight gap parts between the rudder blade and horn, and the propeller wake region to ensure that the complex flows were precisely captured. In addition, a finer mesh was created in the free surface where incident waves were expected to travel in the computational domain. For the regular wave simulations (Chapters 5 – 9), the free surface mesh refinement was carried out by generating 80 cells per wavelength and 20 cells per wave height.

This is based on the guidelines for ship CFD applications from ITTC (2011). According to these recommendations, a minimum of 80 cells wavelength was required on the free surface, while a minimum of 20 cells should be used in the vertical direction where the free surface is expected. For the irregular wave simulations (Chapter 9), the free surface mesh was generated following the guidelines for ship CFD applications from ITTC (2011) and the recommendations put forward by CSP (2021). According to CSP (2021), the cut-off frequency, referring to the highest wave frequency (the shortest wavelength) to be accurately resolved in the simulation, should be first selected from a wave energy spectrum. In general, cut-off frequency (f_c) to peak frequency (f_p) ratios f_c/f_p should be greater than 2 since relatively low a cut-off frequency may affect properties of resultant spectrum and values of target significant wave height and modal period (ITTC, 2017a). Given the cut-off frequency selected accordingly, 20 grid points for the shortest wavelength were generated in the *x* and *y* directions (ITTC, 2011). It is important to note that a constant cell size for both *x* and *y* directions was applied in the free surface refinement region to ensure simulation stability (Romanowski et al., 2019). In ITTC (2011), there are no definite recommendations regarding how to generate meshes in the vertical direction for irregular waves. Alternatively, 30 grids points for the expected maximum wave height (1.2 × significant wave height) were generated in the *z*-direction according to CSP (2021).

In order to handle the complex motions of the free-running ship model, the dynamic overset grid method was used in this study. This method provides great flexibility in modelling moving bodies compared to the rigid and deforming mesh motion options that may lead to cell quality problems. The overset mesh approach has the distinct advantages of enabling overset regions to move independently without any restrictions while ensuring a high-quality grid. As seen in Figure 4.5, the computational domain with three different regions was designed for the numerical model developed in this thesis: *1) background region, 2) hull overset region, and 3) rudder blade overset region*.

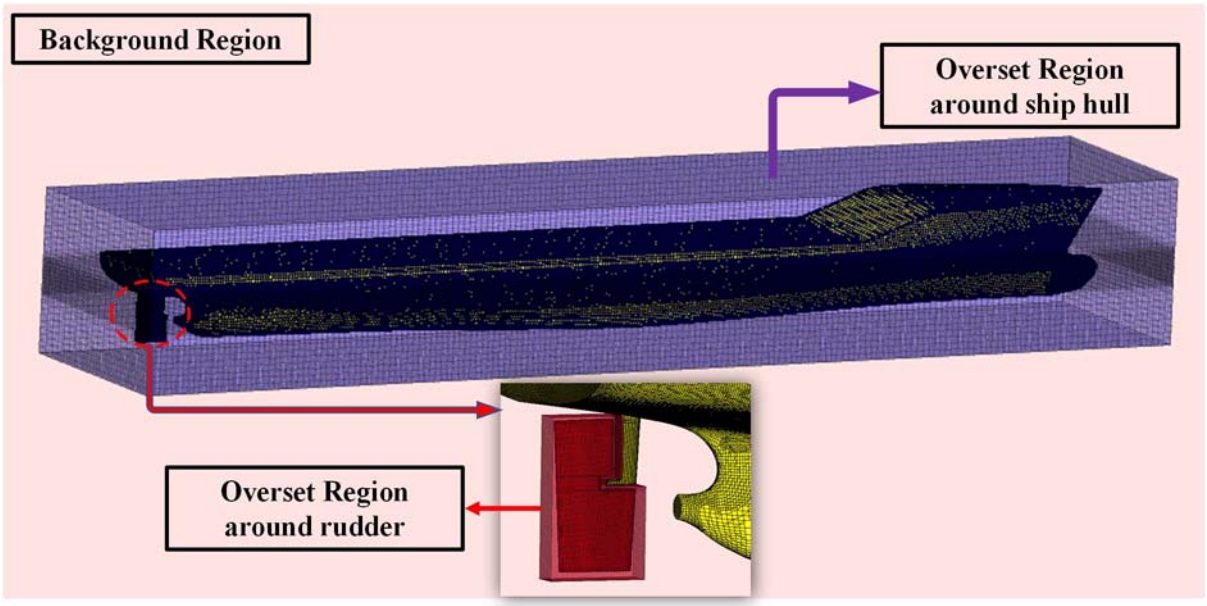

Figure 4.5 Overset mesh configuration of the domain.

The overlapping regions were generated in accordance with the hole-cutting process which couples the overset regions with the background region through the overset interfaces. Three types of cells are created from the hole-cutting process: 1) active cells, 2) inactive cells, 3) acceptor cells. The overset cell information regarding the CFD model is displayed in Figure 4.6 (donor cells are marked as active cells in another region). The value of a flow variable φ of the acceptor cell of one region is obtained by a weighted linear interpolation scheme from the donor cells (the active cells) in another region:

$$\varphi = \sum_{i=1}^{n} \omega_i \varphi_i \tag{4.13}$$

in which ω_i is the interpolation weighting factor and φ_i is the value of the dependent variable φ at the donor cell (the subscript i runs over all the donor nodes of an interpolation element). Siemens (2020) can be consulted for detailed information on the overset mesh technique. The background region enclosing the entire solution domain was generated to implement the far-field boundary conditions which determine the environmental conditions in the CFD simulations. The overlapping region which was tailored to the ship hull made it possible to simulate the full 6-DOF motions of the ship during manoeuvring. The rudder overset region was defined with the intention of enabling the rudder deflection based on the types of ship manoeuvres. It should be noted that the distance of the gap part between the rudder and rudder root was adjusted to obtain valid interpolations between the grids.

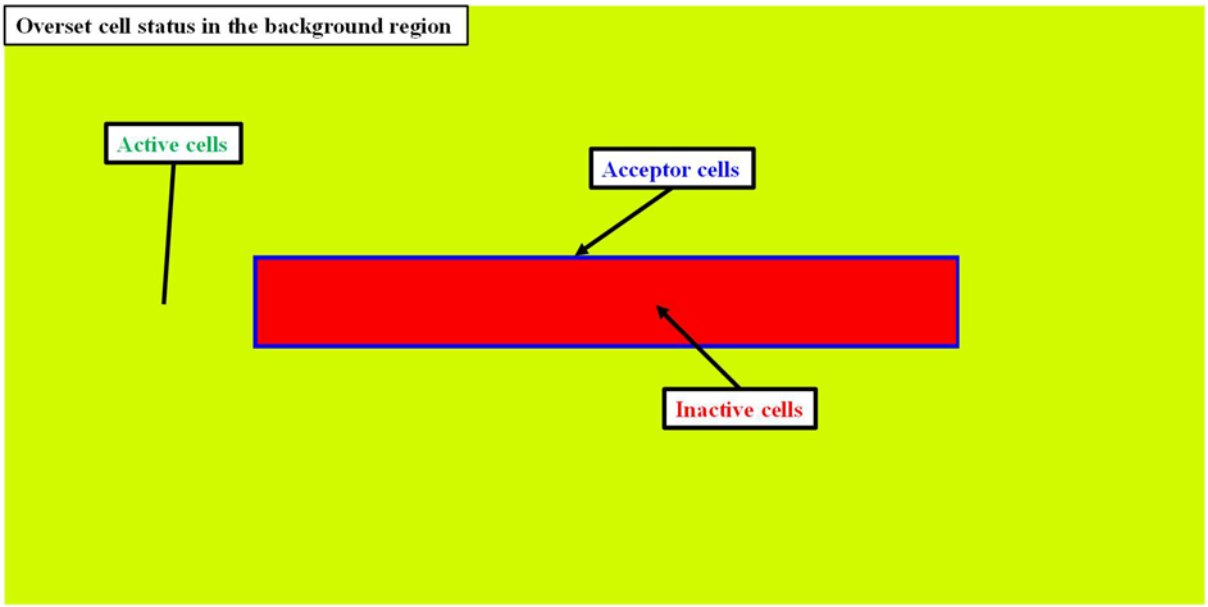

(a) Overset cell status in the background region

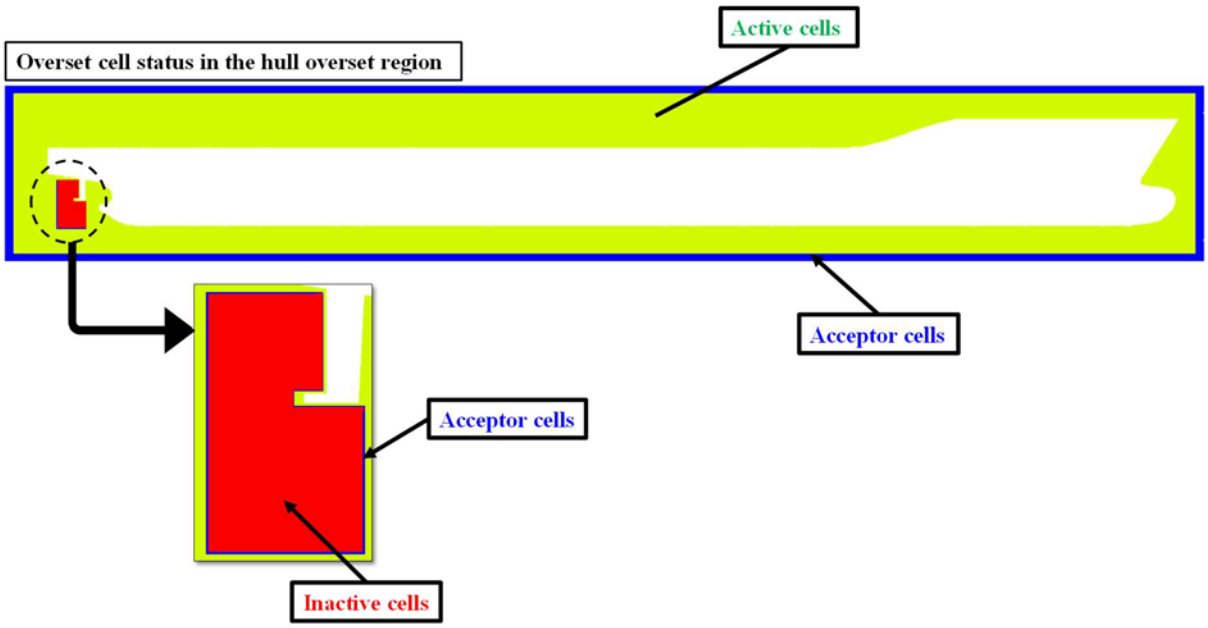

(b) Overset cell status in the hull overset region

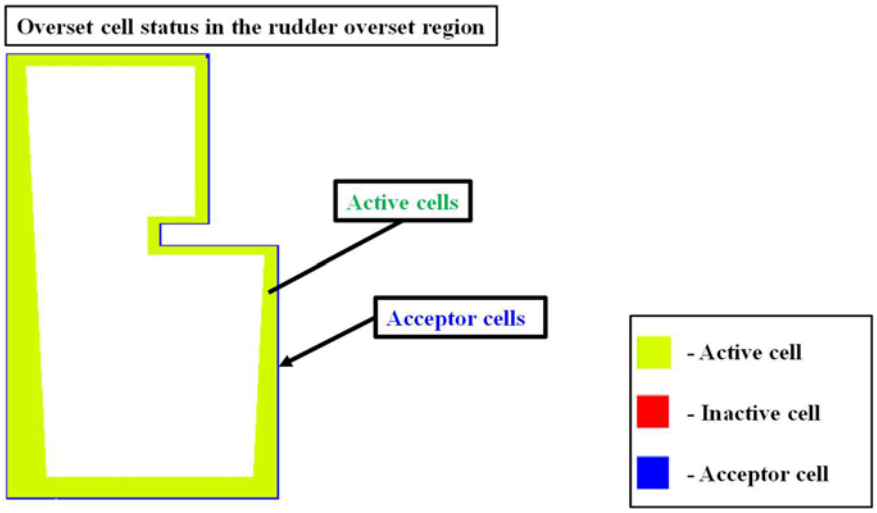

(c) Overset cell status in the rudder overset region

Figure 4.6 Overset cell status in each region.

4.3.6. Determination of the time step

There are several approaches to choose the time step of a CFD simulation for stability in the numerical solution. The Courant number (CFL) condition is the most widely used to evaluate the time step requirements of a transient simulation for a given grid size and flow velocity. The CFL number formula is defined as below:

$$\mathrm{CFL} = \frac{U\Delta t}{\Delta x} \tag{4.14}$$

where U denotes the flow velocity, Δt indicates a representative time step of the simulation and Δx is the mesh cell dimension. It is generally equal to 1 or less for numerical stability.

In addition to the CFL condition, the time step can be decided by the flow features. For the prediction of ship manoeuvrability in regular waves (Chapters 5 - 9), at least 100 time steps per period for regular waves were used based on ITTC (2011). When it comes to the free-running simulations in irregular waves (Chapter 9), a minimum of 60 time steps per period for the shortest waves were used, in accordance with the related procedures and guidelines of ITTC (2011). It should be noted that the shortest wave period can be estimated by determining the cut-off frequency, as stated in the previous sub-section. Regarding the numerical simulations in shallow water and currents (Chapters 10 and 11), the use of $\Delta t \leq 0.01L/U$ was applied for the time step (Δt) selection, with L and U representing ship length and ship speed, respectively (ITTC, 2011).

4.3.7. Computational domain and boundary conditions

For accurate resolution of flow around structures, it is imperative in CFD calculations to apply the proper initial and boundary conditions that provide a good approximation to the solution of the problem (Date and Turnock, 1999).

The boundary conditions applied to the computational domain were slightly different depending on the features of the problem solved. For free-running CFD simulations in waves (Chapters 5 – 9), two types of computational domains were created for this work's ship manoeuvre simulations: one for calm water and the other for waves. On each computational domain, different initial and boundary conditions were chosen to represent the KCS model being manoeuvred in the calm water or waves conditions. Figure 4.7 illustrates the computational domain with the imposed boundary conditions and the dimensions of the domain. For the opposite faces in the x-direction, a velocity inlet boundary condition was applied. The side walls and bottom wall were set as a velocity inlet while the top boundary was modelled as a pressure outlet condition to represent an open sea, which means deep water and infinite air conditions. The ship hull and the rudder blade were defined as no-slip wall boundary conditions. For the calm water simulation, the damping capability of the software was applied at the up-and-down stream boundaries and side walls with a damping length equal to 1.0 L_{BP} (~3.06 m.) to prevent undesired Kelvin wave reflection. For the wave simulations, on the other hand, the boundaries at the vertical directions used the wave forcing capability with a forcing length equal to 1.0 L_{BP} (~3.06 m.) from the boundaries. As mentioned by Ferziger and Peric (2020), the velocity and the volume fraction of water are forced towards the theoretical solution of Fenton (1985) in the forcing zone. Thus, the ship-induced disturbance of incoming waves gradually vanishes in the forcing zone, which helps to avoid reflections of waves from the boundaries. The forcing zone applied throughout all the simulations in waves are depicted in Figure 4.8, in which relative zone distance indicates the relative distance between a cell and the nearest boundary of the forcing zone (Siemens, 2020). ITTC (2011) emphasises that the computational domain boundaries should be positioned at a sufficient distance away from the ship to minimise their influence on the solution. The locations of the boundaries were

determined based on previous research performing wave simulations. Table 4.2 shows the findings of all boundary locations.

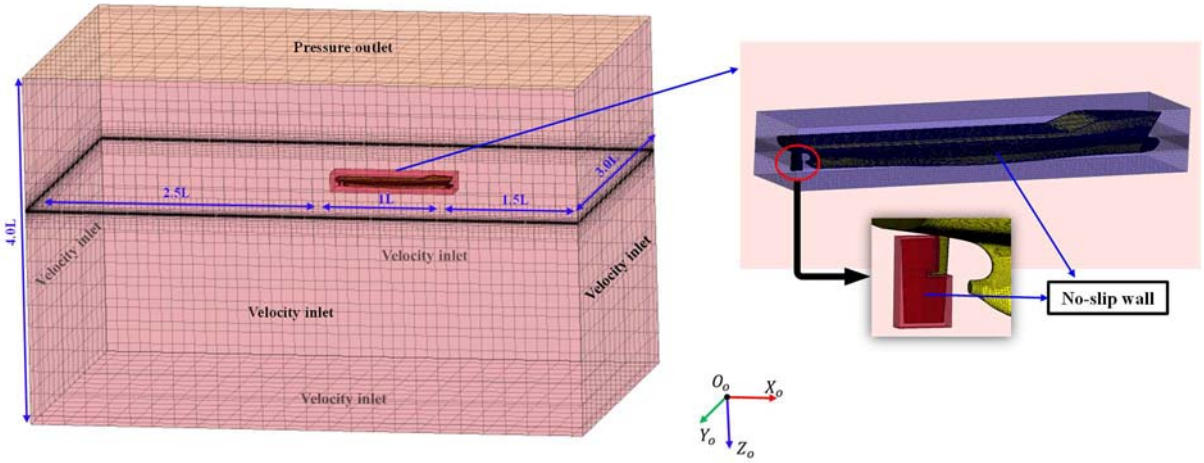

Figure 4.7 The computational domain with the imposed boundary conditions (Chapter 5 – 9).

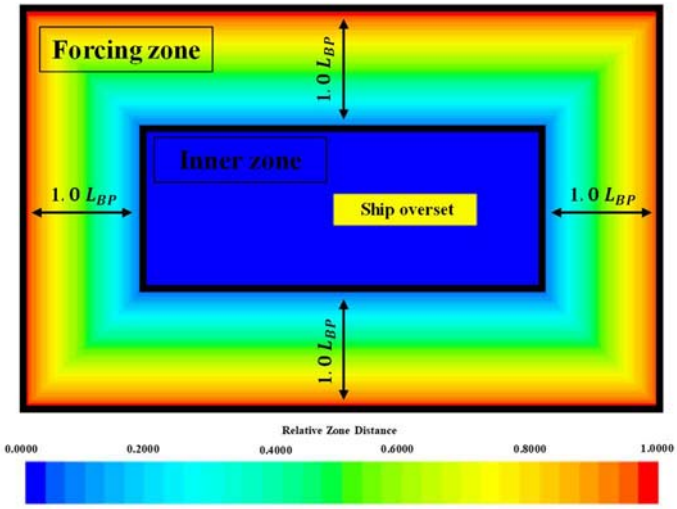

Figure 4.8 A schematic view of the forcing zone in the CFD simulations in waves.

Table 4.2 Boundary distances from the ship in similar previous work.

References	Directions				
	Upstream	Downstream	Up	Bottom	Transverse
Tezdogan et al. (2015)	$1.15L_{BP}$	$4.5L_{BP}$	$1L_{BP}$	$2.3L_{BP}$	$2.5L_{BP}$
Wang et al. (2017)	$1.5L_{BP}$	$3.0L_{BP}$	$0.5L_{BP}$	$1.0L_{BP}$	$1.5L_{BP}$
The current CFD	$1.5L_{BP}$	$2.5L_{BP}$	$1.1L_{BP}$	$2.9L_{BP}$	$1.5L_{BP}$

For free-running CFD simulations in shallow water (Chapter 10), an overview of the computational domain with the imposed boundary conditions is depicted in Figure 4.9. The upstream, side, and top boundaries were modelled as a velocity inlet boundary condition which helps to avoid a velocity gradient between the fluid and the wall. The downstream boundary

was selected as a pressure outlet. A no-slip wall boundary condition was imposed at the bottom boundary with an aim to represent the presence of the sea floor; in particular, the bottom wall was designed to be stationary with respect to the earth-fixed reference to mimic reality. For the surfaces of the moving bodies (i.e., the hull and the rudder), no-slip wall boundary conditions were applied. It should be stressed that the possible occurrence of wave reflection from the walls was prevented by means of applying the VOF wave damping capability of the software package with a damping length equal to 1.0 L_{BP} (~3.06 m.) at the vertical boundaries (i.e., the upstream, downstream, and side walls).

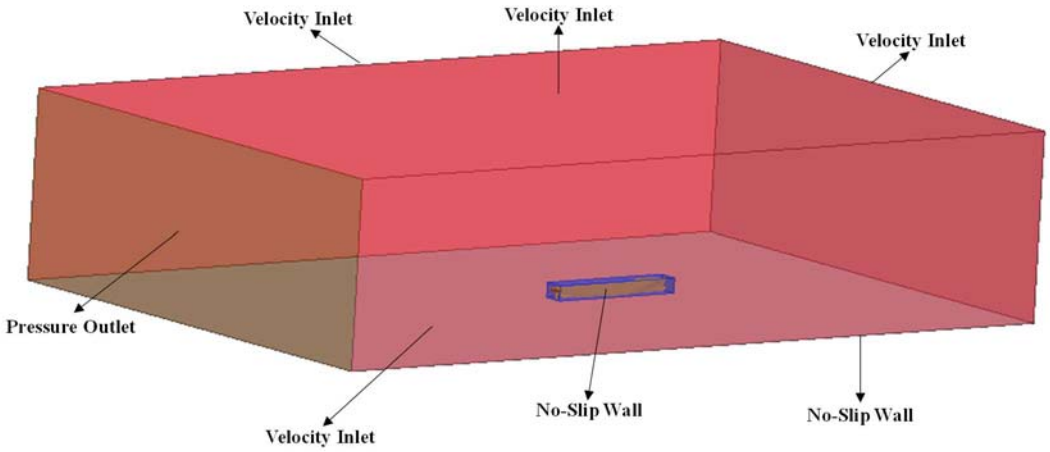

Figure 4.9 The domain with the applied boundary conditions for shallow water simulations.

For free-running CFD simulations in currents (Chapter 11), a general view of the background and overset regions with the notations indicating the applied boundary conditions is illustrated in Figure 4.10, and the locations of the boundaries are presented in Figure 4.11. As can be seen, a velocity inlet boundary condition was applied at the upstream, downstream, side, and bottom boundaries. The speed and direction of the flow at all inlet boundaries were set to the corresponding values of the current. Hence, the constant propagation of the ocean current with a specific speed and direction could be achieved in the computational domain. A pressure outlet boundary condition was imposed at the top boundary. The ship hull and rudder blade were both selected as no-slip boundary conditions. It was observed that the presence of strong currents resulted in undesired wave reflections at the vertical boundaries of the domain during the computations, by moving the Kelvin wake generated by the manoeuvring ship quickly towards the walls. In order to mitigate wave reflection from the walls, the VOF wave damping capability of the software package with a damping length equal to 1.6 L_{BP} (~5.0 m.) was applied at the vertical boundaries. It is worth mentioning that the size of the background domain generated in this particular study was larger than that used in Chapters 5 – 10 due to the possible occurrence of wave reflection from the walls under strong current conditions. The remarkable difference from the domain created in Chapters 5 – 10 is that the downstream and side boundaries were located 4.9 L_{BP} and 2.9 L_{BP} away from the ship body, respectively, as wave reflection from the boundaries was prominent. The dimension of the domain in this study has been determined based on a trial-and-error procedure and by repeating the free-running simulation in the strongest current to avoid wave reflections.

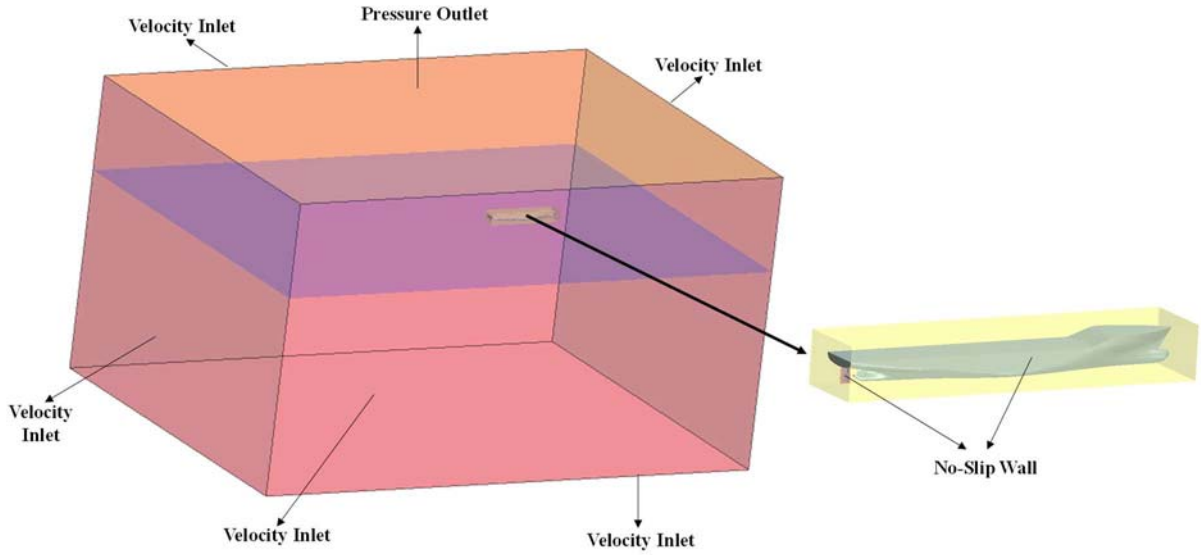

Figure 4.10 The schematic view of the background and overset regions and the applied boundary conditions for the free-running simulations.

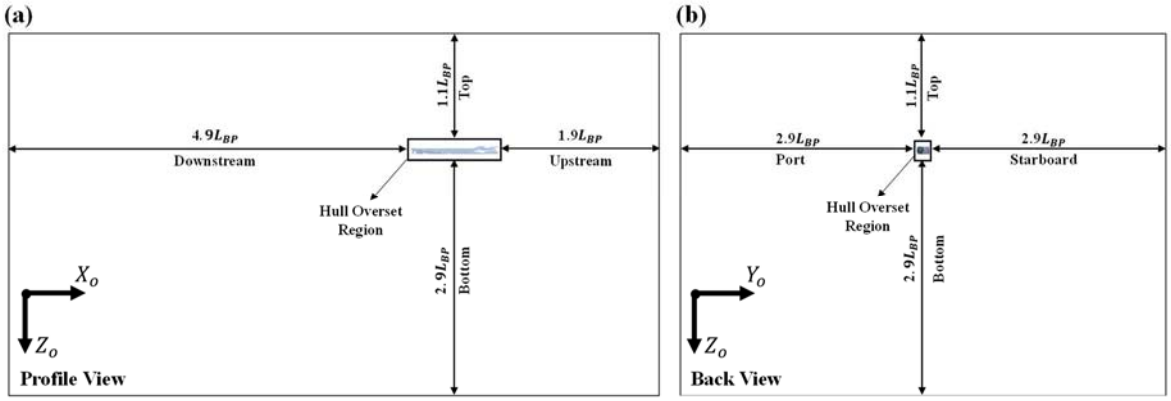

Figure 4.11 The dimensions of the computational domain for the free-running simulations, (a) profile view of the domain, (b) back view of the domain.

Special care is needed when dealing with the motion of each region. Different motion capabilities were assigned to each computational region for the free-running simulations, which enabled the self-propelled ship to efficiently complete the prescribed manoeuvres in the computational domain with limited size (as shown in Figure 4.12). Without such motion capabilities, the CFD model developed in this thesis would not have been able to achieve a complete manoeuvre in a fixed background region which could not cover the whole course of the manoeuvring ship. In this thesis, difficulties arising from the limited size of the computational domain were overcome by defining different motions for each computational region. The ship overset region tailored to the ship hull was designed to freely move in full six degrees of freedom according to the DFBI module, while the rudder overlapping region was compelled to follow the ship but can be deflected based on the rudder controller that will be presented in Section 4.3.9. The motion of the background region was defined to follow the ship motion only with respect to the horizontal plane motions (i.e., surge, sway, and yaw) to enable

the free surface to remain within the refined free surface grids during the simulations.

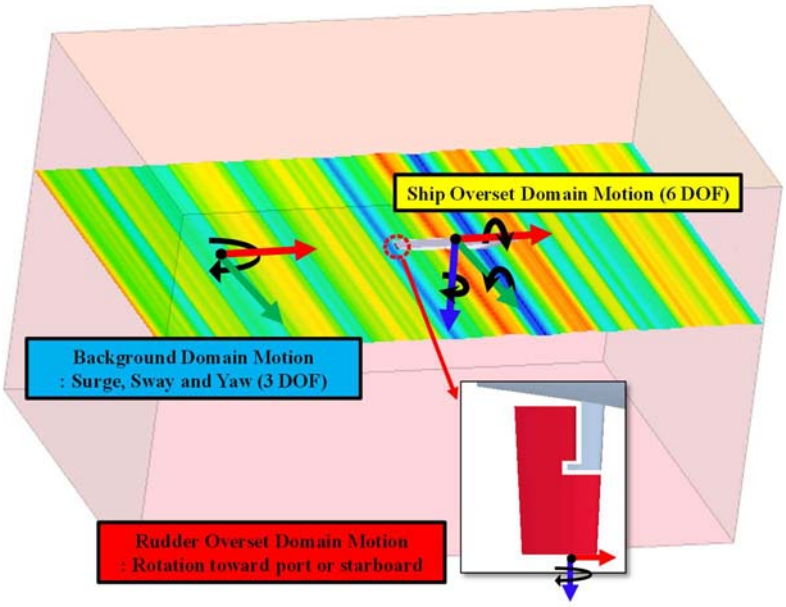

Figure 4.12 The view of the motions of the generated domains.

4.3.8. Wave generation

The generation of non-linear regular waves in the free-running simulation (Chapters 5 – 9) was achieved by applying the fifth-order Stokes wave model which was proposed by Fenton (1985). A fifth-order wave is modelled with a fifth-order approximation to the Stokes theory of waves, which can more closely describe a realistic wave propagation than a first-order wave (Siemens, 2020). The wave profile and the wave phase velocity vary depending on the wave depth and wave height. The VOF method has been used to great effect in modelling the Stokes regular waves by Tezdogan et al. (2015).

The irregular waves generated in the numerical simulation (Chapter 9) were based on the JONSWAP spectrum, which was derived from fetch-limited observations made in the North Sea and described by Hasselmann et al. (1973). The JONSWAP formulation used in this analysis can be expressed as follows:

$$S_J(\omega) = A_\gamma S_{PM}(\omega)\gamma^{\exp\left(-0.5\left(\frac{\omega-\omega_p}{\sigma\omega_p}\right)^2\right)} \tag{4.15}$$

$$A_\gamma = 1 - 0.287\ln(\gamma) \tag{4.16}$$

$$S_{PM}(\omega) = \frac{5}{16}({H_s}^2{\omega_p}^4)\omega^{-5}\exp\left(-\frac{5}{4}\left(\frac{\omega}{\omega_p}\right)^{-4}\right) \tag{4.17}$$

$$\sigma = \begin{cases} 0.07 & (\omega \le \omega_p) \\ 0.09 & (\omega > \omega_p) \end{cases} \tag{4.18}$$

where ω and ω_p represent the incident wave frequency and modal wave frequency, respectively. A_γ is the normalising factor with γ referring to the non-dimensional peak-

enhancement factor (γ =3.3). $S_{PM}(\omega)$ is the Pierson-Moskowitz spectrum, H_s is the significant wave height, and σ denotes the spectral width parameter.

4.3.9. Control mechanism

Three different types of ship manoeuvres were performed for the KCS in this thesis: 1) course keeping control, 2) turning circle manoeuvre, and 3) 20/5 zigzag manoeuvre.

Regarding the course keeping control, the following control module was designed to evaluate the course-keeping capability of the ship:

$$\delta(t) = K_p e(t) + K_i \int_0^t e(t)dt + K_d \frac{de(t)}{dt} \tag{4.19}$$

$$e(t) = \psi(t) - \psi_c \tag{4.20}$$

where t indicating the time (s) elapsed after the start of the ship manoeuvre, $\delta(t)$ the rudder angle (º), $\psi(t)$ the instantaneous yaw angle (º) at a given time, ψ_c the target yaw angle (º) which was defined at 0° to keep the ship straight. K_p, K_i, and K_d represent the proportional, integral, and derivative control gains, respectively. For the CFD model in this thesis, the control gains were determined by the trial-and-error method ($K_p = 5, K_i = 0.05, and\ K_d = 3$). As seen in Figure 4.13, the target yaw angle is determined from the course-keeping module and the PID controller computes the necessary rudder deflection angle with the consideration of the difference between the instantaneous yaw angle and target yaw angle to enable the ship to sail straight.

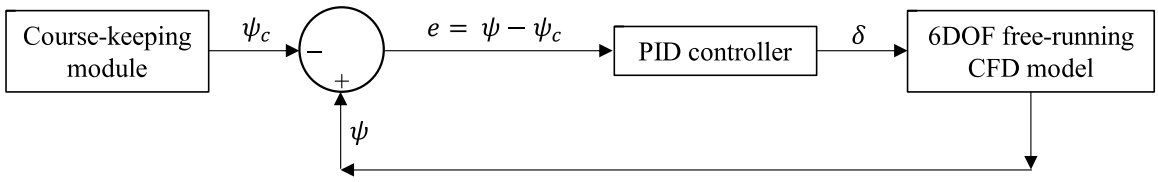

Figure 4.13 The block diagram of the autopilot applied to the CFD model for course-keeping manoeuvres.

To evaluate the turning capability of the ship, the standard turning circle manoeuvres were carried out based on the control function given in Equation (4.21):

$$\delta(t) = \max(-35, \min(0, -\mathrm{k}t)) \tag{4.21}$$

in which k is the maximum rudder rotational rate. The maximum rudder rate is set to k = 20.1º/s corresponding to 2.32º/s on full scale according to the experimental data. From the definitions above, the rudder angle is turned to 35 degrees and kept constant until the vessel completes a turning circle test.

As for the modified 20/5 zigzag manoeuvre, the control function is given as follows:

$$\delta(t) = \begin{cases} \min(kt, 20)\text{, 1st Rudder Execution } (t_1 \le t \le t_2) \\ \max(20 - k(t - t_2), -20)\text{, 2nd Rudder Execution } (t_2 \le t \le t_3) \\ \min(-20 + k(t - t_3), 20)\text{, 3rd Rudder Execution } (t_3 \le t \le t_4) \end{cases} \quad (4.22)$$

in which t_i denotes the ith time for rudder execution. When the ship was advancing forward on a straight course at self-propulsion condition, the rudder blade was first deflected by 20º towards the port side at the maximum rudder rate (1st rudder execution). The ship started to react by turning towards the port side. When the ship heading angle was 5º off the initial course, the rudder was then deflected by 20º towards the starboard side (2nd rudder execution). After the counter rudder angle was applied, the ship initially continued turning to the port with decreasing yaw velocity until it changed sign, so that the ship finally turned to the starboard in response to the rudder deflection. When the heading angle reached 5º in the starboard direction, the rudder was reversed again to the port side (3rd rudder execution).

4.4. Summary

The general methodology used in the thesis has been presented in this chapter. In line with the methodology provided, this thesis performed the free-running simulations prescribed in the following main chapters of the thesis.

5. FREE-RUNNING CFD SIMULATIONS FOR DIFFERENT REGULAR WAVE DIRECTIONS

5.1. Introduction

Understanding a ship manoeuvring performance in a real seaway is of great importance since it is intimately related to navigational safety at sea. Lack of knowledge on the manoeuvring behaviour of a ship may result in marine casualties. According to a recent investigation, navigational casualties from collision and grounding incidents accounted for more than 44% of all marine incidents. The main underlying cause was examined and found to be inadequate human action (EMSA, 2020). Without a doubt, these accidents stem from inappropriate manoeuvring actions by Master Mariners and navigation officers who are responsible for ship operations with particular attention to navigation safety. It is also reported that a large number of marine accidents are associated with rough sea weather over the past few years (Zhang and Li, 2017). An in-depth understanding of the manoeuvring performance of a ship in real sea states is therefore necessary for proper decision-making about ship handling and consequently navigational safety at sea.

It has been observed in real operations that vessels can experience various environmental loads such as waves, wind, and currents during their operations at sea. Among these external disturbances, waves have been considered as the most prominent factors causing significant changes in a ship's manoeuvring behaviour. However, the wave effects on the manoeuvring performance of a ship have still not been extensively studied despite the growing awareness of the importance of understanding a ship's manoeuvrability in waves (IMO, 2014; ITTC, 2017b; IMO, 2021; ITTC, 2021c). This may be due to the high cost of the experimental equipment or the limitation of the theoretical method for resolving complicated wave problems, as reviewed in Chapter 3.

To the best of this author's knowledge, there exists no specific study investigating the effects of wave directions on the course-keeping ability and the turning capability of a ship. Therefore, the aim of this chapter is to fill this gap by performing free-running CFD simulations in waves of different directions. In this chapter, free-running CFD models based on an unsteady RANS approach were developed in accordance with the numerical modelling framework presented in Chapter 4. Each simulation was modelled in five different wave directions, namely head wave, bow wave, beam wave, quartering wave, and following wave. The simulations of self-propulsion in waves were first conducted to achieve the approach speed. Following this, course-keeping manoeuvres were performed to evaluate the course-keeping qualities of a ship in different wave headings. Finally, the turning abilities in waves were investigated by conducting turning manoeuvres.

This chapter is organised as follows: In Section 5.2, a list of simulation cases applied to the current CFD model is illustrated. Afterwards, the specific numerical setup of the CFD model is introduced in Section 5.3. Following this, Section 5.4 provides details of the simulation results from this work, including validation and verification studies. Finally, a brief summary of the research presented in this chapter is provided in Section 5.5.

5.2. Goal and Scope

The primary goal of this chapter is to investigate the effects of wave directions on the course keeping and turning capabilities of the KCS model, providing a comprehensive understanding of the manoeuvrability of the ship in waves.

Course keeping and turning manoeuvres were carried out in six different conditions, as described in Table 5.1 and Figure 5.1. The approach speed of 14.5 knots (7.459 m/s) in full scale was chosen for the ship manoeuvre in both calm and head sea conditions (Cases 1 and 2) because of the existence of the available experimental results for comparison while the service speed is 24 knots (12.345 m/s). It should be noted that, despite using the same propeller speed, the approach speeds for the rest of the simulations (Cases 3 - 6) vary depending on the incident wave directions, (13.38 RPS).

A wave with height $H = 0.048\,m$ and period $T = 1.4\,s$ in model scale was employed for the simulations (length ratio $\lambda/L_{BP} = 1.0$ and wave steepness $H/\lambda = 0.016$). These values correspond to a wave height of $3.61\,m$ and period of $12.14\,s$ in full-scale. The encounter frequency of the wave, ω_e, was calculated as $\omega_e = \omega[1 - (\omega U cos\mu)/g]$, where ω is the wave frequency, U is the ship forward speed, μ is the ship's heading angle relative to the wave direction, and g denotes the gravitational acceleration.

Table 5.1 The simulation cases to which the CFD model is applied.

Case no. C	Approach speed U_0 (m/s)	Propeller rev. (RPS)	Wave height H (m)	Encounter Angle μ (degrees)	Encounter Freq. ω_e (rad/s)	Encounter Period T_e (s)	Wave/ship length λ/L_{BP}
1	0.86	10.56	Calm water	- (Calm sea)	-	-	-
2	0.86	13.38	0.048	180 (Head sea)	6.257	1.004	1.00
3	0.95	13.38	0.048	225 (Bow sea)	5.863	1.071	1.00
4	1.07	13.38	0.048	270 (Beam sea)	4.490	1.399	1.00
5	1.03	13.38	0.048	315 (Quartering sea)	2.987	2.103	1.00
6	1.05	13.38	0.048	0 (Following sea)	2.332	2.694	1.00

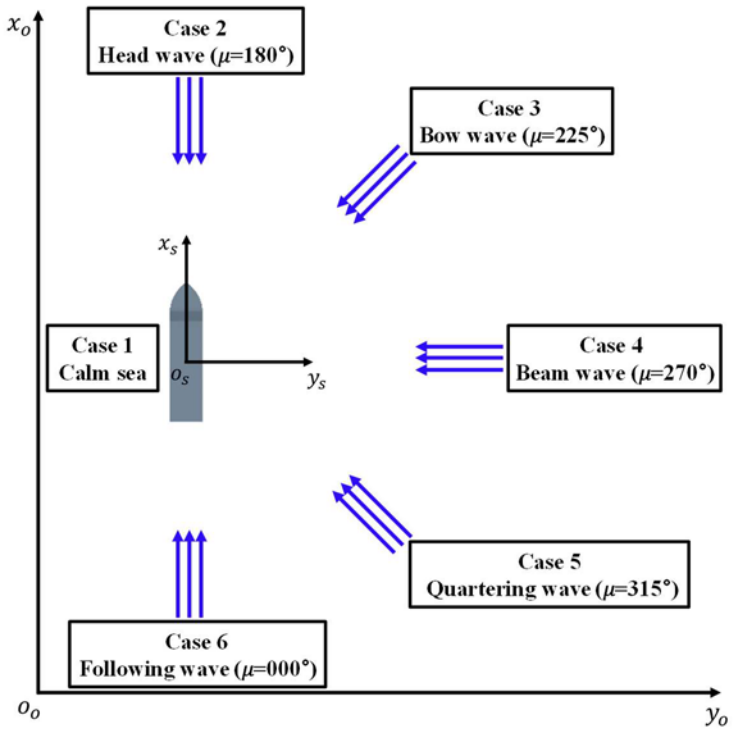

Figure 5.1 Schematic view of all the cases applied in this study for ship manoeuvrability.

5.3. Numerical Modelling

The numerical modelling conducted in the current CFD simulations was in accordance with that reported in Chapter 4, Section 4.3.

Figure 5.2 displays the general overview of the simulation mesh, while the surface grids and prism layers on the KCS hull and the rudder are demonstrated in Figure 5.3. The total grid number applied to the calm water (Case 1) and wave (Cases 2 - 6) simulations is 6.90 million and 7.19 million, respectively.

As stated in Section 4.3.6, ITTC (2011) recommends that at least 100 time steps per period for regular waves should be used for the wave simulation. In this study, therefore, the time step size of all the simulations for the ship manoeuvre was set to $\Delta t = 0.005$, which is two times lower than the recommended guidelines of ITTC (2011) to ensure a reliable solution.

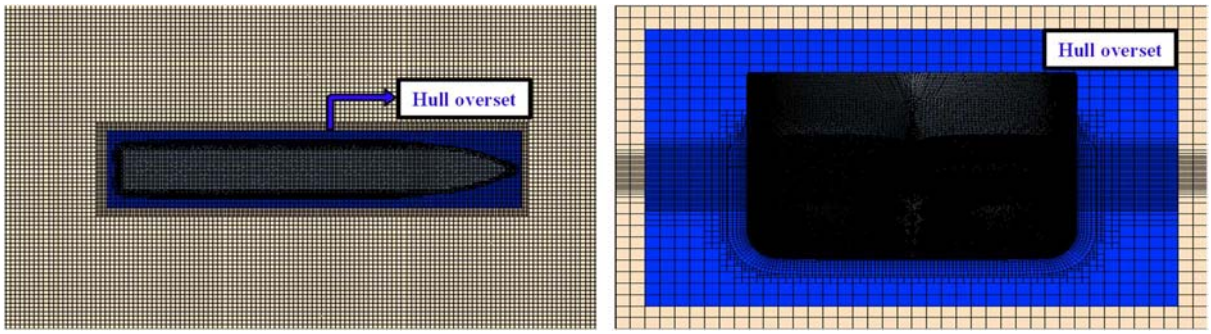

a)

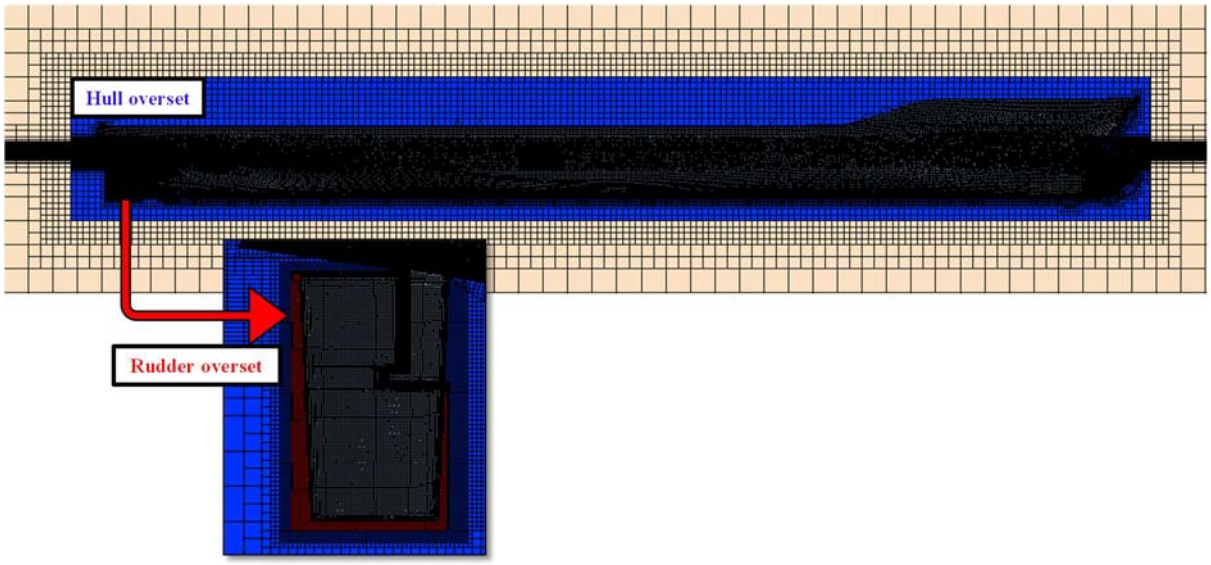

b)

Figure 5.2 Computational mesh: a) Top and front view b) profile view of the domain.

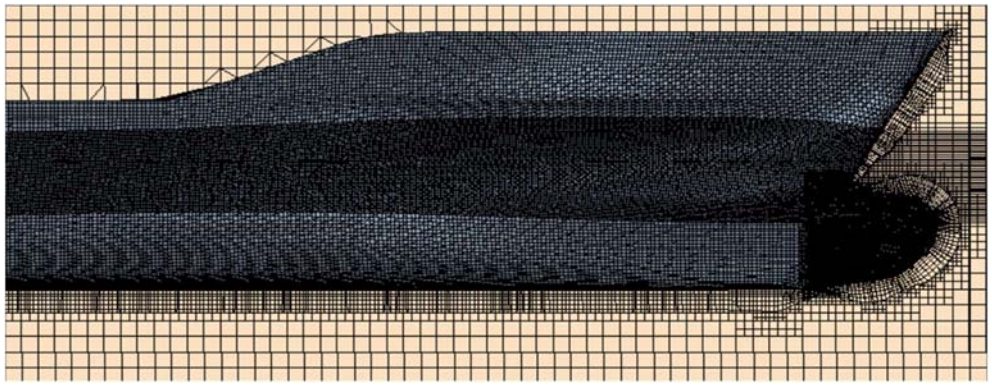

a)

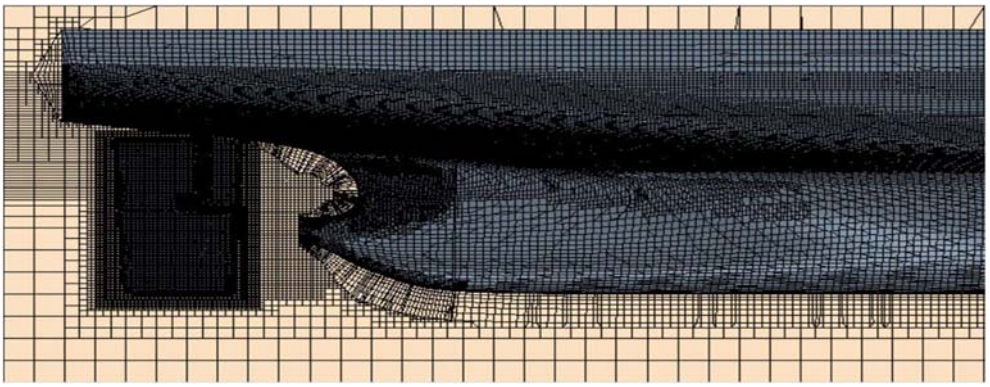

b)

Figure 5.3 Surface grids and prism layers on the a) bow b) stern of the KCS hull and rudder.

5.4. Results

5.4.1. Open-water characteristics

Hydrodynamic propeller characteristics, including the thrust created by a propeller and the required torque to generate that thrust, can be measured in an open water test. Before conducting the manoeuvring simulations, the open-water test of the modelled actuator disk was simulated and compared with the experiments performed by Hiroshima University (SIMMAN, 2020). The open water simulation was carried out for the same conditions as the experimental ones with a wide range of advance coefficients J varying from 0.05 to 0.95. Thrust coefficients K_T, torque coefficients K_Q, and efficiency η_0 for each advance ratio J were calculated from the predicted thrust and torque. Table 5.2 and Figure 5.4 show the CFD calculation results and comparison results. The results showed that both the thrust and the torque were slightly overpredicted as the propeller load decreased ($J \geq 0.4$), whereas they were underpredicted at a higher load ($J < 0.4$). The expected self-propulsion point of the KCS ranged from J = 0.4 to J = 0.6, where the predicted thrust and torque showed excellent agreement with the experiments with errors up to 1.6%. This indicates that the actuator disk based on the body force method can predict the open-water curves regarding the thrust and torque. This actuator disk model was used for all the CFD simulations in this study.

Table 5.2 Propeller open water test results.

J	CFD			Experiment (SIMMAN, 2020)			Error of K_T (%)	Error of K_Q (%)	Error of η_0 (%)
	K_T	K_Q	η_0	K_T	K_Q	η_0			
0.0455	0.4442	0.0655	0.0491	0.4659	0.0685	0.0492	4.66	4.41	0.26
0.1433	0.4107	0.0611	0.1532	0.4398	0.0648	0.1546	6.61	5.71	0.97
0.2203	0.3900	0.0585	0.2337	0.3993	0.0597	0.2345	2.32	2.01	0.33
0.3085	0.3492	0.0533	0.3216	0.3551	0.0540	0.3225	1.66	1.41	0.26
0.3926	0.3075	0.0481	0.3988	0.3083	0.0482	0.3990	0.26	0.23	0.03
0.4884	0.2626	0.0424	0.4808	0.2605	0.0421	0.4800	-0.81	-0.64	-0.16
0.5948	0.2042	0.0351	0.5502	0.2010	0.0347	0.5478	-1.59	-1.15	-0.43
0.6849	0.1567	0.0290	0.5890	0.1531	0.0285	0.5843	-2.35	-1.54	-0.79
0.7753	0.1064	0.0218	0.6003	0.1029	0.0213	0.5941	-3.40	-2.34	-1.04
0.8716	0.0501	0.0140	0.4945	0.0480	0.0137	0.4835	-4.43	-2.11	-2.28

0.9593	-0.0037	0.0066	-0.0855	-0.0035	0.0067	-0.0803	-5.71	0.75	-6.52

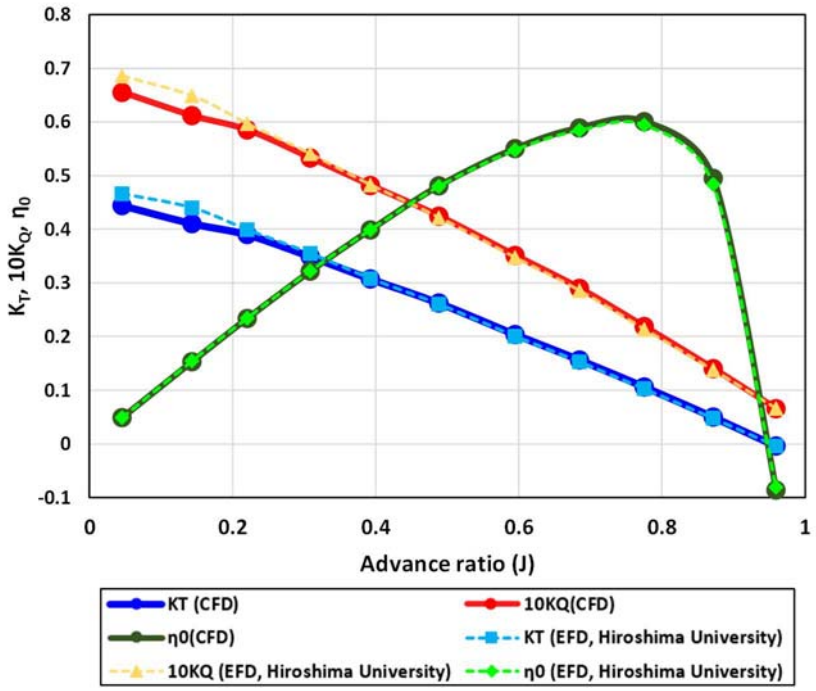

Figure 5.4 Propeller open water test results and comparison.

5.4.2. Verification study

A verification study was carried out to quantify the numerical uncertainties of the CFD models. Spatial and temporal convergence analyses were undertaken independently to investigate proper grid-spacing and time step. For mesh convergence behaviour, the Grid Convergent Index (GCI) approach based on the extrapolation of Richardson (1911) was adopted according to Celik et al. (2008) and a brief description is given below. In the same manner, the GCI method can also be employed for a time step convergence study as stated in Song et al. (2020b).

Let N_1, N_2 and N_3 denote the total number of grids applied for the numerical computations and h_1, h_2 and h_3 are representative grid sizes. ΔV_i represents the volume of the ith cell and refinement factors r_{21} and r_{32} are defined by the following expressions:

$$r_{21} = \frac{h_2}{h_1} \tag{5.1}$$

$$r_{32} = \frac{h_3}{h_2} \tag{5.2}$$

$$h_j = \left[\frac{1}{N_j}\sum_{i=1}^{N_j}(\Delta V_i)\right]^{1/3}, \qquad j = 1,2,3 \tag{5.3}$$

For a temporal convergence study, the definition of time refinement rate can be given by $r_{21} = \Delta t_2/\Delta t_1$ and $r_{32} = \Delta t_3/\Delta t_2$. It should be taken into account that the refinement factor should

be greater than 1.3 according to Celik et al. (2008).

The apparent order of the method, p, is calculated by the formula

$$p = \frac{1}{\ln(r_{21})}\left|\ln\left|\frac{\varepsilon_{32}}{\varepsilon_{21}}\right| + q(p)\right| \tag{5.4}$$

$$q(p) = \ln\left(\frac{r_{21}^{p} - s}{r_{32}^{p} - s}\right) \tag{5.5}$$

$$s = 1 \cdot sgn\left(\frac{\varepsilon_{32}}{\varepsilon_{21}}\right) \tag{5.6}$$

In Equation (5.6) $\varepsilon_{32} = \phi_3 - \phi_2$ and $\varepsilon_{21} = \phi_2 - \phi_1$ are the differences between coarse-medium and medium-fine solutions, where ϕ_1, ϕ_2, ϕ_3 correspond to the solutions with fine, medium, and coarse input parameters (i.e. grid-size for the mesh convergence study or time-step for the temporal convergence study).

The extrapolated values are defined as:

$$\phi_{ext}^{21} = \frac{r_{21}^{p}\phi_1 - \phi_2}{r_{21}^{p} - 1} \tag{5.7}$$

In the same way, ϕ_{ext}^{32} is calculated by $\phi_{ext}^{32} = (r_{32}^{p}\phi_2 - \phi_3)/(r_{32}^{p} - 1)$.

The definition of approximate relative error (e_a^{21}) and extrapolated relative error (e_{ext}^{21}), respectively, can be described by:

$$e_a^{21} = \left|\frac{\phi_1 - \phi_2}{\phi_1}\right| \tag{5.8}$$

$$e_{ext}^{21} = \left|\frac{\phi_{ext}^{12} - \phi_1}{\phi_{ext}^{12}}\right| \tag{5.9}$$

Eventually, the fine-grid convergence index is obtained as follows:

$$GCI_{fine}^{21} = \frac{1.25 e_a^{21}}{r_{21}^{p} - 1} \tag{5.10}$$

In this study, the verification parameters of the advance, transfer, and tactical diameter for the spatial and temporal convergence studies were investigated. These parameters were identified by ITTC (2021b) to which reference can be made for more detailed information on the definition of a turning manoeuvre. The relevant indices are illustrated in Figure 5.5.

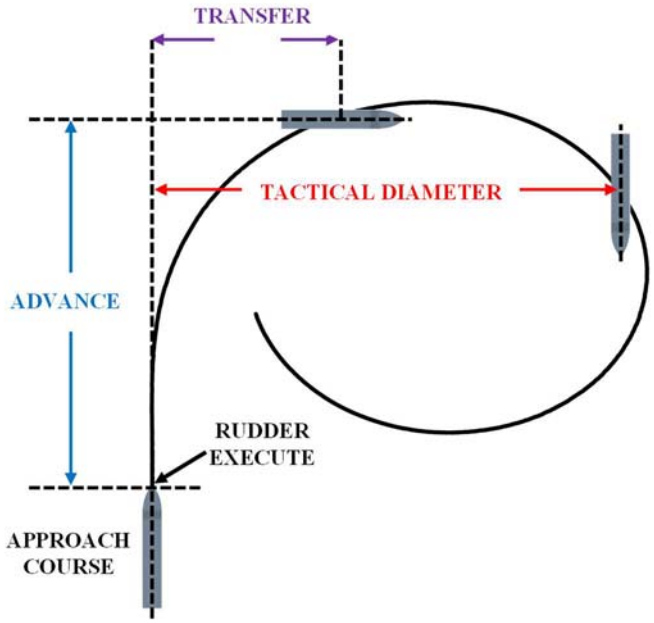

Figure 5.5 The definitions of a turning circle.

The head wave simulation (Case 2) was chosen for the spatial convergence study. The grid convergence test was performed with three different resolutions of grids, which are regarded as fine, medium, and coarse meshes corresponding to grid numbers of 7,189,514 cells, 4,825,180 cells, and 2,735,883 cells.

Table **5.3** shows the required parameters for the calculation of the spatial discretization error. The ship advance, transfer, and tactical diameter were used as the key variables. As can be seen from

Table **5.3**, numerical uncertainties of 0.11%, 0.28%, and 0.06% were calculated for the computed ship advance, transfer, and tactical diameter, respectively.

The head wave simulation (Case 2) was also selected for the temporal convergence study. Three different time steps were employed based on a uniform refinement ratio of 2, starting from $\Delta t = 0.005s$. Table 5.4 describes the required parameters of the calculation of the temporal discretization error. The ship advance, transfer, and tactical diameter were used as the key variables. As can be seen from Table 5.4, numerical uncertainties of 0.161%, 0.196%, and 0.043% were calculated for the computed ship advance, transfer, and tactical diameter, respectively.

Table 5.3 Calculation of the discretization error for the spatial convergence study, key variables: Advance, transfer, and tactical diameter.

	Advance	Transfer	Tactical diameter
N_1	7,189,514	7,189,514	7,189,514
N_2	4,825,180	4,825,180	4,825,180
N_3	3,153,041	3,153,041	3,153,041
r_{21}	1.14	1.14	1.14
r_{23}	1.15	1.15	1.15
ϕ_1	7.866m	3.089m	7.968m
ϕ_2	7.924m	3.141m	8.024m
ϕ_3	8.598m	3.662m	9.131m
ε_{32}	6.74E-01	5.21E-01	$1.11\mathrm{E}+00$
ε_{21}	5.82E-02	5.18E-02	5.60E-02
s	1	1	1
e_a^{21}	0.74%	1.68%	0.70%
q	−1.69E-01	−1.61E-01	−1.98E-01
p_a	$1.72\mathrm{E}+01$	$1.62\mathrm{E}+01$	$2.10\mathrm{E}+01$
ϕ_{ext}^{21}	$7.86\mathrm{E}+00$	$3.08\mathrm{E}+00$	$7.96\mathrm{E}+00$
e_{ext}^{21}	0.08%	0.22%	0.05%
GCI_{fine}^{21}	0.11%	0.28%	0.06%

Table 5.4 Calculation of the discretization error for the temporal convergence study, key variables: Advance, Transfer, and Tactical diameter.

	Advance	Transfer	Tactical diameter
Δt_1	$0.005s$	$0.005s$	$0.005s$
Δt_2	$0.01s$	$0.01s$	$0.01s$
Δt_3	$0.02s$	$0.02s$	$0.02s$
r_{21}, r_{32}	2	2	2
ϕ_1	$7.86582m$	$3.089m$	7.968m
ϕ_2	$7.84181m$	$3.109m$	$7.996m$
ϕ_3	$7.76073m$	$3.214m$	8.313m
ε_{32}	−8.11E-02	1.04E-01	3.17E-01
ε_{21}	−2.40E-02	2.02E-02	2.81E-02
e_a^{21}	0.31%	0.65%	0.35%
p_a	$1.76\mathrm{E}+00$	$2.37\mathrm{E}+00$	$3.49\mathrm{E}+00$
ϕ_{ext}^{21}	$7.876\mathrm{E}+00$	$3.084\mathrm{E}+00$	$7.965\mathrm{E}+00$
e_{ext}^{21}	0.128%	0.157%	0.034%
$GCI_{\Delta t_1}^{21}$	0.161%	0.196%	0.043%

5.4.3. Validation study

Experimental and numerical results were compared to evaluate the uncertainties of this work's CFD model. The turning manoeuvres performed in calm water (Case 1) and head seas (Case 2) were carried out first for the validation study. The procedure to conduct a turning manoeuvre requires achieving the self-propulsion condition at the approach speed. The target speed was 0.86 m/s (14.5 knots at full scale) in both Case 1 and Case 2 and the actuator disk speed was frozen after the ship achieved the self-propulsion condition. Following this, the turning manoeuvres were conducted by controlling the rudder according to the turning manoeuvre module presented in Chapter 4, Section 4.3.9. The computed essential manoeuvring indices and hydrodynamic characteristics for the KCS model were validated against the available experimental data from Hiroshima University (Yasukawa et al., 2021). It should be noted that the experimental uncertainties in the critical manoeuvring quantities are not available in the literature, and thus could not be included in this study.

The predicted major parameters of the ship turning manoeuvre were compared to those from their experiments (Yasukawa et al., 2021) as shown in Table 5.5 and Table **5.6**. The simulated results were found to be in good agreement with the experiments with errors up to 5% in calm water and 8% in head seas, respectively. The actuator disk model applied to the current CFD approach was able to accurately represent the effects of the real propeller on the self-propulsion condition with respect to the rotational speed and thrust. Not only that, but the predicted turning indices, i.e., advance, transfer, tactical diameter as well as time to 90°/180° yaw angle change, also showed reasonable results, with the measured results with errors varying from −7.78% to 3.28%. This indicates that the CFD model developed in this study can resolve the hull-propeller-rudder interaction affecting the ship manoeuvre characteristics with reasonable accuracy during turning manoeuvres.

Table 5.5 Comparison of the main parameters of a standard turning circle manoeuvre in calm water.

Parameters	CFD	EFD (Yasukawa et al., 2021)	Error (%)
RPS at self-propulsion point	10.56	10.40	1.58
Advance (m)	9.30	9.29	0.01
Transfer (m)	3.95	4.16	−4.86
Time for yaw 90 degrees (s)	15.45	15.64	−1.22
Tactical diameter (m)	9.94	9.66	2.89
Time for yaw 180 degrees (s)	31.50	30.50	3.28

Table 5.6 Comparison of the main parameters of a standard turning circle manoeuvre in head waves.

Parameters	CFD	EFD (Yasukawa et al., 2021)	Error (%)
RPS at self-propulsion point	13.38	13.2	1.36

Advance (m)	7.86	8.20	-4.11
Transfer (m)	3.09	3.35	-7.78
Time for yaw 90 degrees (s)	12.52	13.29	-5.81
Tactical diameter (m)	7.97	8.37	-4.83
Time for yaw 180 degrees (s)	23.74	25.32	-6.24

Figure 5.6 and Figure **5.7** illustrate the comparisons of the time histories of the ship speeds, ship motions, propeller thrust, and torque during a turning manoeuvre in calm water and regular head waves. It is worth noting that the time was shifted to match the beginning of the rudder execution time for the correct comparison with the experimental results. It is evident that the simulation results were consistent with the experiments regarding surge velocity and yaw velocity for both calm and head seas, though slight discrepancies were observed for sway velocity in both cases. It should be noted that ship surge velocity reduced considerably due to the increased resistance after the rudder execution to starboard $35°$ for the turning manoeuvre and reached the steady speed of approximately 50% and 60% of the approach speed (0.86 m/s) in calm water and head waves, respectively.

As for the ship seakeeping behaviour in Figure 5.6 and Figure **5.7** (d - f), the large discrepancy of roll motion between the CFD prediction and experimental measurement was noted, while the pitch and heave motions showed a reasonable match with the experiments. The discrepancy concerning the roll motion may be caused by two possible reasons. The first is the experimental uncertainty of KG (the vertical distance between the keel and the centre of gravity). The uncertain KG position in CFD calculations may give rise to the disagreement between the simulation and experiment since the properties of the roll motion are mainly determined by the height of centre of mass. Another reason is the body force approach applied to the CFD model, which did not take into account the side force of the propeller during the turning manoeuvre (Broglia et al., 2015; Dubbioso et al., 2016). The limitation of the simplified actuator disk model may lead to a difference in the roll response from the experimental results.

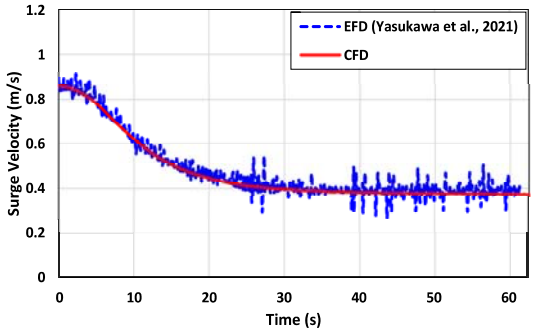

(a) Surge velocity

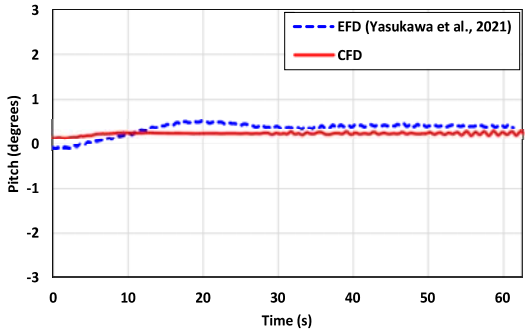

(e) Pitch displacement

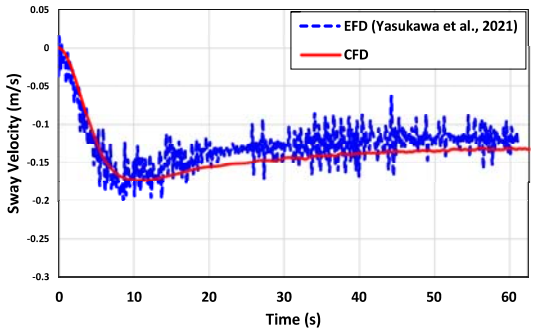

(b) Sway velocity

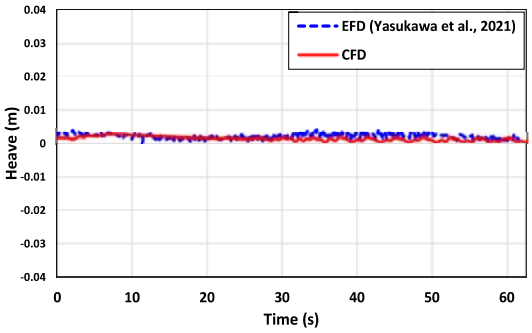

(f) Heave displacement

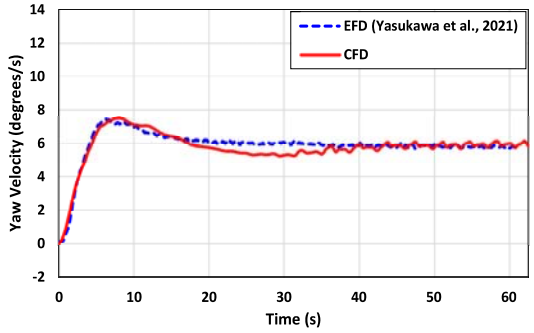

(c) Yaw velocity

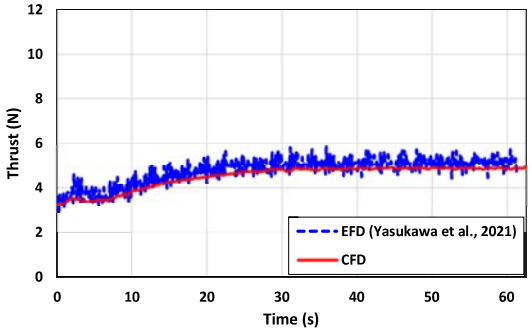

(g) Thrust

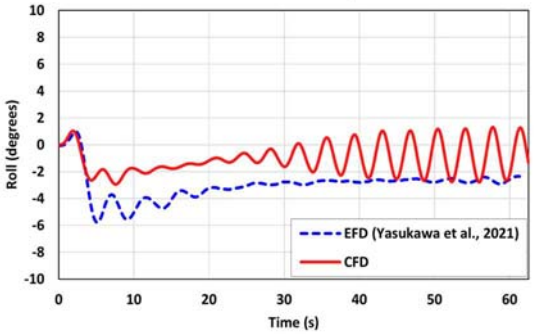

(d) Roll displacement

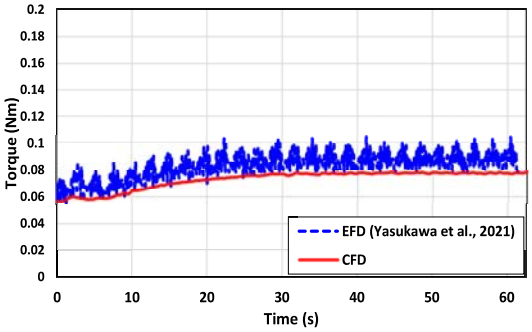

(h) Torque

Figure 5.6 Comparisons of the time histories of the ship velocities, motions, and propeller characteristics during the turning manoeuvre in calm water.

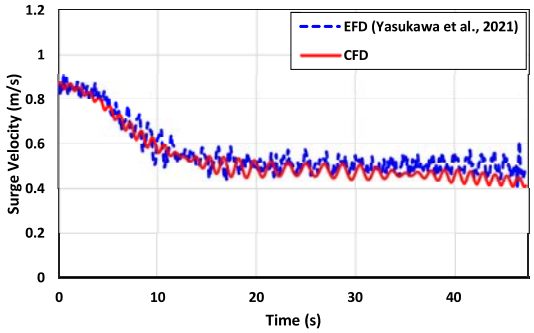

(a) Surge velocity

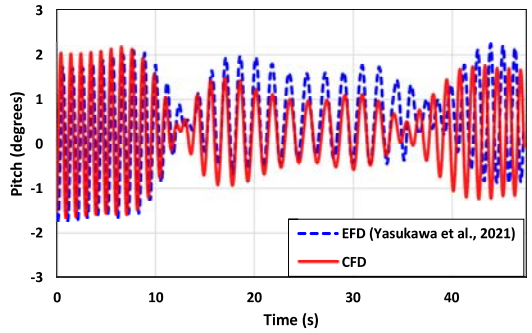

(e) Pitch displacement

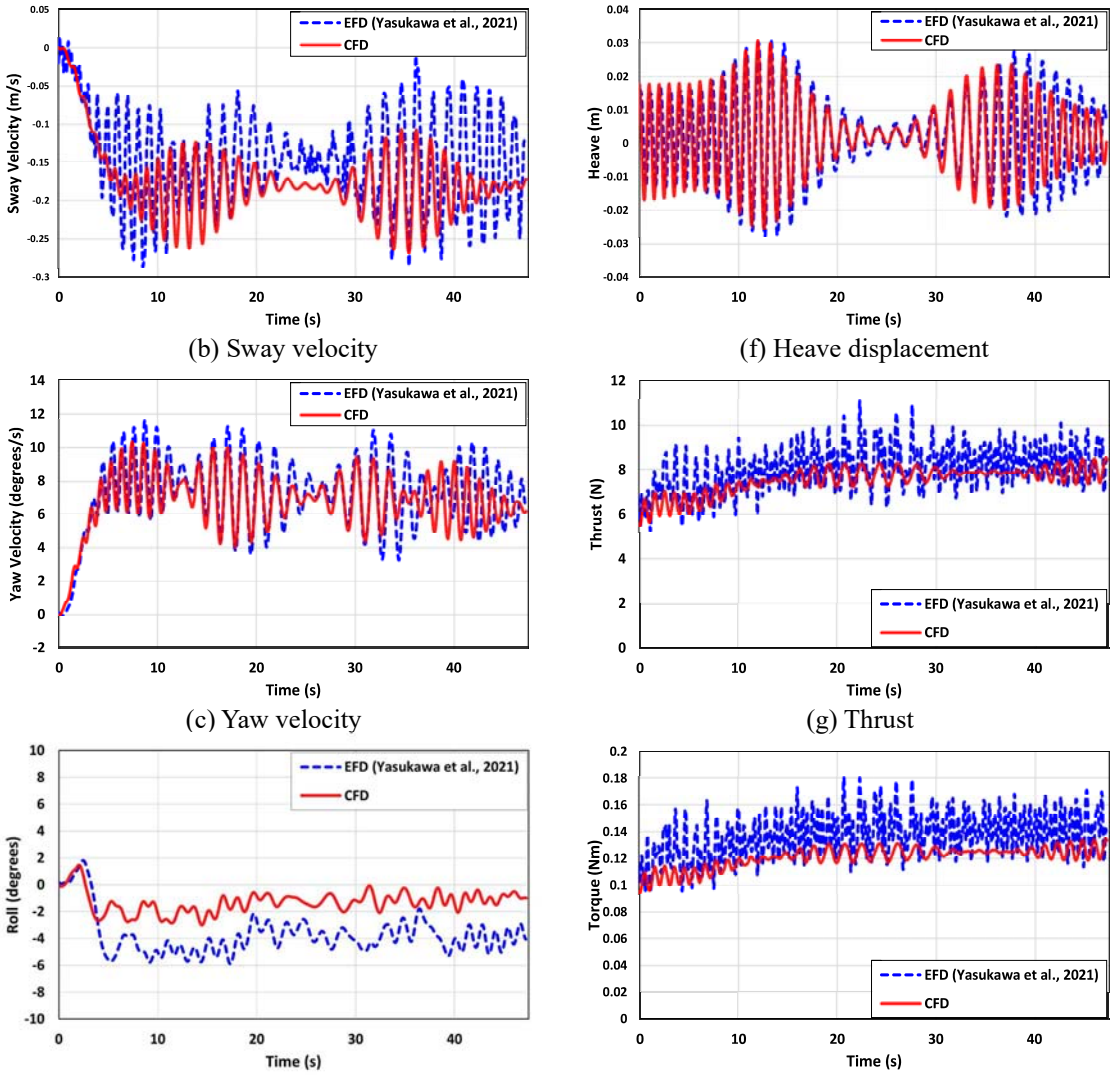

Figure 5.7 Comparisons of time histories of ship velocities, motions, and propeller characteristics during the turning manoeuvre in head wave.

Figure **5.8** (a) and (b) describe the turning trajectories in calm water and head seas, respectively. The CFD results of turning circle trajectories for both cases are in reasonable agreement with the measurements. The calculated turning trajectory in calm water was slightly larger than that of the experimental data, whereas the trajectory in head waves was slightly smaller than that of the measurements. Despite these different patterns of the turning trajectories in both cases, the important turning indices related to the ship turning manoeuvre were estimated fairly well with a maximum error of about 7.8% using the current CFD approach as can be seen from the results listed in Table 5.5 and Table **5.6**. This comparison indicates that the present numerical approach can provide an overall assessment of the manoeuvring performance in both calm sea and waves.

With this comparison, the current CFD approach can be argued to be validated and can be applied for further examinations. This free-running CFD model was therefore used throughout all the simulations.

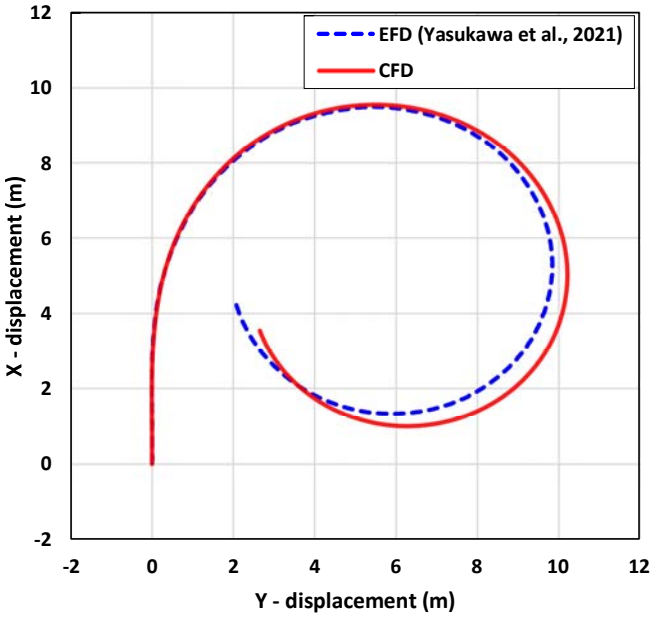

(a) Trajectory in calm water

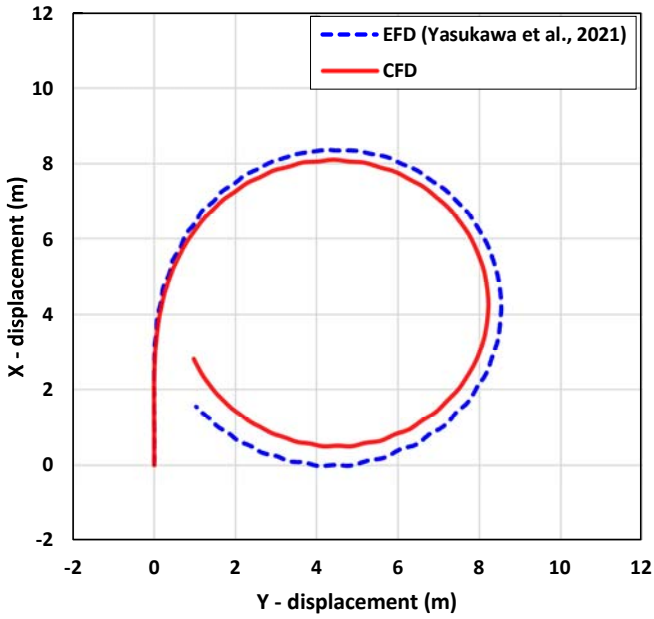

(b) Trajectory in head waves

Figure 5.8 Comparisons of turning trajectories in a) calm water and b) head waves.

5.4.4. Self-propulsion

The self-propulsion condition is a required procedure that should be accomplished before starting the ship turning manoeuvre. The results obtained from the self-propulsion computations can provide an investigation into the manoeuvring performance of a ship under

the same propeller revolution for different wave conditions. It is worth noting that the self-propulsion simulations were conducted with 6 degrees of freedom, with the moving rudder controlled by the feedback controller to maintain the ship's course before starting the turning manoeuvre. As listed in Table 5.1, the nominal approach speed for both calm and head sea conditions (Cases 1 and 2) was set to be 0.86 m/s with a propeller speed of 10.56 RPS and 13.38 RPS, respectively. For the rest of the simulations (Cases 3 - 6), the speed of the propeller at self-propulsion was set to be 13.38 RPS, which equals to the revolution of the head wave case.

Figure 5.9 shows the comparisons of the time histories of the approach speed, ship resistance, pitch motion, and heave motion under the self-propulsion conditions for all the cases. The Fourier Series (FS) (Tezdogan et al., 2015; Wang and Wan, 2018) was utilised to analyse the harmonic CFD results due to wave motion. The average value of the time history of the obtained results was calculated by the 0th harmonic FS term and the mean amplitude of the oscillation of the values was quantified by the 1st harmonic FS term. The obtained FS results are given in Table 5.7.

As Figure 5.9 and Table 5.7 jointly show, the propeller speed was increased by 27% in the head wave compared with that in calm water in order to achieve the approach speed (0.86 m/s), while the total resistance also increased by 226% due to the incident waves. As stated previously, regular waves with the length ratio of $\lambda/L_{BP} = 1.0$ and height of $H = 0.048\,m$ were applied throughout all the simulations. When the ship was advancing forward in waves, she experienced substantial changes in the forward speed and resistance. The increase of the mean forward speed was predicted to be 9.9% for the bow wave, 24% for the beam wave, 21% for the quartering wave, and 22% for the following wave when compared to the head wave case. Similarly, the decrease in ship resistance was found to be 6% for the bow wave, 30% for the beam wave, 27% for the quartering wave, and 29% for the following wave. From this observation, the ship operation in the head wave can lead to a drastic increase in fuel consumption.

The comparisons between the time histories of the ship motions in various wave conditions are presented in Figure 5.9 (c) and (d) to better understand the effects of wave directions on the ship motions. It has to be stated that the frequency of ship motions in waves is determined by the wave encountering frequency. Short-term oscillations of the ship motions with regular periodicity were observed in head waves whereas relatively long-term oscillations were found in following waves within a given period due to the wave encounter frequency. The amplitude of ship motions was found to be closely related to the wave direction. The pitch motion was considerably increased in head and bow seas with a mean amplitude of 1.84º and 1.87º, whilst the pitch in beam waves was almost negligible with a value of 0.4º. Also, the decrease in the amplitude of pitch oscillation was predicted to be 95% for the beam sea, 49% for the quartering sea, and 78% for the following wave, compared with the head wave case. As for the heave motion, the largest oscillation amplitude was predicted in beam waves with a value of 0.025m which is almost equal to that of the incident wave: only a difference of 4%. Also, the increase in the heave amplitude was found to be 12% for the bow sea and 27% for the beam sea, while the reduction was estimated to be 53% for the quartering sea and 94% for the following sea, compared to the head wave case.

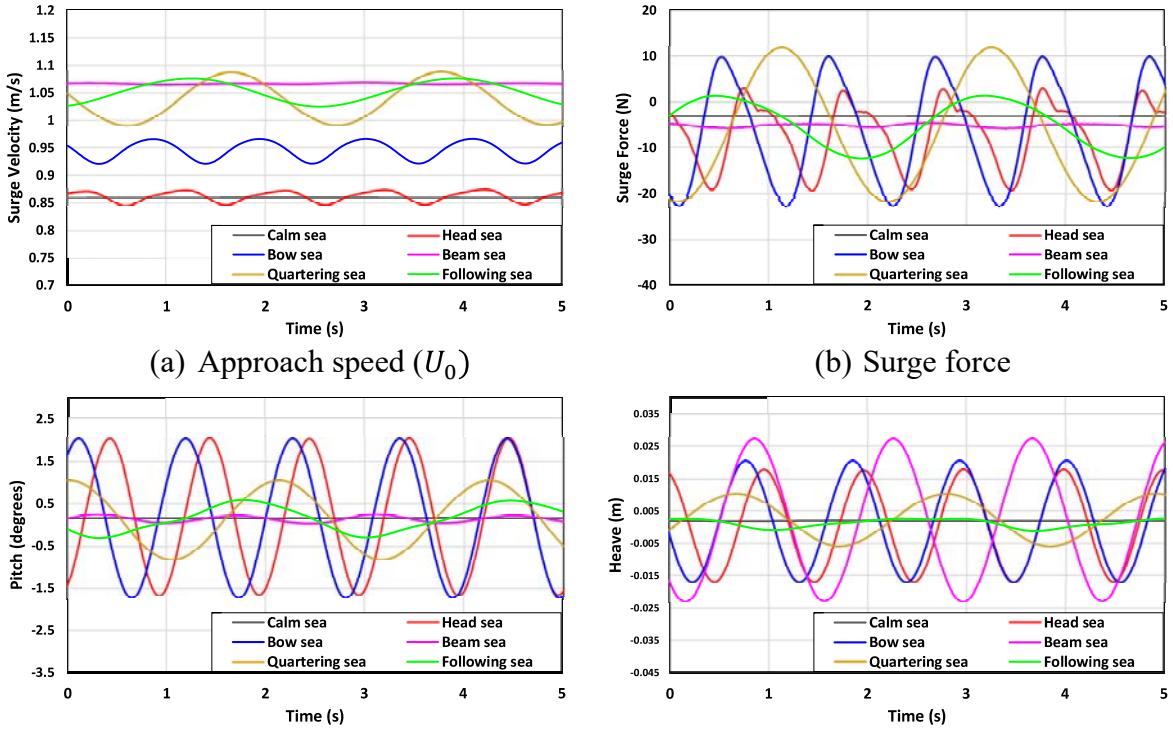

(a) Approach speed (U_0) (b) Surge force

(c) Pitch displacement (d) Heave displacement

Figure 5.9 Time histories of the approach speed, ship resistance, pitch motion and heave motion for all cases.

Table 5.7 Fourier Series analysis of the approach speed, ship resistance, pitch motion and heave motion at self-propulsion.

Case no.	Approach speed U_0 (m/s)		Resistance F_x (N)		Pitch displacement (degrees)		Heave displacement (m)	
C	0th FS term	1st FS term	0th FS term	1st FS term	0th FS term	1st FS term	0th FS term	1st FS term
1 (Calm sea)	0.860	-	3.237	-	0.002	-	0.144	-
2 (Head sea)	0.860	0.013	7.318	9.240	0.180	1.842	0.000	0.017
3 (Bow sea)	0.945	0.024	6.723	15.548	0.170	1.876	0.002	0.019
4 (Beam sea)	1.067	0.008	5.186	0.438	0.123	0.095	0.002	0.025
5 (Quartering sea)	1.038	0.048	5.336	16.843	0.127	0.931	0.002	0.008
6 (Following sea)	1.049	0.025	5.215	6.619	0.135	0.399	0.001	0.001

The instantaneous free surface elevation at the self-propulsion condition is shown in Figure 5.10 in which the Kelvin waves generated by the advancing ship are clearly visible. In the head wave case (b), the rudder angle was deflected towards the starboard 35° during the moments when the wave trough passed on the midship of the model based on the experimental data. In the same way, for the rest of the simulations in waves, the rudder started to be deflected during the moments when the wave trough passed on the midship of the ship. However, it is worth noting that Kim et al. (2019) stated that the timing of rudder deflection has little influence on the low-frequency manoeuvring characteristics of a ship.

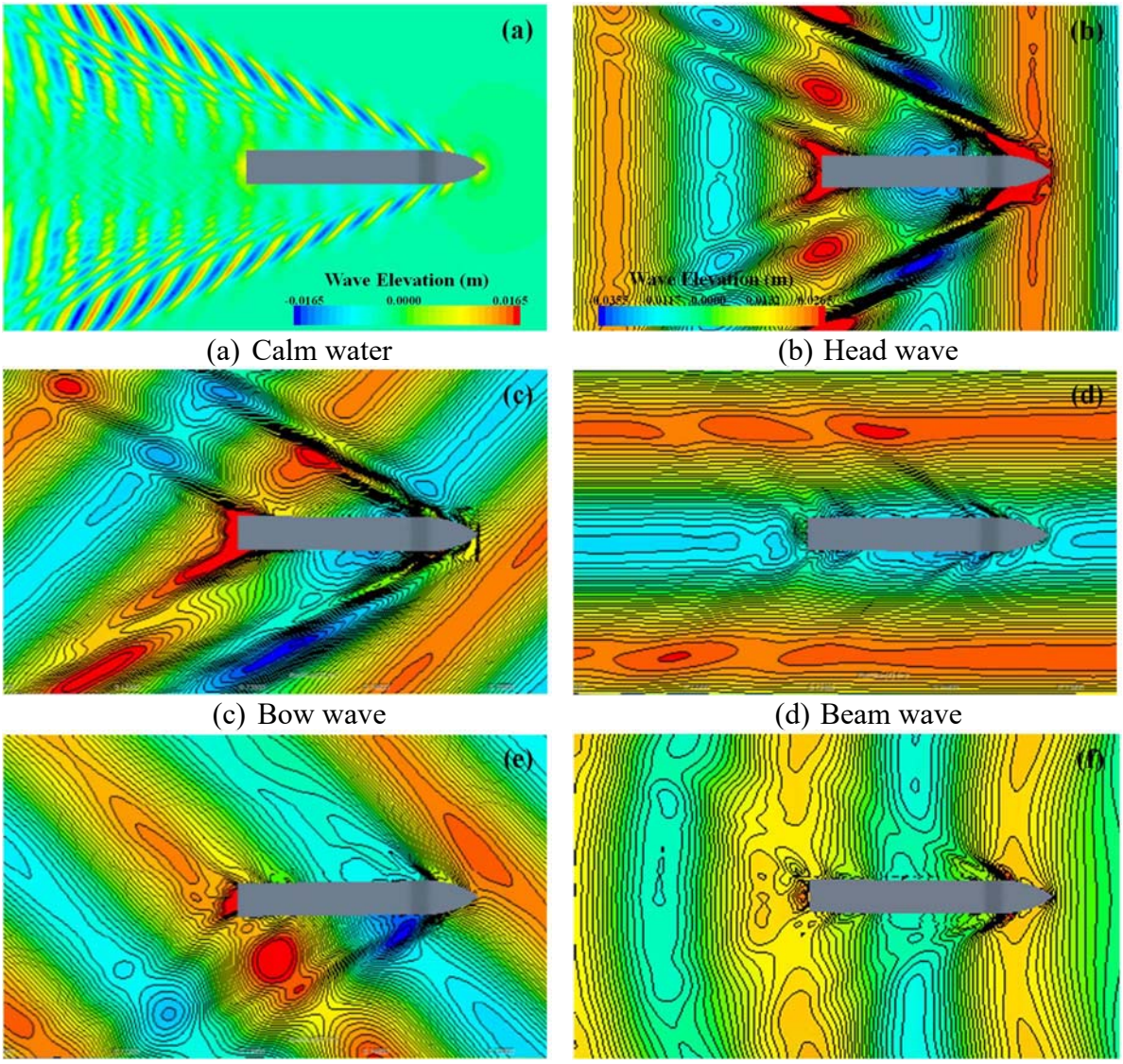

(a) Calm water (b) Head wave

(c) Bow wave (d) Beam wave

(e) Quartering wave (f) Following wave

Figure 5.10 Free surface elevation at self-propulsion condition before conducting the turning manoeuvre.

5.4.5. Course keeping control

Given that, in general, ships have planned schedules, voyage plans could be determined with a careful route arrangement in consideration of critical safety factors related to route characteristics before a voyage commences. A navigation route in the voyage plan is separated into different straight-line segments, each of which is denoted by the true course between two consecutive waypoints. In navigation practice, the true course can generally be regarded as the target heading angle to be set as input in the auto-pilot system, implying that course keeping control using the autopilot can be identical to automatic heading control. Hence, a vessel sailing at sea may be deviated from its original course when the heading angle deviation from the target heading angle occurs. In this sub-section, the course keeping capabilities of the ship in waves are evaluated based on this automatic heading control mode (as described in Chapter 4, Section 4.3.9). It is also worth mentioning that recently developed autopilot systems are

capable of correcting the ship's course to return to the original course, using the new route control function in which a route is automatically created between the current position and destination (though this is not studied in the present work).

The key advantage of the present CFD approach is that it can predict not only the combined seakeeping and manoeuvring performance but also the course keeping ability under different wave conditions. Wang et al. (2017), for example, carried out free-running CFD simulations successfully to evaluate the course keeping ability of the ONR Tumblehome ship in waves using the fully nonlinear unsteady RANS method. Unfortunately, to the best of this author's knowledge, no well-documented experimental tests for the course keeping behaviour of the KCS model in waves are available. Though, as presented in Section 5.4.3, good agreement was observed for the yaw velocity in response to the rudder deflection, which is the most influential factor for the course keeping control. Thus, it is considered to be acceptable to investigate the course keeping ability in waves by using the current CFD model.

Figure 5.11 and Figure **5.12** illustrate the time evolution of the rudder, yaw angle, and yaw velocity during the course-keeping manoeuvre for all simulation cases. Based on the applied coordinates system, the positive value of the rudder angle indicates the rudder deflection for making the ship's heading to port, whereas the negative value indicates the deflection for making the ship's heading to starboard. A plus sign of yaw angle and velocity refers to the direction of rotation to starboard, whilst a minus sign refers to the direction of rotation to port. It should be noted that the simulated results for the course keeping ability showed a similar trend between the rudder angle and the yaw angle since the rudder controller depends largely on the yaw deviation defined in Equation (4.19). However, it should be borne in mind that the maximum execution angle of the rudder can be changeable according to the coefficients of the PID controller.

As presented in Figure 5.11 (a) and (b), the rudder control was not critical to maintain a desired heading of the ship in both calm water and head waves. As for the calm water case, the yaw angle was kept to be almost 0° with the rudder deflection about 1.8°. It is worth noting that an advancing ship has a small yaw moment caused by the asymmetric pressure distribution acting on the rudder blade, due to the discharge flow of the propeller, which can result in the small rudder deflection. Concerning the head wave simulation, the maximum execution angle of the rudder was noted to be about 0.8° with the small fluctuation. The maximum yaw velocity was also predicted to be 0.008°/s in calm water and 0.009°/s in head wave. As seen in Figure 5.10 (a) and (b), the wave patterns are symmetric when the ship is advancing straight forward in both calm and head seas. This means that there is almost no pressure difference on both sides of the ship hull, which does not induce lateral force and yaw moments and thus does not induce yaw deviation.

Compared with the calm water and head wave cases, the maximum rudder deflection became noticeably larger in beam and following seas. The rudder deflection in beam and following seas was observed to be 3.1° and 3.7°, respectively. The maximum yaw deviation was also reported to be 0.41° in the beam sea and 0.46° in the following wave, as presented in Figure 5.11 (d) and (f). The maximum yaw velocity was about 0.3°/s for both cases. Similar to the calm water and head sea cases, symmetric wave profiles around the hull were found, which can barely

affect the yaw deviation of the ship, as depicted in Figure 5.10 (d) and (f).

On the other hand, the rudder angle deflection became large to make the ship straight in oblique seas, namely, bow and quartering waves. As presented in Figure 5.10 (c) and (d), asymmetric wave profiles were observed in oblique seas, which may cause a substantial lateral force and yaw moment. The maximum rudder deflection was observed to be 6.8° in the bow sea and 12° in the quartering sea, while the maximum yaw velocity was 2.4°/s and 3.4°/s, respectively. It can be clearly noted that these values showed a larger amplitude of oscillations in the simulations presented in Figure 5.11 (c) and (e) and Figure 5.12 (c) and (e). The maximum value of yaw deviation was also calculated to be 0.6° and 1.4°, respectively. It appears that the oblique seas experienced the large rudder angle deflection based on the rudder feedback controller to control the ship's heading among all the wave simulations.

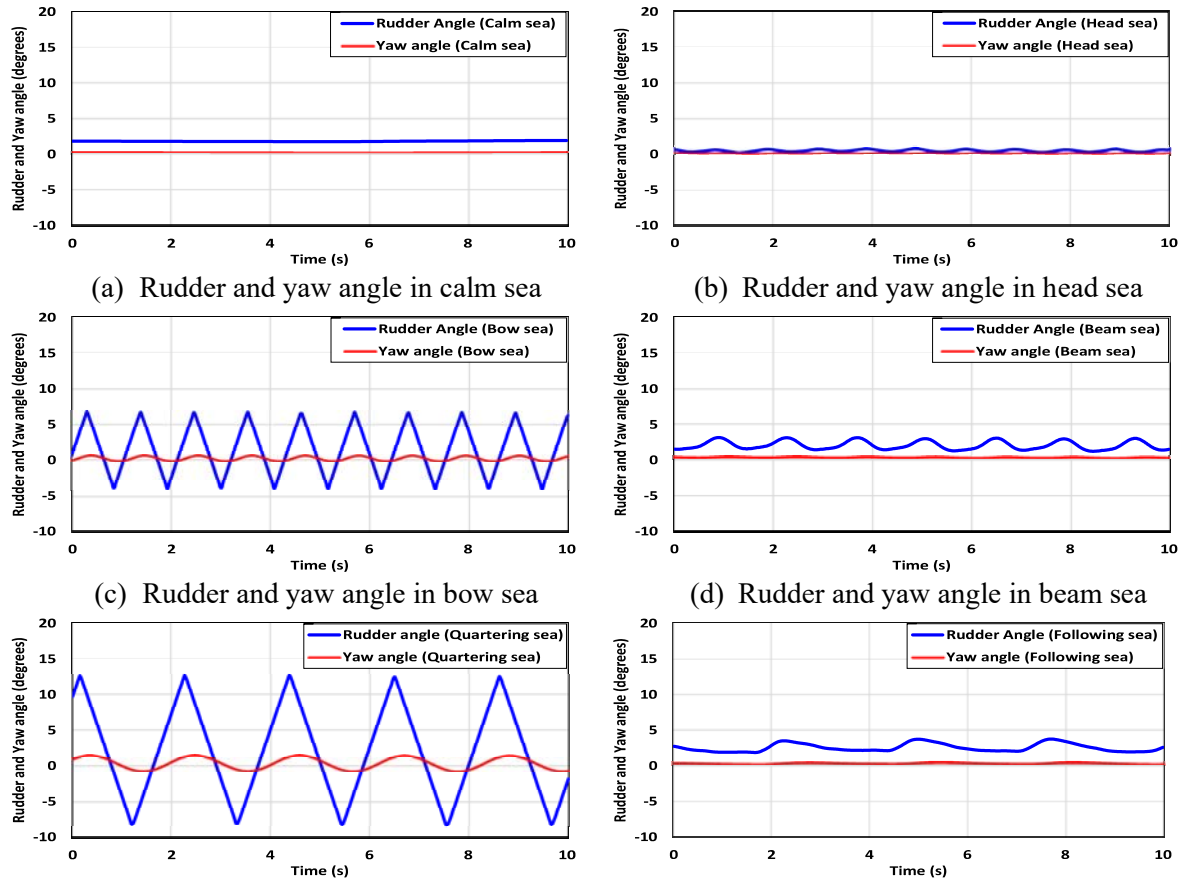

(a) Rudder and yaw angle in calm sea

(b) Rudder and yaw angle in head sea

(c) Rudder and yaw angle in bow sea

(d) Rudder and yaw angle in beam sea

(e) Rudder and yaw angle in quartering sea

(f) Rudder and yaw angle in following sea

Figure 5.11 Time histories of the rudder deflection and yaw angle during the course-keeping manoeuvre in (a) calm sea, (b) head sea, (c) bow sea, (d) beam sea, (e) quartering sea, and (f) following sea.

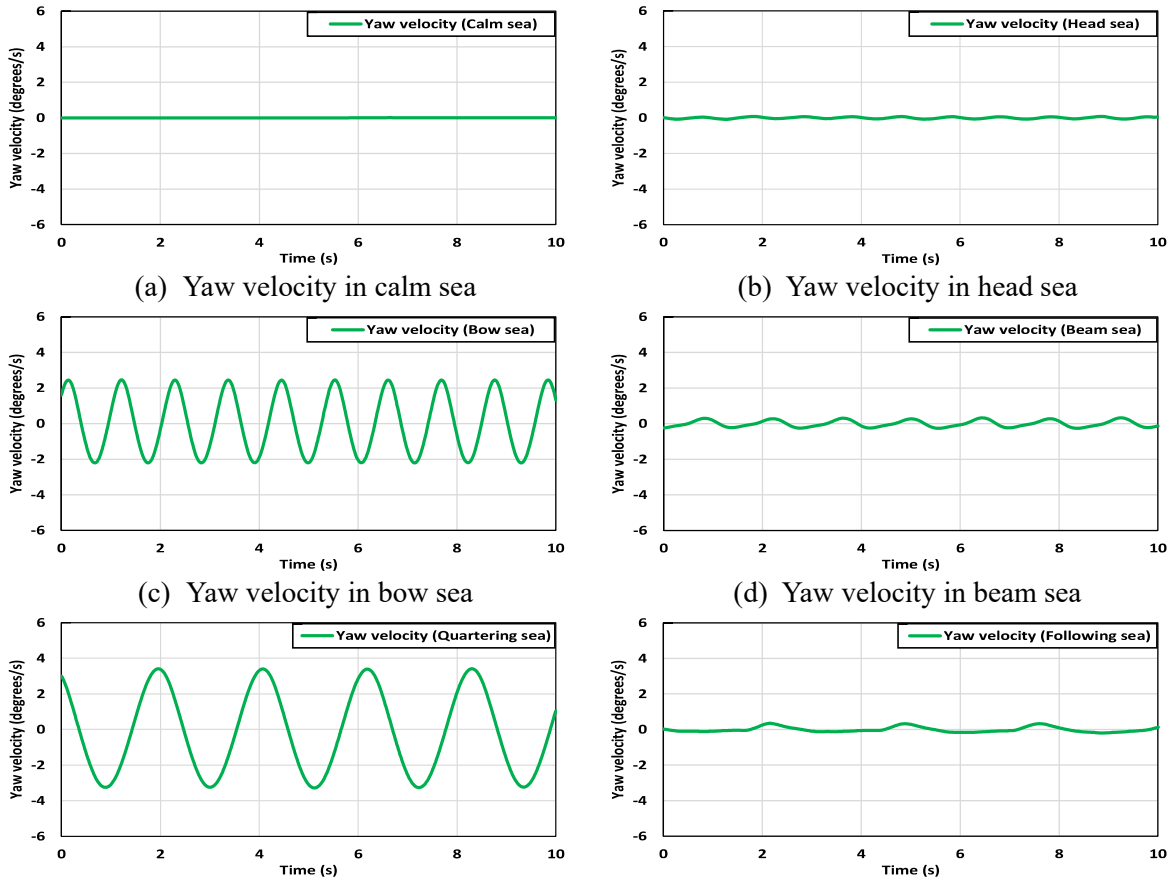

(a) Yaw velocity in calm sea

(b) Yaw velocity in head sea

(c) Yaw velocity in bow sea

(d) Yaw velocity in beam sea

(e) Yaw velocity in quartering sea

(f) Yaw velocity in following sea

Figure 5.12 Time histories of yaw velocity during the course-keeping manoeuvre in (a) calm sea, (b) head sea, (c) bow sea, (d) beam sea, (e) quartering sea, and (f) following sea.

Figure 5.13 illustrates the predicted ship path comparison under course keeping control for all the simulations. Most of the paths for the simulated cases in waves were clearly different from the trajectories obtained in the calm water condition. The trajectories can be affected by the complex interaction of hull-propeller-rudder under the incident waves. A very small deviation from the original course was noticed in both calm water and head seas, which can be believed to achieve good course-keeping control. The oscillating deviation of the trajectory from the original path was found in beam seas, which may be due to the strong lateral force induced by incident beam waves. It can be seen that the increasing deviations from the original course were observed in the bow, quartering and following seas, which indicates a relatively poor performance of course keeping control compared with other cases. The bow sea experienced the largest deviation from the original course, which is due to the strong lateral force and yaw moment caused by the oblique sea. For the same reason, the quartering wave also suffered a large deviation. The ship's course in the following sea was observed to be more biased towards the starboard side than the calm and head sea cases. This may be due to a larger pressure difference acting on the rudder surface as a result of the interaction between the wave and the propeller-induced flow, which makes the ship's heading more towards the starboard side. From

the predicted CFD results, it can be derived that the course keeping performance of a ship in a rough bow sea can be a very challenging task.

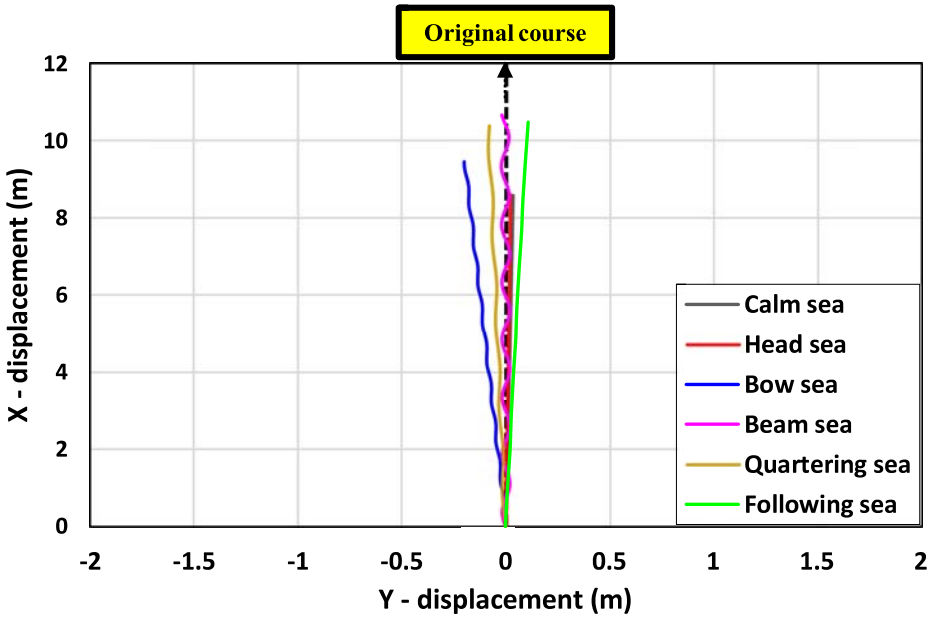

Figure 5.13 Comparison of the predicted trajectories in waves.

In navigation practice, there exists a certain delay from the time when the rudder angle is given by the controller to the moment the response of the steering engine is completed (Yan et al., 2020). However, the feedback controller applied to the present CFD model did not consider the steering delay, which may result in some discrepancy between the CFD results and the actual rudder response. For example, Wang et al. (2017) also conducted the course keeping manoeuvre in waves using the feedback controller without the consideration of the steering delay. The comparison between the predicted rudder response and the measurements showed some discrepancy in terms of the rudder deflection frequency. Given this, it should be noted that the steering delay is also an important factor for the course keeping control.

5.4.6. Turning circle manoeuvre

This sub-section outlines the free-running CFD computations of a standard turning manoeuvre in waves. For all manoeuvring simulations in waves, the ship is moving forward at a constant speed and the rudder is executed to a maximum rudder angle of 35° in the starboard direction at maximum rudder rate. The ship responds turning towards the starboard side. The manoeuvre is completed when the 360° turn is achieved.

Throughout all the simulations, the turning circle test with only the yaw angle variation up to 360° was carried out according to the general procedure (ITTC, 2021b). A 720° turn is also recommended in order to fully assess environmental effects, but this requires a huge computation time and hence high computational resources. Thus, in this study, a 720° turn was not investigated, assuming that the 360° turn provides sufficiently valuable information about the manoeuvring characteristics of a ship in waves.

5.4.6.1 Time histories during turning and turning indices

The obtained time histories of the ship velocities, forces, and moment during the turning circle manoeuvre in waves are illustrated in Figure 5.14, in which the representative wave-encounter directions are marked with black dashed-lines. Unlike other hydrodynamic problems such as ship resistance and seakeeping, the present manoeuvre simulations experience instantaneous variations of wave-encounter conditions during the ship's turning. Such instantaneous variations make the manoeuvring simulations in waves more complex and therefore leads to high computational costs. All values on the graphs are calculated for the model-scale ship geometry.

From Figure 5.14, it can be observed that the ship forward speeds in all cases gradually decreased after steering and almost converged to a similar value slightly below 0.5 m/s with some fluctuations around their mean value. This involuntary speed loss is correlated with a large drift angle, which causes an increase in ship resistance. The maximum speed loss in all wave cases occurred between approximately 20s – 25s after the rudder was deflected. After this, a slight increase in the forward speed was seen when the ship experienced beam, quartering, and following waves, whereas a slight decrease was observed in head and bow waves. Because of this, the time histories of the forward speed in waves became rather similar despite the large differences in the approach speeds at an early stage of the turning manoeuvre. The predicted speed loss between the initial approach speed and the steady mean value was 48% in the head sea, 51% in the bow sea, 56% in the beam sea, 54% in the quartering sea, and 55% in the following sea. It should be noted that the surge forces largely oscillated during the turning manoeuvre in waves, but the oscillations significantly decreased at the moment when the ship experienced the incident wave from the port or starboard beam. The surge velocities also followed the same trend.

When it comes to the sway velocities and forces, they showed rapid increases until about 10s after the rudder was deflected to the starboard and then gradually converged to similar values with some oscillations induced by the waves. The converged mean values of the sway velocities were reported to be approximately -0.18 m/s in the head sea, -0.19 m/s in the bow sea, -0.18 m/s in the beam sea, -0.17 m/s in the quartering sea, and -0.16 m/s in the following sea. The largest fluctuations in the sway velocities and forces were also observed at the moment when the ship encountered beam seas, whereas the smallest fluctuations were found under both the head and following sea conditions. As for the yaw velocities and moments, relatively large fluctuations clearly occurred when the ship encountered oblique waves. The yaw rates were maximum, occurring about 7s after the rudder deflection. Then, they converged quickly to the values which were estimated to be 6.60 º/s in the head sea, 7.82 º/s the in the bow sea, 7.84 º/s in the beam, 8.04 º/s in the quartering sea, and 7.35 º/s in the following sea.

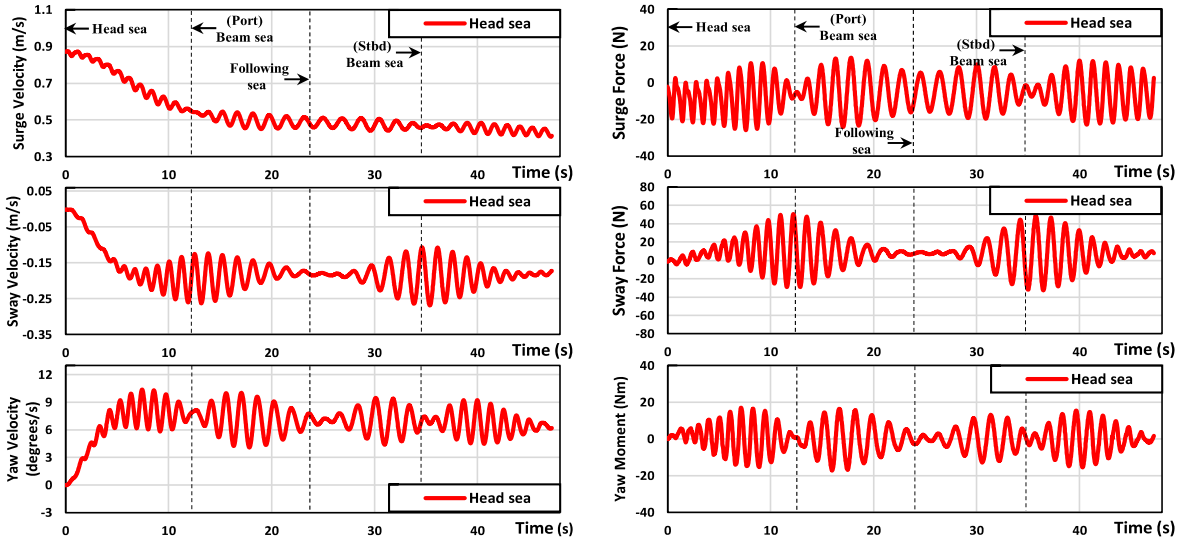

(a) Head wave (Case 2)

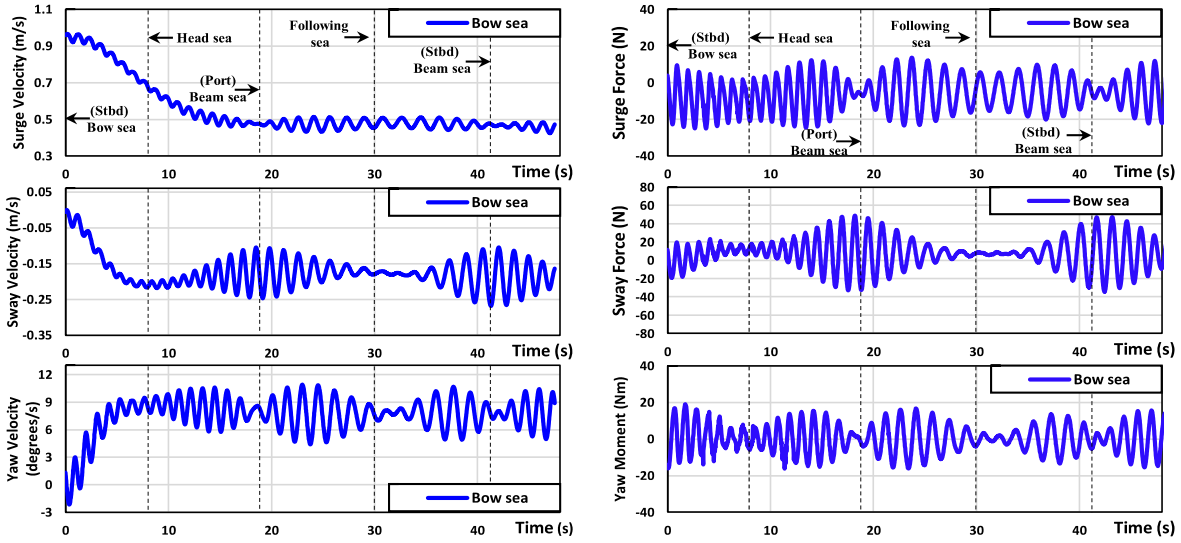

(b) Bow wave (Case 3)

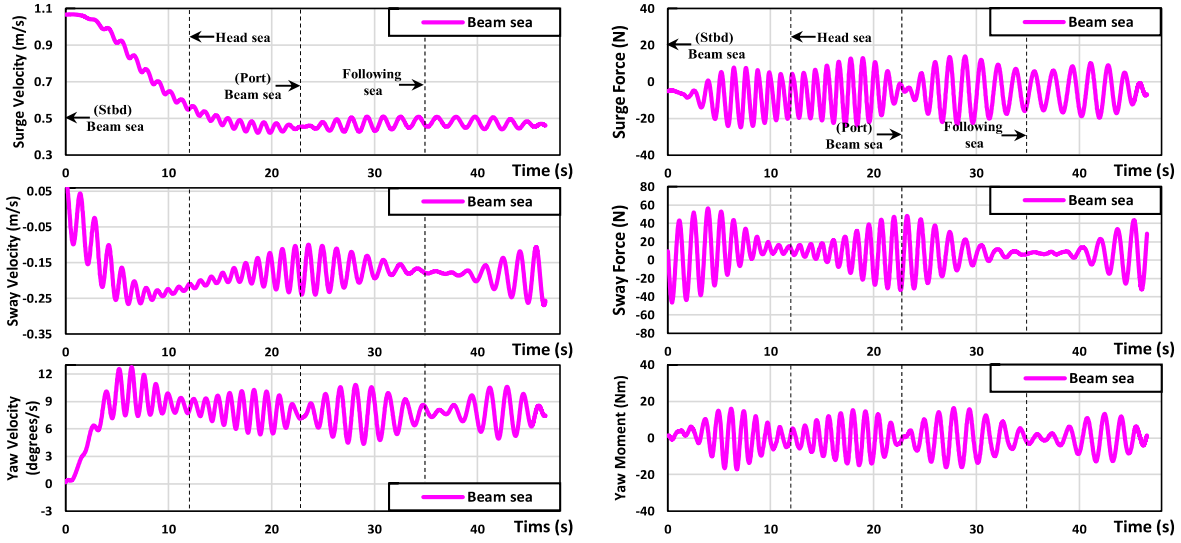

(c) Beam wave (Case 4)

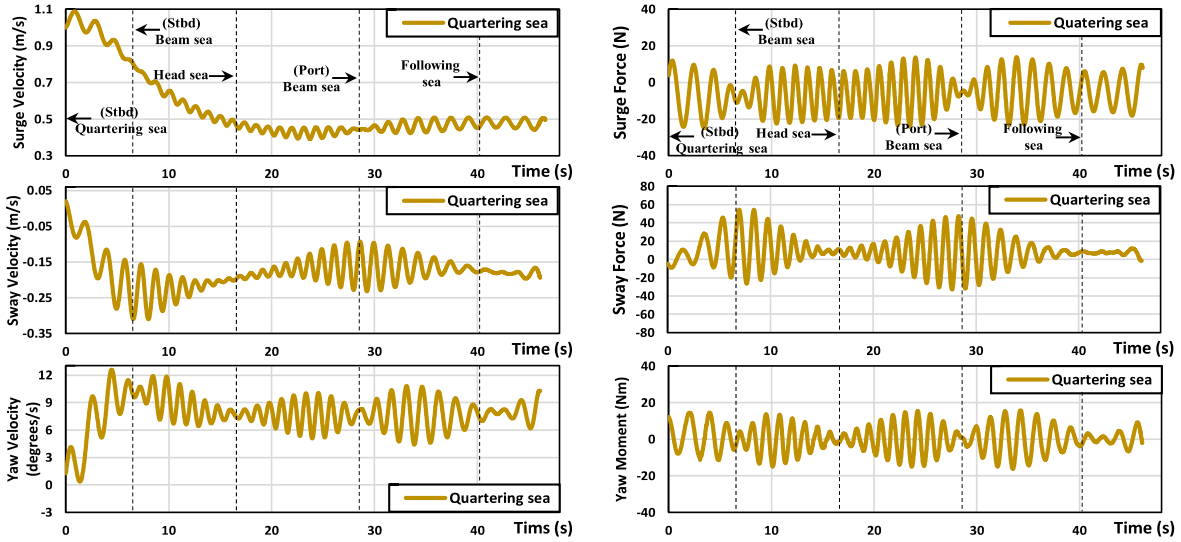

(d) Quartering wave (Case 5)

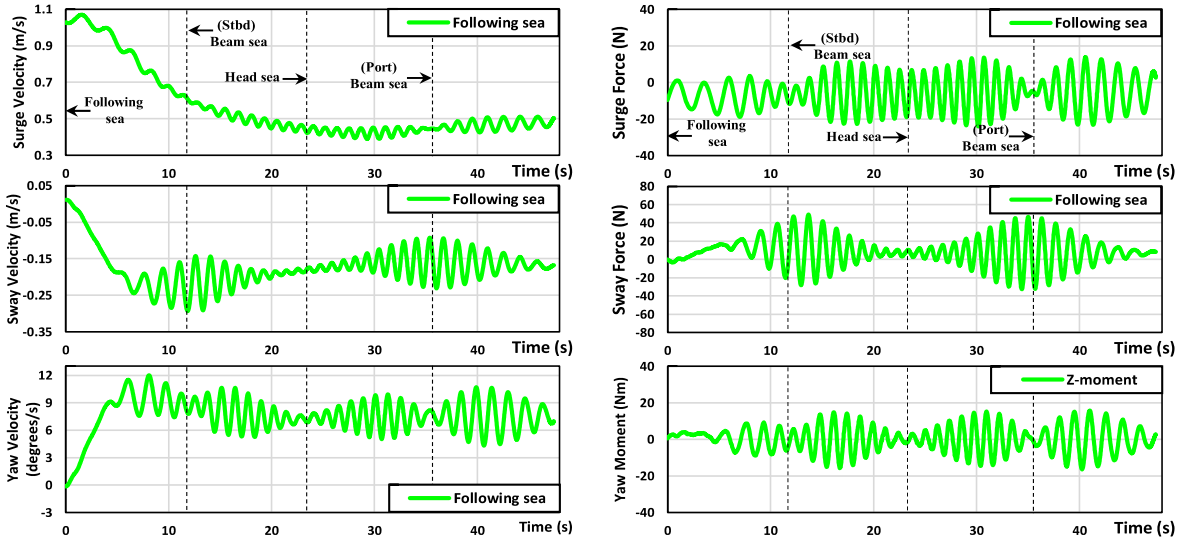

(e) Following wave (Case 6)

Figure 5.14 Time histories of the ship velocities, forces, and moment during a turning manoeuvre in waves.

The critical turning indices experienced by the ship for all cases are reported in Table 5.8. The turning parameters were closely associated with the ship's horizontal motions during the turning manoeuvre. Thus, the hydrodynamic forces and moment acting on the ship in the horizontal plane were identified as the most important factors from the manoeuvring point of view: the surge force (added resistance), sway force, and yaw moment (Skejic and Faltinsen, 2008). During the ship's turning, the resultant forces and moment were induced by complex interactions between the rudder, propeller, hull, and waves. In particular, the imposed incident wave conditions had a great influence on the hydrodynamic forces and moment. As a result, there was a high probability that the turning circle trajectory would be deformed when compared to that observed in calm water (Case 1). The ship advance would be closely correlated to the ship velocities in the horizontal plane (surge, sway, and yaw velocities). In general, the greater forward speed and the longer time for the yaw angle to change by 90º, the larger the ship advance can be. Although the 90º turn time was relatively long, the minimum

advance was observed in the head sea (Case 2) because the forward speed was the lowest at the beginning of the turning manoeuvre. The advance in the bow sea (Case 3) was far greater than that of the head sea case (Case 2) due to the relatively large forward speed and the long 90° turning time. It was noted that the beam (Case 4), quartering (Case 5), and following wave (Case 6) had caused a larger yaw moment than that in the head and bow wave as the ship started turning in waves. This accelerated the ship's yaw velocities, and 90° turns were achieved much earlier under the beam, quartering, and following seas. The ship advances were predicted larger than the head sea case due to the large forward speeds despite the short time to 90º turn in the beam, quartering, and following sea.

The ship transfer was also found to have a close correlation with surge, sway, and yaw velocities. The larger surge and sway velocity and the longer time to turn by 90º may lead to the greater transfer. The relatively small transfer was predicted in the head and bow wave cases due to the relatively small surge and sway velocities, despite the long time to turn by 90º. In the early stage of the turning, it can be seen that the lateral forces in the beam, quartering, and following waves appeared to be larger than those observed in the head and bow waves. Such a large sway force accelerated the ship's sway velocities, and relatively large sway velocities were achieved under the beam, quartering, and following waves. Although the time taken for the 90º turn was short, the ship transfers were observed greater than in the head and bow sea cases due to the large surge and sway velocities. The tactical diameters were also clearly found dependent on the direction of waves. It was revealed that the relatively large tactical diameters were observed in the beam, quartering, and following sea cases under which a large lateral force and yaw moment were observed at the early stage of the turning.

Table 5.8 CFD results: turning indices in regular waves.

Parameters (CFD results)	Head sea (Case 2)	Bow sea (Case 3)	Beam sea (Case 4)	Quartering sea (Case 5)	Following sea (Case 6)
Advance (m)	7.86 **$(2.57L_{BP})$**	8.85 **$(2.90L_{BP})$**	9.10 **$(2.98L_{BP})$**	8.44 **$(2.76L_{BP})$**	8.95 **$(2.81L_{BP})$**
Transfer (m)	3.09 **$(1.01L_{BP})$**	3.10 **$(1.01L_{BP})$**	3.43 **$(1.12L_{BP})$**	3.25 **$(1.06L_{BP})$**	3.56 **$(1.16L_{BP})$**
Time for yaw 90 degrees (s)	12.52	13.09	11.92	11.23	11.76
Tactical diameter (m)	7.97 **$(2.61L_{BP})$**	7.82 **$(2.56L_{BP})$**	8.17 **$(2.67L_{BP})$**	8.29 **$(2.68L_{BP})$**	8.86 **$(2.90L_{BP})$**
Time for yaw 180 degrees (s)	23.74	24.38	23.15	22.79	23.43

The turning ability of the ship is considered satisfactory if the ship advance does not exceed 4.5 ship lengths (L_{BP}) and the tactical diameter does not exceed 5.0 ship lengths in the turning circle manoeuvre, according to the standards for ship manoeuvrability (IMO, 2002). All the obtained results of the turning manoeuvre were evaluated by the IMO criteria in Figure 5.15. From this comparison, it is seen that the turning ability of the KCS in waves can be regarded as satisfactory.

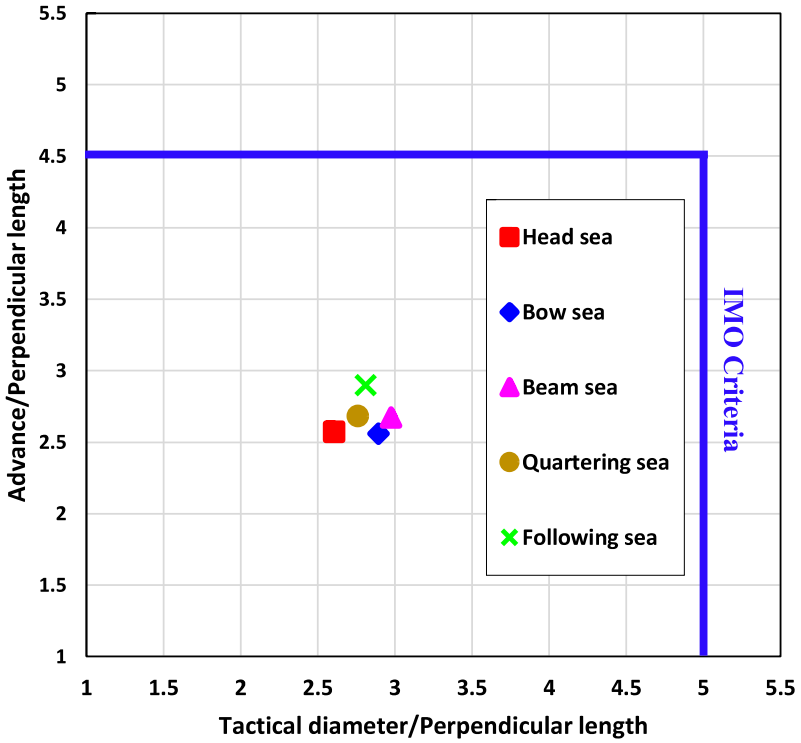

Figure 5.15 Comparison of the predicted turning indices in waves with IMO turning criteria.

All the calculated turning trajectories of the KCS in waves are depicted in Figure 5.16. It should be noted that all the rudder execution points were shifted to the specific location (0,0) in order to provide the correct comparisons of the turning trajectories. It is evident that some oscillations were estimated when the ship experienced starboard or port beam waves, which may cause large fluctuations of the sway velocities and forces.

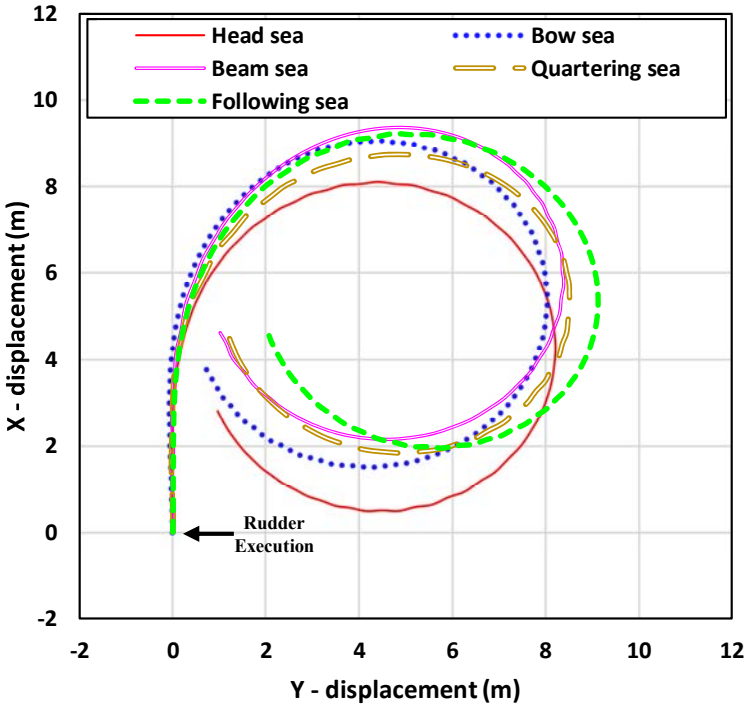

Figure 5.16 Comparison of the predicted turning circle trajectories in waves.

5.4.6.2 Wave-induced motions during turning manoeuvre

Figure 5.17 shows the time evolutions of ship motions, i.e., heave and pitch, as well as pitch moment and heave force during the turning manoeuvre. In the figure, it can be clearly seen that the ship motions, force, and moment experienced considerable oscillations due to the high-frequency wave-induced motions. In addition, such frequencies continued to change during the turning manoeuvre due to instantaneous variations in the ship's velocity and wave-encounter direction. For example, a ship advancing in the head wave (Case 2) encountered the head wave (0° turn), the port beam wave (90° turn), following wave (180° turn), starboard beam wave (270° turn), and head wave (360° turn) in series after starting the starboard turning manoeuvre. The ship's turning has contributed to continual changes in the wave-encounter frequency, consequently the ship motion frequency in waves.

It can be seen from Figure 5.17 that the wave-induced pitch motions showed significant variations in the amplitudes and frequencies of the motion during the turning circle manoeuvre according to the wave-encounter conditions. The maximum pitch motions were noted to be approximately 2º when the ship experienced the head or bow wave during the ship turning. On the other hand, the minimum pitch motions were almost 0º in the presence of the beam seas. The pitch moment also followed the same trend. In the same manner, the heave motion also experienced the instantaneous variations of the amplitudes and frequencies of the vertical motion during the ship turning. The maximum heave displacement for all wave cases was predicted to be 0.03 m when encountering the port beam wave; on the other hand, the heave motion almost disappeared when the ship encountered the following waves. The seakeeping results presented in Figure 5.17 indicate that the ship motions showed qualitatively and

quantitatively the same trend although phase differences were observed.

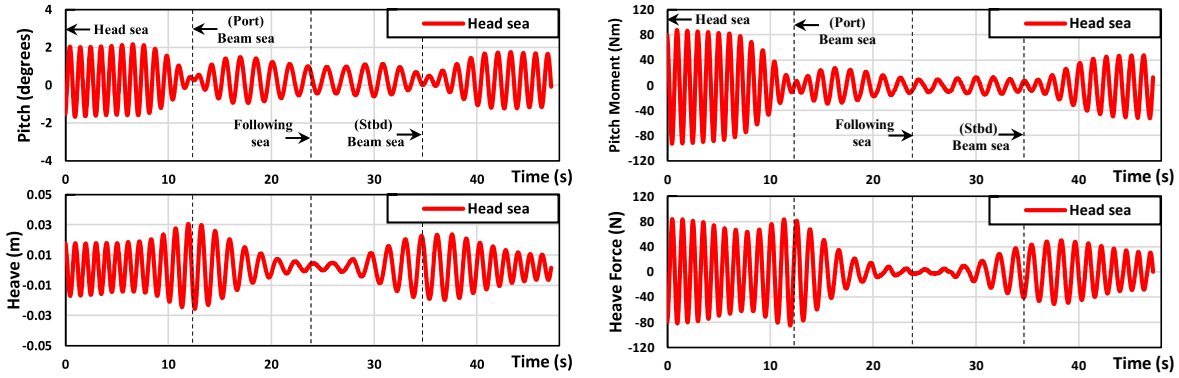

(a) Head wave (Case 2)

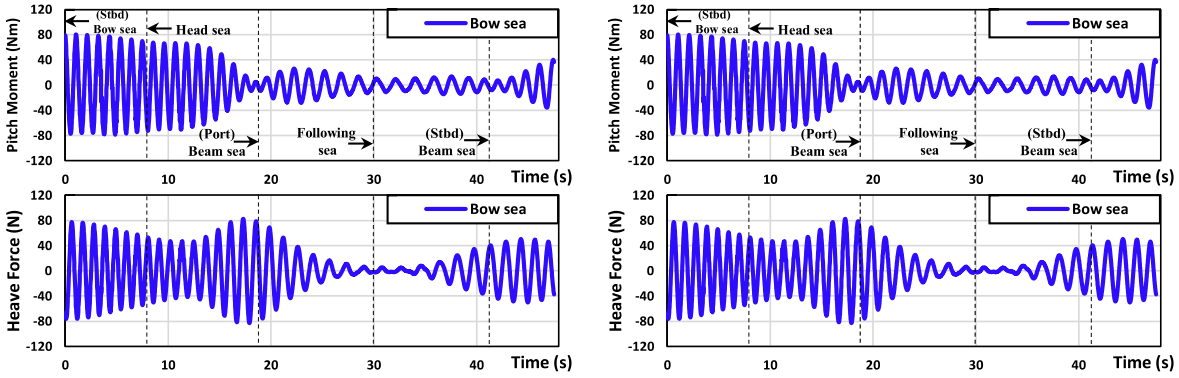

(b) Bow wave (Case 3)

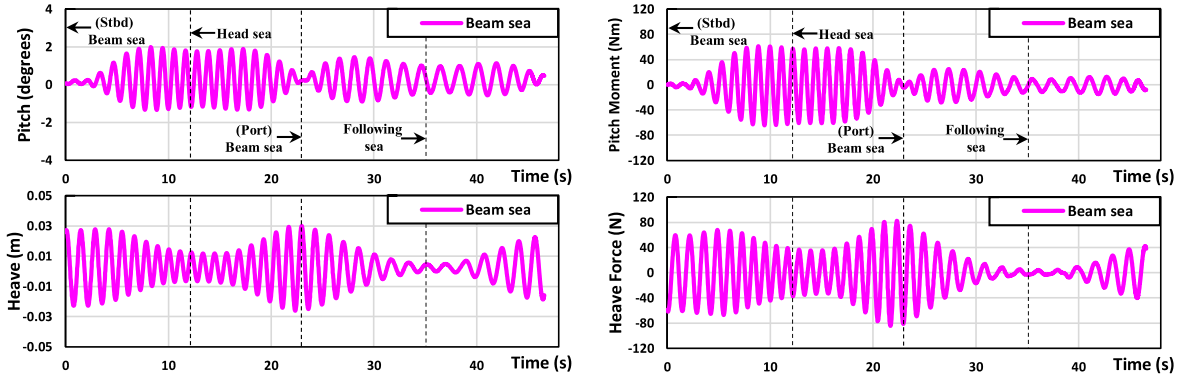

(c) Beam wave (Case 4)

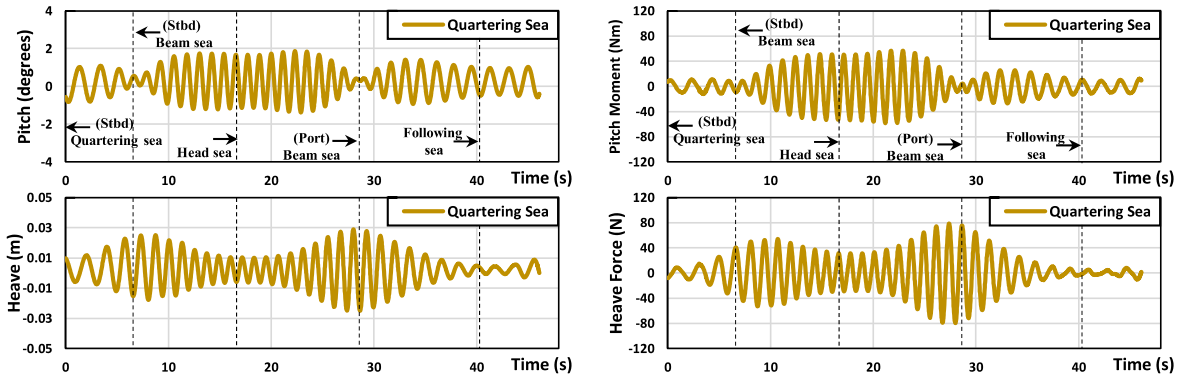

(d) Quartering wave (Case 5)

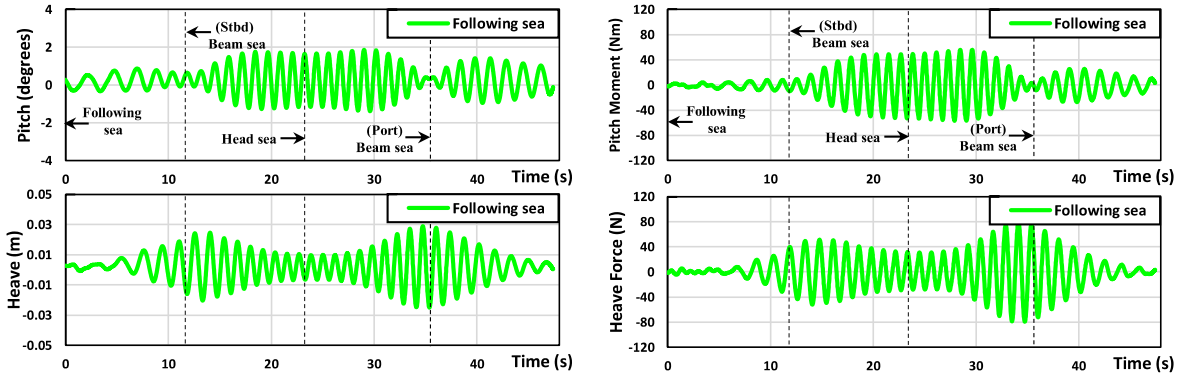

(e) Following wave (Case 6)

Figure 5.17 Time histories of pitch, heave, pitch moment, and heave force during a turning manoeuvre in waves.

5.5. Concluding Remarks

In this chapter, free-running CFD simulations to predict the manoeuvring performance of the KCS model in waves of different propagation directions were carried out by means of a fully nonlinear URANS model. This enables the objectives set in this chapter to be achieved by identifying the effects of wave directions on the manoeuvrability of the ship. The main results drawn from this chapter can be listed as follows:

1) A verification study was carried out to quantify the numerical uncertainties of the present CFD models. Spatial and temporal convergence analyses were examined. It was shown in detail that the ship advance and transfer values, as well as the tactical diameter, showed uncertainty levels of less than 0.2% for the ship manoeuvring simulation in the head wave case when calculated using the Grid Convergence Index (GCI) method.

2) For the validation of the present CFD model, the free-running simulations in calm water and head waves were modelled using the numerical approach presented in Chapter 4, Section 4.3. It was revealed that the current CFD model predicted the turning indices, i.e., advance, transfer, tactical diameter as well as time to 90°/180° yaw angle change, within a range of −7.78% to 3.28% of the experimental data. For the time histories of the ship speeds, seakeeping motions, and propeller characteristics, the simulation results showed good agreement with the experiments. It was demonstrated that the present CFD approach can be a reliable tool to assess a ship's manoeuvre in waves.

3) For the ship self-propulsion predictions, the approach speed under the same propeller revolution was calculated for each individual wave condition. From the CFD calculations, it was observed that the minimum approach speed was found to be 0.86 m/s in the head sea condition, whereas the maximum approach speed was noted to be 1.067 m/s in the beam sea condition. This is due to the fact that the ship resistance significantly varies according to the incident wave directions. As for the seakeeping motions at self-propulsion condition, the head and bow seas considerably increased the

pitch motion, which was almost negligible in the beam sea. However, the beam wave caused the largest oscillation amplitude of the heave motion.

4) For the course keeping manoeuvres in waves, five different directions were considered to evaluate the effects of wave directions on the course-keeping ability of the ship. For the head seas, the rudder control was found not critical to keep the ship straight. The maximum rudder angle was determined to be 0.8°, guaranteeing a good course-keeping ability. However, a relatively large deflection of the rudder angle was observed in oblique waves when the ship would keep moving forward. The rudder deflection was estimated up to approximately 7° in the bow seas and 12° in quartering seas. This poor performance of course keeping control caused a large deviation from the original course. It is concluded that the wave propagation directions can significantly affect the course-keeping ability of a ship, which consequently leads to deviations from the original course.

5) For the standard turning circle manoeuvres in waves, the predicted turning manoeuvring indices and trajectories in different waves were compared, from which it is concluded that the wave propagation directions have a considerable influence on the manoeuvring behaviour of a ship. The ship motions as well as the hydrodynamic forces and moments acting on a ship experienced considerable fluctuations during the turning manoeuvre due to the high-frequency wave-induced motions. The low-frequency responses caused by the ship manoeuvring motion were also observed.

6. FREE-RUNNING CFD SIMULATIONS FOR DIFFERENT REGULAR WAVE LENGTHS

6.1. Introduction

It is critical to estimate the manoeuvring behaviours of ships in waves since it is closely associated with navigation safety at sea. The influence of waves has been known so significant on the manoeuvrability of a ship as causing the high-frequency wave-induced motions (Wang and Wan, 2018). From the hydrodynamics perspective, such an iterative pattern on ship motions may highly lead to substantial changes in a ship's manoeuvring performance. Meanwhile, the wave frequency in deep water only depends on the wavelength based on the linear wave theory. That implies that wavelength is the key parameter to determine a ship's manoeuvrability. It has been noted in real operations that a ship can encounter various wave conditions. According to a study by Toffoli and Bitner-Gregersen (2017), wavelengths were estimated to range from about 1.5m up to approximately 900m in a fully developed wind sea. In this regard, it seems necessary to investigate a ship's manoeuvrability under various wavelength conditions, which can provide a proper understanding of the relationship between wavelengths and ship manoeuvring performances in a real seaway.

In fact, several researchers have begun to investigate a ship's manoeuvrability in waves due to an increasing demand in understanding the ship's manoeuvre against various wave effects (IMO, 2014; ITTC, 2017b; IMO, 2021; ITTC, 2021c). Nevertheless, due to its brevity, a few remarkable studies managed to discuss the impact of wavelengths on the manoeuvring performance of particular ships. To give some examples, Kim et al. (2019) conducted free-running experiments to examine manoeuvring behaviours of the KRISO Very Large Crude-oil Carrier 2 (KVLCC2) in accordance with various wavelengths. Sanada et al. (2019) examined the manoeuvring performance of the Office of Naval Research Tumblehome (ONRT) surface combatant at different wavelengths. These studies jointly show that the effects of wavelengths on a ship's manoeuvrability largely differ depending on the ship types. For the KVLCC2 in waves, the manoeuvring characteristics (turning trajectories and critical manoeuvring quantities) were found to vary significantly with the wavelength. On the other hand, the variation of such manoeuvring characteristics of the ONRT with respect to wavelengths was revealed much smaller than the KVLCC2. Although being informative for confirming the relation between wavelengths and ship manoeuvring behaviours, the past research studies were not able to offer detailed insight into the understanding on manoeuvring performances of various commercial vessels against different wavelengths. It is because the scope of the past research was limited with some specific benchmarking models, i.e., ONR Tumblehome and KVLCC2. Thus, in order to draw more meaningful information for general application, it is highly believed that the manoeuvrability of other ship types under different wavelength conditions should also be further investigated.

In this context, this study was motivated to extend the knowledge of wave effects on the manoeuvrability of the KRISO Container Ship (KCS) model; which is the benchmark ship hull of a container ship but not investigated thoroughly in the past research. This chapter aims to predict the wavelength effects on the ship manoeuvring behaviours using a Computational

Fluid Dynamics (CFD) based technique which enables resolving the complex interactions between hull, rudder, and propeller in waves.

This chapter is organised as follows: Section 6.2 gives a list of the simulation cases to which the current CFD model is applied. Afterwards, in Section 6.3, the specific numerical setup of the CFD model is described. Next, the CFD results obtained from the free-running simulations in waves are provided in Section 6.4. Finally, concluding observations are given in Section 6.5.

6.2. Goal and Scope

This chapter deals with the effects of wavelengths on a ship's manoeuvring performance in waves. Although ship handling characteristics can be broken into several parts, this study mainly focuses on the course keeping ability and turning capability in different wavelengths.

Table 6.1 and Figure 6.1 jointly illustrate six different conditions adopted in this study for the free-running simulation. The calm water case was carried out to investigate the manoeuvring characteristic of the KCS without any external disturbances. For the wave conditions, the effects of the incident regular waves with wavelength to ship length ratios λ/L_{BP} = 0.7, 1.0, 1.3, 1.6, and 2.0 were examined during ship manoeuvres (the wave height H=0.048m and wave encounter angle $\mu = 225^{o}$ are constant for all the cases). As evidenced in the previous chapter, oblique waves were identified as critical conditions significantly affecting the course-keeping control of a ship. The bow waves ($\mu = 225^{o}$) were therefore chosen in this work to examine the selected cases. The encounter frequency of the wave, ω_e, is calculated as $\omega_e = \omega[1 - (\omega U \cos\mu)/g]$, where ω is the wave frequency, U is the ship forward speed, μ is the ship's heading angle relative to the wave direction, and g denotes the gravitational acceleration. It has to be mentioned that the CFD analyses were carried out using deep water conditions.

Table 6.1 The simulation cases to which the CFD model is applied.

Case no. C	Approach speed U_0 (m/s)	Propeller rev. (RPS)	Wave height H (m)	Encounter Angle μ (degrees)	Encounter Freq. ω_e (rad/s)	Encounter Period T_e (s)	Wave/ship length λ/L_{BP}
1	1.094	13.38	Calm water	- (Calm sea)	-		-
2	0.904	13.38	0.048	225 (Bow sea)	7.267	0.865	0.70
3	0.945	13.38	0.048	225 (Bow sea)	5.863	1.071	1.00
4	1.024	13.38	0.048	225 (Bow sea)	5.088	1.235	1.30
5	1.050	13.38	0.048	225 (Bow sea)	4.506	1.394	1.60
6	1.054	13.38	0.048	225 (Bow sea)	3.943	1.594	2.00

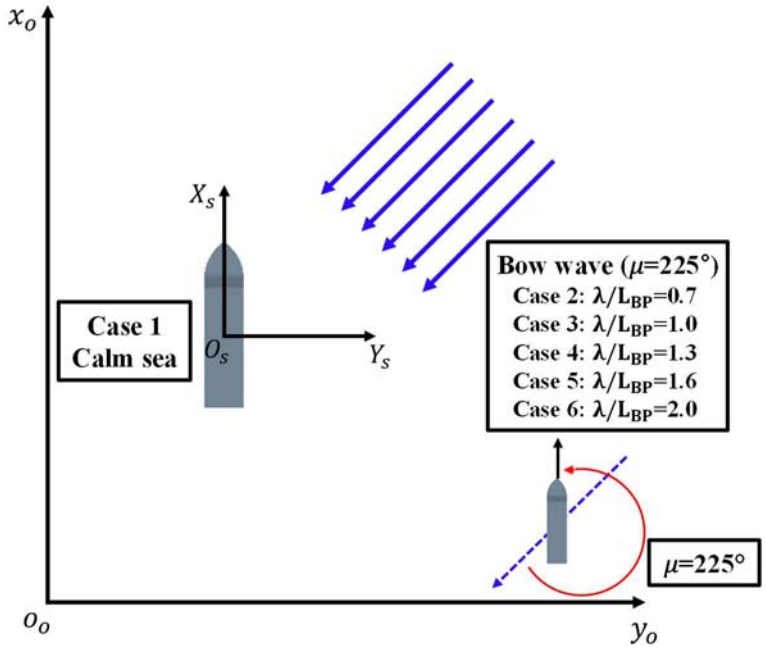

Figure 6.1 A schematic view of the simulation cases applied to this study.

6.3. Numerical Modelling

The numerical setup for the current CFD simulations was based on that presented in Chapter 4, Section 4.3.

The obtained mesh for the CFD manoeuvring simulations of the KCS in this chapter is presented in Figure 6.2. The total grid number for each manoeuvring simulation is shown in Table 6.2. It should be noted that the total cell numbers differ due to variation in the wavelength conditions, in which at least 80 cells per wavelength were created, as explained in Chapter 4, Section 4.3.5.

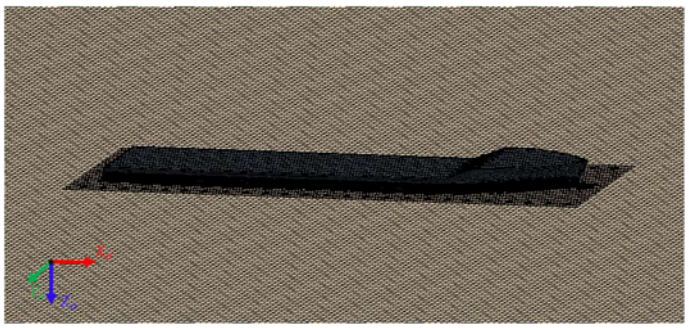

a) Mesh for the ship and free surface

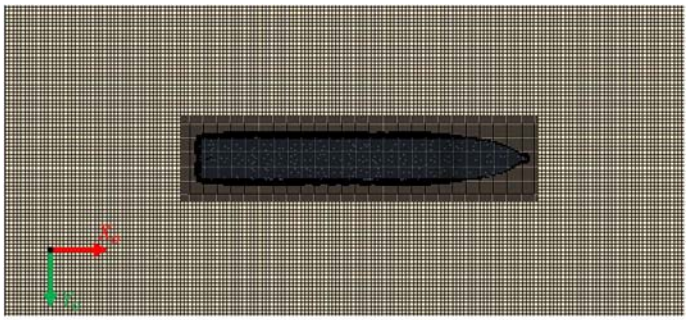

b) Top view cross-section of the domain

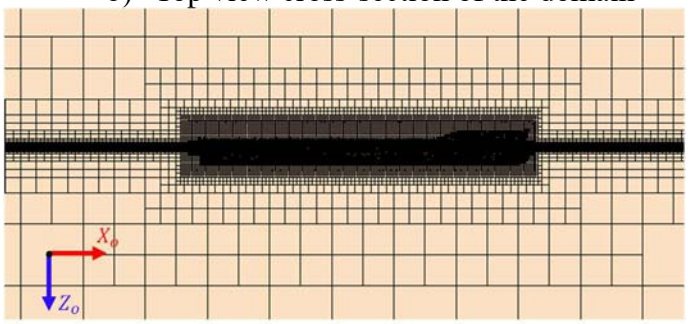

c) Profile view cross-section of the domain

Figure 6.2 Mesh structure of the computational domain.

Table 6.2 The total cell numbers for manoeuvring simulations.

Case no.	Total cell number
1 (Calm water)	5,391,040
2 (Bow wave, $\lambda/L_{BP} = 0.7$)	11,411,380
3 (Bow wave, $\lambda/L_{BP} = 1.0$)	7,189,514
4 (Bow wave, $\lambda/L_{BP} = 1.3$)	6,372,141
5 (Bow wave, $\lambda/L_{BP} = 1.6$)	5,348,493
6 (Bow wave, $\lambda/L_{BP} = 2.0$)	4,776,950

The time step was chosen based on the recommendation of ITTC (2011) throughout all the simulations, as performed in the previous chapter. According to the recommendation, at least 100 time steps per encounter period should be used for the wave simulation. Given this, the time step size was chosen to be 0.005s, which satisfies this condition for all the wave cases.

6.4. Results

6.4.1. Self-propulsion

The time histories of the predicted approach speed, ship resistance, pitch motion, and heave motion at self-propulsion for all the cases are shown in Figure 6.3. The unsteady time histories of the CFD results were analysed by Fourier Series (FS). The average value of the time history of the obtained results was quantified by the 0th harmonic FS term, while the mean amplitude of the oscillation of the values was expressed by the 1st harmonic FS term. It is worth noting that the zeroth and first FS term have been regarded as the fundamental components in the linear system. In this study, the 0th and 1st order terms for the force and motions were calculated, as given in Table 6.3.

It should be borne in mind that regular waves with height of H = 0.048 m and wave encounter angle μ=225º were applied throughout all the wave simulations, only changing the wavelength. As stated previously, the wavelength to ship length ratio (λ/L_{BP}) ranged from 0.7 to 2.0. Figure 6.3 (a) shows a significant change in the approach speed of the KCS when the ship was advancing forward in waves of different wavelengths. The mean approach speed in the calm water was reported to be 1.094 m/s corresponding to 18.45 knots in full scale (Froude number= 0.20). The reduction of the mean forward speed was observed to be 17.4% for the λ/L_{BP}=0.7, 13.6% for the λ/L_{BP}=1.0, 6.4% for the λ/L_{BP}=1.3, 4.0% for the λ/L_{BP}=1.6, and 3.7% for the λ/L_{BP}=2.0 when compared to the calm water case. This is because the ship resistance increases with the reduction of the wavelength at a given wavelength range ($0.7 < \lambda/L_{BP} < 2.0$). It should be noted that the approach speed and ship resistance oscillated considerably in long waves ($\lambda/L_{BP} > 1.0$), but the oscillations significantly decreased when the ship advanced in short waves ($\lambda/L_{BP} = 0.7$).

Figure 6.3 (c) and (d) present the comparisons of the ship motion time histories in different wavelength conditions. From this figure, it was observed that the frequency of ship motions in waves was closely related to the wave encountering frequency. Short-term oscillations of the ship motions with regular periodicity were noticed in the shorter waves, whereas relatively long-term oscillations were found in longer waves in a given period. The amplitude of ship motions was also found to vary depending on the wavelength. The wave steepness (H/λ) was identified as the important factor involved in the amplitude of the pitch motion. It should be reminded that the wave height was kept constant for all the wave simulations, which indicates the wave steepness decreased with the increase in the wavelength. The increase of wavelengths (=the decrease of wave steepness) generally led to a decrease in the pitch moment, causing the pitch amplitude to decrease. In other words, the greater the steepness of the wave, the larger the amplitude of the pitch can be. Exceptionally, the largest pitch motion was noticed at the bow waves of λ/L_{BP} =1.0 with a mean amplitude of 1.87º. Carrica et al. (2011) state that the maximum pitch response occurs when the encounter frequency (f_e) is equal to the natural pitch frequency (f_n). In this study, the encounter frequency at the bow waves of λ/L_{BP} =1.0 was calculated at 0.93hz, which is very close to the natural frequency of the KCS pitching system as seen in the previous chapter. Regarding the heave motion, the largest oscillation amplitude was found in the bow waves of λ/LBP =2.0 with a mean value of 0.002m. The amplitude of the heave motion was found to increase as the wavelength increased, which was the opposite trend compared to the pitch motion. It is worth mentioning that the amplitude of the vertical motion gets closer to the wave amplitude when the wavelength along the ship length becomes longer (Liu et al., 2020).

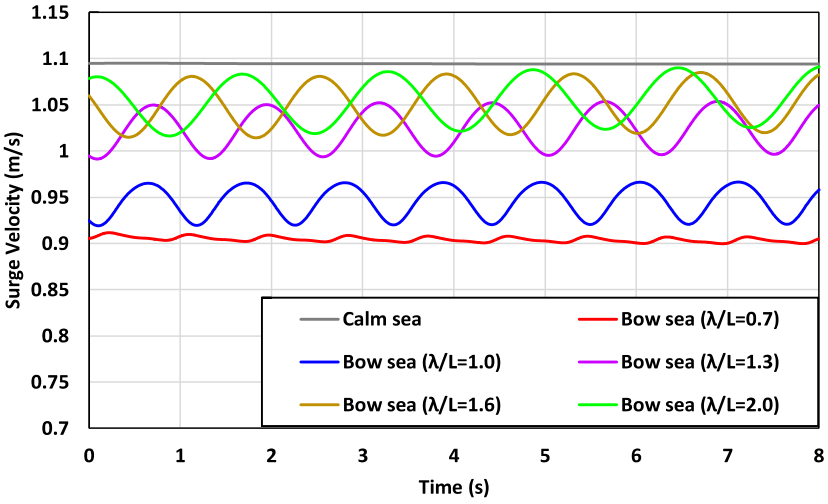

(a) Approach speed (U_0)

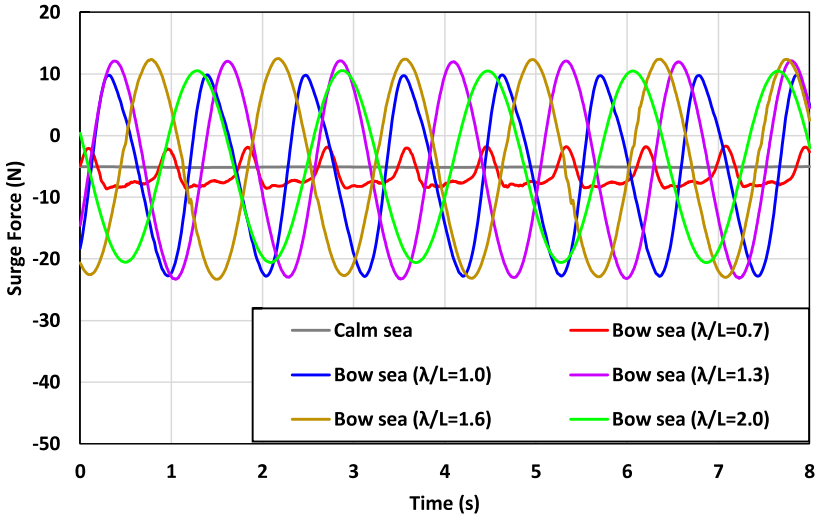

(b) Ship resistance (F_x)

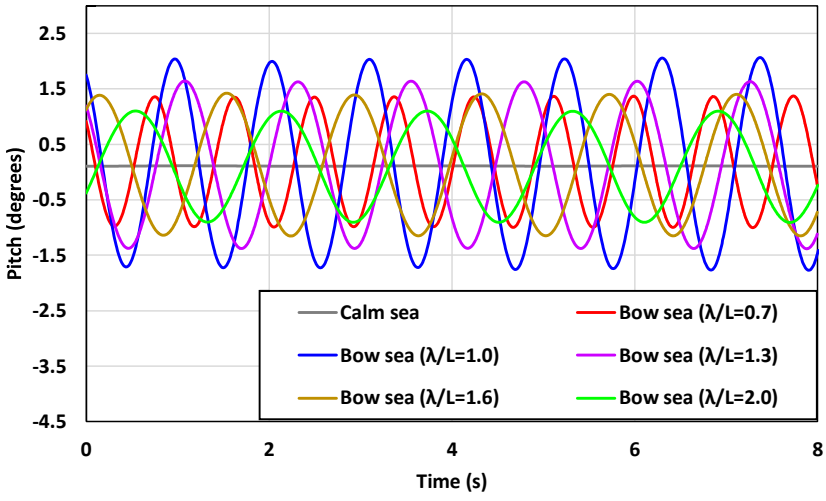

(c) Pitch displacement

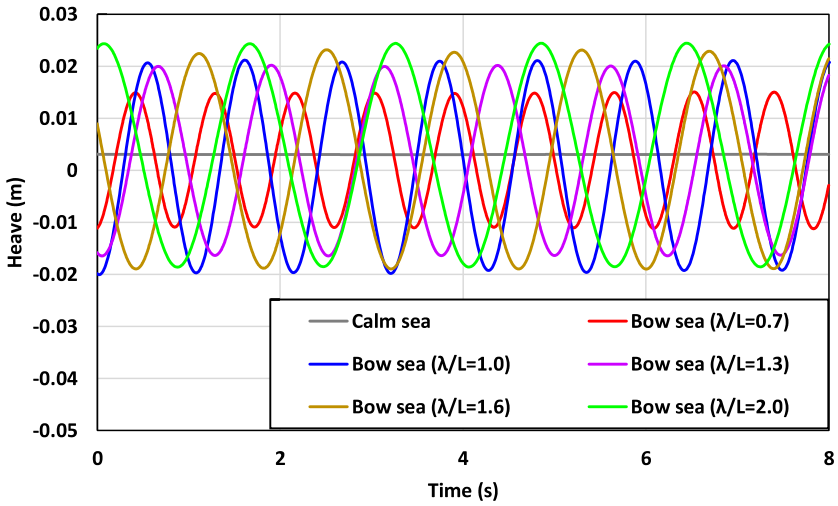

(d) Heave displacement

Figure 6.3 Time histories of the approach speed, ship resistance, pitch motion and heave motion for all cases.

Table 6.3 Fourier series analysis of the approach speed, ship resistance, pitch motion and heave motion at self-propulsion.

Case no.	Approach speed U_0 (m/s)	Resistance F_x (N)		Pitch displacement (degree)		Heave displacement (m)	
C	0th FS term	0th FS term	1st FS term	0th FS term	1st FS term	0th FS term	1st FS term
1 (Calm sea)	1.094	5.136	-	0.111	-	0.003	-
2 (Bow sea, $\lambda/L_{BP} = 0.7$)	0.904	6.470	2.082	0.175	1.139	0.002	0.013
3 (Bow sea, $\lambda/L_{BP} = 1.0$)	0.945	6.723	15.548	0.170	1.876	0.002	0.019
4 (Bow sea, $\lambda/L_{BP} = 1.3$)	1.024	4.930	17.029	0.094	1.499	0.001	0.018
5 (Bow sea, $\lambda/L_{BP} = 1.6$)	1.050	5.168	17.869	0.130	1.311	0.001	0.020
6 (Bow sea, $\lambda/L_{BP} = 2.0$)	1.054	5.102	15.477	0.118	0.999	0.003	0.022

The global wave pattern around the KCS under course keeping control is depicted in Figure 6.4 in which the Kelvin waves generated by the advancing ship are clearly visible. It was revealed from the figure that the free surface elevation pattern changed for changing wavelengths.

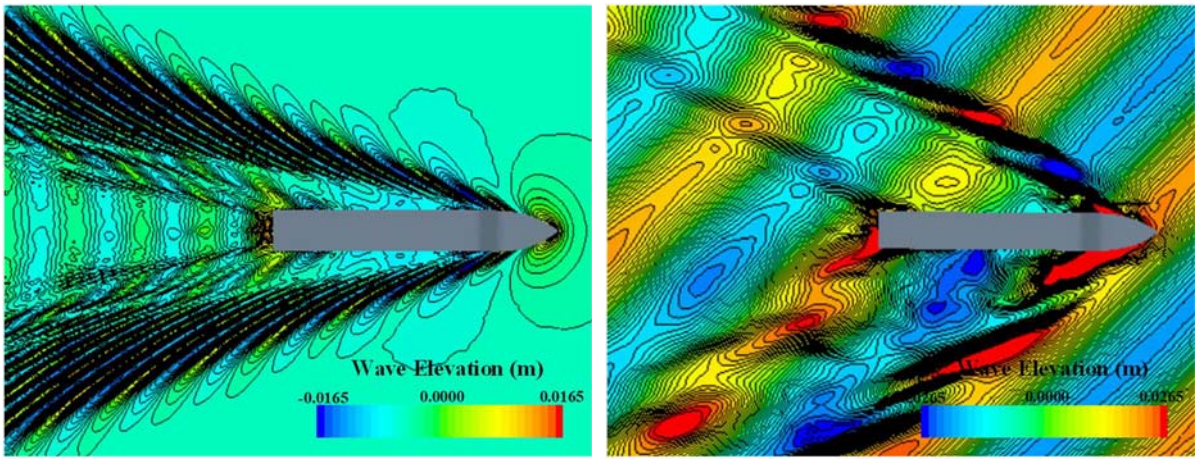

(a) Calm water (b) Bow wave ($\lambda/L_{BP} = 0.7$)

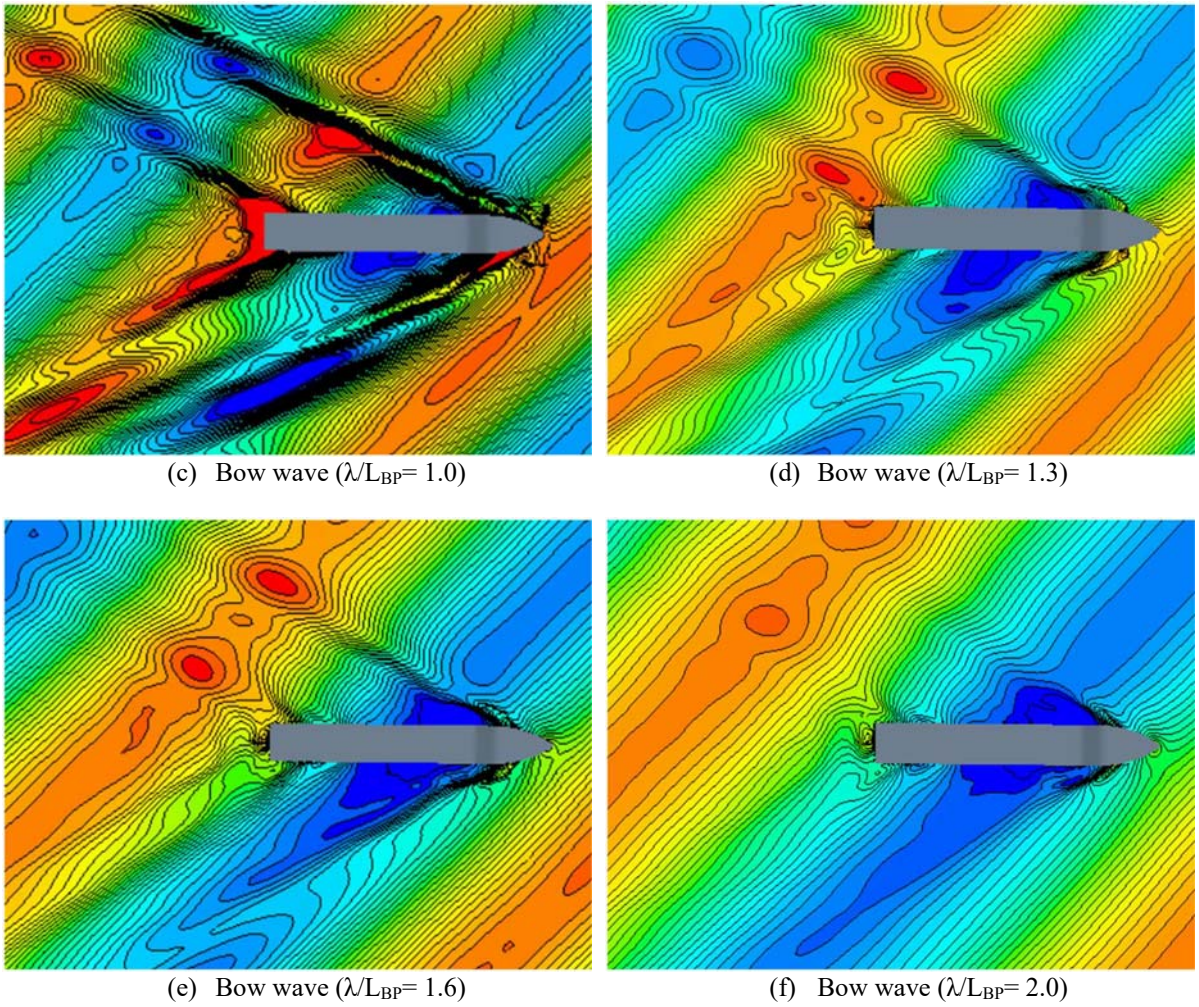

(c) Bow wave (λ/L_{BP}= 1.0) (d) Bow wave (λ/L_{BP}= 1.3)

(e) Bow wave (λ/L_{BP}= 1.6) (f) Bow wave (λ/L_{BP}= 2.0)

Figure 6.4 Free surface elevation at self-propulsion for all cases.

6.4.2. Course keeping control

Figure 6.5 andFigure **6.6** present the time histories of the rudder deflection angle, yaw angle, and yaw rate for each case when the ship was advancing forward based on the course-keeping control module. The signs of these values were determined in accordance with the coordinate systems established for modelling. As shown in Figure 6.5 (a), the rudder deflection was found to be very small under course keeping control in calm water since there are no environmental loads. The ship's heading angle was kept to be almost 0º with a maximum rudder deflection of 2.0º. The yaw velocity was also maintained to be almost 0 º/s as seen in Figure 6.6 (a). The small port rudder deflection may be closely related to a right-handed propeller effect which induces asymmetric pressure distribution acting on the rudder blade. Such an uneven pressure distribution generated a small yaw moment to move the bow to starboard. Thus, the rudder was deflected to the port side to control the ship's heading angle. It should be noted that when the ship was moving forward at a constant speed, the symmetric wave profile around the hull was clearly observed, as seen in Figure 6.4 (a). This would result in the even pressure distribution on both sides of the hull, which does not generate lateral force and yaw moments and consequently does not induce yaw deviation.

The amplitude of the rudder deflection became comparatively large in the bow waves, compared to the calm water condition. Similar maximum rudder deflections were estimated in all bow waves within a value of 7º as seen in Figure 6.5 (b) – (f). As can be seen in these figures, rudder control is critical to maintain a desired heading of the ship in bow seas, regardless of the wavelength. The maximum yaw angle deviations were also observed to be about 1º, while the maximum yaw rates were predicted to be about 2 º/s for all wave cases as seen in Figure 6.6 (b) - (f). However, the steering frequency was found to differ depending on the wavelength, despite the same autopilot gains. The shorter wavelength was applied, the more frequent rudder deflection was observed. It has to be stated that the high steering frequency has been considered not to satisfy the requirements of navigation practice, as discussed in Yan et al. (2020). The authors stated that in real navigation practice, there exists a certain delay from the time when the rudder angle is given by the controller to the moment that the response of the steering engine is completed. Thus, it can be expected that the ship's heading control is more challenging in short waves in real operation. As presented in Figure 6.4 (b) – (f), asymmetric wave profiles were clearly noticed in bow seas as opposed to calm sea, which may lead to a substantial lateral force and yaw moment with consequent changes in the ship's heading angle.

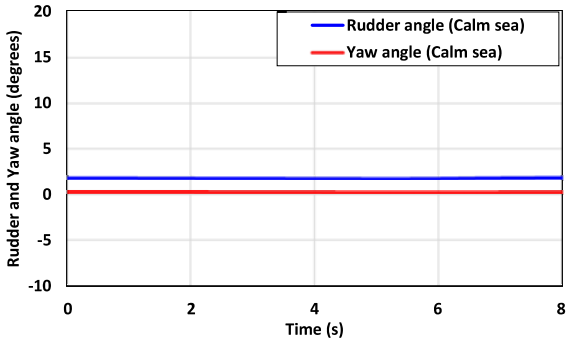

(a) Calm water

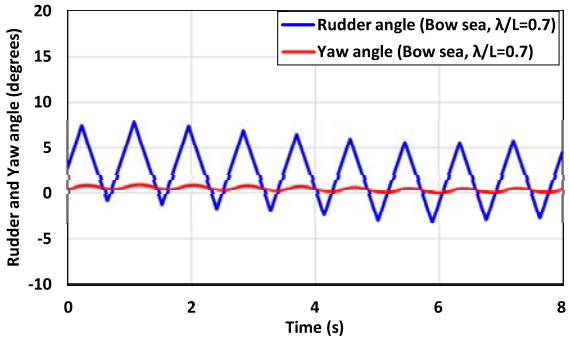

(b) Bow wave (λ/L_{BP} = 0.7)

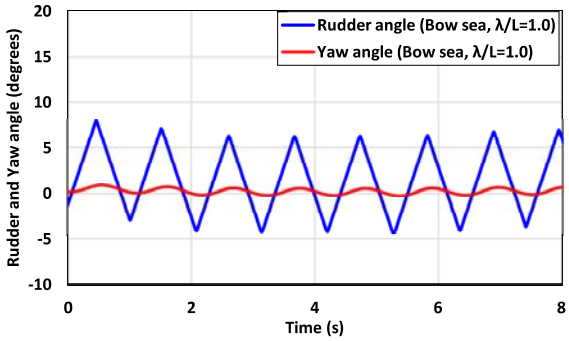

(c) Bow wave (λ/L_{BP}= 1.0)

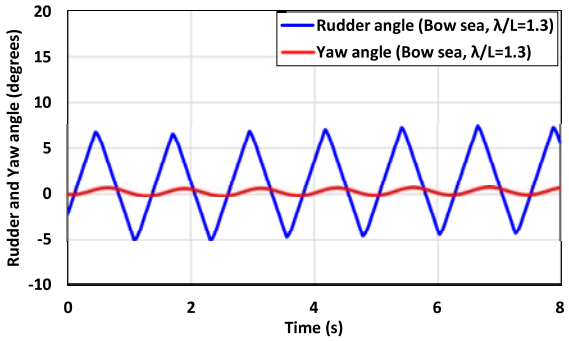

(d) Bow wave (λ/L_{BP}= 1.3)

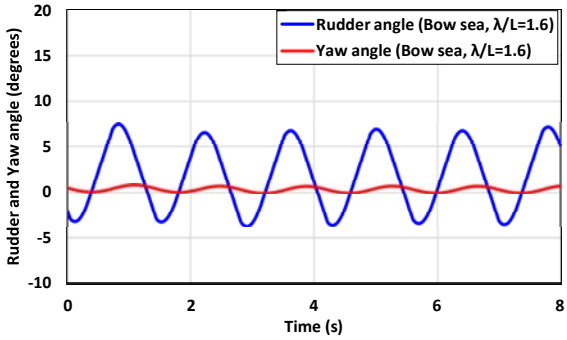

(e) Bow wave (λ/L_{BP}= 1.6)

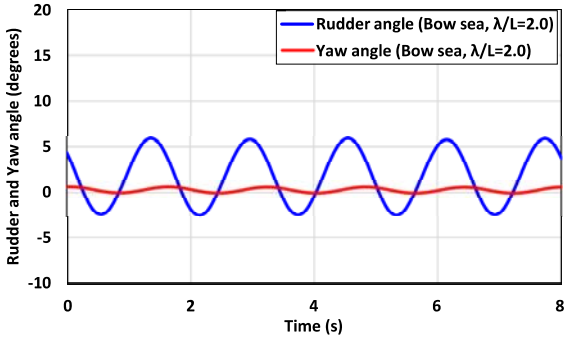

(f) Bow wave (λ/L_{BP}= 2.0)

Figure 6.5 Time histories of the rudder deflection and yaw angle under course keeping control in (a) calm sea, (b) bow sea (λ/L_{BP} = 0.7), (c) bow sea (λ/L_{BP} = 1.0), (d) bow sea (λ/L_{BP} = 1.3), (e) bow sea (λ/L_{BP} = 1.6), and (f) bow sea (λ/L_{BP} = 2.0).

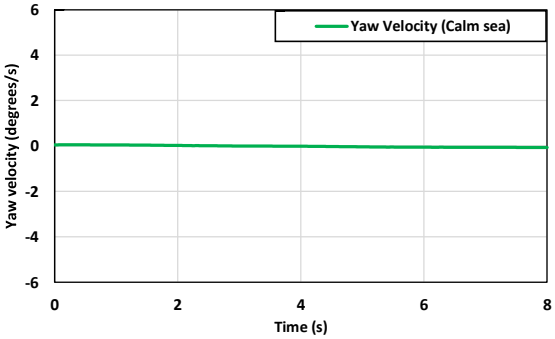

(a) Calm water

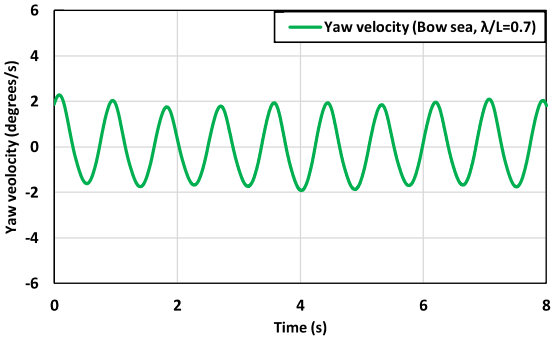

(b) Bow wave (λ/L_{BP} = 0.7)

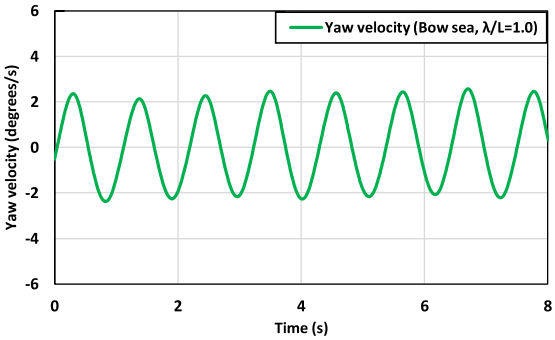

(c) Bow wave (λ/L_{BP}= 1.0)

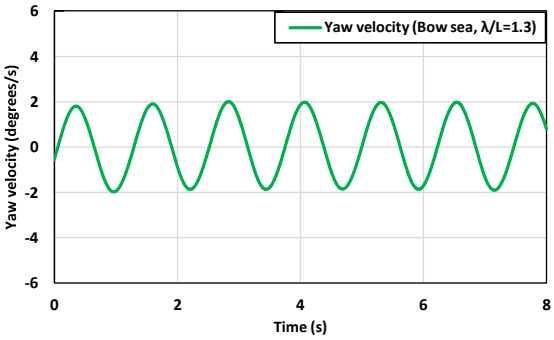

(d) Bow wave (λ/L_{BP}= 1.3)

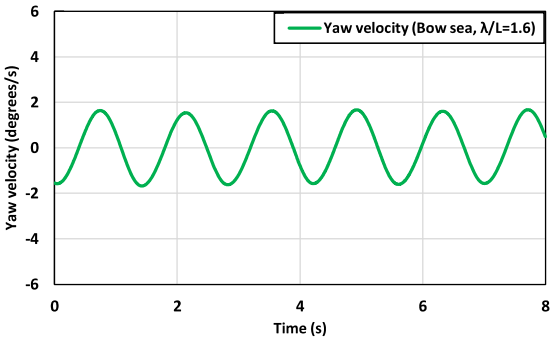

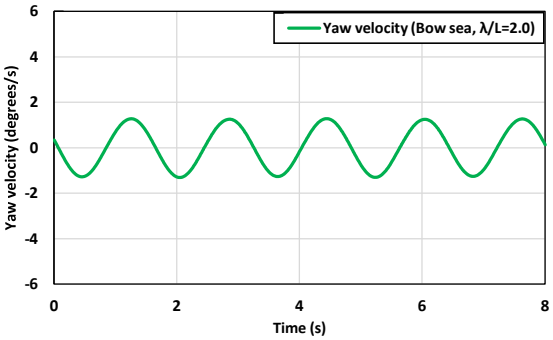

(e) Bow wave (λ/L_{BP}= 1.6) (f) Bow wave (λ/L_{BP}= 2.0)

Figure 6.6 Time histories of the yaw velocity under course keeping control in (a) calm sea, (b) bow sea (λ/L_{BP} = 0.7), (c) bow sea (λ/L_{BP} = 1.0), (d) bow sea (λ/L_{BP} = 1.3), (e) bow sea (λ/L_{BP} = 1.6), and (f) bow sea (λ/L_{BP} = 2.0).

In order to visualise and explain the behaviour of the vessel under course keeping control, the snapshots of the pressure distribution patterns and wave elevations, and the time history of the ship's yaw moment were taken in a given period encounter and are shown in Figure 6.7. The pictures are the snapshots from the simulation of Case 2. In the figure, the pressure was non-dimensionalised by dividing it by the dynamic pressure ($1/2\rho V_{ship}^2$). Phase A (t/T_e=0.00) clearly shows that the surface pressure on the starboard bow was larger than that on the port bow when the wave crest passed on the ship's bow, as seen in Figure 6.7 (a) – (b). The surface pressure on the port-stern side of the vessel was also observed to be larger than that on the starboard-stern side. Such a pressure distribution caused the maximum yaw moment to turn the ship to the port side, as shown in Figure 6.7 (c). When the ship was positioned in Phase B (t/T_e=0.25), the yaw moment acting on the ship was predicted at zero although the pressure difference between the starboard and the port side was clearly identified. This may be because the pressure difference existed near the centre of mass, which caused only the ship trajectory drift. When the wave crest subsequently passed on the midship of the ship (Phase C, t/T_e=0.50), the pressure on the starboard-stern side was much larger than the port-stern side. In addition, the port-bow showed a larger surface pressure compared to the starboard-bow. The pressure distribution observed in Phase C led to the maximum yaw moment to turn the ship to the starboard side. Similar to Phase B, the surface pressure distribution on the hull in Phase D (t/T_e=0.75) did not cause the yaw moment. The ship's heading angle was predicted to change depending on the pressure distribution on the hull by the oblique wave, while the rudder was deflected to control the yaw angle.

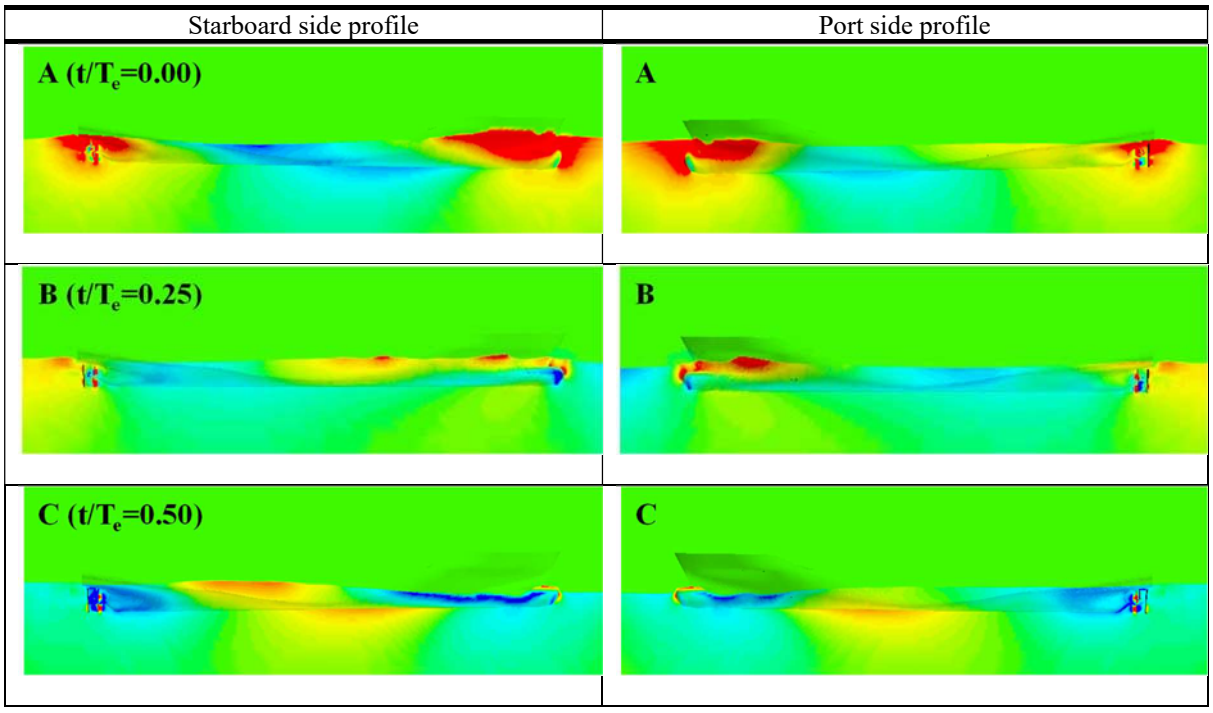

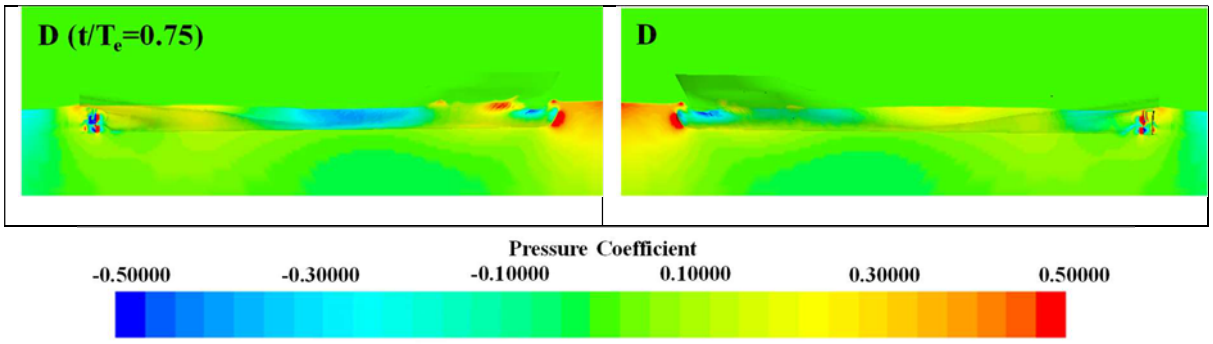

(a) The pressure coefficient on the hull surface

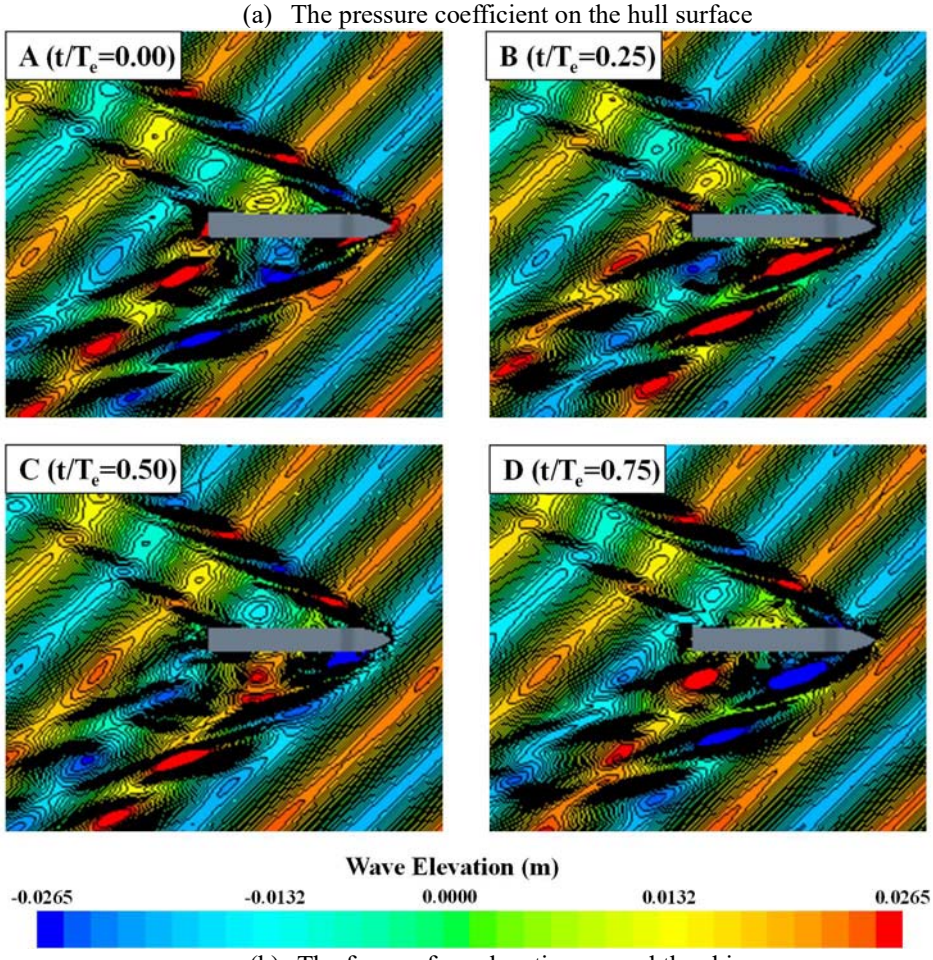

(b) The free surface elevation around the ship

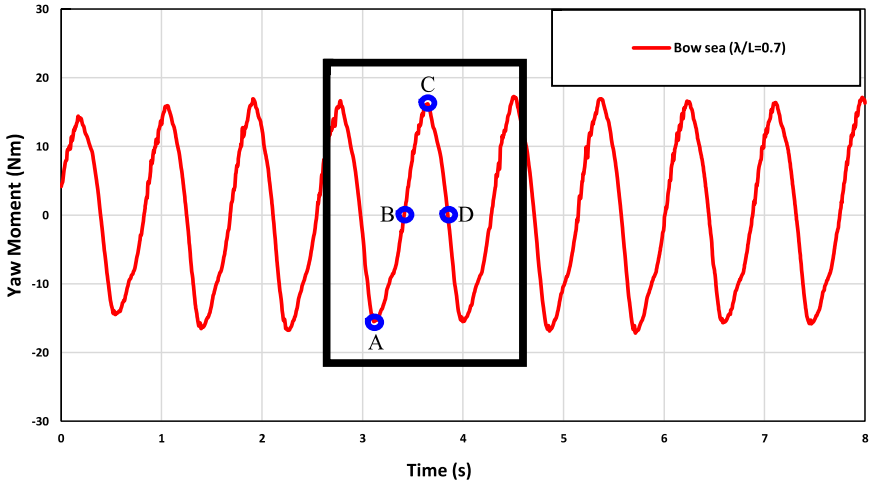

(c) The time history of the yaw moment acting on the hull

Figure 6.7 The snapshots of the pressure distribution patterns and free surface elevations, and the time history of the ship's yaw moment in a period of encounter under course keeping control.

Figure 6.8 presents the predicted ship trajectories under course keeping control for all the cases. The relatively large deviation from the original course was observed in the short wave conditions (λ/L_{BP} = 0.7 and 1.0), whereas a very small deviation was noticed for the rest of the cases. This can be explained by the effect of the wave drift force on the ship, which was observed to be more significant in the shorter wave conditions. The more the number of encounter waves at a given period may lead to the stronger the impact of the wave drift force on the ship. As a result of this, the ship advancing forward in the short wave conditions was noted to be more drifted, as shown in Figure 6.8. The ship trajectory drift directions were similar to the wave propagation direction. The predicted ship paths revealed that the deviation of the ship's course was dependent on the wavelength under oblique wave conditions. It was also estimated that the long wavelength conditions can cause the course of the ship to oscillate continuously near the planned route. It should be noted that the course keeping capability might be further improved when applying the optimum gains of the feedback controller with sufficient propulsion power.

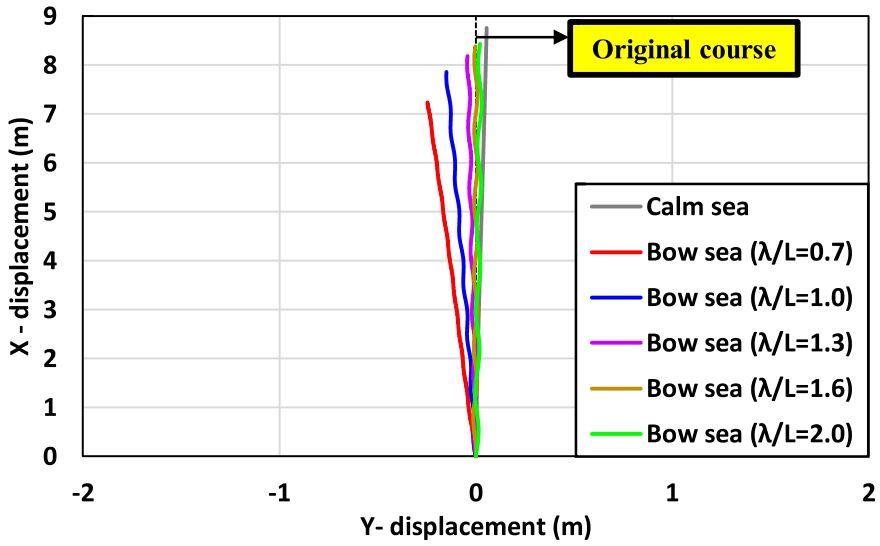

Figure 6.8 Comparison of the predicted trajectories for all the cases.

6.4.3. Turning circle manoeuvre

The turning manoeuvrability of a ship can be assessed through the standard turning circle manoeuvre. In this study, the starboard turning tests were simulated to investigate the ship's turning ability. In the turning manoeuvre, the ship was moving forward at the approach speed and the rudder angle deflection towards 35° starboard was executed at maximum rudder rate. Subsequently, the ship started to respond turning in that direction. The ship model used for the turning circle manoeuvres was the same as that of the course keeping simulations with a propeller revolution of 13.38 RPS. Throughout all the simulations, the turning circle manoeuvres with only the heading angle variation up to 360° were performed based on the general procedure (IMO, 2002).

6.4.3.1 Time histories during turning and turning indices

Figure 6.9 illustrates the time histories of the predicted ship velocities, forces and moment during the standard turning manoeuvre. All values on the graphs are expressed in model-scale. Several black dash lines are depicted to represent the representative wave-encounter directions during the ship's turning to starboard. In order to execute the turning circle test, the rudder angle was deflected towards the starboard 35° during the moments when the wave trough passed on the midship of the model. It should be noted that the timing of rudder deflection has little influence on the manoeuvring behaviours of a ship, as discussed in the study of Kim et al. (2019).

When the ship was sailing forward, the pressure distribution acting on the ship hull was found to vary depending on the wavelength of bow waves. This caused differences in the added resistance induced by the incident waves, and thus the ship experienced changes in the forward speed according to the wave condition. The propulsion characteristics were also influenced by the high-frequency wave-induced motions and the orbital wave-particle velocities (Liu et al., 2020). Such complex interactions between the ship and waves played a significant role in determining the behaviour of the turning manoeuvre.

In general, considerable fluctuations were observed in the ship velocities as well as the hydrodynamic forces and moments acting on the ship during the ship's turning because of the high-frequency wave-induced motions. As for the ship forward velocities as shown in Figure 6.9 (a) – (f), they showed a gradual decrease after the rudder execution and finally converged to between 0.43 m/s and 0.5 m/s with some fluctuations around their mean value depending on the wavelength condition. This involuntary speed loss was caused by an increase in ship resistance, which is closely associated with a large drift angle while the ship is turning. The maximum speed loss for the calm water was noted approximately 30s after the rudder was deflected, whereas the maximum speed loss for wave cases occurred between about 16s – 25s after the rudder execution. The speed loss rate between the initial approach speed and the steady mean value was estimated to be 54% for the calm water, 48% for the λ/L_{BP}=0.7, 50% for the λ/L_{BP}=1.0, 56% for the λ/L_{BP}=1.3, 58% for the λ/L_{BP}=1.6, and 56% for the λ/L_{BP}=2.0. It was observed that the surge forces fluctuated significantly during the ship's turning manoeuvre under wave conditions, but the fluctuations almost disappeared at the moment when the ship experienced the port or starboard beam waves. Likewise, the surge velocities also showed similar trends.

For the sway velocities and forces, as shown in Figure 6.9 (a) – (f), they tend to increase rapidly until approximately 8s after the rudder deflection to starboard and then showed a tendency to converge to similar values. The converged average values of the sway velocities were predicted to be -0.18 m/s for the calm water, -0.17 m/s for the λ/L_{BP}=0.7, -0.18 m/s for the λ/L_{BP}=1.0, -0.19 m/s for the λ/L_{BP}=1.3, -0.2 m/s for the λ/L_{BP}=1.6, and -0.19 m/s for the λ/L_{BP}=2.0. The oscillations in the sway velocities and forces were observed to be larger when the ship experienced beam waves, whilst the relatively small oscillations were found under both the head and following seas. Regarding the yaw velocities and moments, the fluctuation magnitude varied depending on the wave-encounter direction. The largest fluctuations were clearly observed when the ship experienced the quartering waves. The maximum yaw rates occurred approximately 6s after the rudder execution. Then, yaw velocities gradually converged to the values which were predicted to be 7.31º/s for the calm water, 7.80º/s for the λ/L_{BP}=0.7, 7.87º/s for the λ/L_{BP}=1.0, 8.20º/s for the λ/L_{BP}=1.3, 8.33º/s for the λ/L_{BP}=1.6, and 8.05º/s for the λ/L_{BP}=2.0.

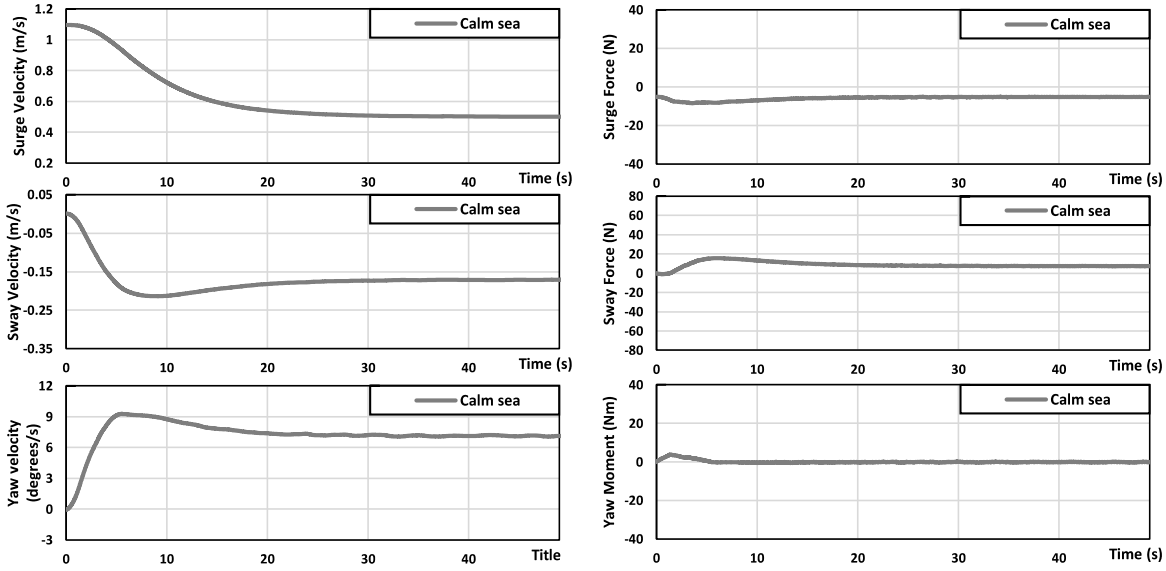

(a) Calm water

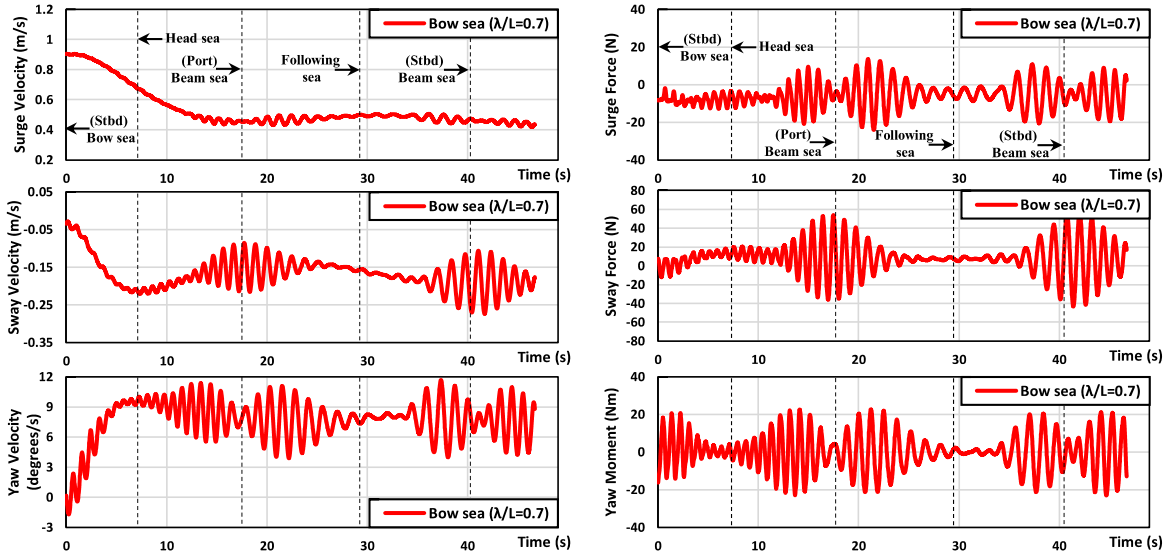

(b) Bow wave ($\lambda/L_{BP} = 0.7$)

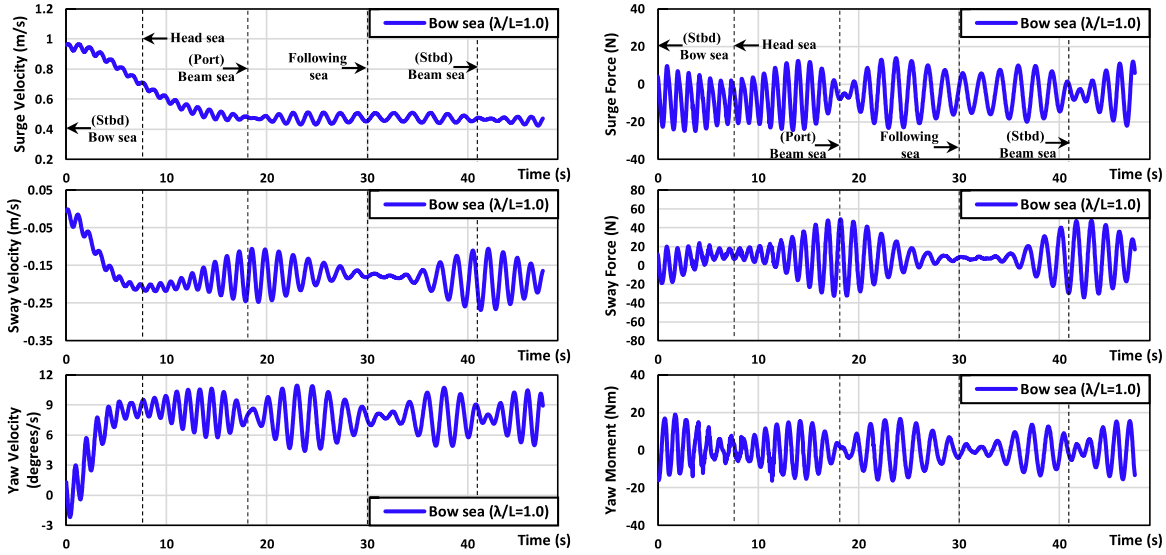

(c) Bow wave (λ/L_{BP}= 1.0)

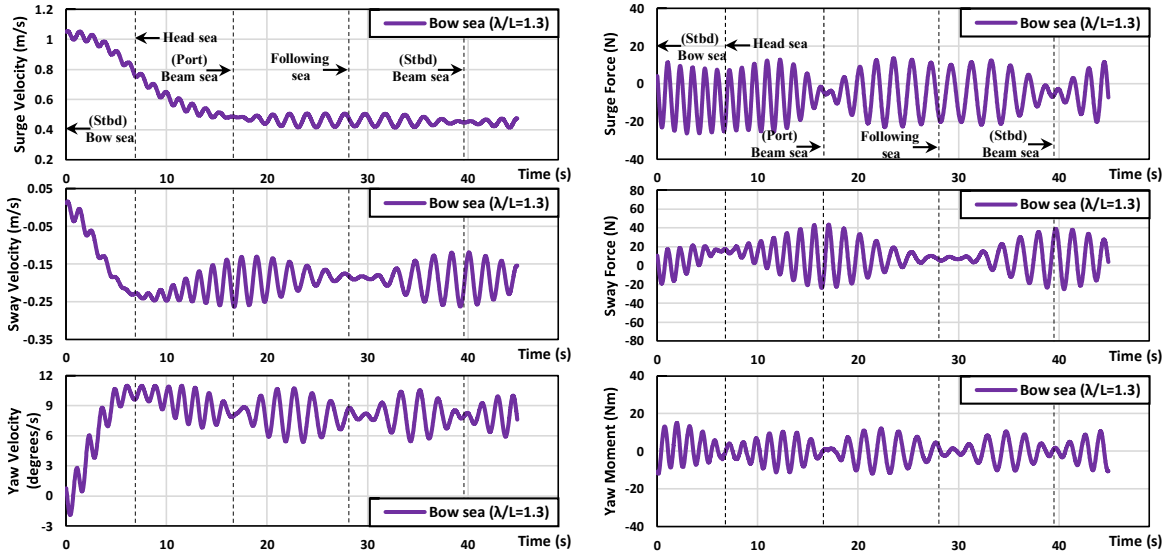

(d) Bow wave (λ/L_{BP}= 1.3)

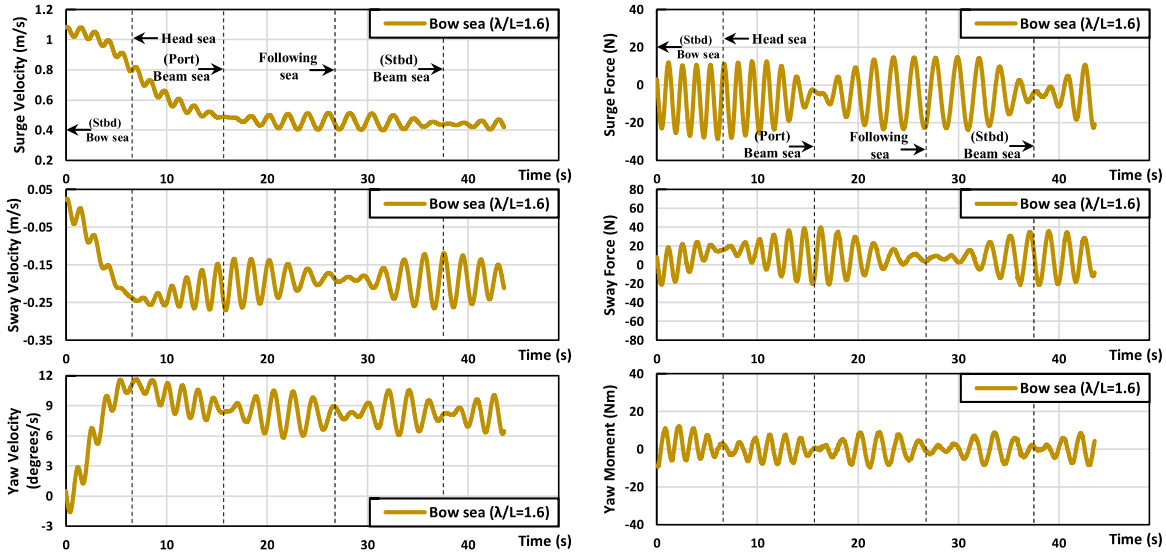

(e) Bow wave (λ/L_{BP}= 1.6)

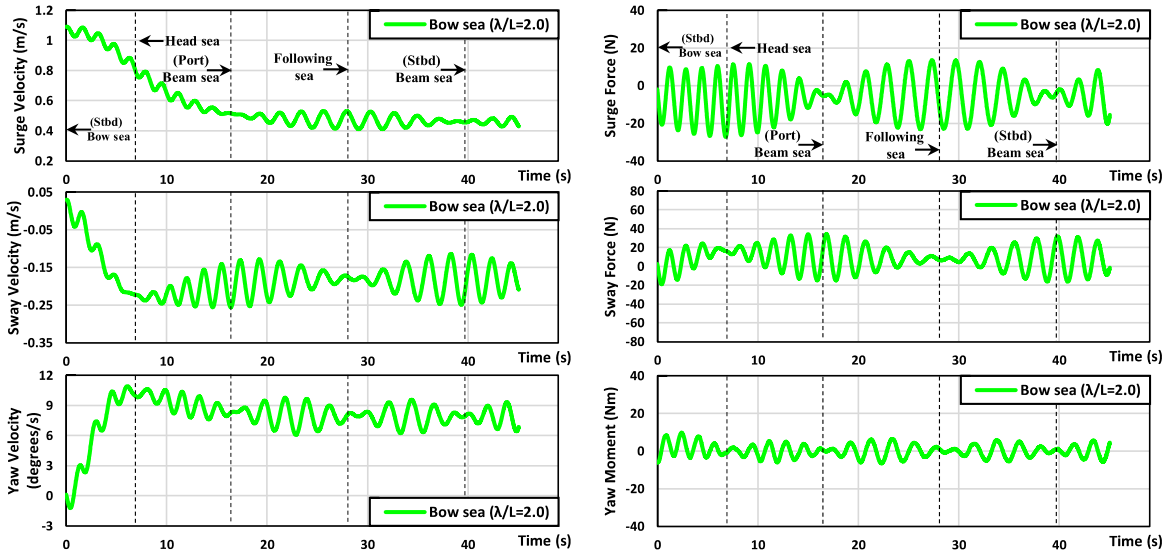

(f) Bow wave (λ/L_{BP}= 2.0)

Figure 6.9 Time histories of the ship velocities, forces, and moment during the turning manoeuvre in waves.

Table 6.4 shows the comparison of the turning manoeuvring quantities associated with the ship's turning ability. In real navigation, the advance, transfer, and tactical diameter have been recognised as the most critical manoeuvring quantities to understand the ship's manoeuvring performance at sea. These indices were closely correlated to the ship's horizontal motions during the turning circle manoeuvre. Accordingly, the hydrodynamic forces and moment acting on the ship in the horizontal plane were identified as the main factors involved in the critical manoeuvring parameters. These forces and moments on ship turning in waves resulted from complex interactions between the rudder, propeller, hull, and waves. In particular, the imposed wavelength conditions had a significant effect on the hydrodynamic forces and moment during the turning manoeuvre. The turning circle trajectories were found to differ depending on the wavelength. As for the ship advance and transfer, the ship velocities in the horizontal plane (surge, sway, and yaw velocities) played an important role in determining these distances. In

general, the greater forward speed and the longer time to turn by 90º, the larger the advance and transfer can be. The maximum advance and transfer distances were observed in cam water (Case 1) due to the relatively large forward speed and the long 90º turning time. Although the 90º turn time was relatively long, the ship experienced the minimum advance and transfer in the bow waves of λ/L_{BP} =0.7 (Case 2) because the forward speed was the lowest at the beginning of the turning manoeuvre. Interestingly, despite the relatively small forward speed, the advance and transfer for the λ/L_{BP} =1.0 (Case 3) were similar to those observed for the λ/L_{BP} =1.3 and 1.6 (Cases 4 and 5) due to the longer time to turn by 90º. It was noted that the λ/L_{BP} =1.3 and 1.6 cases caused a larger yaw moment than that for the λ/L_{BP} =1.0 as the ship started turning in waves. This accelerated the ship's yaw velocities, and 90° turns were achieved much earlier. In the same manner, the ship advancing in the bow waves of λ/L_{BP} =1.3 and 1.6 experienced larger sway velocities than the λ/L_{BP} =1.0 case. Among the wave cases, the maximum advance and transfer were predicted in the bow waves of λ/L_{BP} =2.0 (Case 6) due to the relatively large ship's speeds. As seen in Figure 6.9, the λ/L_{BP} =1.3, 1.6, and 2.0 conditions caused a large lateral force and yaw moment in the early stage of the turning, and hence large sway and yaw velocities were observed. The tactical diameters were also clearly found dependent on the wavelength. It was revealed that the relatively large tactical diameters were observed in the bow waves of λ/L_{BP} =1.3, 1.6, and 2.0 under which large lateral force and yaw moment were observed at the early stage of the turning.

Table 6.4 CFD results: turning indices in calm water and regular waves.

Parameters (CFD results)	Calm sea (Case 1)	Bow sea (λ/L_{BP}= 0.7) (Case 2)	Bow sea (λ/L_{BP}= 1.0) (Case 3)	Bow sea (λ/L_{BP}= 1.3) (Case 4)	Bow sea (λ/L_{BP}= 1.6) (Case 5)	Bow sea (λ/L_{BP}= 2.0) (Case 6)
Advance (m)	9.55 **$(3.13L_{BP})$**	7.96 **$(2.60L_{BP})$**	8.83 **$(2.89L_{BP})$**	8.81 **$(2.88L_{BP})$**	8.71 **$(2.85L_{BP})$**	8.94 **$(2.92L_{BP})$**
Transfer (m)	4.07 **$(1.33L_{BP})$**	2.69 **$(0.88L_{BP})$**	3.09 **$(1.01L_{BP})$**	3.02 **$(0.99L_{BP})$**	3.01 **$(0.98L_{BP})$**	3.36 **$(1.09L_{BP})$**
Time for yaw 90 degrees (s)	12.31	12.21	13.08	11.71	11.24	11.59
Tactical diameter (m)	9.82 **$(3.21L_{BP})$**	7.03 **$(2.29L_{BP})$**	7.82 **$(2.56L_{BP})$**	7.74 **$(2.53L_{BP})$**	7.60 **$(2.49L_{BP})$**	8.23 **$(2.69L_{BP})$**
Time for yaw 180 degrees (s)	24.20	23.35	24.38	22.49	21.56	22.20

Figure 6.10 describes the comparison of the predicted turning trajectories of the KCS for all the cases. For the correct comparisons of the trajectories, all the rudder execution points were shifted to the origin point (0,0). Generally, it was found that the size of the turning circle was found to have a proportional relationship to the wavelength. It is worth noting that very similar trajectories can be found in the bow waves of λ/L_{BP} =1.0, 1.3, and 1.6, like the turning indices. The smallest turning circle of the KCS was observed in the bow waves of λ/L_{BP} = 0.7, which may be attributed to the shortest wavelength. In addition, the instantaneous free surface elevation around the ship hull during the starboard turning manoeuvre in the bow waves is presented in Figure 6.11. It should be noted that the generated Kelvin wave by the manoeuvring

ship was obviously more visible in shorter waves.

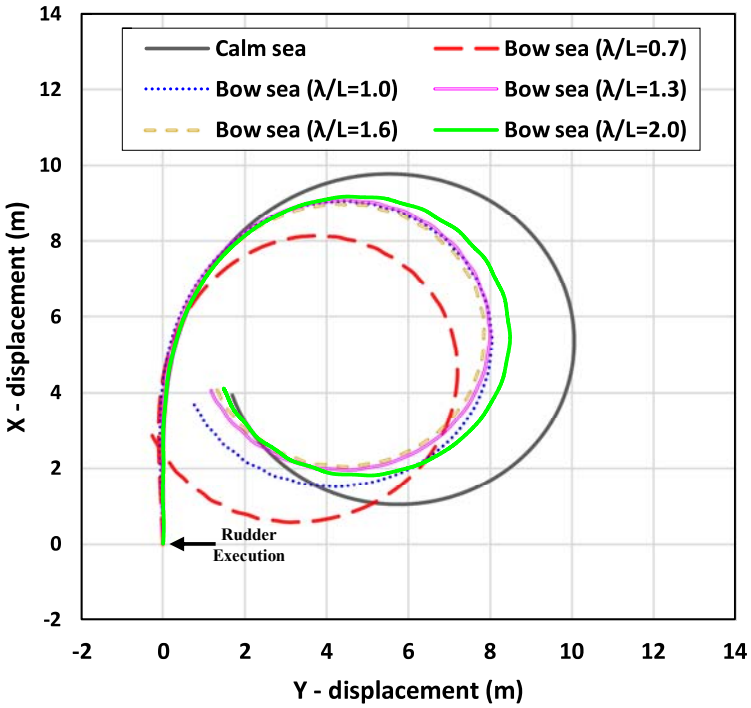

Figure 6.10 Comparison of the predicted turning circle trajectories.

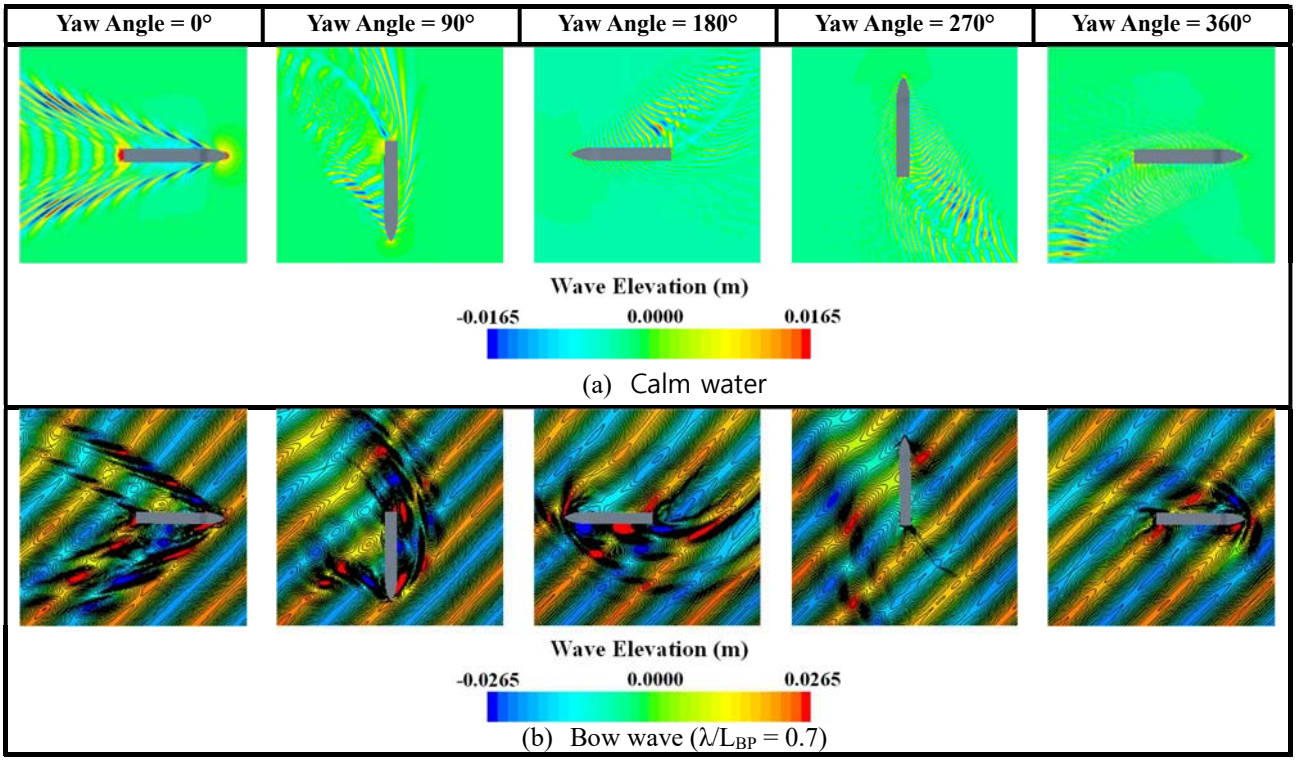

(a) Calm water

(b) Bow wave ($\lambda/L_{BP} = 0.7$)

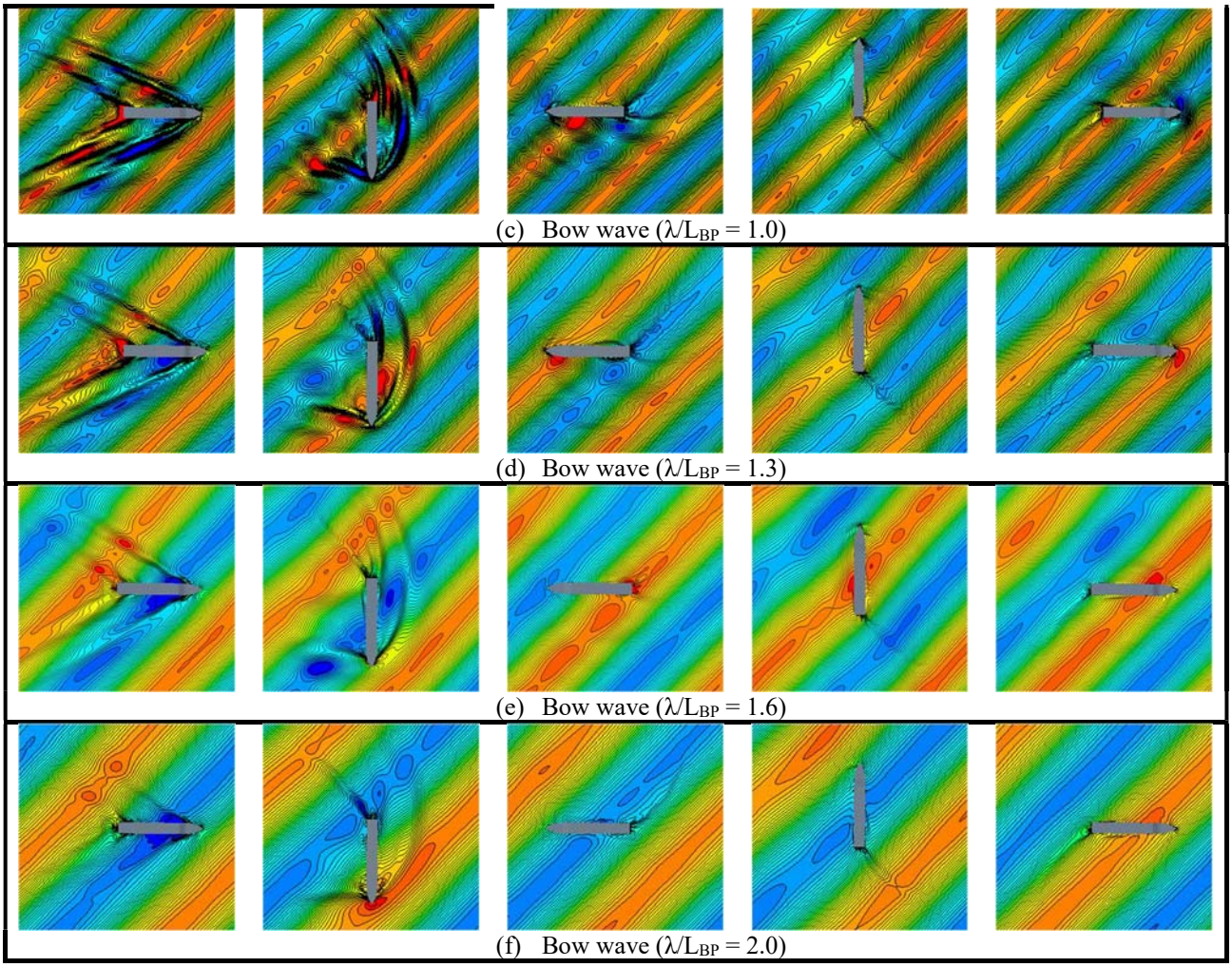

Figure 6.11 The free surface elevation during the standard turning circle manoeuvre in waves.

6.4.3.2 Wave-induced motions during turning manoeuvre

Figure 6.12 shows the time histories of ship motions, i.e., pitch, heave, and roll as well as relevant forces and moments during the standard turning manoeuvre. Unlike the calm water case, the ship motions, forces, and moments were observed to experience considerable oscillations during the ship's turning in waves, which may be attributed to the high-frequency wave-induced motions. In addition, such frequencies continued to change during the ship's turning due to instantaneous variations in the ship's velocity and wave-encounter direction. For example, a ship advancing in the bow waves (Cases 2-6) encountered the starboard bow wave (0° turn), the head wave (45° turn), the port beam wave (135° turn), following wave (225° turn), starboard beam wave (315° turn), and starboard bow wave (360° turn) in series after starting the starboard turning manoeuvre. The ship's turning has contributed to continual changes in the wave-encounter frequency, consequently the ship motion frequency in waves.

It can be clearly seen from Figure 6.12 (a) that the pitch motion and moment in calm water converged to almost zero value without any fluctuations during the turning manoeuvre. The heave motion and force in calm water also followed a similar trend. On the other hand, it was

revealed from Figure 6.12 (b) - (f) that the waves have a great influence on the ship's motions, forces, and moments during the ship's turning. While the ship was turning, the maximum pitch motion and moment were found when the ship experienced the head or bow waves whereas the minimum values were noted in beam waves. As for the heave motion and force, the maximum amplitudes were predicted when encountering the beam waves, while the minimum values were observed under the following sea conditions. Such variations in the ship motions, forces, and moments were observed more clearly in shorter waves, shown in Figure 6.12 (b) - (c).

As discussed in Hasanvand and Hajivand (2019), the roll motion was observed to be significantly affected by the turning manoeuvre (Figure 6.12 (a) - (f)). When the rudder was deflected to the hard-over angle (35°), the forces acting on the rudder blade caused the ship to heel to the starboard (to the centre of the turning circle). These initial roll angles were estimated in all the cases within a value of 2º. Subsequently, the ship was heeled to the port side (to the outside) due to the hydrodynamic forces and the centrifugal force acting on the hull. The maximum roll angles were noted to be 5.7° for the calm water case, 4.4° for the λ/L_{BP}=0.7, 4.4° for the λ/L_{BP}=1.0, 4.7° for the λ/L_{BP}=1.3, 5.4° for the λ/L_{BP}=1.6, and 6.0° for the λ/L_{BP}=2.0. The ship's roll angles finally converged to between 1 and 2 degrees with some fluctuations around their average value. It should be borne in mind that the roll motion can vary depending on several factors such as the rudder angle, the approach speed, and the loading condition.

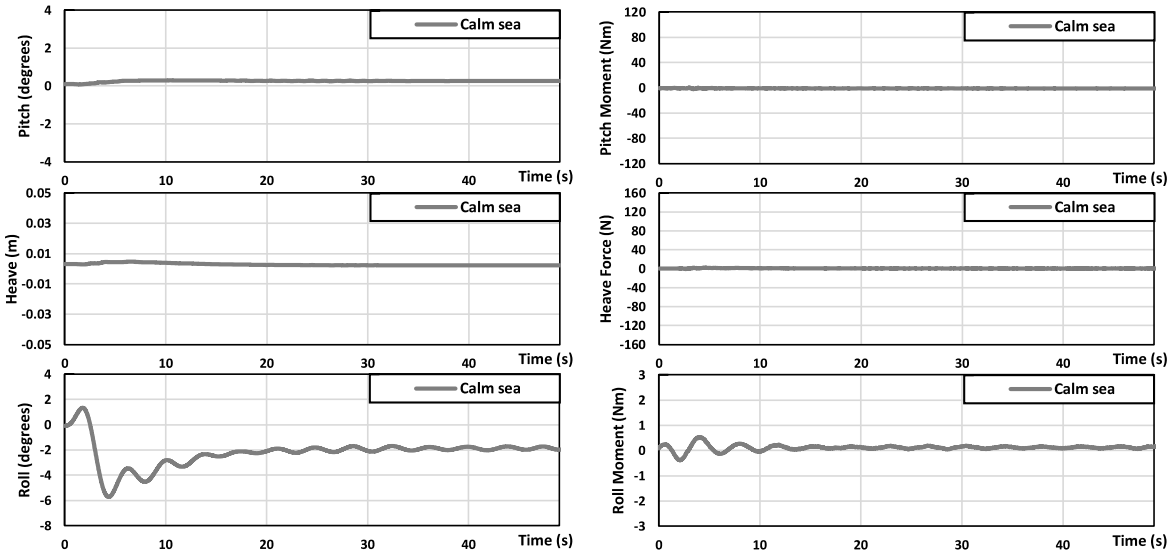

(a) Calm water

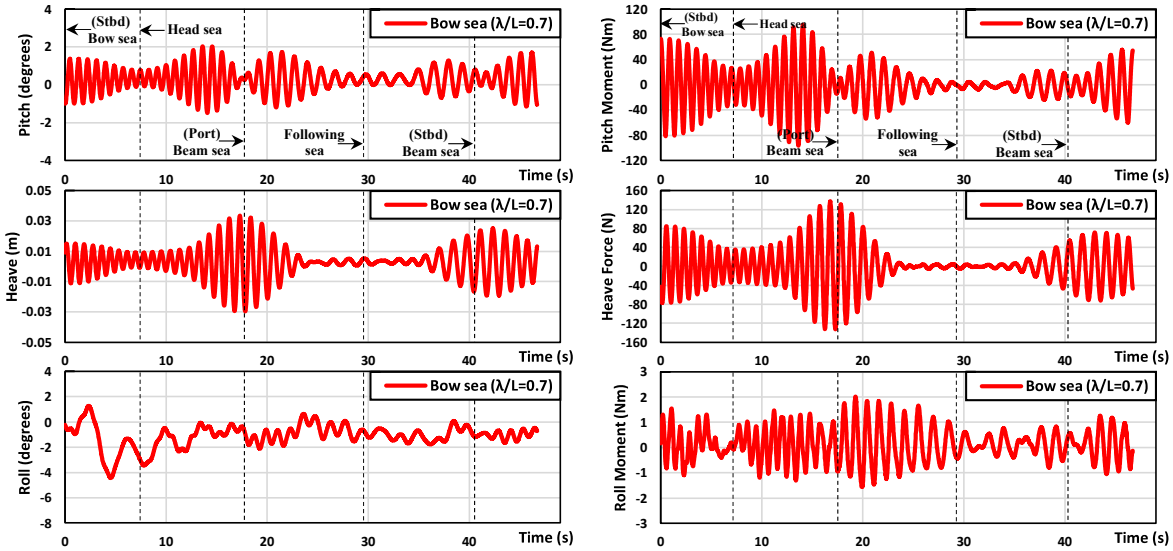

(b) Bow wave ($\lambda/L_{BP} = 0.7$)

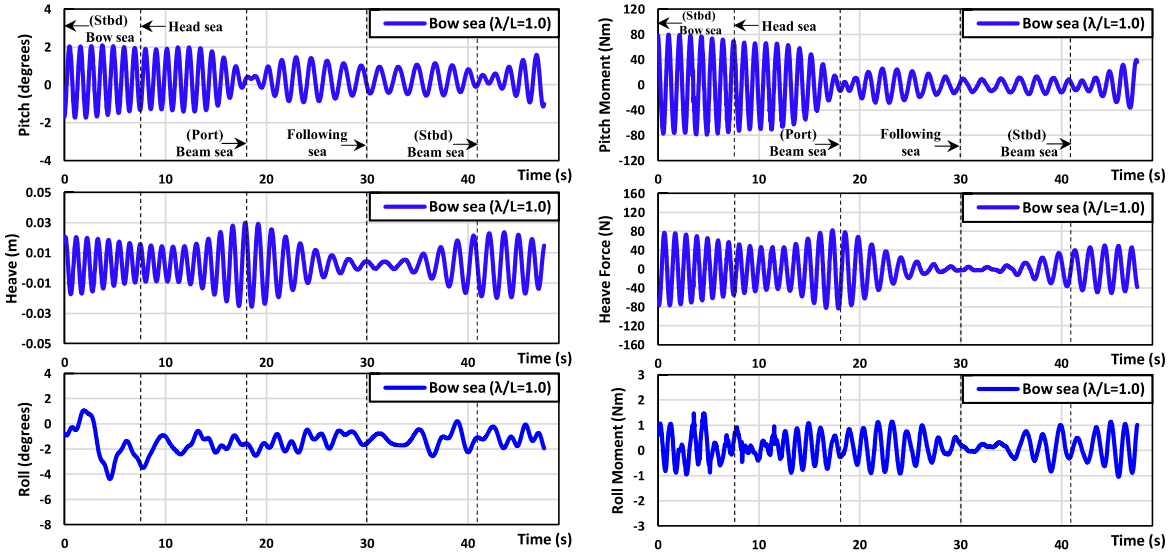

(c) Bow wave ($\lambda/L_{BP} = 1.0$)

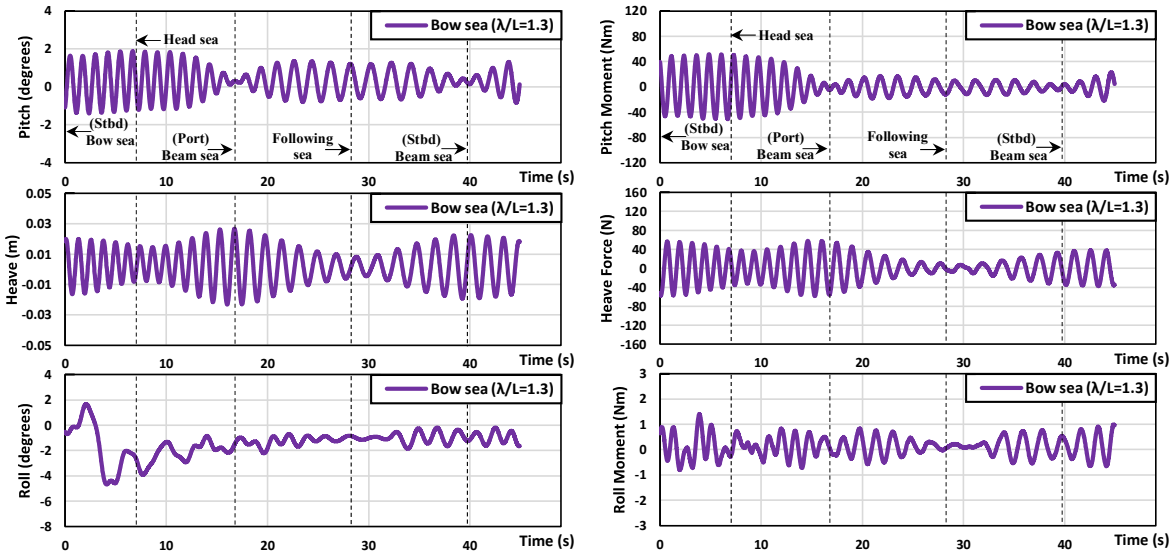

(d) Bow wave (λ/L_{BP}= 1.3)

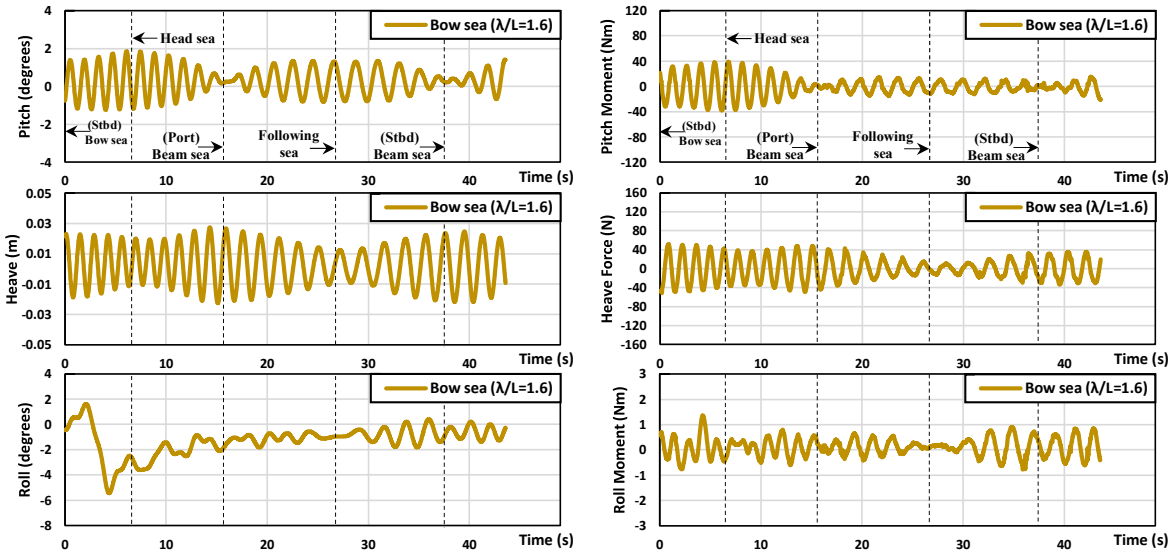

(e) Bow wave (λ/L_{BP}= 1.6)

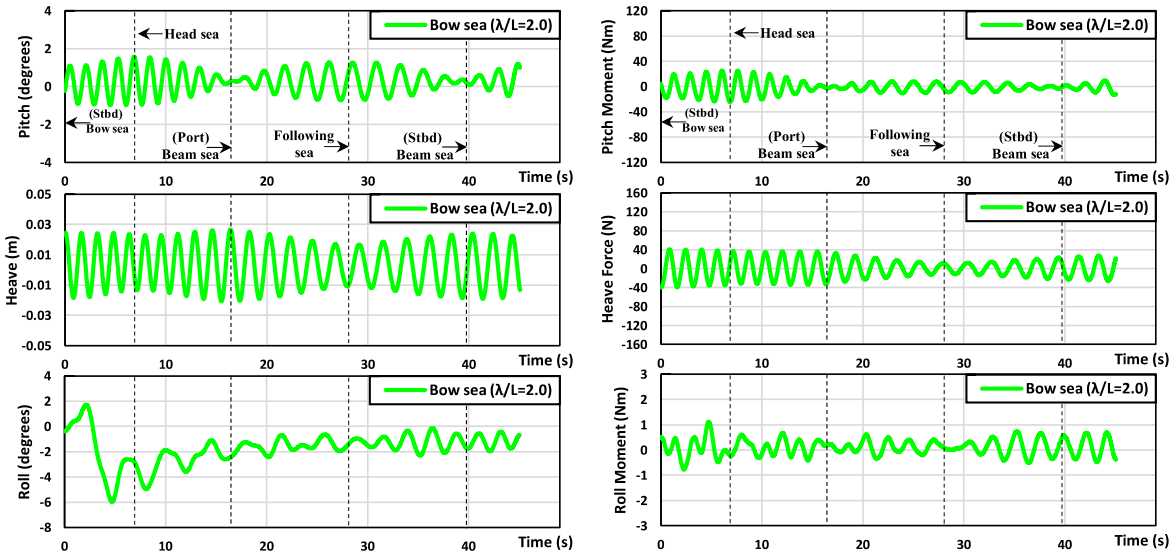

(f) Bow wave (λ/L_{BP}= 2.0)

Figure 6.12 Time histories of ship motions, forces and moments acting on the ship during turning manoeuvres.

6.5. Concluding Remarks

This chapter has demonstrated the effectiveness of the free-running CFD model to predict the ship's manoeuvrability under various wave conditions. As coupled with the 5th-order Stokes wave model and wave forcing capability, this model was successful in providing an understanding of the manoeuvring behaviour of the KCS in different wavelength conditions. With the provision of time history data regarding the critical manoeuvring quantities, the simulation results were able to directly indicate the correlations between the ship's manoeuvrability and wavelength, which confirmed the impact of the wavelength on the manoeuvring performance of the ship in regular waves. The key findings of this research can be highlighted as follows:

1) For the course keeping manoeuvres in waves, the approach speed was found to have a strong correlation with the wavelength. The approach speed was noted to increase with the increase in the wavelength at a given wavelength range ($0.7 \leq \lambda/L_{BP} \leq 2.0$). The minimum approach speed was observed to be 0.904 m/s for the λ/L_{BP}=0.7, whilst the maximum approach speed was noted to be 1.054 m/s for the λ/L_{BP}=2.0. The seakeeping motions also differed depending on wavelength conditions. The largest oscillation amplitude was identified in the bow waves of λ/L_{BP} =1.0, whereas the largest heave motion was found in the bow waves of λ/L_{BP} =2.0. As for the course keeping capabilities, simulation results revealed that the rudder control was a critical element to keep the ship straight in all bow wave conditions. Similar large rudder deflections were predicted approximately 7º in all bow waves, regardless of the wavelength. However, the steering frequency was found to vary significantly depending on the wavelength. The frequency of the rudder deflection was confirmed to have an inverse relation to the wavelength.

2) For the standard turning circle manoeuvres in waves, it was identified that the critical manoeuvring turning quantities were strongly affected by the wavelength and thus lead to significant changes in the turning trajectories. The minimum value of the advance, transfer, and tactical diameter was estimated under the shortest wavelength of λ/L_{BP} =0.7 with a minimum turning circle radius. Interestingly, similar manoeuvring indices and trajectories were estimated in the bow waves of λ/L_{BP} =1.0, 1.3, and 1.6. The longest wavelength of λ/L_{BP} =2.0 caused the maximum increase of the manoeuvrability parameters which are the closest to the quantities of the calm water condition.

3) The instantaneous free surface elevation around the ship during the course keeping and turning manoeuvres were presented for all cases. When the ship was moving forward under course keeping control, the symmetric wave profile around the hull was clearly observed in calm water. On the other hand, the ship advancing forward in the bow seas experienced asymmetric wave profiles as opposed to the calm water case, which may lead to a substantial lateral force and yaw moment with consequent changes in the ship's heading angle. In addition to this, the generated Kelvin wave by the ship performing the turning manoeuvre was obviously more visible in shorter waves.

7. FREE-RUNNING CFD SIMULATIONS FOR DIFFERENT REGULAR WAVE HEIGHTS

7.1. Introduction

Ships encounter different wave heights in real sea states. Various wave heights can lead to substantial changes in the behaviour of a ship during manoeuvring, and hence a ship's manoeuvrability in waves should be accurately evaluated to ensure navigational safety at sea.

A ship's performance is highly dependent on sea conditions affected by waves. From a hydrodynamic point of view, sea waves affect ship motions and loads, as well as ship's manoeuvring performance. In other words, the manoeuvring behaviour can be affected by a combination of wave characteristics such as wave height, length, and directions when a ship sails in waves. Sea states can be practically described by the Beaufort scale proposed by the World Meteorological Organisation (from Beaufort 0 to Beaufort 12). It should be noted that Beaufort scale 12 defines waves of height greater than 14 metres. In this regard, it is thought that the wave height could lead to substantial changes in the ship resistance and thus the loss of speed, which was highly expected to affect the manoeuvring characteristics of a ship in waves. It supports the argument of this chapter that a proper understanding of the relationship between wave heights and ship manoeuvring behaviours in real sea conditions is necessary.

Recently, a growing demand for understanding the manoeuvring performance of a ship in waves has emerged as reviewed in Chapter 3 (IMO, 2021; ITTC, 2021c). However, to date, current research on the effect of wave heights on a ship's manoeuvring performance has been highly limited in number as well as in scope. Extensive experimental and numerical investigations on the manoeuvrability of a vessel in waves were performed within the European funded Project SHOPERA, as presented in (Papanikolaou et al., 2015; el Moctar et al., 2016; Papanikolaou et al., 2016; Sprenger et al., 2016). In their research, the manoeuvring characteristics of the KVLCC2 and DTC ship models were comprehensively investigated in different wave conditions (parameters of variation: wave direction, wave period, wave height), contributing to the establishment of a benchmark and validation database regarding manoeuvring problems in waves. Kim et al. (2019) carried out a series of free-running experiments to investigate the manoeuvring characteristics of the KRISO Very Large Crude-oil Carrier 2 (KVLCC2) under three different wave height conditions. The key findings of the previous studies were that the ship's manoeuvring behaviours are greatly influenced by the impact of wave heights. In this regard, this study raised a further question on the relation between wave heights and various types of ships. It is because the manoeuvring characteristics of a ship obviously can vary depending on the types and dimensions of subject vessels. Therefore, in order to draw more generalised and meaningful information, it was highly thought that the manoeuvring characteristics of other ship types under different wave height conditions should be examined. Given the lack of previous research on wave effects on a ship's manoeuvrability, the research reported in this chapter was motivated to investigate the effect of wave heights on the manoeuvring performance of the KRISO Container Ship (KCS) model; which has been used in a wide range of research studies but not studied for the manoeuvring behaviours in different wave height conditions. Therefore, this research offers better insight

into a container ship's manoeuvrability in a real seaway. It is expected the results generated will be appliable to most conventional container ships.

The remainder of this chapter will continue by illustrating a list of the simulation cases to which the current CFD model is applied in Section 7.2, followed by a description of the specific numerical setup of the CFD model in Section 7.3. Then, the obtained results and their analysis are provided in Section 7.4. Finally, concluding remarks are drawn in Section 7.5.

7.2. Goal and Scope

The principal goal of this chapter is to investigate the effects of wave heights on a ship's manoeuvrability in waves, with particular attention to the self-propulsion, course-keeping control, and turning capability in various wave heights.

As seen from Table **7.1** and Figure **7.1**, this study designed six manoeuvring simulations: one for calm water and the others for the waves. As for the wave conditions, the effects of incident regular waves with the wave heights H = 0.032m, 0.048m, 0.064m, 0.080m, and 0.096m were investigated during free-running manoeuvres (the wave length to ship length ratio λ/L_{BP} = 1.0 and wave encounter angle μ = 225º). The wave heights considered are ranged from 2.4m to 7.2m in full-scale. For the approach speed, it was found to vary depending on the wave height under the same propeller speed (13.38 RPS), which resulted from the differences in the added wave resistance acting on the ship. Since the research reported in Chapter 5 revealed that course-keeping capabilities could be clearly evaluated in oblique seas, this chapter has chosen bow quartering waves (μ = 225º). It should be noted that the conducted free-running simulations were subjected to deep water conditions.

Table 7.1 The simulation cases to which the CFD model is applied.

Case no. C	Approach speed U_0 (m/s)	Propeller rev. (RPS)	Wave height H (m)	Encounter Angle μ (degrees)	Encounter Period T_e (s)	Wave steepness H/ λ	Wave/ship length λ/L_{BP}
1	1.094	13.38	Calm water	- (Calm sea)	-	-	-
2	1.004	13.38	0.032	225 (Bow quartering sea)	1.055	0.010	1.00
3	0.945	13.38	0.048	225 (Bow quartering sea)	1.071	0.016	1.00
4	0.876	13.38	0.064	225 (Bow quartering sea)	1.087	0.021	1.00
5	0.811	13.38	0.080	225 (Bow quartering sea)	1.104	0.026	1.00
6	0.737	13.38	0.096	225 (Bow quartering sea)	1.123	0.031	1.00

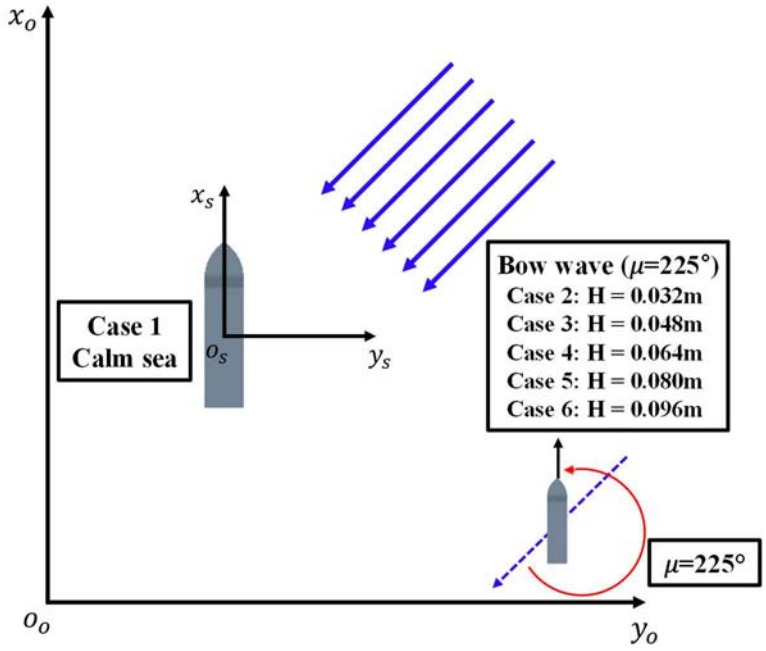

Figure 7.1 A schematic view of the simulation cases.

7.3. Numerical Modelling

The free-running CFD simulations for this chapter were designed in agreement with the numerical setup reported in Chapter 4, Section 4.3.

The schematic of the computational domain generated in this study is described in Figure **7.2**. To simulate ship manoeuvres in waves, the free surface grid refinement was performed based on the practical guidelines for ship CFD applications from ITTC (2011). The recommendation suggests that a minimum of 80 grid points per wave length and 20 grid points per wave height should be generated on the free surface to avoid wave dissipation. In this study's CFD work to ensure reliable wave propagation during the ship's manoeuvres, a minimum of 80 cells per wave length was used in the x and y directions (horizontal directions). Additionally, a minimum of 20 cells was generated in the z direction (vertical direction) where the free surface was expected. For the calm water simulation, the refined grid area for the free surface was kept relatively small, compared to that used in the wave cases. The total grid number applied to the calm water (Case 1) and wave (Cases 2-6) simulations is approximately 5.30×10^6 and 8.31×10^6, respectively.

a) Mesh for the ship and free surface

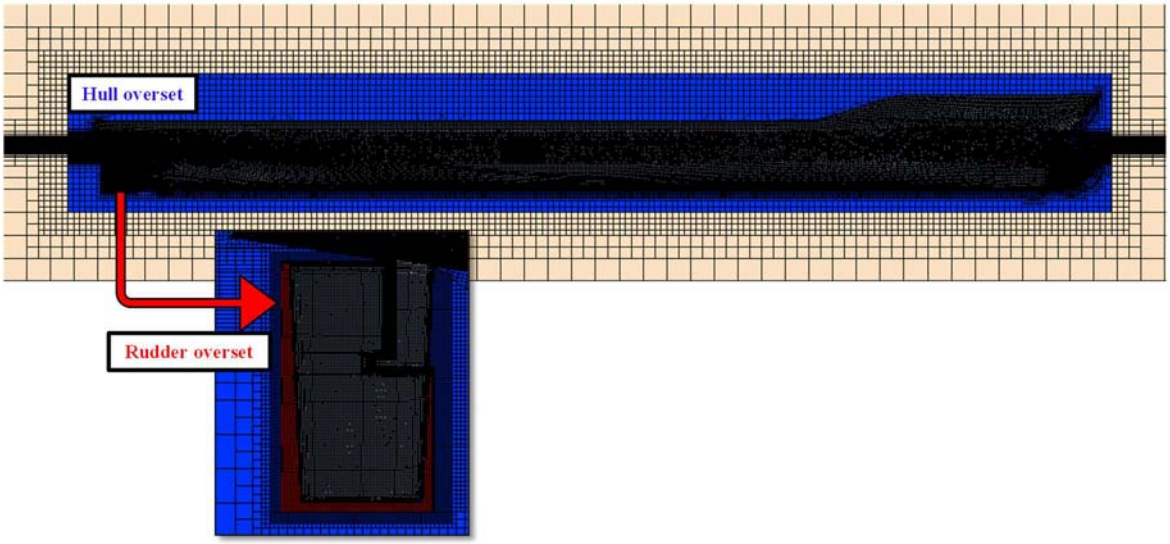

b) Profile view of the computational domain

Figure 7.2 Mesh structure of the computational domain.

Throughout all the simulations in this chapter, the time step was determined at 0.005s which is small enough to ensure an accurate description of the wave propagation. This value meets the guidelines of ITTC (2011) that recommend a minimum of 100 time steps per encounter period for wave simulation.

7.4. Results

7.4.1. Self-propulsion

Prior to the investigation of the ship manoeuvrability in waves, the self-propulsion condition should be initially achieved with the ship free to move in 6 degrees of freedom. Figure 7.3 presents the time histories of the obtained approach speed, ship resistance, pitch motion, and heave motion at the self-propulsion condition for all the cases. Fourier Series (FS) harmonic analysis was used to analyse the unsteady time histories of the CFD results due to wave motions. The 0th harmonic term in FS means the average value of the time history of the obtained results, whilst the 1st harmonic term refers to the mean amplitude of the oscillation of the values. The FS results for the force and motions are presented in Table 7.2.

As Figure 7.3 and Table 7.2 jointly show, the ship performance at the self-propulsion conditions

shows a significant variation on wave heights. It should be reminded that regular waves with the ratio of wave length to ship length, λ/L_{BP}=1.0, and wave encounter angle, μ=225º, were applied throughout all the wave simulations, while only changing the wave heights. The wave height ranged from 0.032m to 0.096m, corresponding to 2.4m to 7.2m in full scale. As seen in Figure 7.3 (a), the increase of the wave height led to a decrease in the average approach speed. The mean forward speed in calm water was observed at 1.094 m/s, which corresponds to 18.45 knots in full scale and a Froude number of 0.20. The reduction of the mean approach speed was predicted to be 8.2% for the H=0.032m, 13.6% for the H=0.048m, 19.9% for the H=0.064m, 25.9% for the H=0.080m, and 32.6% for the H=0.096m, compared to the calm water case. This is because the ship resistance was found proportional to the wave height, as described in Table 7.2 (b). It is worth noting that the ship resistance has a proportional relation with the added wave resistance being commonly proportional to the wave height squared. The oscillation amplitude for the forward speed and ship resistance was significantly increased as the wave heights grow.

As for the pitch and heave motions depicted in Figure 7.3 (c) and (d), it was revealed that the amplitude of the ship motions in waves varied significantly depending on the encountering wave height. The largest pitch motion was predicted at the bow quartering waves of H=0.096m with a mean amplitude of 3.37º, which is 2.5 times greater than that at the bow quartering waves of H=0.032m. This means the pitch excitation moment increases with the growth of the wave height. The heave motion also followed the same trend. The maximum heave motion was also observed at the bow quartering waves of H=0.096m with a mean value of 0.03m, which is 2 times larger than that at the bow quartering waves of H=0.032m. It should be noted that the ship experienced large amplitude ship motions combined with severe bow slamming under large wave height conditions, which could lead to hull damage. Throughout all the wave simulations, the pitch and heave motions showed a similar trend in the ship motion frequency since the same wave length condition (λ/L_{BP} =1.0) is applied to all the wave cases. In addition, the heave responses are non-dimensionalised by wave amplitude (H/2), whereas the pitch responses are non-dimensionalised by wave steepness (H/ λ) in Table 7.2. As seen in the table, Case 2 and Case 3 appeared to have relatively large non-dimensional motion amplitudes, compared to the rest of the cases. This can be explained by the fact that the encounter frequencies of Case 2 (f_e=0.947Hz) and Case 3 (f_e=0.934Hz) are close to the natural frequency of the heaving and pitching system ($f_n \approx 0.93$Hz), as observed in Chapter 5.

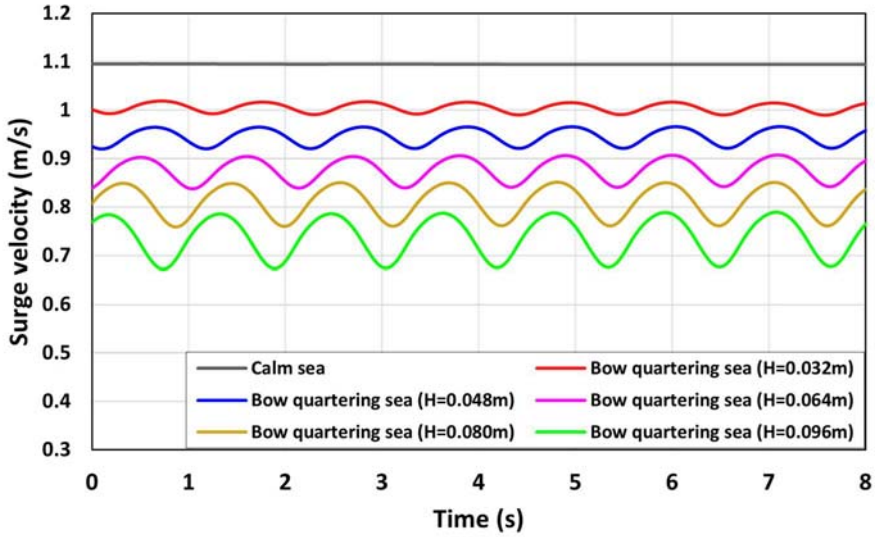

(a) Approach speed (U_0)

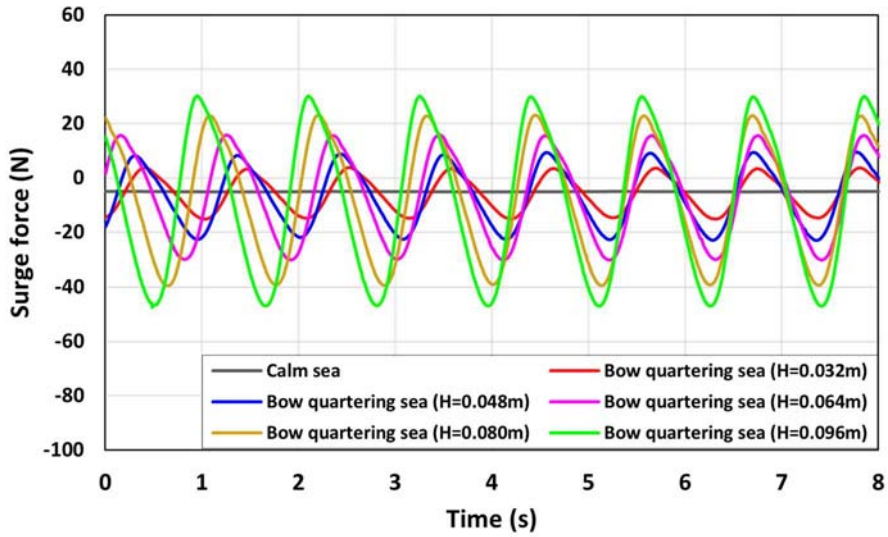

(b) Ship resistance (F_x)

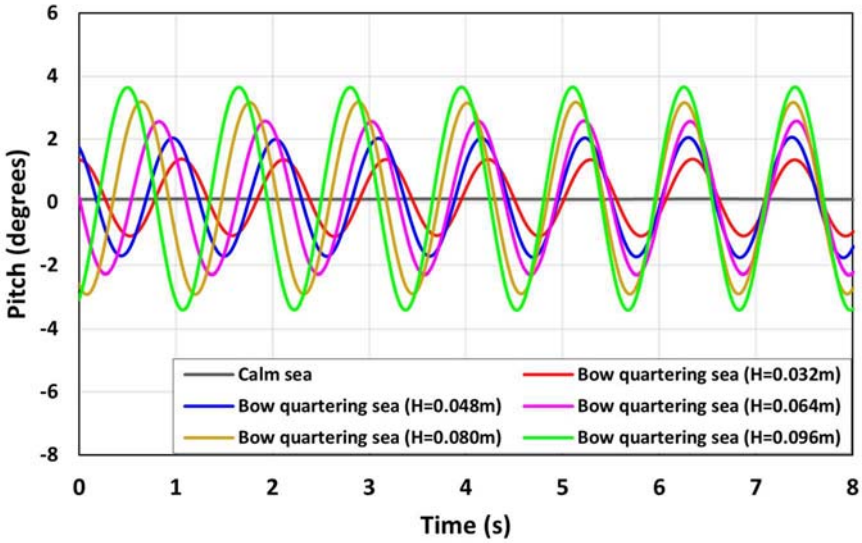

(c) Pitch displacement

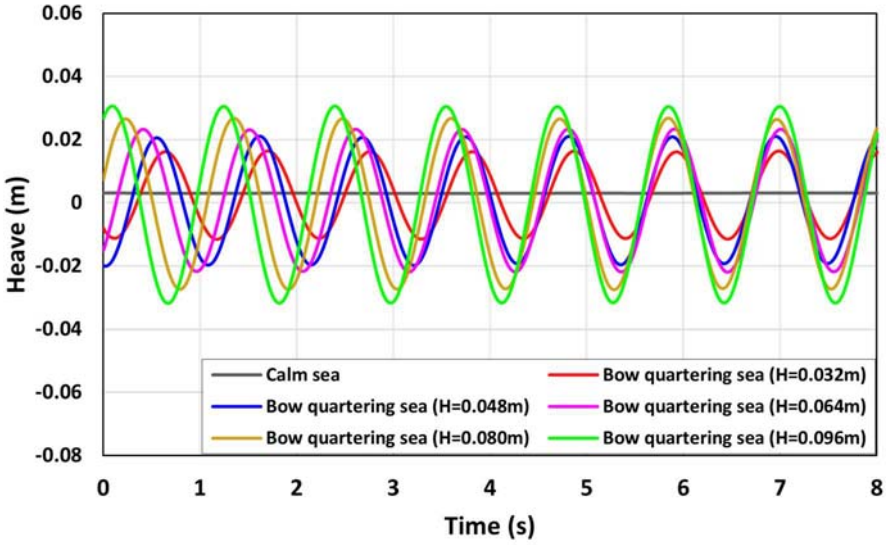

(d) Heave displacement

Figure 7.3 Time histories of the a) approach speed, b) ship resistance, c) pitch motion and d) heave motion for all the cases.

Table 7.2 Fourier series analysis of the approach speed, ship resistance, pitch motion and heave motion at self-propulsion conditions.

	Case 1 (Calm sea)	Case 2 (H=0.032m)	Case 3 (H=0.048m)	Case 4 (H=0.064m)	Case 5 (H=0.080m)	Case 6 (H=0.096m)
Approach speed U_0						
0th FS term (m/s)	1.094	1.004	0.945	0.876	0.811	0.737
Resistance F_x						
0th FS term (N)	5.136	5.740	6.723	6.601	7.707	8.931
1st FS term (N)	-	8.583	15.548	21.649	29.102	35.237
Pitch displacement						
0th FS term (degrees)	0.111	0.135	0.170	0.104	0.121	0.203
Non-dimensionalised 0th FS term	-	12.896	10.826	4.967	4.623	6.464
1st FS term (degrees)	-	1.227	1.876	2.402	3.007	3.367
Non-dimensionalised 1st FS term	-	117.212	119.473	114.728	114.900	107.213
Heave displacement						
0th FS term (m)	0.003	0.002	0.002	0.001	0.000	0.000
Non-dimensionalised 0th FS term	-	0.125	0.083	0.031	0.000	0.000
1st FS term (m)	-	0.014	0.019	0.022	0.026	0.030
Non-dimensionalised 1st FS term	-	0.875	0.792	0.687	0.650	0.625

7.4.2. Course keeping control

Figure **7.4** andFigure **7.5** present the time histories of the rudder deflection angle, ship's heading angle, and yaw velocity under the course keeping manoeuvres. As seen in Figure **7.4** (a) and Figure **7.5** (a), it was revealed that the course keeping manoeuvre in calm water is not an issue because there are no external disturbances. The ship's yaw angle and yaw velocity were kept to be almost 0º and 0º/s, respectively, while the rudder deflection was fixed at 2º. This small rudder deflection towards the port side resulted from a right-handed propeller effect, which caused the asymmetric pressure distribution acting on the rudder surface. The resultant uneven pressure distribution induced a small yaw moment to turn the ship's heading to the starboard. Thus, the rudder angle was slightly deflected to the opposite side to control the ship's heading. Figure **7.6**, as an example, displays the snapshots of the axial flow velocities around the rudder and the pressure distributions on the rudder under the course keeping manoeuvre (Case 1). When the ship was moving forward in calm water, a non-uniform flow generated by the actuator disk caused the pressure difference between the starboard and the port of the rudder blade. This led to a small rudder normal force, and thus caused the yaw moment to make the ship turn to the starboard to a small extent. It is worth noting that the actuator disk model accounts for the axial and tangential (swirl) velocities induced by the propeller and its effects on the flow.

It can be seen that the rudder deflection angle became larger in the oblique waves compared to the calm water case. This is because an asymmetric wave profile around the ship was generated when the ship is advancing forward in the oblique seas, which may cause a substantial lateral force and yaw moment and consequently induce yaw deviation. During the course keeping manoeuvres in waves, the behaviours of the rudder deflection and yaw angle were found to vary depending on the wave height conditions. Although similar maximum rudder angles were deflected in all bow quartering seas within a value of 7.5º as shown in Figure **7.4** (b) – (f), the starboard rudder deflection became relatively dominant as the wave height increased. It

resulted from the fact that a higher wave height induced a larger yaw moment to change the ship's heading to the port side under the starboard bow quartering waves. Likewise, the oscillation amplitude of the yaw velocities also increased with the growth of wave heights as seen in Figure **7.5** (b) – (f). The predicted ship trajectories under the course keeping manoeuvres are depicted in Figure **7.7**. The ship advancing in the calm water achieved good course-keeping control by showing a very small deviation from the original course. For wave cases, all the ship paths were clearly different from the trajectory predicted in the calm sea. The maximum deviation from the original course was noted in the highest wave (H = 0.096m) whereas the minimum deviation was observed in the lowest wave (H = 0.032m). It revealed that higher wave heights can lead to a large deviation from the planned route and thus cause relatively poor performance of the course keeping control. In addition, it was estimated that the high wave height conditions can cause the course of the ship to oscillate significantly during the manoeuvre. It should be noted that the optimum control gains for minimising the yaw deviation can further improve the steering capability.

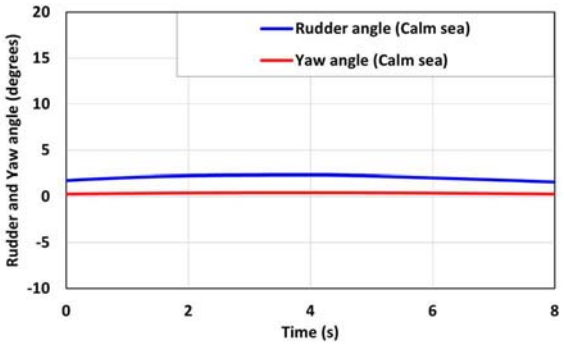

(a) Calm water

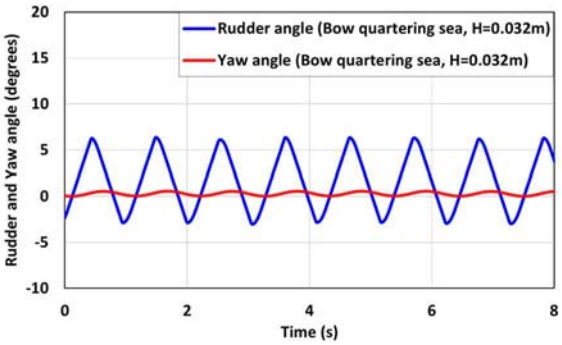

(b) Bow quartering wave (H = 0.032m)

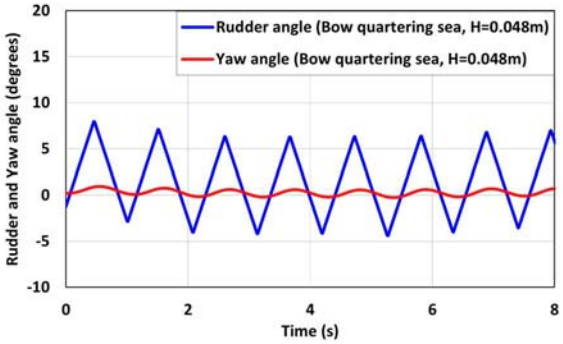

(c) Bow quartering wave (H = 0.048m)

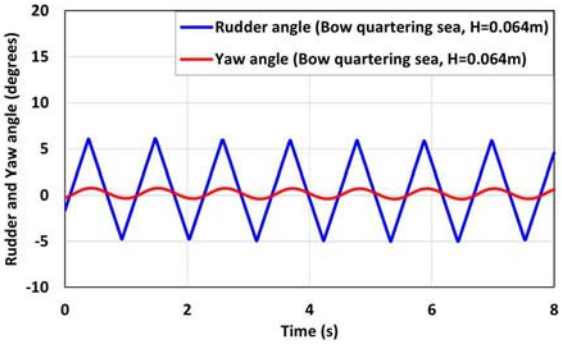

(d) Bow quartering wave (H = 0.064m)

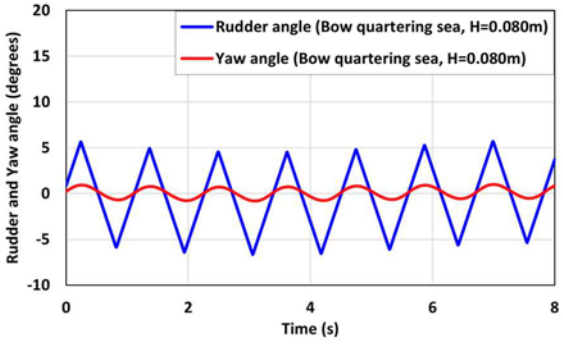

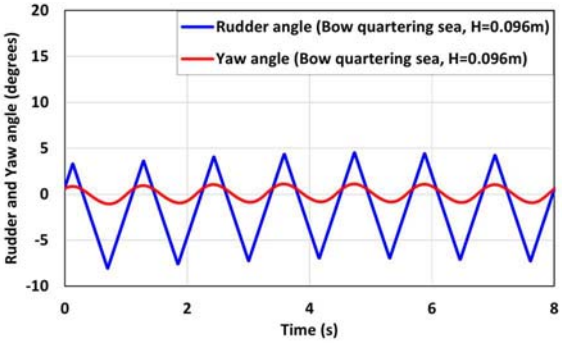

(e) Bow quartering wave (H = 0.080m) (f) Bow quartering wave (H = 0.096m)

Figure 7.4 Time histories of the rudder deflection and yaw angle at self-propulsion in (a) calm sea, (b) bow quartering sea (H = 0.032m), (c) bow quartering sea (H = 0.048m), (d) bow quartering sea (H = 0.064m), (e) bow quartering sea (H = 0.080m), and (f) bow quartering sea (H = 0.096m).

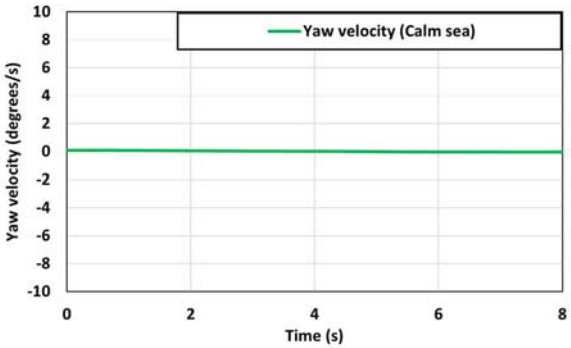

(a) Calm water

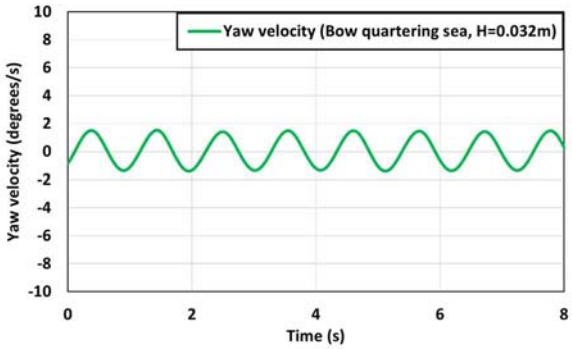

(b) Bow quartering wave (H = 0.032m)

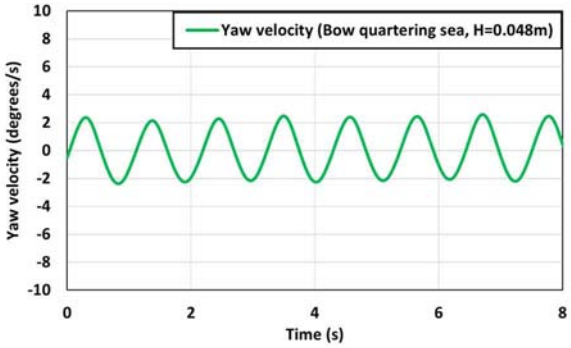

(c) Bow quartering wave (H = 0.048m)

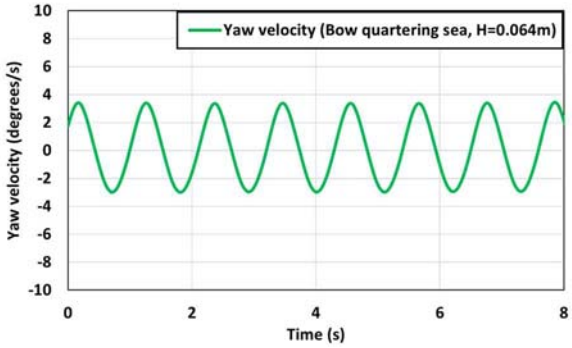

(d) Bow quartering wave (H = 0.064m)

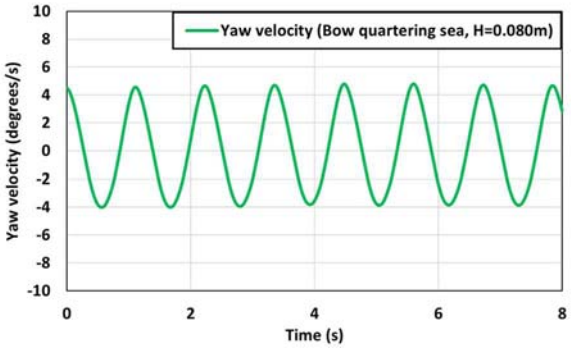

(e) Bow quartering wave (H = 0.080m)

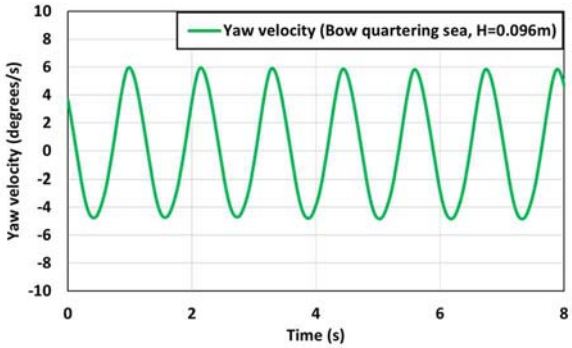

(f) Bow quartering wave (H = 0.096m)

Figure 7.5 Time histories of the yaw velocity at self-propulsion in (a) calm sea, (b) bow quartering sea (H = 0.032m), (c) bow quartering sea (H = 0.048m), (d) bow quartering sea (H = 0.064m), (e) bow quartering sea (H = 0.080m), and (f) bow quartering sea (H = 0.096m).

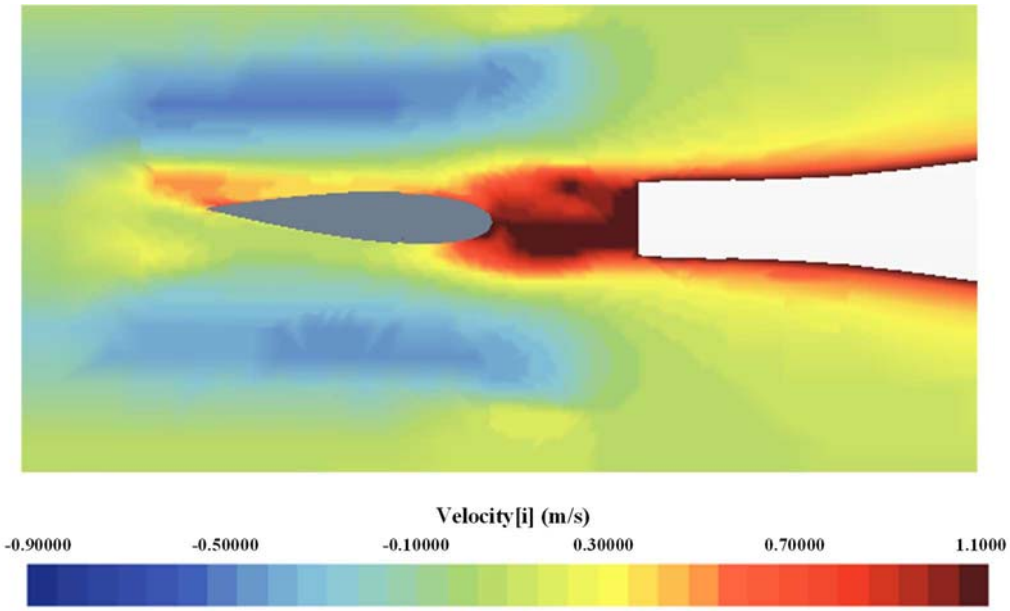

(a) Axial flow velocity around the rudder

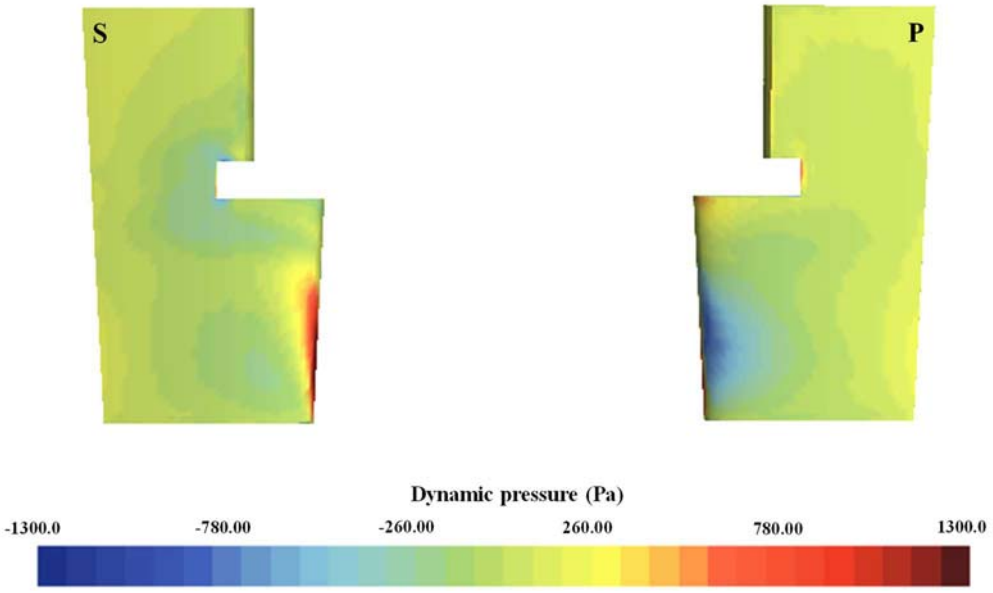

(b) Pressure distribution on the rudder blade, S: starboard profile, P: port profile

Figure 7.6 The snapshots of the axial flow velocities around the rudder and the pressure distributions on the rudder under the course keeping manoeuvre.

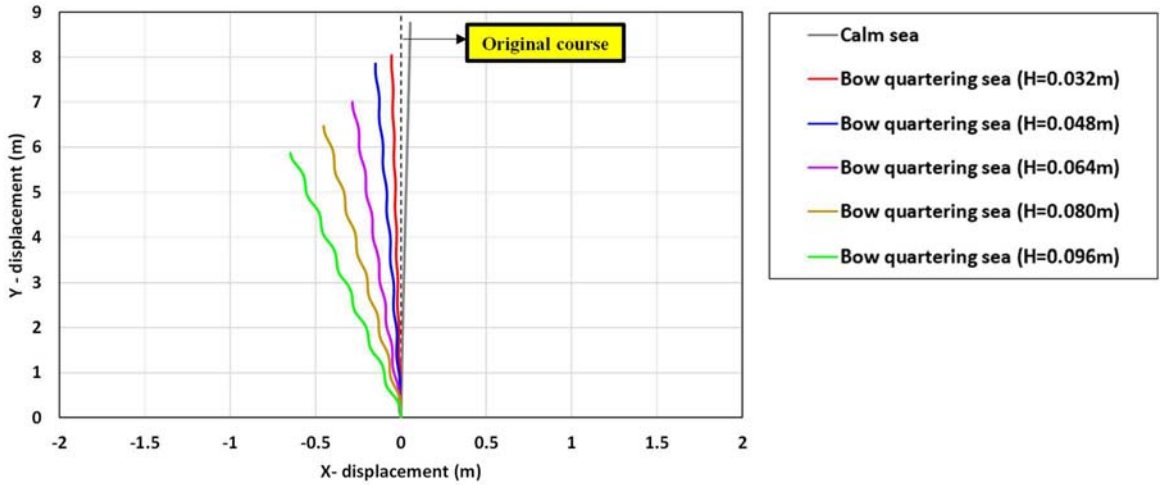

Figure 7.7 Comparison of the predicted trajectories for all the cases.

7.4.3. Turning circle manoeuvre

This sub-section will outline the simulation results of a standard turning manoeuvre. In turning circle manoeuvres, the ship was advancing forward at an approach speed and the rudder was deflected to a maximum 35-degree angle in the starboard direction. It should be noted that the rudder started to be executed during the moments when the wave trough passed on the midship. The ship started to react by turning to the starboard side and the manoeuvre was completed when the 360° turn is achieved.

7.4.3.1 Time histories during turning and turning indices

In Figure 7.8 all the obtained ship trajectories of the turning circle manoeuvre are displayed. In the figure, all the rudder execution points were shifted to the origin point (0,0) for the correct comparisons of the turning trajectories between each case. It was clearly demonstrated that higher wave heights can lead to larger changes in the turning trajectory when compared to the ship's inherent turning ability in calm water. In other words, the significant deformation of the turning circle path occurred under the higher wave height conditions, compared to the calm water case. It can be seen that the ship trajectories were drifted in the bow quartering waves as the ship was influenced by continuous wave drift forces during the manoeuvre (the drift directions were observed to be similar to the wave propagation direction).

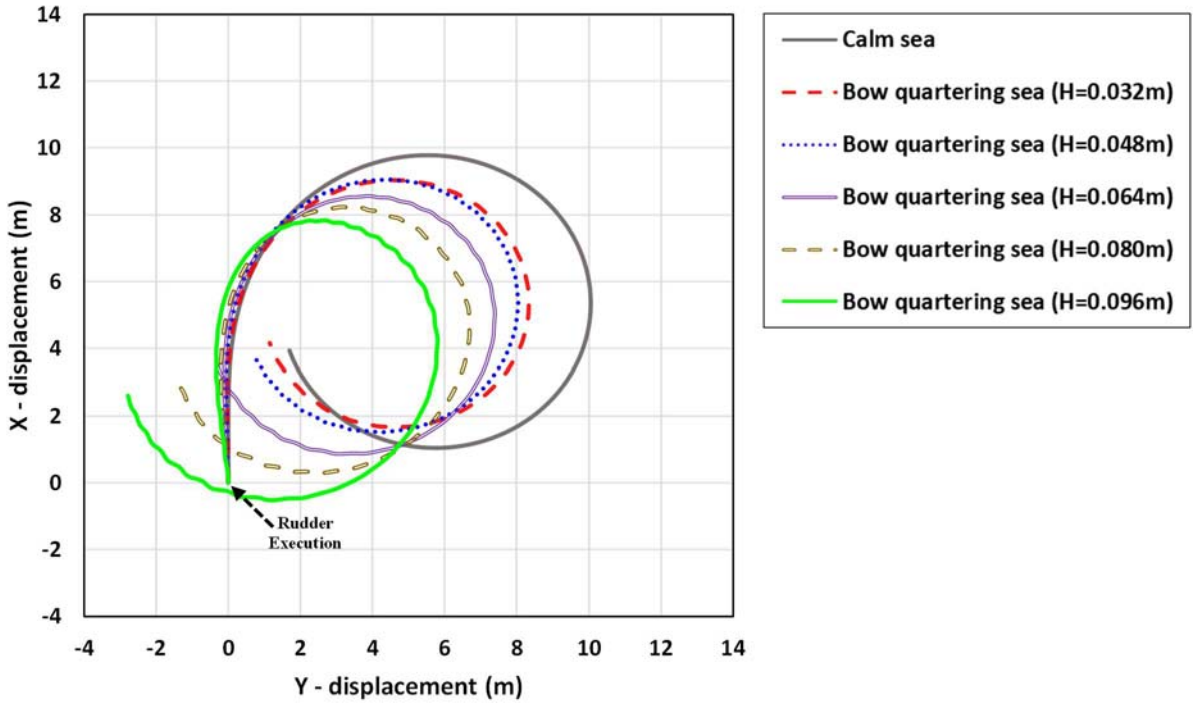

Figure 7.8 Comparison of the predicted turning circle trajectories.

To quantify the turning capability for all cases, the CFD results in terms of the critical turning indices are reported in Table **7.3**. In addition, Figure **7.9** shows the time histories of the predicted ship velocities, forces, and moments during the turning manoeuvre. Table **7.3** and Figure **7.9** jointly show, the maximum ship advance from the origin point was predicted to be $3.13L_{BP}$ in calm water (Case 1) since the approach speed was much larger than the wave cases. For the wave cases (Cases 2 - 6), the advance was found to mainly decrease with the increase in the wave height. This was due to the relatively smaller approach speed despite the longer 90° turning time as the wave height increased. The trend observed for the ship transfer was found similar to the ship advance. The transfer reached a maximum of $1.33L_{BP}$ under the calm water condition. For the wave conditions, the transfer showed a decreasing trend with the increase of the wave height. This was attributed to the relatively smaller forward and sway velocity in the initial phase of the turn and the longer time taken for 90° turn. The tactical diameters were also clearly identified to be dependent on the wave height. They followed the same trend as the advance and transfer of the case ship, exhibiting a decreasing tendency with the increase of the wave height.

Clearly different from the calm water case, the ship manoeuvring in waves experiences high-frequency fluctuations of the kinematic and dynamic quantities during the turning manoeuvre (Figure **7.9**), mainly due to the high-frequency wave-induced motions. Larger fluctuation amplitudes occur under the higher wave height conditions, closely associated with the trajectory oscillation experienced by the ship in waves, as seen in Figure 7.8.

Table 7.3 CFD results: turning indices in calm water and regular waves.

Parameters (CFD results)	Case 1	Case 2	Case 3	Case 4	Case 5	Case 6
Advance (m)	9.55 **$(3.13L_{BP})$**	8.79 **$(2.88L_{BP})$**	8.83 **$(2.89L_{BP})$**	8.35 **$(2.73L_{BP})$**	8.04 **$(2.63L_{BP})$**	7.70 **$(2.52L_{BP})$**
Transfer (m)	4.07 **$(1.33L_{BP})$**	3.24 **$(1.05L_{BP})$**	3.09 **$(1.01L_{BP})$**	2.68 **$(0.88L_{BP})$**	2.24 **$(0.73L_{BP})$**	1.17 **$(0.38L_{BP})$**
Time for yaw 90 degrees (s)	12.31	12.18	13.08	13.44	14.18	15.10
Tactical diameter (m)	9.82 **$(3.21L_{BP})$**	8.09 **$(2.65L_{BP})$**	7.82 **$(2.56L_{BP})$**	7.17 **$(2.35L_{BP})$**	6.54 **$(2.14L_{BP})$**	5.63 **$(1.84L_{BP})$**
Time for yaw 180 degrees (s)	24.20	23.19	24.38	24.93	26.26	27.31

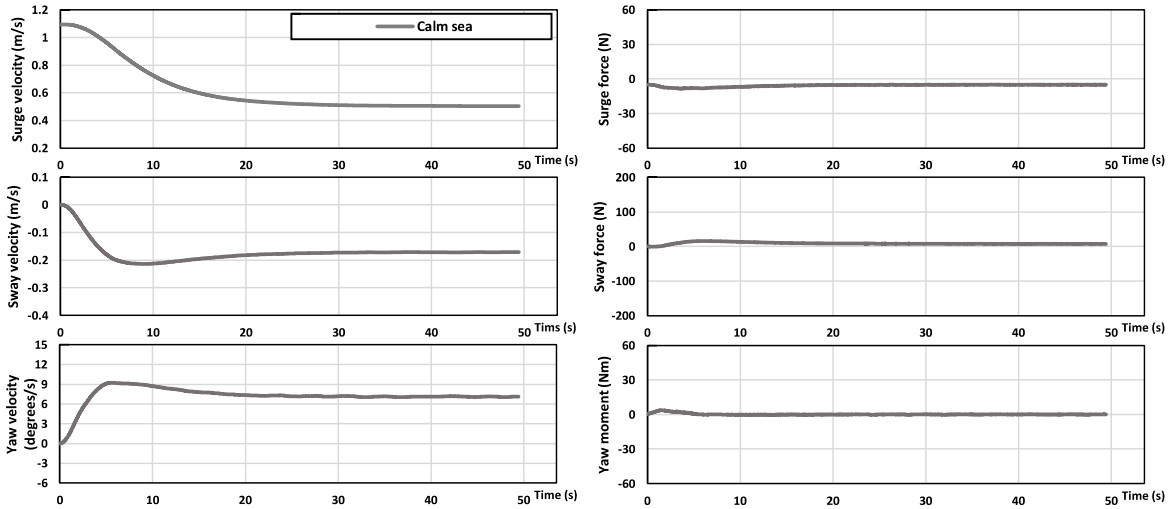

(a) Calm water

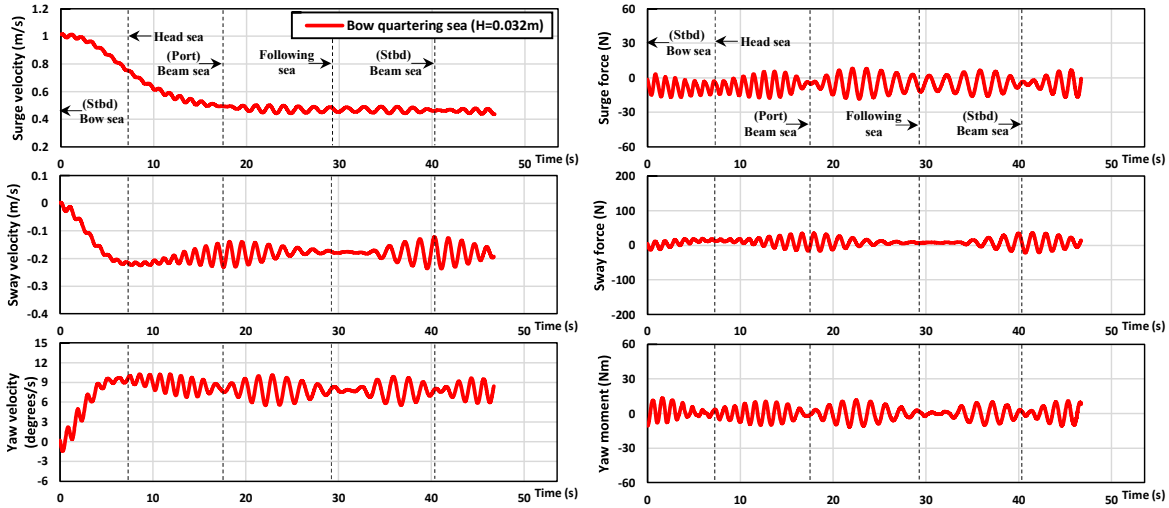

(b) Bow quartering wave (H = 0.032m)

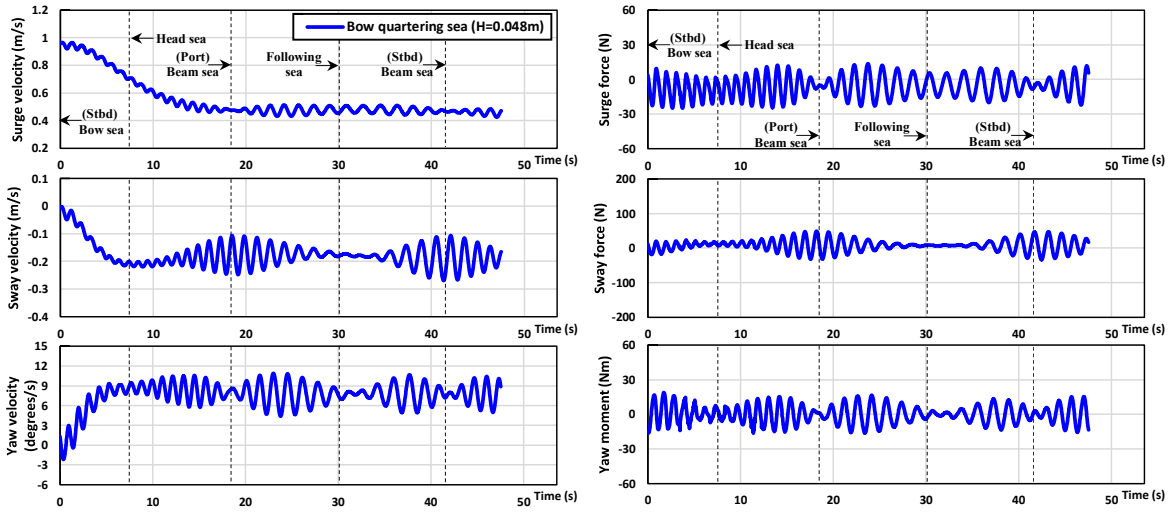

(c) Bow quartering wave (H = 0.048m)

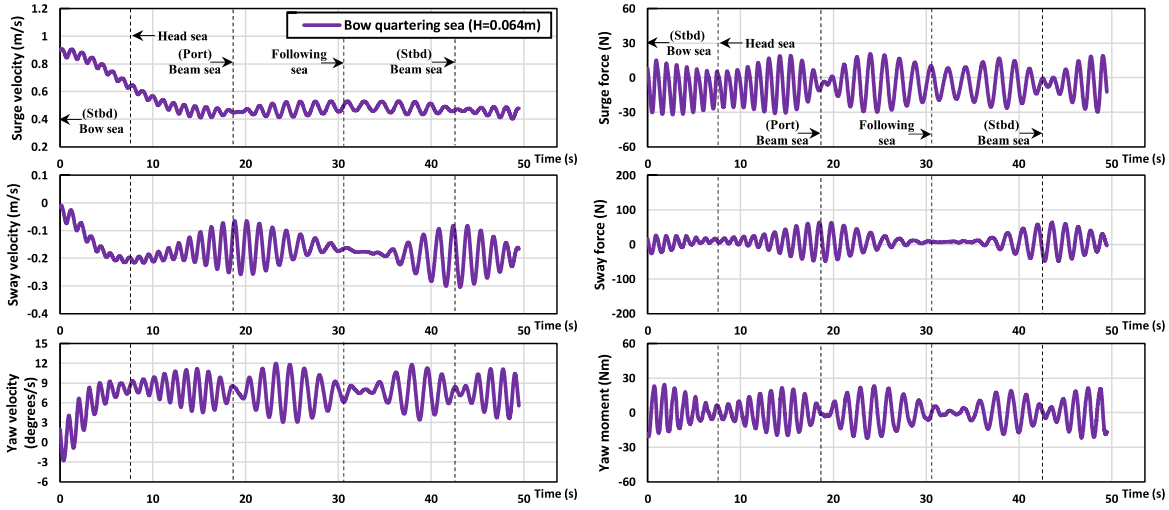

(d) Bow quartering wave (H = 0.064m)

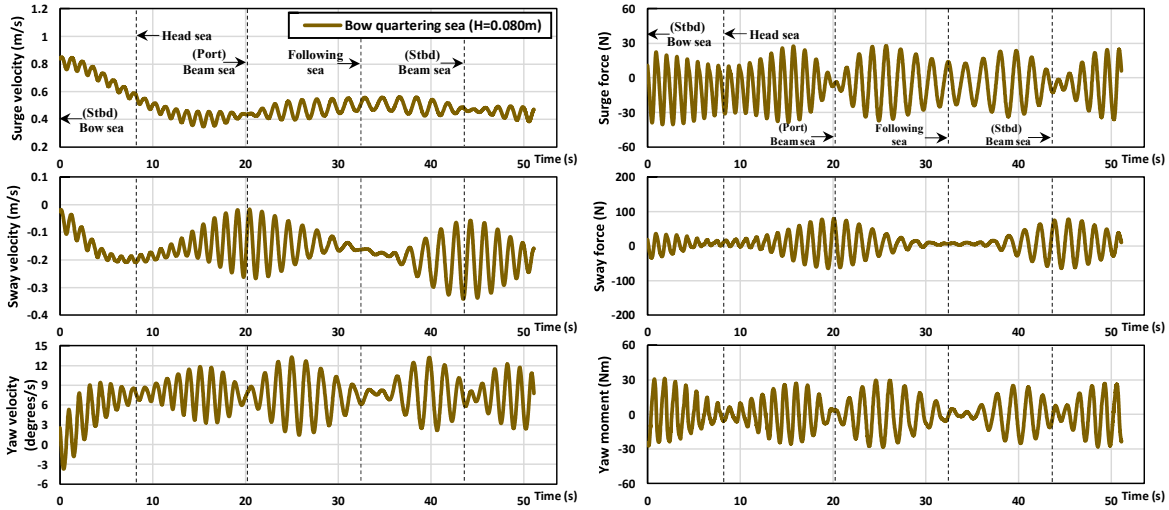

(e) Bow quartering wave (H = 0.080m)

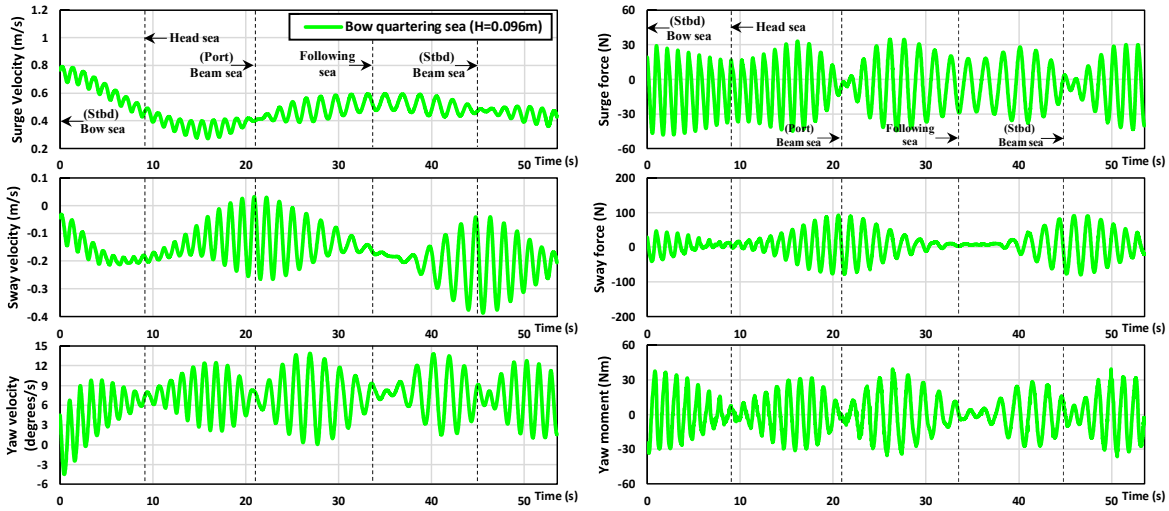

(f) Bow quartering wave (H = 0.096m)

Figure 7.9 Time histories of the ship velocities, forces, and moment during a turning manoeuvre in waves.

7.4.3.2 Wave-induced motions during turning manoeuvre

Figure 7.10 presents the time histories of ship motions, i.e., heave and pitch, as well as pitch moment and heave force. The oscillation amplitudes of the ship motions were found to change continuously during the ship's turning manoeuvre due to the instantaneous variations in the wave-encounter directions. For example, the ship advancing in the bow quartering seas (Case 2 - 6) experiences the starboard bow quartering wave (0° turn), the head wave (45° turn), the port beam wave (135° turn), the following wave (225° turn), the starboard beam wave (315° turn), and the starboard bow quartering wave (360° turn) in series after the start of the starboard turning manoeuvre. In addition, the wave-encounter frequencies were also observed to continue to change due to the variations in the ship's velocity and the wave-encounter direction during the ship's turning, which consequently affects the ship motion frequencies in waves.

As expected, it was found that the excitation force and moments increased with an increase in the wave height and thus the amplitude of the pitch and heave appeared to be larger in the higher wave heights. During the ship's turning, the pitch oscillations reached the maximum when the ship experienced the bow quartering waves whereas the minimum pitch motions were predicted under the starboard or port beam waves. As stated previously, the pitch motions tend to have relatively large amplitudes when the encountering frequency is close to the natural frequency of the pitching system.

Contrary to the pitch motion, the maximum heave amplitudes were observed when encountering the starboard or port beam waves while the ship was turning. This was also closely associated with the ratio of wave length to ship length. As the ship started tuning in waves, the wave length became relatively longer than the ship length. When the ship encountered the beam waves (135° turn or 315° turn), the ship breadth can be regarded as the relevant length which is relatively smaller than the wave length. It may lead to the maximum

heave amplitude which is almost equal to the wave height. The minimum heave motions were predicted when the ship encountered the following waves.

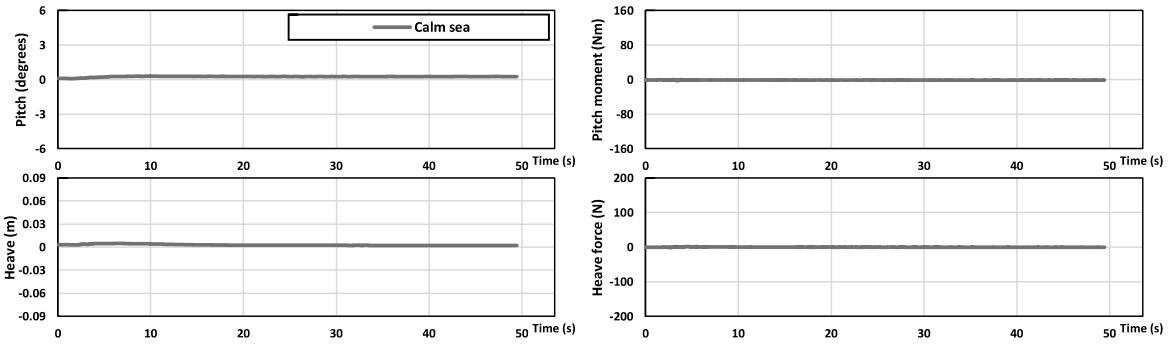

(a) Calm water

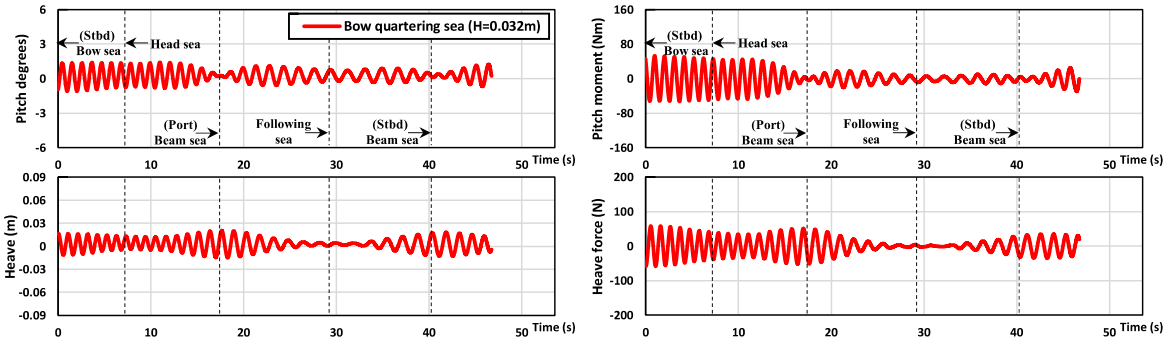

(b) Bow quartering wave (H = 0.032m)

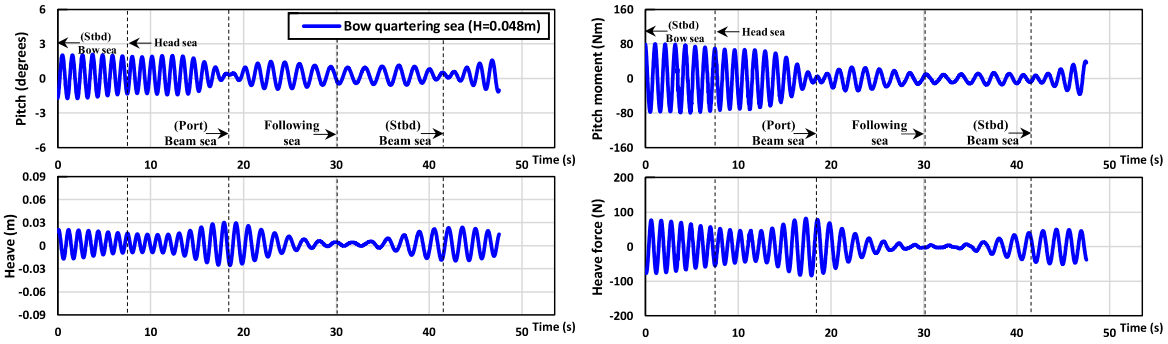

(c) Bow quartering wave (H = 0.048m)

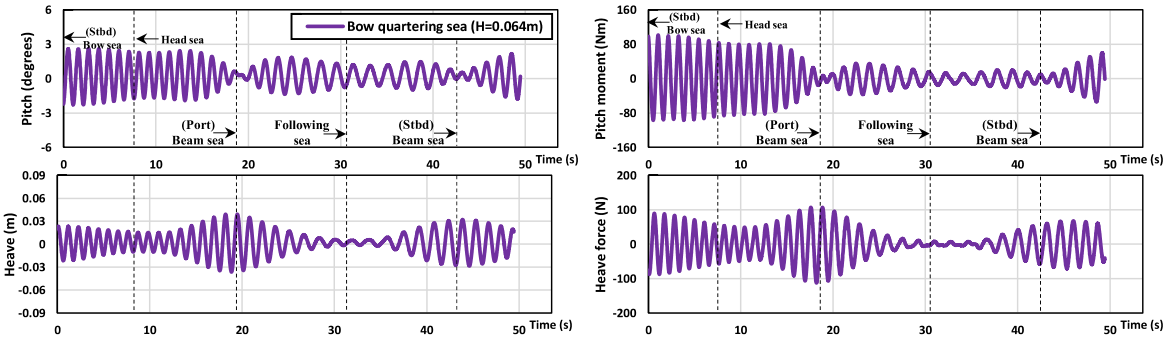

(d) Bow quartering wave (H = 0.064m)

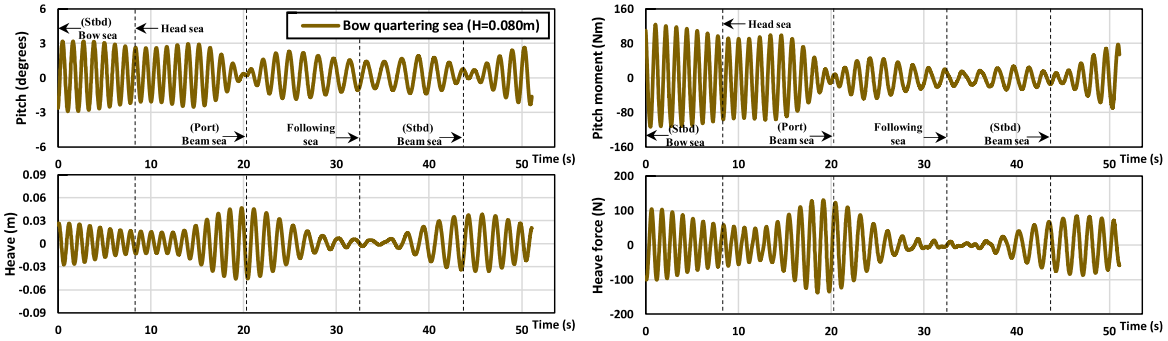

(e) Bow quartering wave (H = 0.080m)

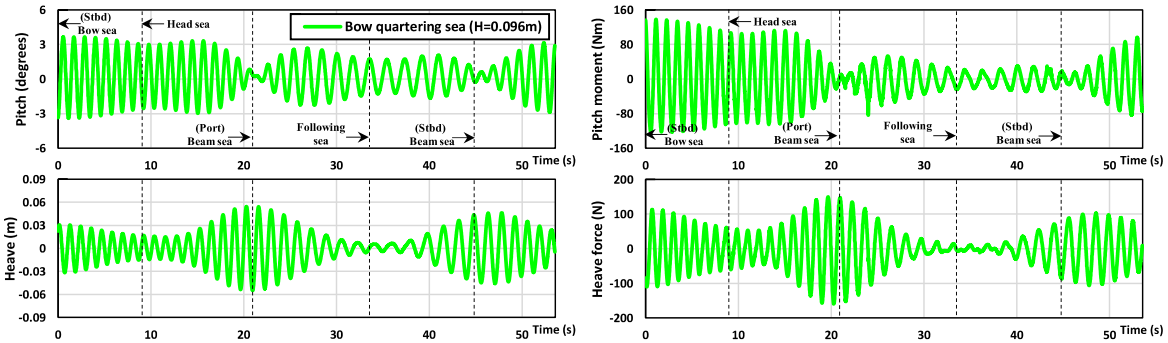

(f) Bow quartering wave (H = 0.096m)

Figure 7.10 Time histories of pitch, heave, pitch moment, and heave force during a turning manoeuvre.

7.5. Concluding Remarks

This chapter has filled the research gap on the manoeuvring performance of the KCS in different wave heights. With the analysis of the correlations between the ship manoeuvrability and the wave height, the findings of this study are helpful in identifying the effects of the wave height on the manoeuvring behaviour of the ship in a real sea state. As computational facilities become more powerful and more accessible, this free running CFD method will be an accurate and efficient way to predict the ship's manoeuvrability in waves. The key findings of this study can be summarised as follows:

1) It was identified that the self-propulsion conditions showed significant variation

depending on the wave height. The averaged approach speed was found to decrease with the increase of the wave height at a given wave height range ($0.032m \leq H \leq 0.096m$), corresponding to 2.4m to 7.2m in full scale. Compared to the calm water case, the maximum reduction of the approach speed was predicted 32.6% for H=0.096m whereas the minimum reduction was observed to be 8.2% for H=0.032m under the same propeller revolution. Since the pitch excitation moment increased with the increase of the wave height, the largest pitch motion was predicted for the highest wave. The heave motion also followed the same trend.

2) For the course keeping manoeuvres, the behaviours of the rudder deflection and yaw angle were strongly affected by the wave height. Although similar maximum rudder angles were observed to be within a value of 7.5° in all bow quartering waves, the starboard rudder deflection became relatively dominant as the wave height increases. It is associated with the fact that a higher wave height causes a larger yaw moment to change the ship's yaw angle to the port side under the starboard bow quartering waves. In addition, higher wave heights resulted in a large deviation from the original course and thus caused poor performance of the course keeping control.

3) For the standard turning circle manoeuvres, the critical turning indices were found to be directly correlated to the ship velocities in the horizontal plane (surge, sway, and velocities) which differed significantly depending on the wave height. For the wave cases, the ship advance was predicted to mainly decrease with the increase in the wave height. This resulted from the relatively smaller approach speed despite the longer 90° turning time as the wave height increased. It should be noted that the lower wave height caused a larger yaw moment to turn the ship to the starboard side as the ship started turning in bow quartering waves, which has an influence on the time to turn by 90° and 180°. The ship transfer and tactical diameter also followed the same trend as the advance. Compared to the calm water case, the turning circle trajectories were identified to be significantly deformed under the higher wave height conditions. The wave forces and moments caused the drift of the ship trajectories, and the drift directions were found to be similar to the wave propagation direction. For the seakeeping behaviour during the ship's turning, the maximum amplitude of the pitch was observed when the ship experienced the bow quartering waves whereas the minimum pitch motions were predicted under the starboard or port beam waves. Contrary to the pitch motion, the heave oscillations reached maximum when encountering the starboard or port beam waves. The minimum heave motions were observed when the ship experienced the following waves.

8. FREE-RUNNING CFD SIMULATIONS FOR A SHIP WITH PROPULSION SYSTEM FAILURE IN REGULAR WAVES

8.1. Introduction

With a growing reliance on shipping activities, the ever-increasing maritime traffic has posed a considerable threat to navigational safety at sea. According to a marine accident investigation (EMSA, 2020), the most frequent cause of accidents over 2014-2019 was reported to be "Loss of control – Loss of propulsion power" which accounted for 22% of all casualty events reported, as shown in Figure 8.1. This type of incident was also examined to be mainly related to commercial cargo ships. The loss of ship propulsion is one of the most hazardous events observed in marine transportation since it has a strong adverse effect on a ship's manoeuvrability in real sea states. Such poor ship manoeuvrability in areas of high-density traffic or narrow waterways could lead to further serious navigation casualties associated with collision, contact, and grounding incidents. Considering these potential dangers, predicting the manoeuvring performance of a vessel in case of any propulsion loss is critical for proper decision-making about ship handling to ensure navigation safety at sea. It is worth noting that the Port State Control (PSC) has categorised the propulsion failure into the critical deficiency items which are not in compliance with inspection standards and thus cause the detention of the ship (IMO, 2020). In practice, the Port State Control Officers (PSCOs) carry out the inspection of foreign ships by the port governing states to verify the condition of the vessel, ensure the equipment onboard complies with the requirements of international conventions and that the vessel is manned and operated in accordance with international law.

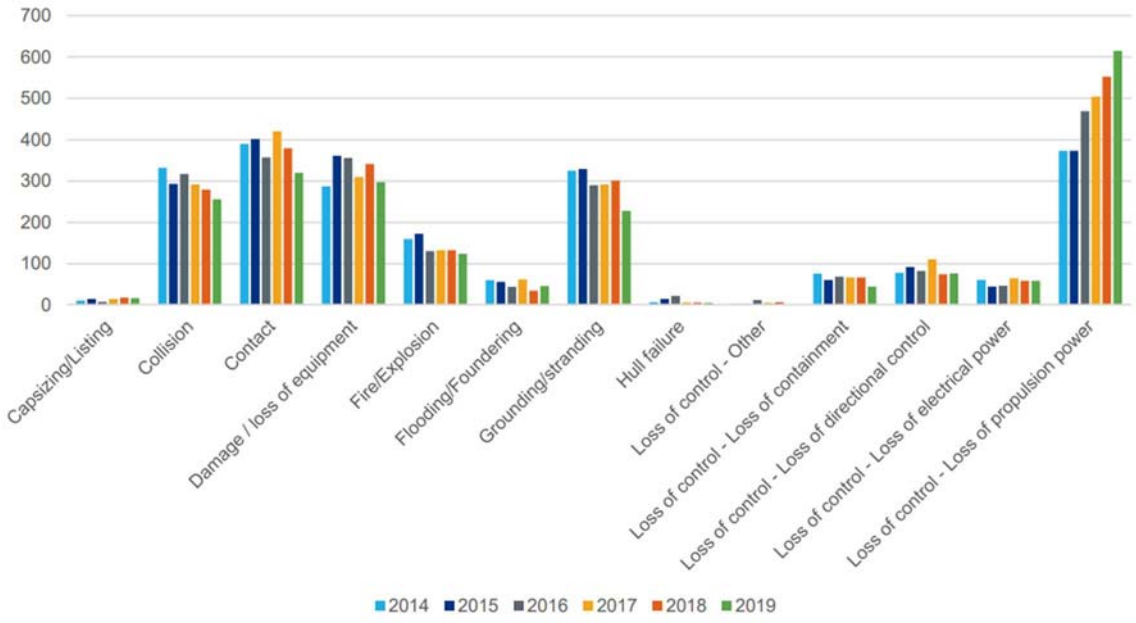

Figure 8.1 Distribution of casualty events with a ship over the period 2014-2019, adapted from EMSA (2020).

The manoeuvring behaviour of a ship is highly dependent on the propulsion power (Hasnan et al., 2019). A study by Yasukawa and Yoshimura (2015) identified the rudder inflow velocity induced by a rotating propeller as a key parameter to determine the rudder normal force which directly affects the steering capability. The greater inflow velocity leads to the larger rudder normal force which then guarantees good manoeuvrability. Hence, the failure of the propulsion system is expected to adversely influence a ship's manoeuvring performance by decreasing the inflow velocity to the rudder, and consequently the sufficient rudder force cannot be achieved. All commercial vessels are likely to experience the propulsion loss incident which commonly results from the main engine failure. Considering this, navigation officers who are responsible for ship handling and navigation should be fully acquainted with the ship's manoeuvrability in the propulsion failure condition to ensure navigation safety at sea. These points underlie the main argument of this study, that the investigation into the relationship between the propulsion failure and the manoeuvring performance of commercial ships in real sea states is necessary.

As reviewed in Chapter 3, the numerous academic studies described above only addressed the ship's manoeuvrability in normal operating conditions in which all machinery related to the navigation system are working properly. It is an undeniable fact that the past studies have the advantage of being informative in confirming the manoeuvring performance of ships in normal conditions. However, they were not able to offer insight into the understanding of the ship's manoeuvrability under the propulsion failure event in which a rotating propeller should be suddenly in a non-rotating state during manoeuvring. Given the importance of this issue and the lack of previous studies, this chapter was motivated to investigate the manoeuvring performance of the well-known benchmarking KCS in the propulsion system failure. This chapter aims to provide a better understanding of a ship's manoeuvrability experiencing a failed propulsion system in real sea conditions.

The simulation cases examined in this chapter are detailed in the following section. Section 8.3 presents the specific numerical scheme of the current CFD model. Then, the results obtained from this study are provided and discussed in Section 8.4. Finally, in Section 8.5, the concluding remarks of this chapter are listed.

8.2. Goal and Scope

The main goal of this chapter is to evaluate the effects of a propulsion failure on the manoeuvrability of the KRISO Container Ship (KCS) in waves using a fully nonlinear URANS model, with particular emphasis on the course keeping and turning capabilities of the ship.

The self-propulsion computations should be initially conducted before the selected free-running manoeuvres in the propulsion failure condition. As shown in Table 8.1, the self-propulsion simulations were performed in six environmental conditions which cover the whole range of important wave directions: *1) calm water*, *2) head wave*, *3) bow wave*, *4) beam wave*, *5) quartering wave*, and *6) following wave*. Throughout all the wave cases (Cases 2 – 6), a wave with height H=0.048m and period T=1.4s in the model scale was applied, which correspond to a wave height of 3.61m and period of 12.14s in full scale. The wavelength equals to the ship length ($\lambda/L_{BP} = 1.0$) and wave steepness (H/λ) is 0.016. The encounter frequency of the wave, ω_e, was calculated by means of $\omega_e = \omega[1 - (\omega U cos\mu)/g]$, where ω indicates

the wave frequency, U indicates the ship surge speed, μ means the ship's heading angle relative to the wave direction, and g is the gravitational acceleration. All the self-propulsion simulations adopted the propeller revolution rate (RPS) of 13.38 n/sec (n is the rotational speed of the propeller), which is the same propeller speed as that applied for the manoeuvring research of the KCS (the same scale factor of 75.24) in Chapter 5. Figure 8.2 shows the schematic illustration for the simulation cases applied to this study, which includes the course keeping and turning circle manoeuvres either in calm water or in the presence of regular waves. After the self-propulsion conditions were achieved, the rotational speed of the actuator disk was compelled to decrease suddenly from 13.38 n/sec to 0 n/sec according to the propeller speed controller. Successively, the course keeping (Figure 8.2 (a)) and standard turning manoeuvres (Figure 8.2 (b)) without propulsion power were carried out from the stable state of self-propulsion condition, respectively. Manoeuvrability restrictions as the consequence of propulsion loss can be identified by comparing the findings from this study with the manoeuvring results in normal operating conditions from Chapter 5.

Table 8.1 The self-propulsion simulation cases to which the CFD model is applied prior to the course keeping and turning circle manoeuvres in the propulsion failure.

Case	Surge speed U_0 (m/s)	Propeller rev. (RPS)	Wave height H (m)	Encounter Angle μ (degrees)	Encounter Period T_e (s)	Froude Number Fr	Reynolds Number Re
1	1.094	13.38	Calm water	- (Calm sea)	-	0.200	2.63×10^6
2	0.86	13.38	0.048	180 (Head sea)	1.004	0.157	2.07×10^6
3	0.95	13.38	0.048	225 (Bow sea)	1.071	0.173	2.29×10^6
4	1.07	13.38	0.048	270 (Beam sea)	1.399	0.195	2.58×10^6
5	1.03	13.38	0.048	315 (Quartering sea)	2.103	0.188	2.48×10^6
6	1.05	13.38	0.048	0 (Following sea)	2.694	0.192	2.53×10^6

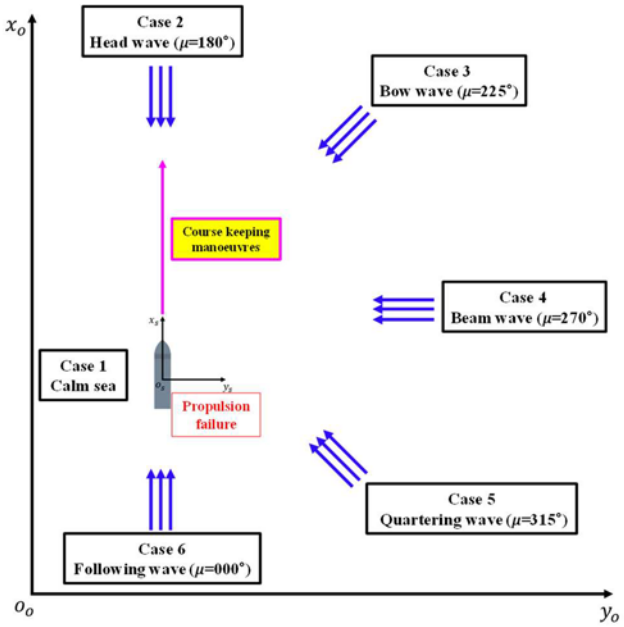

(a) Course-keeping manoeuvres

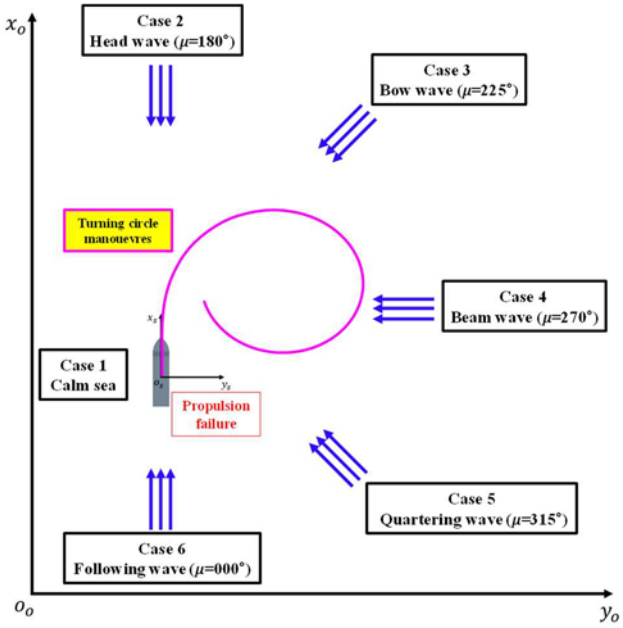

(b) Turning circle manoeuvres

Figure 8.2 Schematic views of the simulation cases applied to this study, (a) course-keeping (b) turning circle manoeuvres.

8.3. Numerical Modelling

The numerical modelling and computational schemes for the current CFD simulations are very similar to those used in the studies presented in Chapter 5. It has to be highlighted that the resulting mesh and the time-step resolution adopted in this chapter are the same as those of Chapter 5.

As stated previously, two different types of free-running manoeuvres were performed to evaluate the effect of the propulsion loss on the ship's manoeuvrability in this chapter: *course keeping control* and *turning circle manoeuvre*. Prior to the start of the free-running manoeuvres under the propulsion failure condition, the self-propulsion computation was first carried out for the propeller revolution of 13.38 RPS with the ship free to move in full 6DOF motion. After the target surge speed was reached, the revolution speed of the actuator disk was compelled to change suddenly according to the propeller control module. This was introduced to represent the failure condition of the ship propulsion system, which is presented by the following expression:

$$n(t) = \begin{cases} n_s \ (t < t_f) \\ 0 \ (t \geq t_f) \end{cases} \tag{8.1}$$

where n(t) is the revolution rate of the actuator disk (RPS) at a given time, n_s is the revolution rate at the self-propulsion point (13.38 RPS in this work), and t_f indicates the time when the propulsion failure started.

8.4. Results

The free-running manoeuvres proposed in this particular study were applied to the KCS model

to estimate the effects of the propulsion loss on the manoeuvring behaviour. The comparison of the results from this study to those with the normal operating condition in Chapter 5 was made with a view to identifying the changes in the ship's manoeuvrability under the failure of the propulsion system. For each manoeuvring simulation, 13440 CPU hours with 40 CPU processors were needed, completed in approximately 336 wall clock hours.

8.4.1. Course keeping control

This sub-section will present the manoeuvring performance of the KCS experiencing the propulsion failure during the course-keeping in both calm water and waves.

As stated previously, the self-propulsion conditions in calm water and waves were initially achieved to reach the target surge speed before the course-keeping control. Figure **8.3** presents the time histories of the ship speed, ship motions, and various hydrodynamic quantities during the course-keeping control for all cases. From the graphs given in the figure, the values on the dotted lines mean the normal operating condition where the ship was moving forward with the propeller rotational speed of 13.38 RPS ($0 < t < 10$). The values on the solid lines indicate the propulsion loss condition in which the propeller speed was set at zero in order to represent the failure of the ship propulsion system ($10 \leq t$).

As for the surge velocity, it was found to vary depending on the wave propagation direction under the same propeller revolution ($0 < t < 10$). This is because the different pressure distribution around the ship hull was caused according to the wave direction, which led to differences in the added resistance in the sailing direction. The surge speed started to decrease after the ship lost its propulsion power ($10 \leq t$) as expected, while the ship resistance also followed the same trend. The speed loss rate between the initial surge speed and the minimum value was predicted at 63% for the calm sea, 79% for the head sea, 70% for the bow sea, 63% for the beam sea, 61% for the quartering sea, and 69% for the following sea within the same period ($10 \leq t \leq 56$). The ship experienced a large reduction in the surge velocity when sailing forward in the head and bow waves, which implies that the waves coming from the ship's bow caused a greater resistance than the other wave headings.

The propulsion failure was also observed to have a great influence on the ship motions under course keeping control. For the heave and pitch motions, the wave-encounter frequency was identified as the key factor leading to significant changes in such motions. The time histories of the encounter frequencies during the course-keeping in waves are displayed in Figure 8.4, where the natural frequencies of the pitching, heaving and rolling system are also indicated. It can be seen from the figure that after the propulsion failure, the ship experienced substantial changes in the encounter frequency of the wave except for Case 4 (the beam wave). Such changes resulted from continual changes in the surge speed as well as the heading angle (i.e., the ship's heading angle relative to the wave direction). It is worth noting that the maximum heave and pitch motions occur when the encounter frequency (f_e) equals, or is close to, the natural frequency of the heaving and pitching motions (f_n). For the KCS model, the natural frequencies of the heaving and pitching system are close to $f_n \approx 0.93$ Hz in which the maximum excitation force is expected to occur, as shown in Chapter 5. The greater the difference between the encounter frequency (f_e) and the natural frequency (f_n), the smaller the excitation force can be, causing the decrease in the amplitude of the heave and pitch motions.

In this study, Case 2 (the head wave) and Case 3 (the bow wave) in the normal condition have frequencies of encounter of 0.995 Hz and 0.933Hz, respectively, both very close to the natural heave and pitch frequencies. When the ship was moving forward in the head or bow waves under the propulsion loss condition, the wave-encounter frequency decreased with the decrease in the surge speed. The decrease of the wave encountering frequency led to an increase in the difference between the encounter frequency and the natural frequency, causing a decrease in the excitation force. Consequently, this caused the heaving and pitching amplitude to decrease, as shown in Figure 8.3 (b) – (c). When the ship was sailing in the quartering and following waves (Figure 8.3 (e) – (f)), on the other hand, it was predicted that the amplitude of the heave and pitch motions slightly increased with the decrease in the surge speed. This is due to the fact that the encounter frequency in such wave conditions becomes slightly close to the natural frequency of the heave and pitch motions as the surge speed decreased. Interestingly, the heave and pitch responses in the beam wave case were almost kept constant since the wave coming from the beam did not change the wave-encounter frequency even though the surge speed of the ship decreased. The heave and pitch motions in calm water (Figure 8.3 (a)) were found to be negligible both under the normal condition and the propulsion failure condition due to the absence of external loads. As for the roll motion, the large amplitude of the roll angle was predicted in the quartering wave condition (Case 5) during the course-keeping compared to the other cases. The possible reason for this could be that the rudder deflection angle became comparatively large in the quartering seas right after the propulsion failure, which may lead to the significant rudder normal force and thus cause the relatively large roll moment.

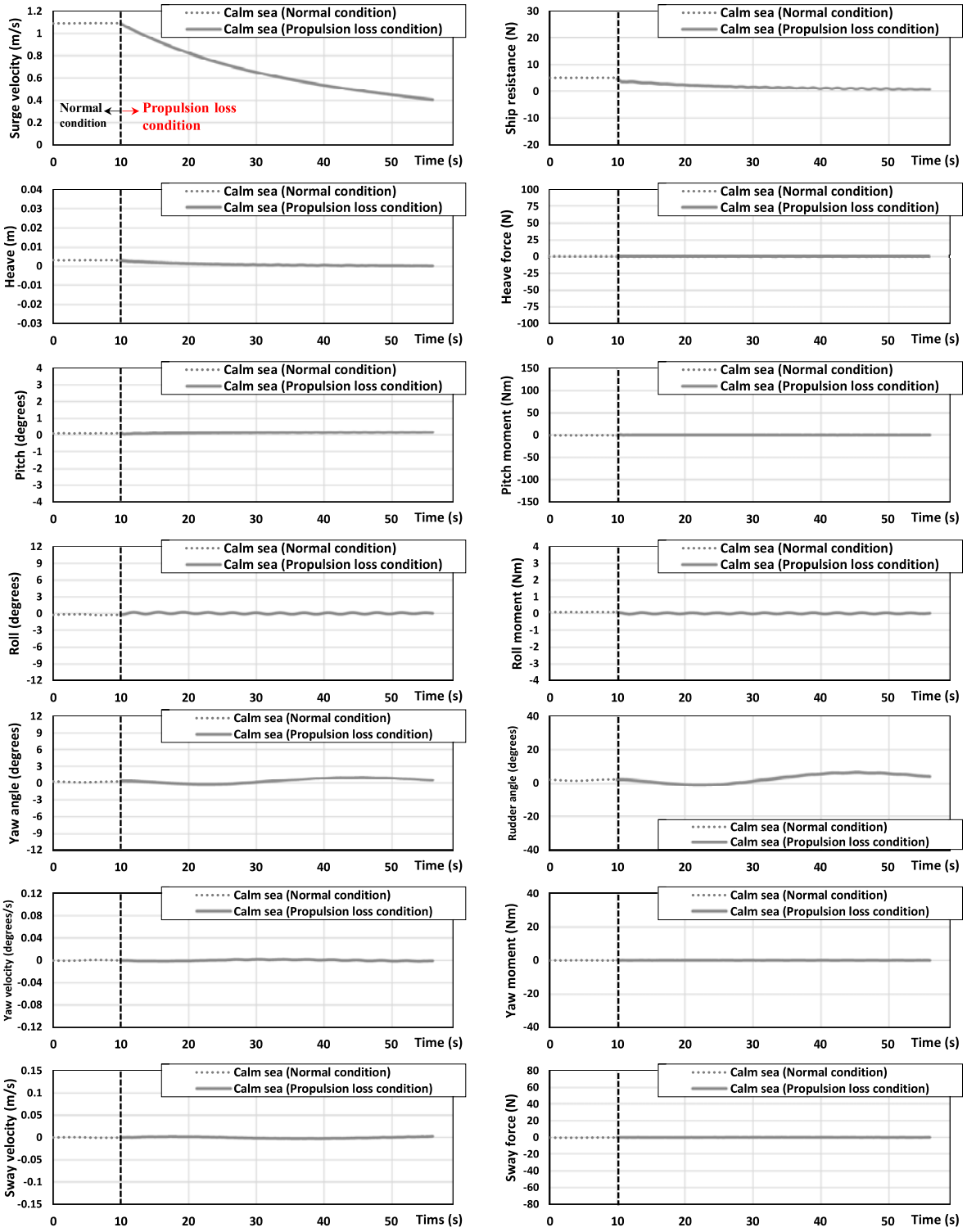

(a) Calm sea (Case 1)

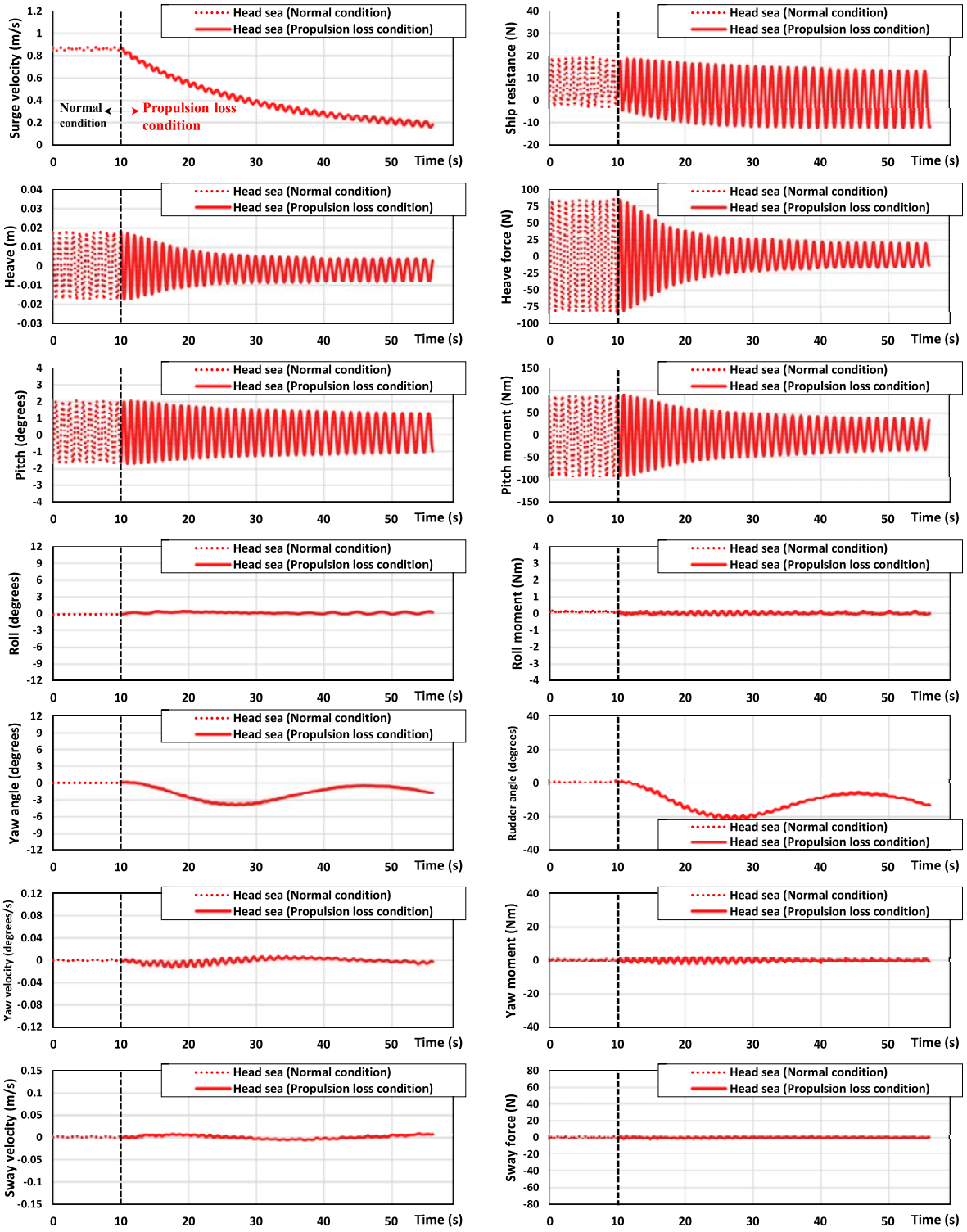

(b) Head sea (Case 2)

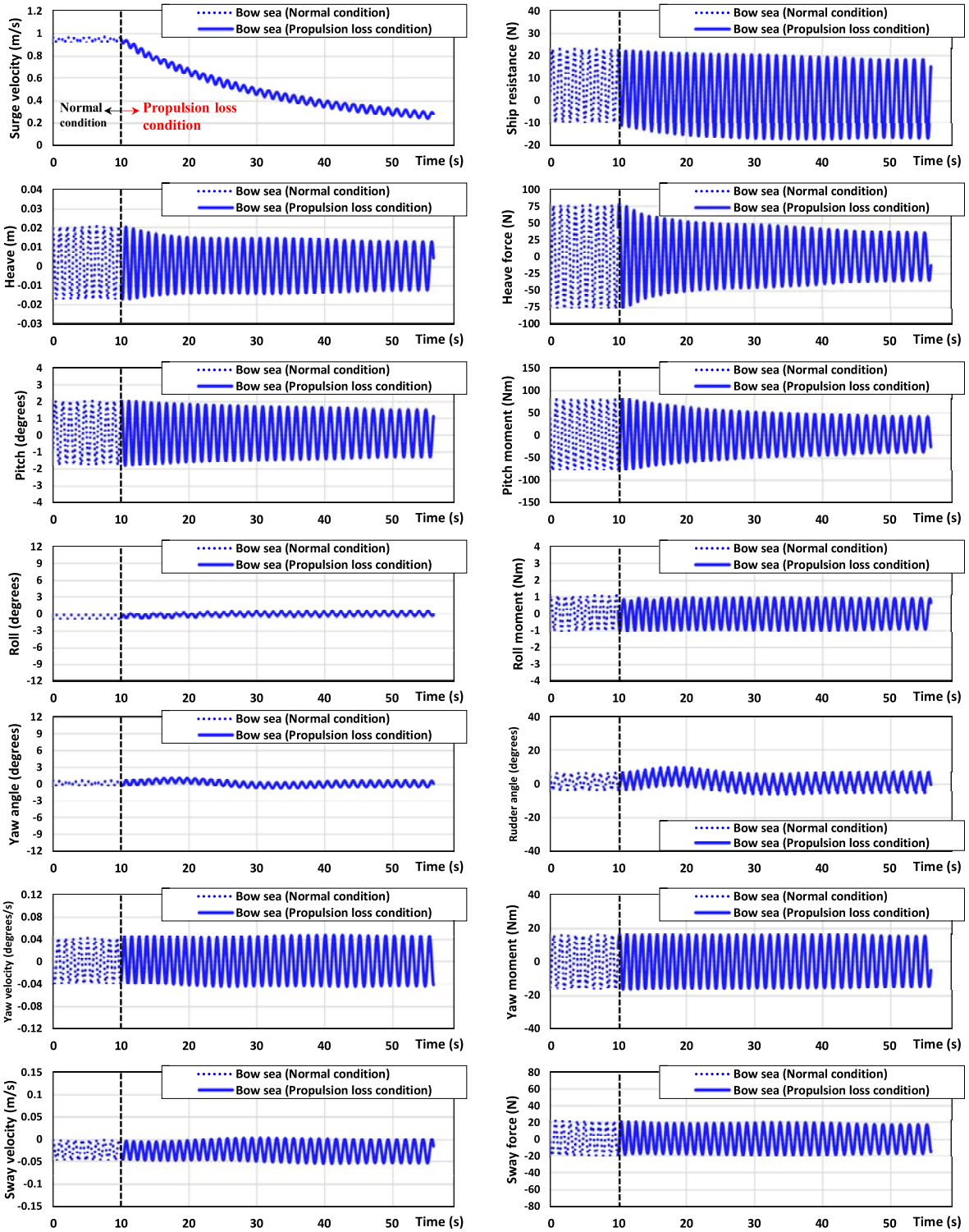

(c) Bow sea (Case 3)

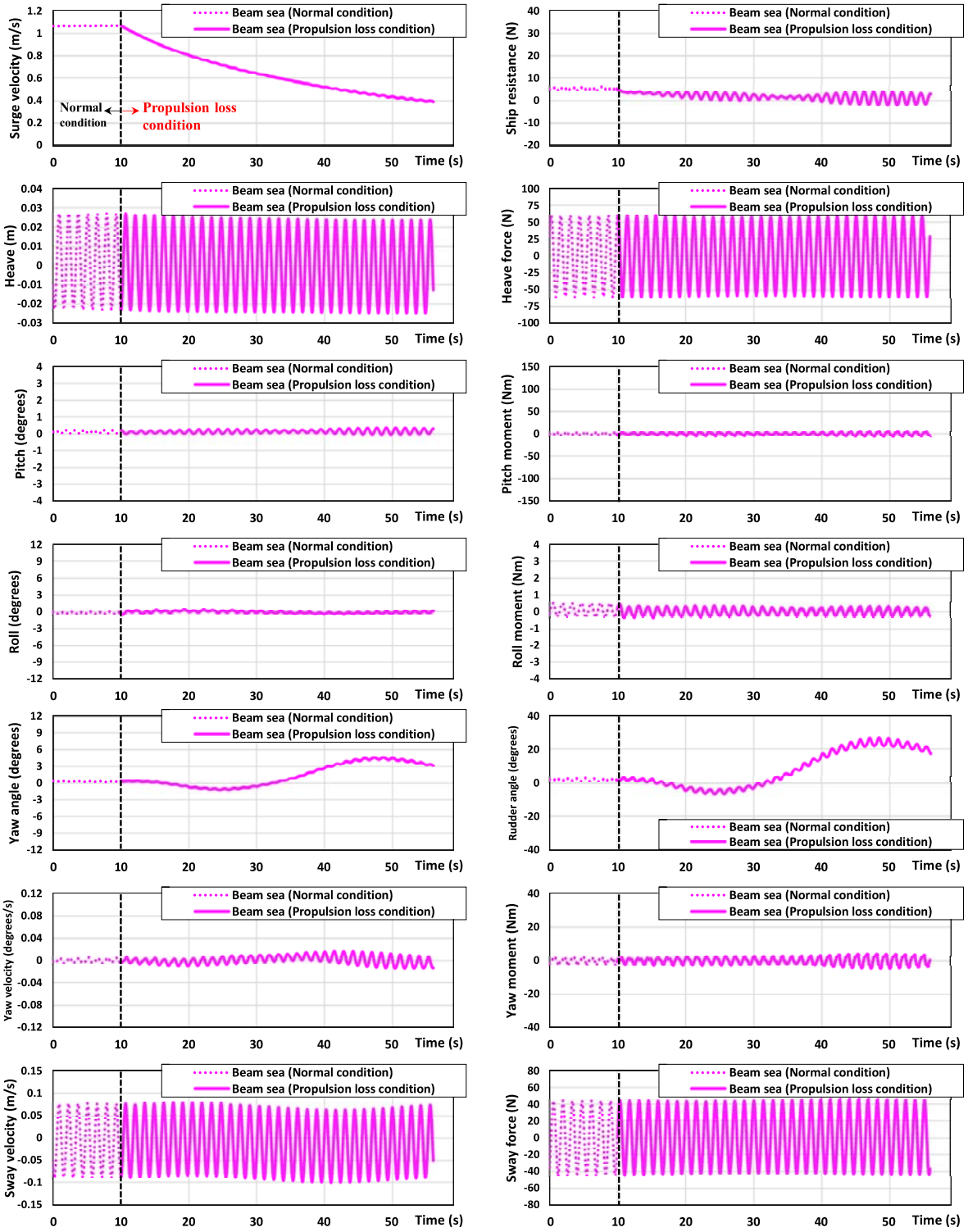

(d) Beam sea (Case 4)

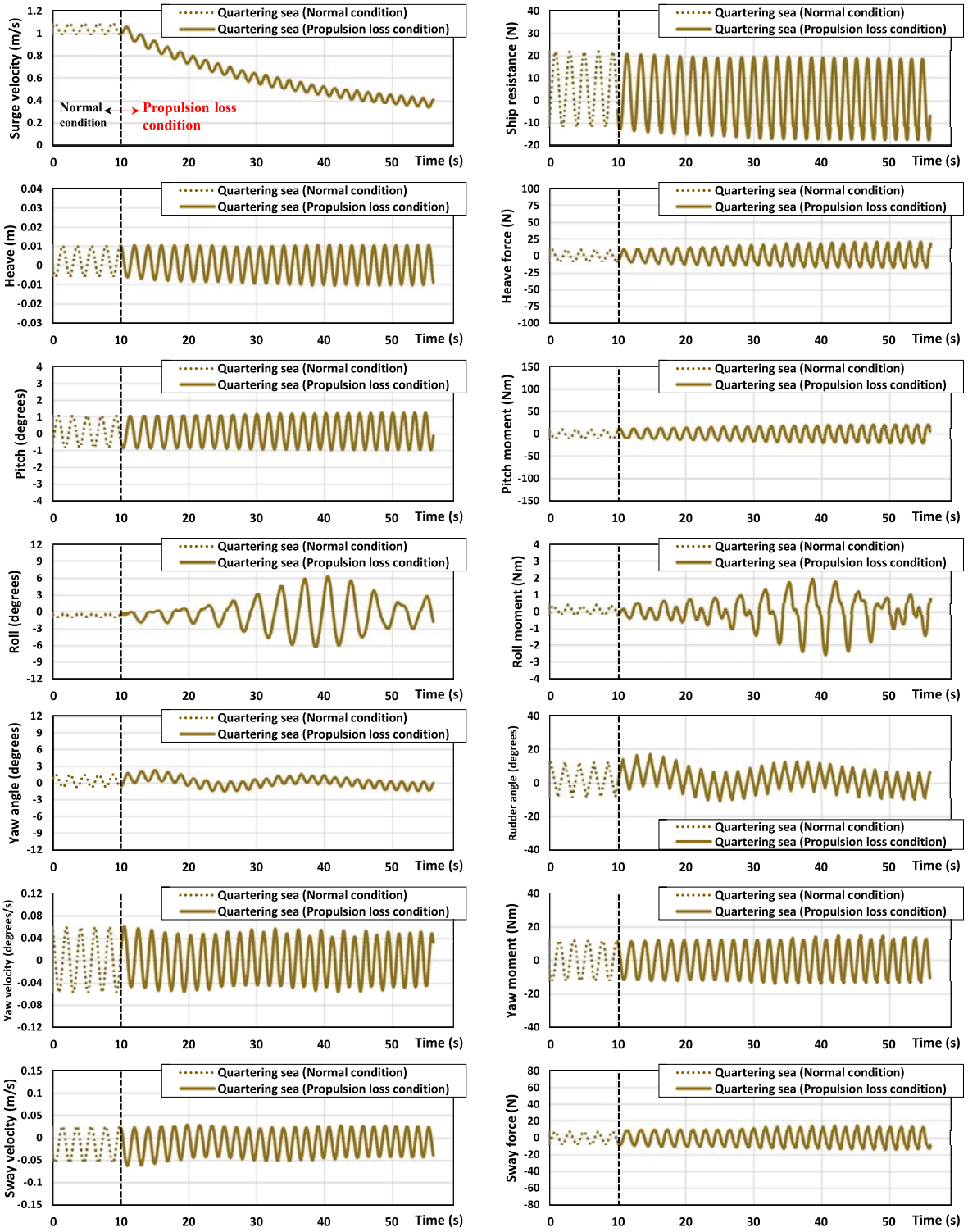

(e) Quartering sea (Case 5)

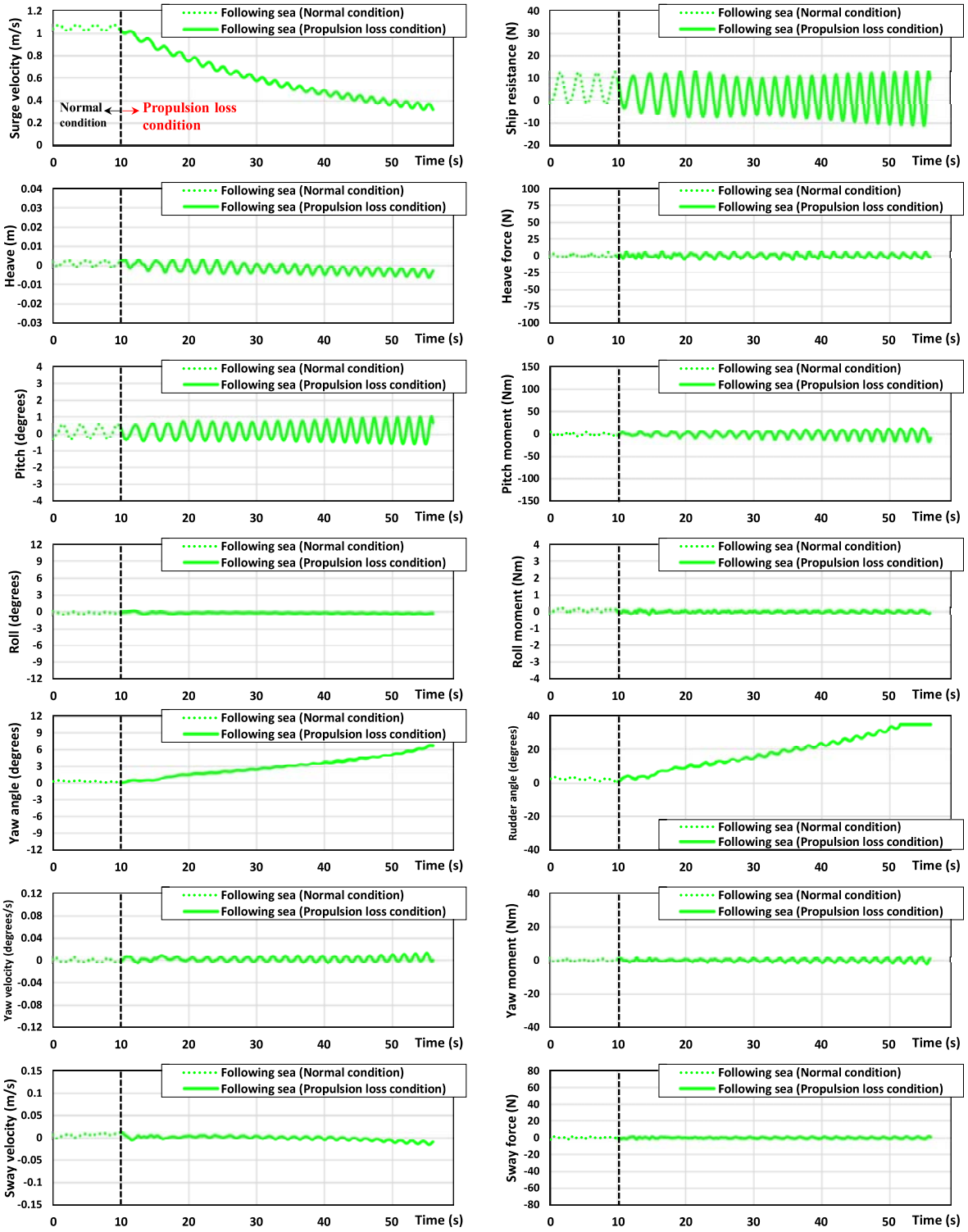

(f) Following sea (Case 6)

Figure 8.3 The time histories of the ship speed, ship motions, and various hydrodynamic quantities during course keeping control.

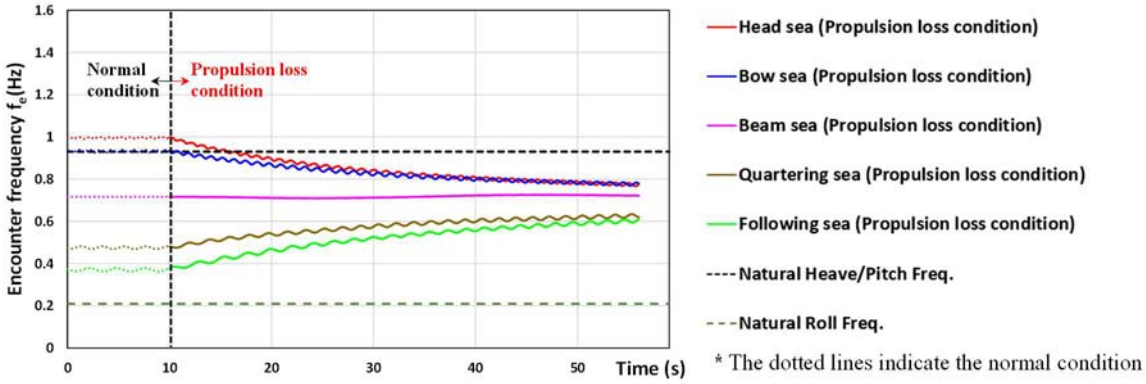

Figure 8.4 The time histories of the encounter frequencies during the course-keeping in waves.

The time histories of different variables related to the course keeping ability for each simulation are also presented in Figure **8.3**: yaw angle, rudder deflection angle, yaw velocity, yaw moment, sway velocity, and sway force. It was identified that the ship's heading control was more challenging in the propulsion loss condition than in the normal condition, such that the rudder deflection became larger after the ship lost its propulsion power. This is because the inflow velocity to the rudder was significantly reduced after the propulsion failure, thus causing the rudder normal force to decrease. The ship's heading control in calm water was not an issue under the propulsion loss because there were no external environmental loads. However, the wave conditions showed different responses in terms of the course keeping control under the propulsion loss. The relatively large deviations of the yaw angle were estimated in the head, beam, and following sea conditions with the large rudder deflections. This stemmed from not only the reduced rudder normal force but also the uneven pressure distributions on the hull caused by the incident wave, generating a yaw moment to change the ship's heading. Interestingly, the oblique wave conditions, namely the bow and quartering seas, showed relatively small changes in the yaw angle within a value of 2° during the manoeuvre. Such small changes in the ship's heading may be closely associated with the pressure distribution on the ship hull caused by the propagating oblique waves.

With the aim of visualisation, Figure 8.5 shows the snapshots of the axial flow velocities around the rudder and the pressure distributions on the rudder in both the normal condition and the propulsion loss condition. The pictures are the snapshots from the simulation of Case 1 (the calm water case). It is seen from Figure 8.5 (a) that the inflow velocity to the rudder in the normal condition was found to be much larger than that in the propulsion failure condition. As mentioned previously, the rudder inflow velocity plays an important role in determining the rudder normal force, affecting the course keeping behaviour of the ship. When the ship was advancing forward in calm water, the pressure difference between the starboard and the port of the rudder blade was formed due to a non-uniform flow created by the actuator disk (Figure 8.5 (b)). This caused a small rudder lift, and thus the yaw moment to turn the ship to the starboard to a small extent. After the ship lost its propulsion power, on the other hand, the pressure acting on the rudder blade was estimated to be comparatively small due to the absence of the propeller-induced flows.

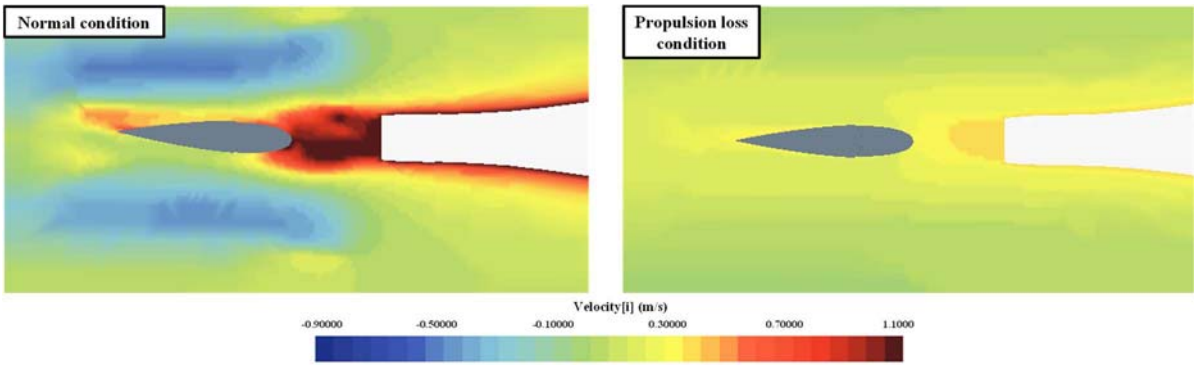

(a) Axial flow velocity around the rudder

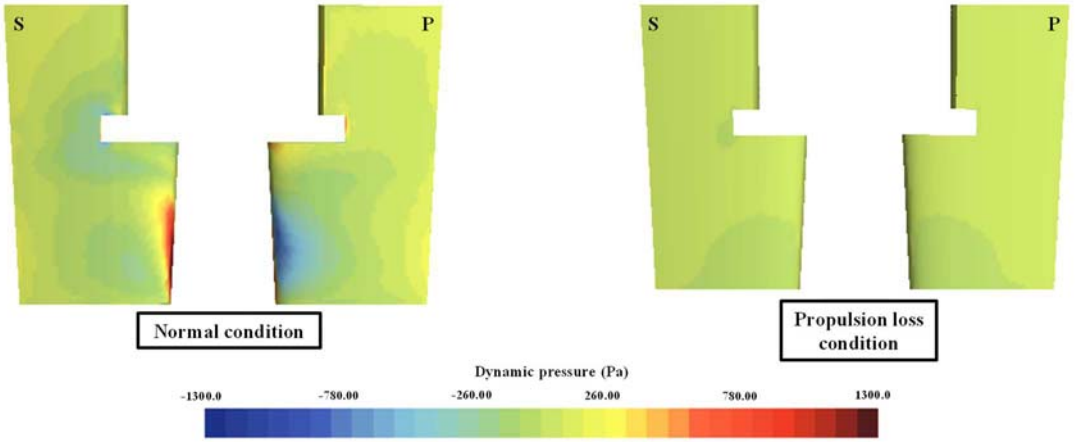

(b) Pressure distribution on the rudder blade, S: starboard profile, P: port profile

Figure 8.5 The snapshots of the axial flow velocities around the rudder and the pressure distributions on the rudder under the course keeping manoeuvre.

A comparison of the predicted ship trajectories during the course-keeping for each case is displayed in Figure 8.6, where dotted lines represent the ship paths in the normal conditions and solid lines indicate ones in the propulsion loss condition. This clearly illustrates the influence of the propulsion system failure on the course keeping behaviour of the ship. As can be seen from the figure the ship under propulsion loss condition experienced unexpected changes in the ship trajectory compared to the normal condition. Such course keeping behaviours resulted from the yaw motion after the ship lost its propulsion power, and the resultant yaw motion is closely associated with the presence of external disturbances as well as the rudder behaviour determined by the PID controller. After the propulsion loss, the ship sailing in calm water experienced the smallest change in the trajectory during the manoeuvre, which indicates the good performance of the course keeping control in calm water. This may be due to the absence of external disturbances which cause lateral forces and yaw moments on the ship. It was found that the following sea condition led to the largest change in the path. This can be explained by the fact that the predicted yaw motion of the ship shown in Figure 8.3 (f) consecutively kept positive values (the starboard turning), which made the ship continue to move to the starboard side. Despite the successful control of the yaw angle, the ship advancing forward in the bow sea experienced a large change in the course because of the wave drift forces and moments. The drift direction of the ship trajectory was estimated to be similar to the wave propagation direction ($\mu = 225°$). Another reason for the large change in the trajectory was found to be the decreasing surge speed as the ship advanced, which strengthened the effect

of the wave drift force on the ship's path. For the rest of the cases (the head, beam, quartering seas), the trajectory changes were noted to some extent due to the wave drift force and the changes in the ship's heading angle. It has to be noted that the ship trajectory could be less deviated from the straight course with different PID gains or by manual steering in real navigation operations. The relatively large oscillations of the ship paths were found under the beam and oblique waves, which was closely related to the sway forces acting on the ship, as shown in Figure 8.6.

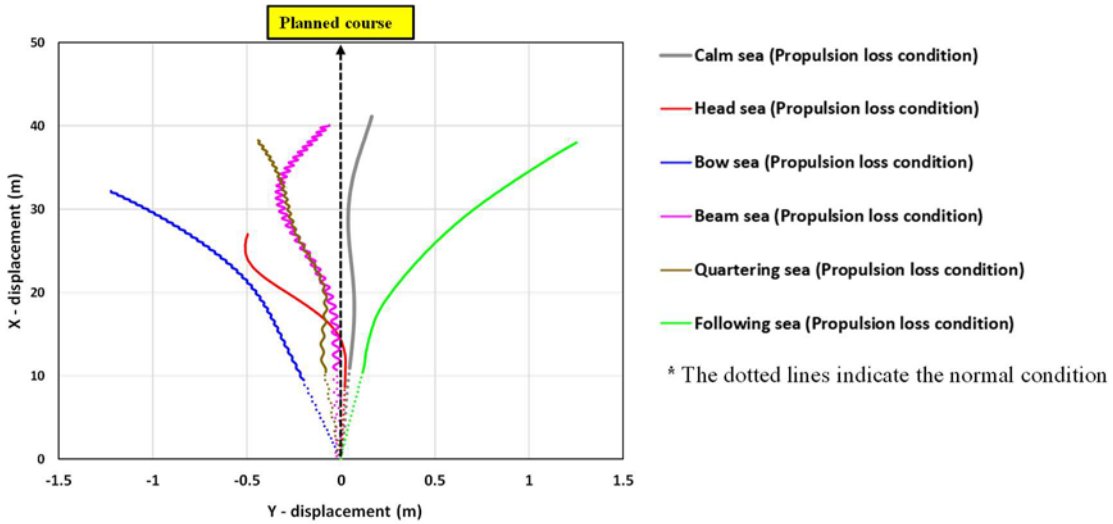

Figure 8.6 The comparison of the predicted trajectories for all the cases.

8.4.2. Turning circle manoeuvre

All the predicted trajectories of the turning circle manoeuvre under both the normal and propulsion loss conditions are presented in Figure 8.7. The starting points of the turning manoeuvre were shifted to the specific location (0,0) for the correct comparisons of the trajectories. For each case, the simulations of both conditions (the normal and propulsion failure conditions) were run for the same simulation duration so that the impacts of the propulsion loss on the ship's manoeuvrability are comparable. It should be noted that the simulations in the normal condition were completed when the heading angle variation up to 360º was achieved. Table 8.2 provides the manoeuvring indices and hydrodynamic loads acting on the rudder and hull in the normal and the propulsion failure conditions, each identified by their case numbers (peak values during the initial phase of the turn and mean values during the steady phase of the turn).

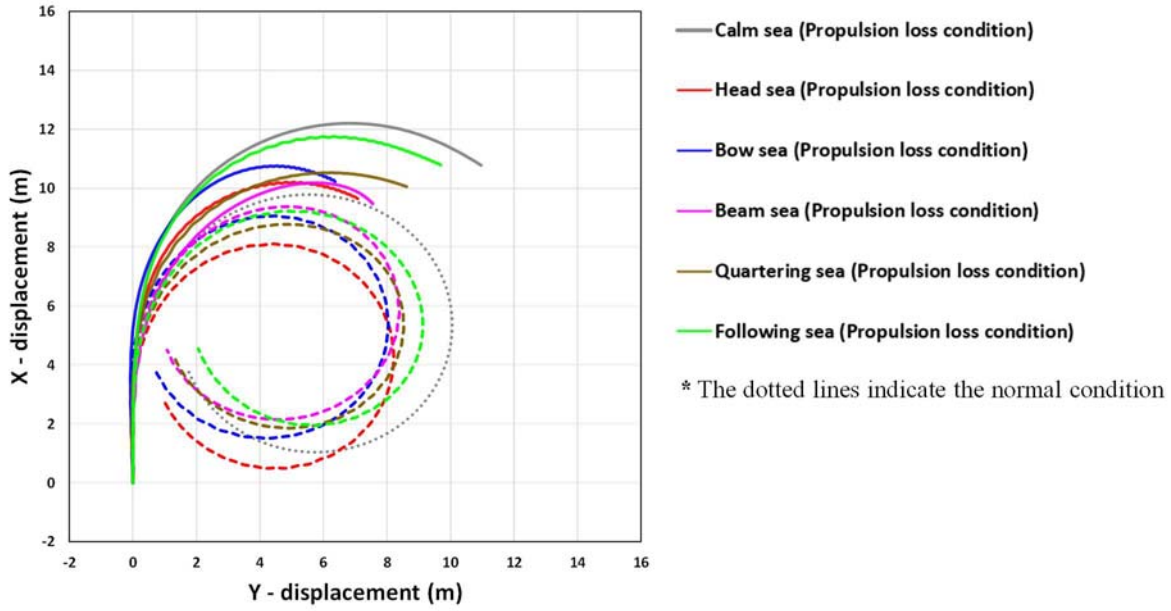

Figure 8.7 The turning circle trajectories in both normal condition and propulsion loss condition.

Table 8.2 CFD results: turning indices and hydrodynamic loads in the normal operating and propulsion failure conditions.

Parameters (CFD results)	Calm sea (Case1)	Head sea (Case 2)	Bow sea (Case 3)	Beam sea (Case 4)	Quartering sea (Case 5)	Following sea (Case 6)
			Normal operating conditions			
Advance (m)	9.55 (3.13 L_{BP})	7.86 (2.57 L_{BP})	8.85 (2.90 L_{BP})	9.10 (2.98 L_{BP})	8.44 (2.76 L_{BP})	8.95 (2.81 L_{BP})
Transfer (m)	4.07 (1.33 L_{BP})	3.09 (1.01 L_{BP})	3.10 (1.01L_{BP})	3.43 (1.12 L_{BP})	3.25 (1.06 L_{BP})	3.56 (1.16 L_{BP})
Time for yaw 90° (s)	12.31	12.52	13.09	11.92	11.23	11.76
Tactical diameter (m)	9.82 (3.21 L_{BP})	7.97 (2.61 L_{BP})	7.82 (2.56L_{BP})	8.17 (2.67 L_{BP})	8.29 (2.68 L_{BP})	8.86 (2.90 L_{BP})
Time for yaw 180° (s)	24.20	23.74	24.38	23.15	22.79	23.43
Rudder loads						
-Peak Y force (N)	-4.38	-5.35	-6.48	-5.61	-6.11	-5.76
-Mean Y force (N)	-2.37	-2.86	-2.85	-2.90	-2.80	-3.09
-Peak Z moment (Nm)	6.51	6.44	7.75	6.20	7.66	6.99
-Mean Z moment (Nm)	3.5	3.33	3.29	3.37	3.25	3.65
Hull loads						
-Mean Y force (N)	7.45	7.36	7.63	5.43	6.61	7.32
-Mean Z moment (Nm)	0.01	-0.54	0.49	0.47	0.5	-0.08
			Propulsion failure conditions			
Advance (m)	11.87 (3.88 L_{BP})	9.94 (3.25 L_{BP})	10.50 (3.43 L_{BP})	9.78 (3.20 L_{BP})	10.07 (3.29 L_{BP})	11.38 (3.72 L_{BP})

Transfer (m)	4.82 (1.58 L_{BP})	3.51 (1.15 L_{BP})	3.21 (1.05 L_{BP})	3.96 (1.29 L_{BP})	3.83 (1.25 L_{BP})	4.22 (1.38 L_{BP})
Time for yaw 90° (s)	19.64	24.03	22.47	17.55	17.01	18.95
Tactical diameter (m)	-	-	-	-	-	-
Time for yaw 180° (s)	-	-	-	-	-	-
Rudder loads						
-Peak Y force (N)	-1.60	-1.84	-2.57	-1.77	-2.29	-2.37
-Mean Y force (N)	-0.04	-0.09	-0.02	-0.03	-0.05	-0.09
-Peak Z moment (Nm)	2.34	2.15	3.11	2.28	2.92	2.94
-Mean Z moment (Nm)	0.06	0.14	0.02	0.04	0.06	0.13
Hull loads						
-Mean Y force (N)	0.40	0.48	-1.07	0.84	0.48	0.15
-Mean Z moment (Nm)	-0.06	-0.20	-0.22	-0.29	-0.12	-0.26

The critical turning parameters are highly dependent on the ship's horizontal motions, namely surge, sway, and yaw motions which are determined by the complex interactions between the hull, propeller, rudder, and environmental loads. Such ship motions have a close correlation with the ship velocities in the horizontal plane (surge, sway, and yaw velocities). In general, the greater the surge speed and the smaller the yaw velocity, the greater the ship advance and transfer can be, as discussed in Chapter 5. For all the cases, it was identified from the figure and the table that the turning capability of the ship was strongly affected by the presence or absence of the propulsion power, thus leading to substantial changes in the turning trajectories. The propulsion loss condition led to notable increases in the advance, the transfer, and the time to turn by 90º, as seen in Table 8.2. This is mainly due to the loss of propulsion power, which caused the decrease in the rudder inflow velocity. Hence, the sufficient rudder normal force was not achieved and thus leading to the longer time to turn by 90º. As a result of this, the ship advance and transfer for the propulsion loss condition were found to be comparatively large despite the small surge speed. The resultant differences in the turning trajectories between the normal and propulsion loss conditions can be found in Figure 8.7.

The predicted time histories of the ship velocities, motions, forces, and moments during the ship's turning manoeuvre are presented in Figure 8.8, in which dotted lines indicate the normal condition and solid lines represent the propulsion failure condition. From Figure 8.8, it was observed that the ship in the normal condition experienced the involuntary surge speed loss after the rudder deflection towards 35° starboard. The speed loss between the initial surge speed and the steady mean value was predicted to range from 48% to 56%, which was due to an increase in ship resistance caused by a large drift angle. The ship in the propulsion loss condition, on the other hand, experienced gradual decreases in the surge velocity after the ship lost its propulsion power and the rudder deflected towards starboard 35°. The propulsion loss was greatly contributed to the speed loss, while increased resistance due to the drift angle accelerated the decrease in the speed. For the sway and yaw velocities, it revealed that they showed a tendency to increase rapidly until a specific time after the rudder deflection and then gradually converged to a certain value in both the normal and propulsion loss conditions. However, such velocities in the propulsion loss condition were found to be noticeably smaller

than those in the normal condition. This shows that the greater rudder inflow velocity may lead to the greater rudder normal force, thus causing the relatively large sway and yaw velocities at the beginning of the turning manoeuvre. As for the propulsion failure conditions, it was noted that the ship sailing in the beam, quartering, and following waves achieved the shorter time to turn 90º than the other cases, showing relatively greater yaw rates during the initial transient phase. Such turning behaviour may result from the complicated interaction between the hull, the rudder, and the incident wave after the ship started turning. It has to be stressed that in all propulsion loss cases a 180º turn could not even be achieved during the turning manoeuvre despite the maximum rudder deflection (35º), such that the differences in the ship trajectory between the normal and propulsion loss conditions were remarkable. It was also identified that the ship trajectories were significantly drifted at the end of the turning manoeuvre due to the large speed loss resulted from the propulsion failure. This implies that the ship with the propulsion failure is incapable of executing a large alteration of course to avoid a close-quarter situation within an appropriate time, which may pose a significant threat to navigational safety.

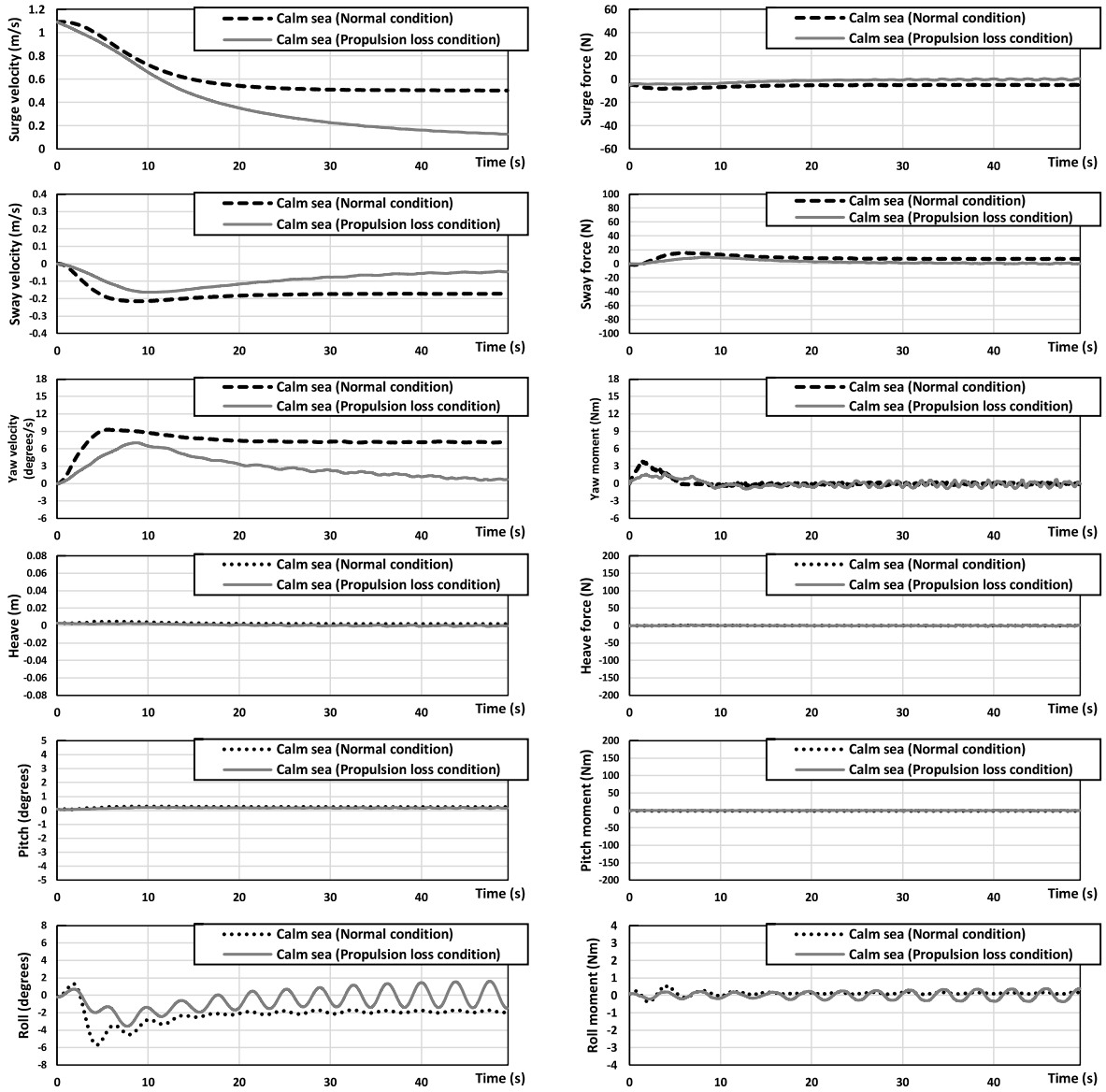

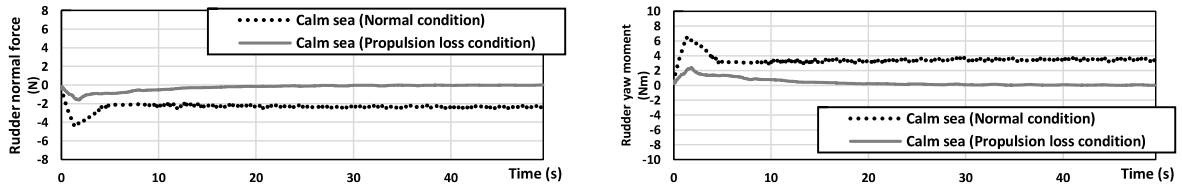

(a) Calm sea (Case 1)

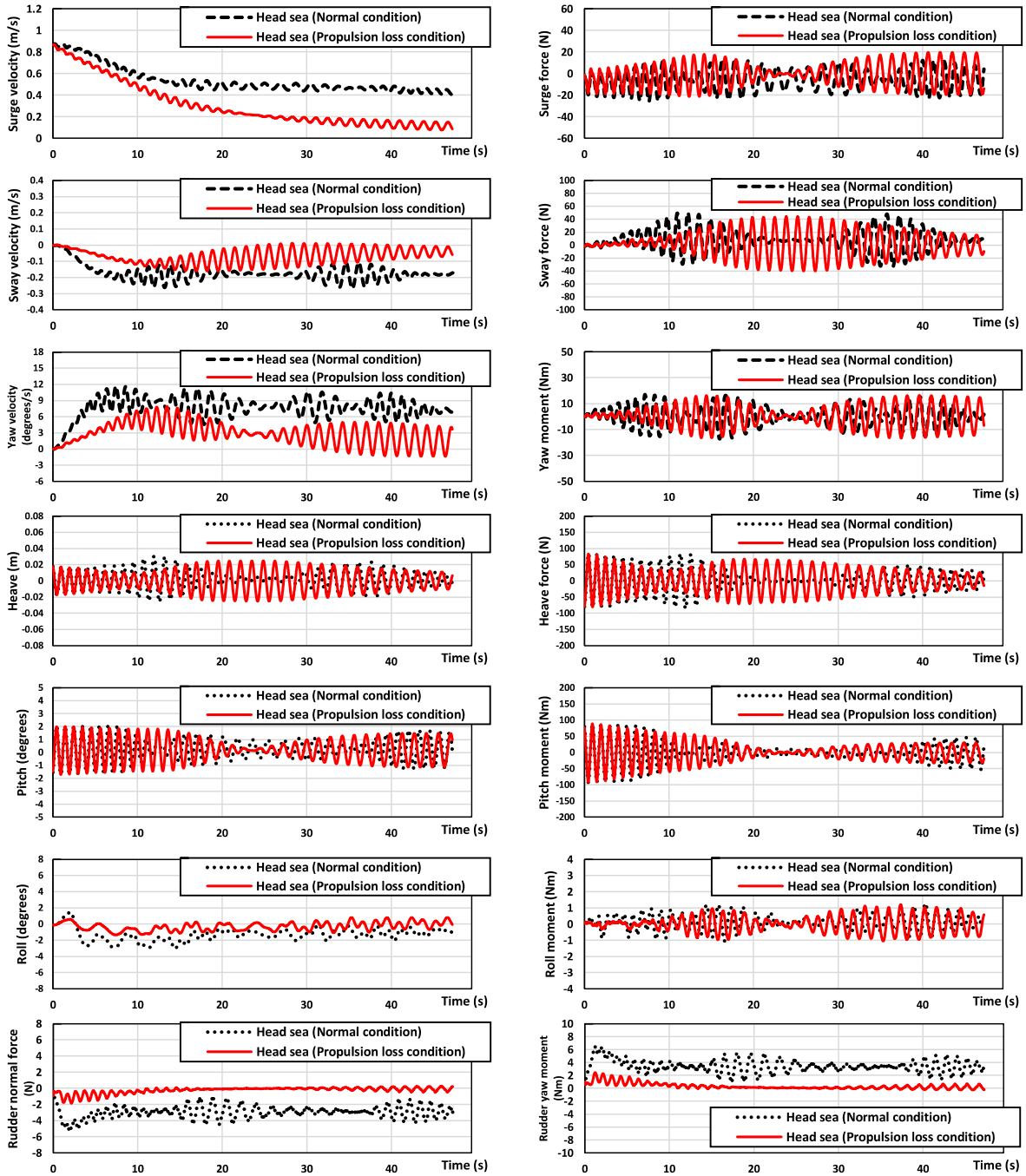

(b) Head sea (Case 2)

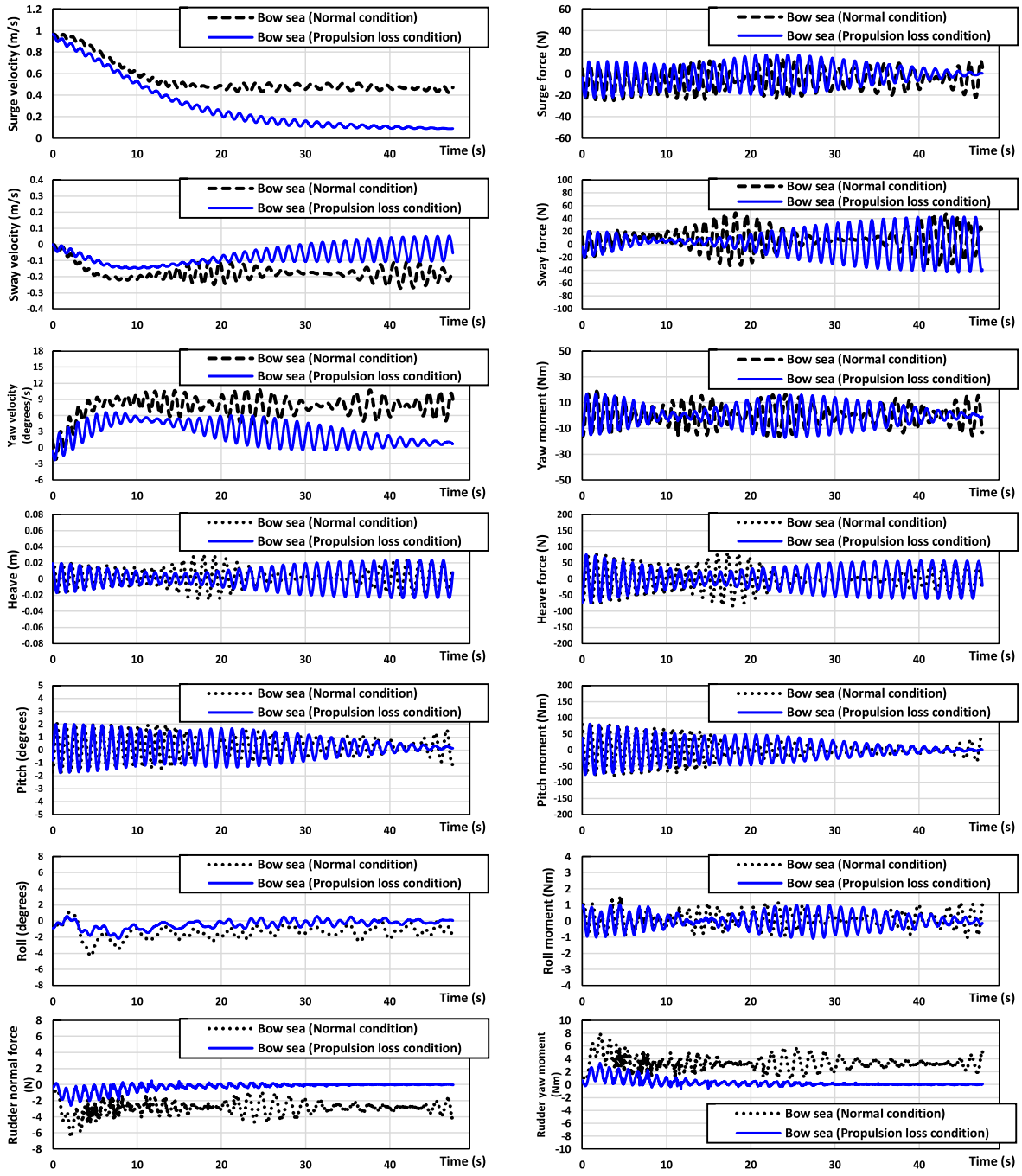

(c) Bow sea (Case 3)

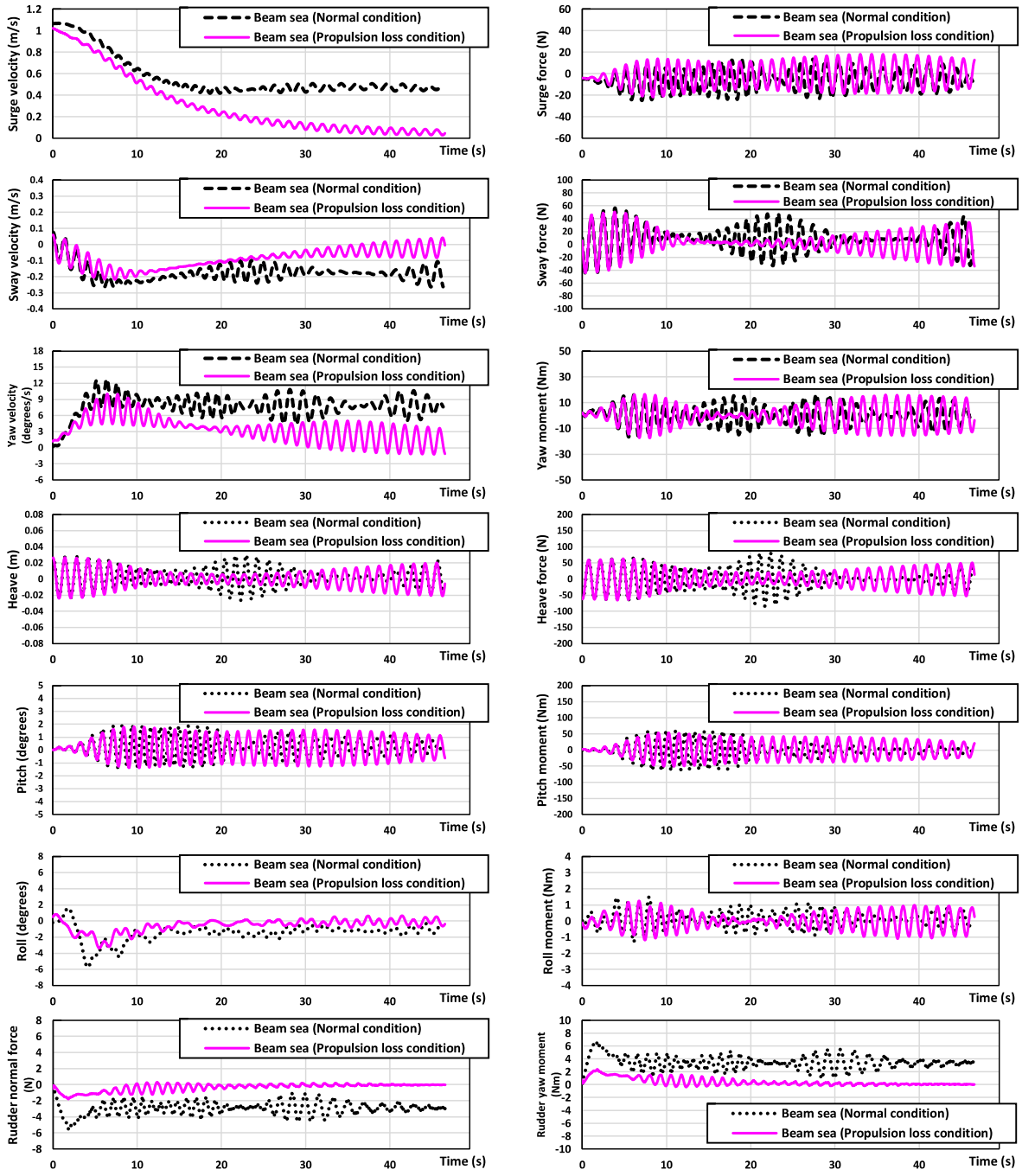

(d) Beam sea (Case 4)

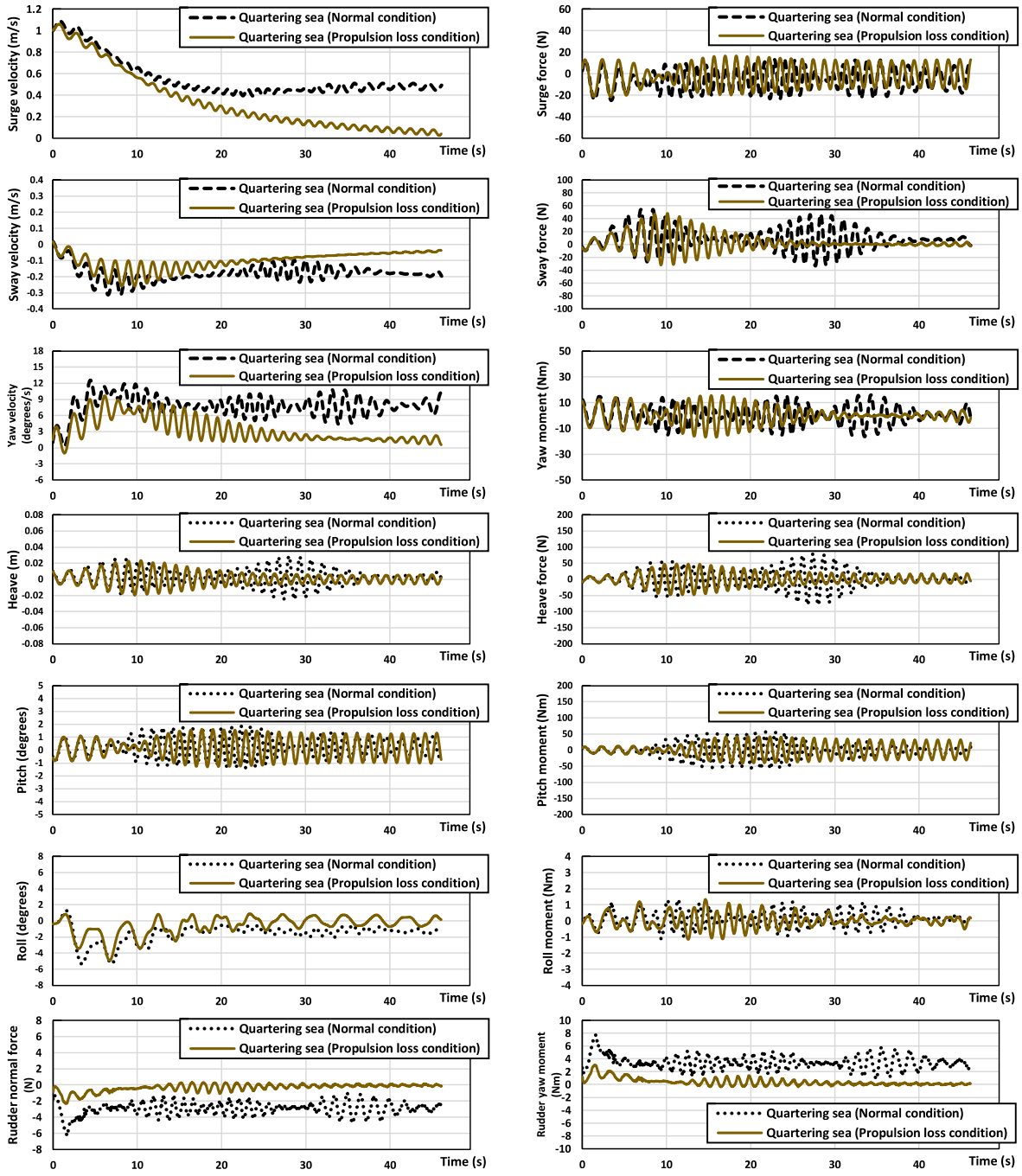

(e) Quartering sea (Case 5)

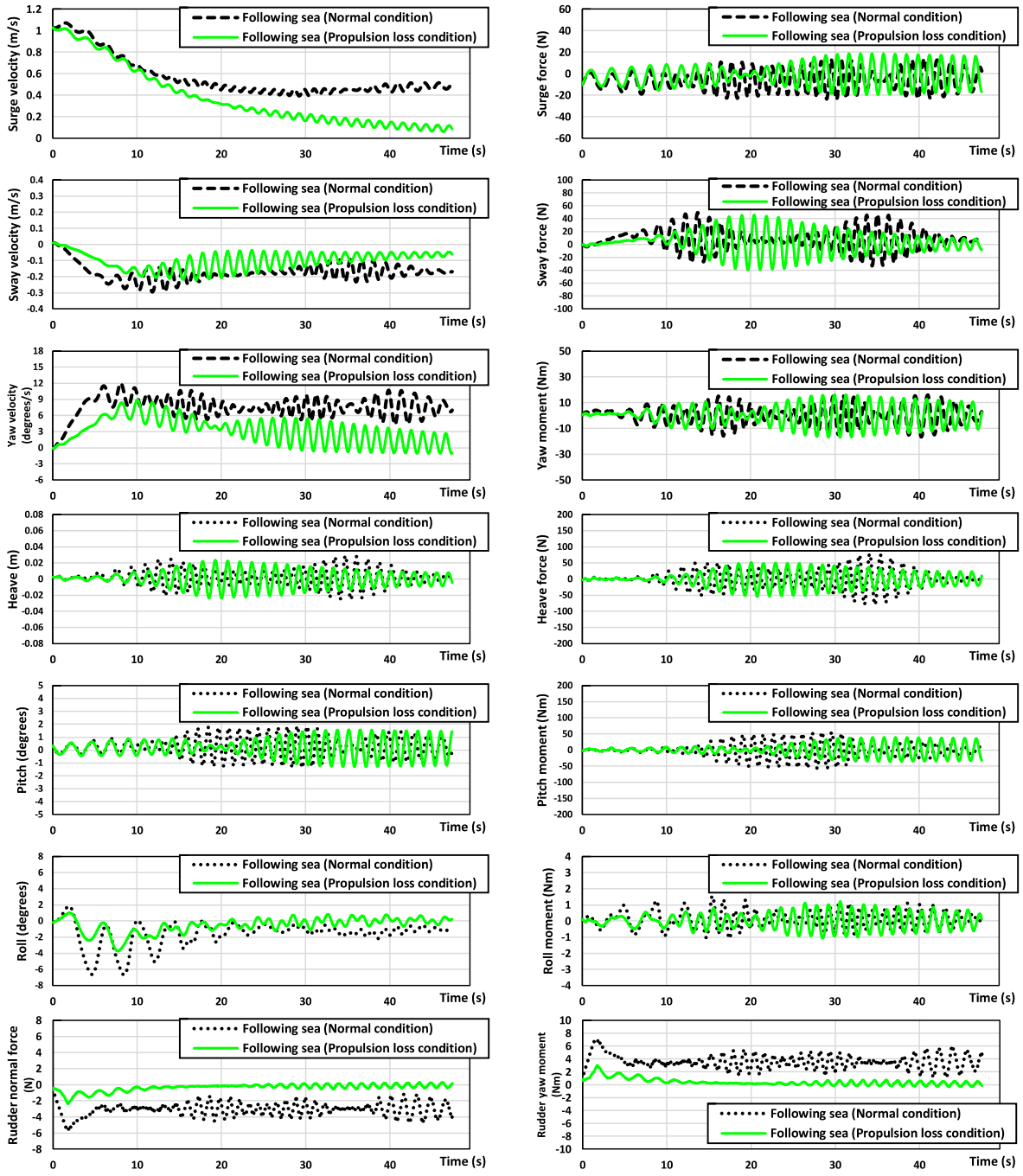

(f) Following sea (Case 6)

Figure 8.8 The time histories of the ship velocities, motions, forces, and moments during the ship's turning manoeuvre.

As Table 8.2 and Figure 8.8 jointly show, the differences in the rudder loads are remarkable between the normal and propulsion loss conditions. During the initial phase of the turn, the maximum of the rudder normal force experienced by the ship in the normal condition was much greater than that in the propulsion loss condition, generating the larger rudder yaw moment. Due to the presence of the surge speed, the ship could generate the rudder normal force and yaw moment to some extent after the propulsion failure. Then, it was found that the ship

manoeuvring in the normal condition also exhibited greater average rudder loads when compared with the propulsion loss condition in terms of rudder normal forces and yaw moments during the steady phase of the turn. It has to be pointed out that the rudder normal force and yaw moment experienced by the ship with the propulsion failure was predicted at almost zero during the steady phase, implying that the ship was incapable of performing the turning manoeuvre. The different turning capabilities being ascribed to such differences in the rudder loads affected the hull forces and moments during the turning manoeuvre.

When it comes to seakeeping performance during the turning manoeuvre, except for the calm water case, high-frequency fluctuations in such values occurred in both normal and propulsion loss conditions, which correlated strongly with the wave-induced motions. Such high-frequency wave-induced motions were found to experience continual changes in the frequency of the ship motions, which was attributed to instantaneous variations in the ship surge speed and wave-encounter direction. For example, the ship turning in the quartering waves (Case 5) encountered the starboard quartering wave (0° turn), starboard bow wave (90° turn), port bow wave (180° turn), port quartering wave (270° turn), and starboard quartering wave (360° turn) in series after starting the starboard turning manoeuvre. The time histories of the encounter frequencies during the turning circle manoeuvres in waves are shown in Figure 8.9, in which the heave, pitch and roll natural frequencies are also shown. It can be seen that the ship performing a given manoeuvre experienced significant differences in the encounter frequency between the normal condition and the propulsion failure condition. Accordingly, it is expected that the differences in the encounter frequency may lead to differences in seakeeping performance in waves between the normal and propulsion loss conditions.

For the heave motion and force in calm water, there were no recognizable differences between the normal and propulsion loss conditions, as seen in Figure 8.8 (a). The vertical motion and force were maintained to be almost zero value without any fluctuations while the ship was turning, due to the absence of external disturbances. A similar trend was recognised with respect to the pitch motion and moment for the calm water case. On the other hand, the ship manoeuvring in waves showed identifiable differences in such motions, forces, and moments depending on whether or not the propulsion failure condition was applied. This resulted from a significant difference in the extent of change in the yaw angle and surge speed during the manoeuvre, which affected the change in the encounter frequency and thus the ship motions. The ship under the normal condition experienced the waves coming from all directions during the turning manoeuvre since the 360° turn was achieved within a given period. Because of this, the normal condition showed remarkably continual changes in the encounter frequency (the repetitive increase and decrease in the frequency during the manoeuvre). Contrarily, the propulsion failure condition showed the heading angle variation ranging only from 134º to 159º and relatively small changes in the yaw angle during the turning manoeuvre caused the ship to experience certain wave-encounter directions during the turning, consequently leading to small changes in the encounter frequency (Figure 8.9). As for the heave motion, Kim et al. (2021a) state that incident beam waves lead to the maximum heave motion and force, which is closely correlated to the ratio of wavelength to ship length. When the ship experiences the beam waves, the breadth of the ship can be considered as the relevant length that is relatively smaller than the wavelength. Such a small relevant length may cause the maximum vertical motion whose

amplitude was almost equal to the incident wave height. Concerning the propulsion loss condition, Case 4 (the beam wave) and 5 (the quartering wave) displayed the maximum vertical motion at the early stage of the turning manoeuvre in which the ship experienced the starboard beam sea (Figure 8.8 (d) and (e)). Case 2 (the head wave) and 6 (the following wave) also showed the maximum amplitude of the heave motion at the middle stage of the manoeuvre, in which the ship encountered the beam waves (Figure 8.8 (b) and (f)). Case 3 (the bow wave) presented the maximum motion at the last stage of the manoeuvre (Figure 8.8 (c)). Contrary to the vertical motion, it was revealed that the incident beam waves caused the minimum pitch motion during the turning manoeuvre. This may be because the beam waves did not generate considerable differences in pressure between the ship's bow and stern, not causing the pitch moment. The pitch motion at the end of the turning manoeuvre for Case 3 (the propulsion loss condition) can be given as a good example (Figure 8.8 (c)) in which the pitch amplitude gradually decreased as the wave-encounter angle (μ) became 090º (port beam sea). In addition to this, it was observed that the smaller difference between the encounter frequency (f_e) and the natural frequency (f_n) led to the increase in the amplitude of the pitch motion, as discussed in Section 8.4.1. When it comes to the roll motion, the rudder normal force played an important role in determining the roll motion while the ship was turning. As the rudder was deflected towards the starboard, the ship was first heeled to the starboard (to the centre of the turning circle) due to the generated rudder lift force. Then, the hydrodynamic forces and the centrifugal force acting on the hull caused the ship to heel to the port side (to the outside). From Figure 8.8 (a) - (f), the ship sailing in the propulsion loss condition showed smaller amplitudes of the roll motion than the normal operating conditions during the manoeuvre for all cases due to the small rudder lift.

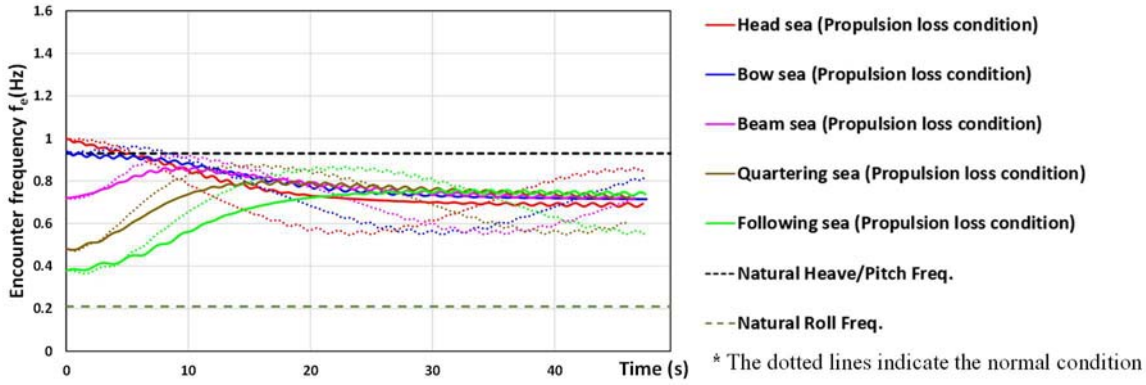

Figure 8.9 The time histories of the encounter frequencies during the turning circle manoeuvre in waves.

Figure 8.10 and Figure 8.11 display the instantaneous free surface elevation around the ship during the turning circle manoeuvre under the normal and propulsion loss conditions, respectively. The free surface elevations around the ship are affected by the interaction of several components including undisturbed incident waves (free waves without consideration of the presence of the ship), diffraction waves (the unsteady perturbation response of the free surface to the presence of the ship), radiation waves (representing the waves generated by the moving ship), Kelvin waves (the wave pattern generated by the advancing ship at non zero

forward speed in calm water), and the wake generated by the propeller. It is seen from the figures that the diffraction and radiation waves around the manoeuvring ship are almost invisible due to the coexistence of other effects such as the incident waves and Kelvin waves, as reported in Ohkusu and Wen (1998). Analysis of the radiation and diffraction wave fields generated by the ship was not a focus of this study, so only the instantaneous free surface elevation around the ship was studied. The Kelvin wave generated by the manoeuvring ship was found to have a strong correlation with the surge speed and wave-encounter direction during the turning. The greater the surge speed, the more visible the Kelvin wave generated by the ship becomes. Besides, the generated Kelvin wave seemed quite clear when the ship experienced the waves from the bow during the turning manoeuvre. For the propulsion failure condition, it is observed from the figures that the generated Kelvin wave almost disappeared after the ship lost its propulsion power due to the much smaller surge speed, compared to the normal condition.

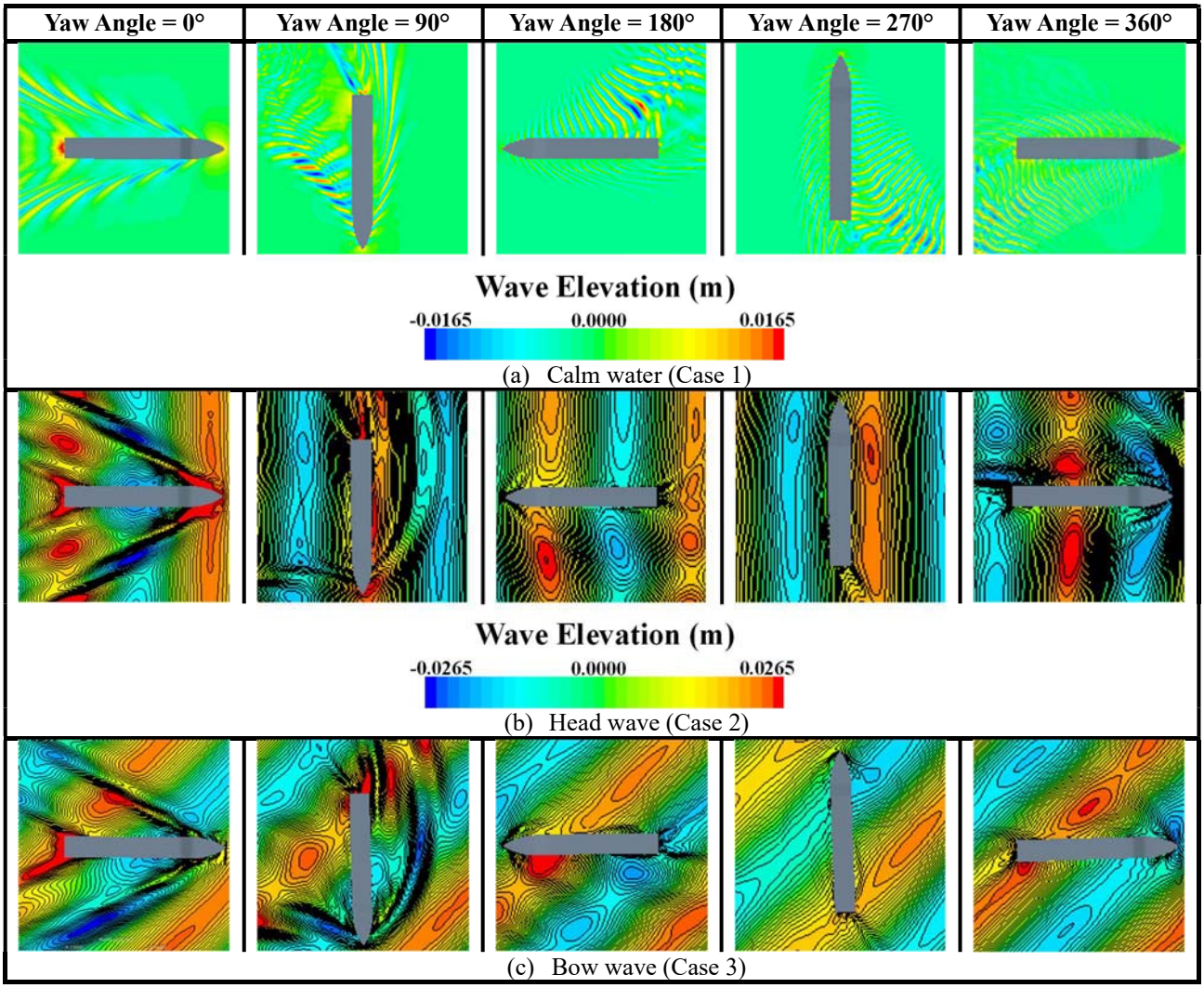

(a) Calm water (Case 1)

(b) Head wave (Case 2)

(c) Bow wave (Case 3)

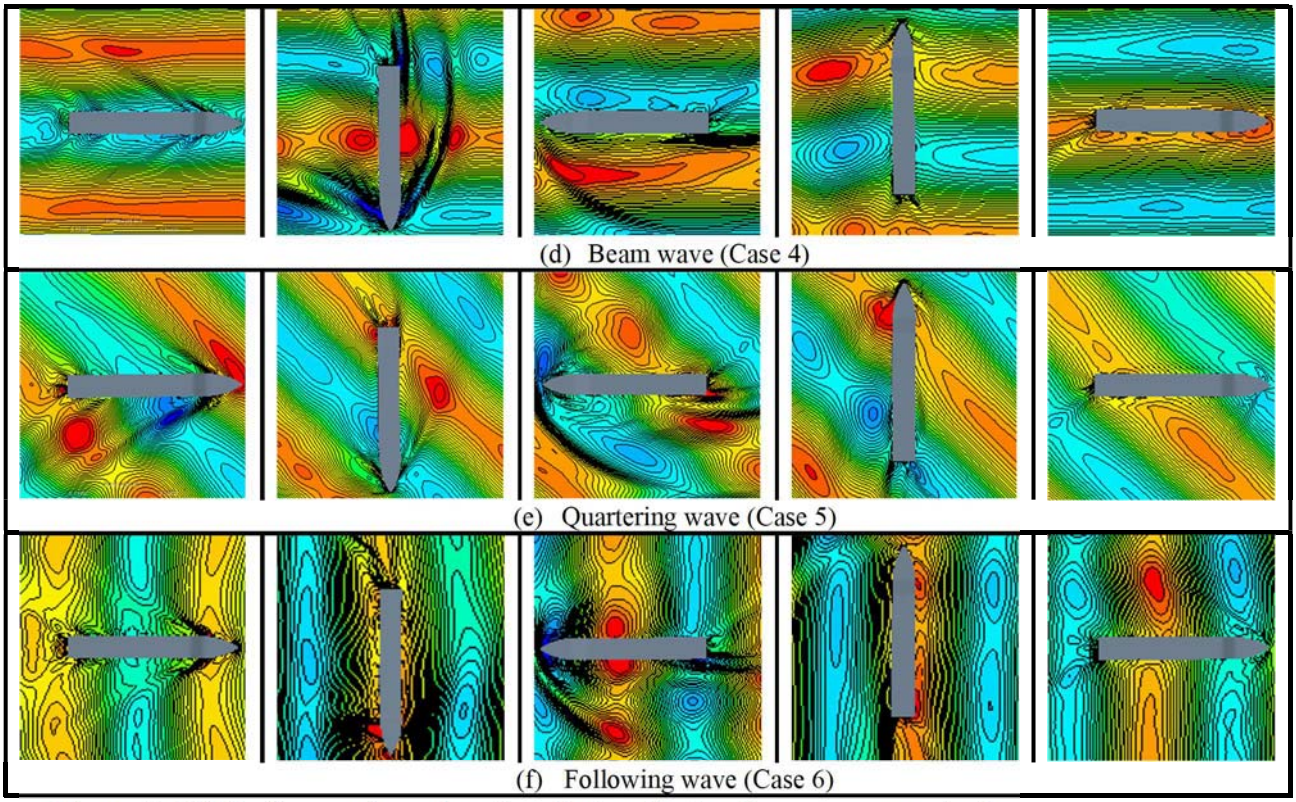

(d) Beam wave (Case 4)

(e) Quartering wave (Case 5)

(f) Following wave (Case 6)

Figure 8.10 The free surface elevation during the turning manoeuvre in the normal operating condition.

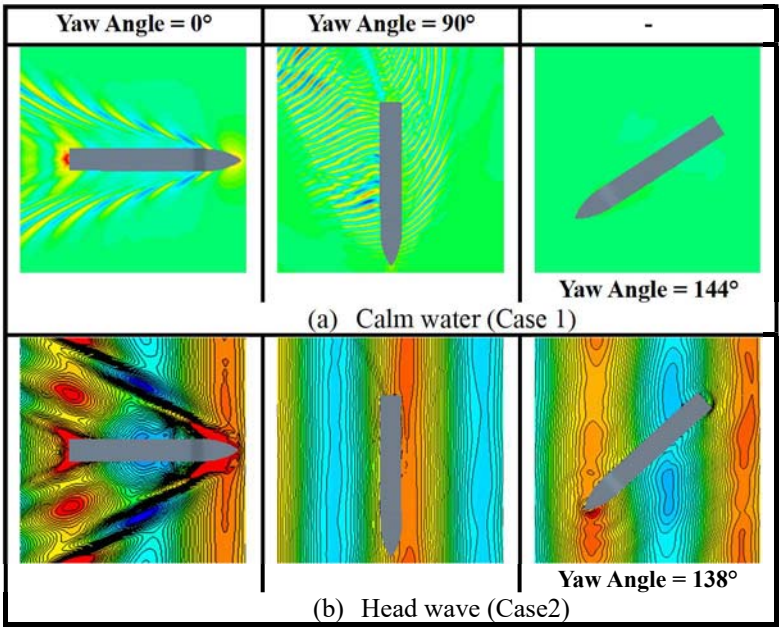

(a) Calm water (Case 1)

(b) Head wave (Case2)

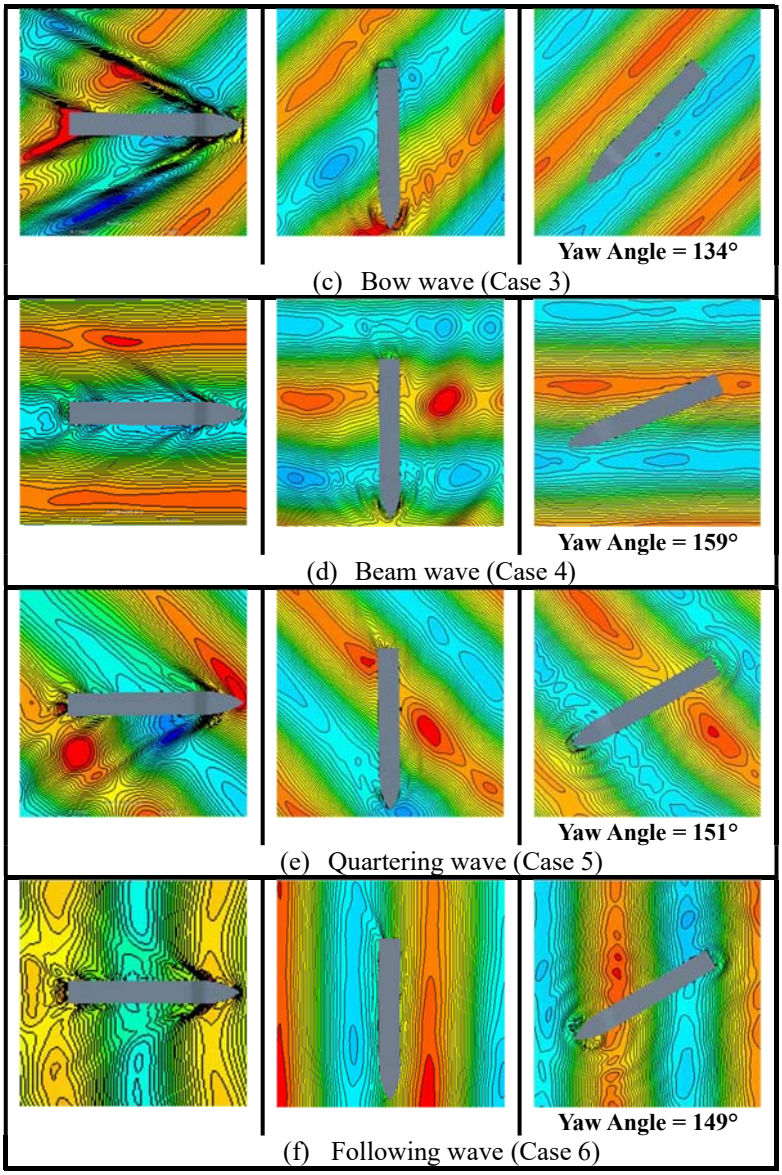

Figure 8.11 The free surface elevation during the turning manoeuvre in the propulsion failure condition.

8.5. Concluding Remarks

This chapter has shown the effect of propulsion failure on the course keeping and turning circle manoeuvres under both the normal and propulsion loss conditions. In examining the ship performances for the normal and propulsion loss conditions, the research findings have demonstrated that the propulsion failure has a significant influence on the course keeping capability, seakeeping performance, and ship manoeuvrability in a real seaway. The key findings of this research can be summarised as follows:

1) The loss of propulsion power strongly affected the heave and pitch responses of the vessel during the course-keeping. This was due to continual changes in the encounter frequency of the wave during the manoeuvre, which resulted from the decreasing surge speed caused by the propulsion loss.

2) It was also found that the yaw angle control based on the PID controller was more challenging in the propulsion failure condition than in the normal condition, such that the rudder deflection became significantly larger after the ship lost its propulsion power. This was associated with the insufficient rudder normal force due to the reduced inflow velocity to the rudder after the propulsion loss. As a result of this, the predicted ship trajectories under the propulsion failure conditions deviated from the planned route much more than that under the normal conditions.

3) The turning behaviour of the ship considerably differed according to the presence or absence of the propulsion power, which caused substantial changes in not only the turning trajectories but also the critical manoeuvring indices. It was revealed that the loss of propulsion power led to noticeable increases in the advance, the transfer, and the time to turn by 90º due to the insufficient rudder lift. It is interesting to note that a 180º turn could not even be achieved under the propulsion loss condition, which implies the poor turning ability of the ship.

4) For the seakeeping behaviour during the ship's turning, the ship under the propulsion loss condition presented notable differences in the ship motions, compared to the normal operating condition. This was also attributed to the insufficient rudder normal force, leading to small changes in the ship's heading angle and consequently causing the ship to encounter certain wave-encounter directions during the turning.

9. FREE-RUNNING CFD SIMULATIONS FOR IRREGULAR WAVES

9.1. Introduction

Ship manoeuvrability studies are usually carried out in calm and regular seas; however, an irregular sea state can better present the real operational conditions at sea, compared to both calm and regular seas. It has been shown that over 40% of marine incidents are related to navigational casualties from collision and grounding (EMSA, 2020). Such casualties are dominantly due to inappropriate ship manoeuvres being highly dependent on the decision of a navigation watch officer, thus highlighting the importance of understanding the manoeuvring behaviour of a ship in a real seaway. A sufficient understanding of a ship's manoeuvrability plays a central role in safe ship handling. It is true that there have been voluminous studies focusing on ship manoeuvrability in calm water in line with the recommendation of the International Maritime Organisation (IMO, 2002), which can to some extent be used to understand the inherent manoeuvrability of a ship. However, the increasing number of navigational incidents has made it essential and urgent that the manoeuvring performance of a ship in real sea states should be studied in detail. Given that the realistic ocean waves in which a vessel navigates are mostly irregular, namely random seas, it is highly believed that the manoeuvring capability of a ship in irregular waves should be extensively investigated to improve understanding of ship manoeuvrability in real sea states. Without a doubt, irregular waves can lead to substantial changes in the manoeuvring performance of a ship compared to that in calm water, which is closely associated with navigational safety at sea. For this reason, this chapter aims to analyse the manoeuvrability of a ship in an irregular seaway.

As stated previously, irregular waves can better represent realistic sea states. Nevertheless, to date, only a few remarkable studies have been devoted to investigating the effect of irregular waves on the manoeuvrability of ships. Hasnan et al. (2019) performed a series of free-running experiments to estimate the turning behaviour of the KCS and KVLCC2 in short-crested irregular head seas. Their key findings showed that irregular head seas led to substantial changes in the turning capabilities of ships including critical turning indices, compared to the calm water case. In this regard, the findings from the study by Hasnan et al. (2019) raised further questions about course-keeping and turning capabilities of a ship in irregular waves of different directions. The reason for this question can be explained by the fact that Kim et al. (2021b) demonstrated the manoeuvring behaviour of a ship depends highly on the wave propagation directions. In particular, the investigation in Kim et al. (2021b) showed course-keeping abilities can be clearly identified in oblique waves, causing a large deviation from the planned route. The effect of wave direction on the manoeuvring performance was studied earlier by Kim et al. (2021b); however, their study was only performed in regular waves. Therefore, it is crucial to evaluate the manoeuvrability of a ship in irregular waves of different directions as well to have better understanding of the ship’s manoeuvring properties in an irregular seaway.

Given this background, the study reported in this chapter was motivated to predict the manoeuvrability of a ship in irregular head and oblique bow seas, using the free-running CFD

approach capable of resolving all physics involved in the manoeuvre. To the best of this author's knowledge, there has been no specific study in the literature up to now focusing on the manoeuvrability of a ship in irregular head and oblique seas, except for the turning ability in irregular head seas. It is also expected that the free-running CFD simulations can help to gain insights into the hydrodynamic characteristics occurring during the manoeuvre by providing the visualisation of the flow field. This chapter therefore aims to develop a comprehensive understanding of the manoeuvring behaviour of a ship in real sea states.

In this chapter, a study of free-running manoeuvres for the KCS container ship was performed in irregular waves, including course-keeping and turning circle manoeuvres, based on the RANS based CFD method. Free-running manoeuvres in both calm water and regular waves were also carried out, with a view to identifying the changes in the ship manoeuvrability in different environmental conditions. During free-running simulations, self-propulsion conditions were firstly achieved to reach the approach speeds. Then, course-keeping manoeuvres from the stable state of self-propulsion condition were executed to evaluate the steering capability under different wave conditions. Finally, the turning qualities of the ship were assessed by performing standard turning circle manoeuvres.

The remainder of this chapter is framed as follows: Section 9.2 presents a list of the cases to be simulated in CFD for manoeuvring analyses. In Section 9.3, a description of the specific numerical modelling of the CFD model is provided. Then, the CFD results obtained from the manoeuvring simulations (such as course-keeping and turning circle manoeuvres) are illustrated in detail in Section 9.4. Finally, conclusions drawn from this chapter are discussed in Section 9.5.

9.2. Goal and Scope

The major goal of this chapter is to analyse the effects of irregular waves on the course-keeping and turning capabilities of the KCS using a fully nonlinear unsteady RANS model, providing a better understanding of the manoeuvrability of a ship in a real seaway.

The cases to be simulated in CFD are shown in Table 9.1 and Figure 9.1. Course keeping and turning manoeuvres were carried out in five environmental conditions, each identified by their case numbers: *1) irregular head sea, 2) irregular bow sea, 3) regular head sea, 4) regular bow sea, and 5) calm sea*. It should be reiterated that self-propulsion conditions were firstly achieved prior to such manoeuvres. As for the irregular wave conditions (Cases 1 and 2), the JONSWAP spectrum was used to generate long-crested irregular seas with a significant wave height of 0.0665m and a peak period of 1.43s in model scale. These values correspond to a significant wave height of 5m and a peak period of 12.4s in full scale, representing sea state 6. It is worth noting that sea state 6 is characterised by "very rough seas" by the World Meteorological Organisation, almost consistent with the adverse conditions defined by IMO (2021). Sea state 6 was thus adopted in this study in response to a rapidly increasing demand for the evaluation of ship manoeuvrability in adverse sea conditions. Regarding regular wave cases, regular waves were characterised by a wave height and period equal to the average height and period of the irregular waves applied in this study for meaningful comparisons of the results. The free-running manoeuvres in calm water were also carried out to address the inherent

manoeuvring qualities of the ship. Note that all free-running simulations were performed using deep water conditions.

Table 9.1 The simulation cases to which the CFD model is applied.

Property	Case no.				
	1	2	3	4	5
Environmental condition	Irregular wave (JONSWAP Spectrum)	Irregular wave (JONSWAP Spectrum)	Regular wave (5th-order Stokes wave)	Regular wave (5th-order Stokes wave)	Calm sea
Significant wave height H_s (m)	0.0665 (5.0 m in full scale)	0.0665 (5.0 m in full scale)	-	-	-
Peak period T_p (s)	1.43 (12.4 s in full scale)	1.43 (12.4 s in full scale)	-	-	-
Average wave height $\overline{H}$ (m)	0.0407 (3.06 m in full scale)	0.0407 (3.06 m in full scale)	0.0407 (3.06 m in full scale)	0.0407 (3.06 m in full scale)	-
Average wave period $\overline{T}$ (s)	1.20 (10.41 s in full scale)	1.20 (10.41 s in full scale)	1.20 (10.41 s in full scale)	1.20 (10.41 s in full scale)	-
Approach speed U_0 (m/s)	0.925	0.943	0.989	0.945	1.094
Propeller rev. (RPS)	13.38	13.38	13.38	13.38	13.38
Encounter angle μ(degrees)	180 (head sea)	225 (bow sea)	180 (head sea)	225 (bow sea)	-
Encounter Freq. f_e (Hz)	-	-	1.276	1.129	-

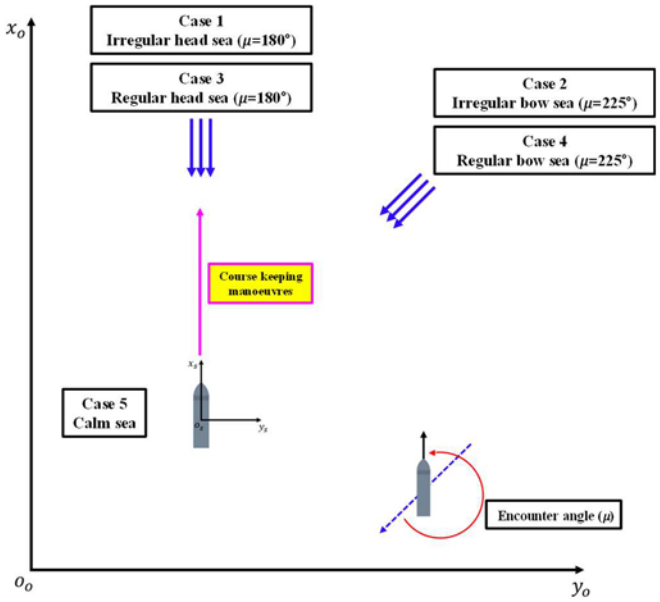

(a) Course-keeping manoeuvres

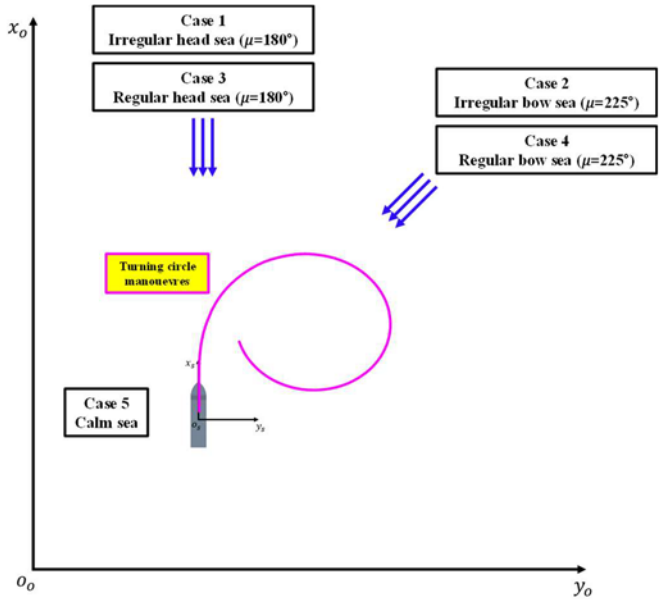

(b) Turning circle manoeuvres

Figure 9.1 Schematic views of the simulation cases applied to this study, (a) course keeping manoeuvres (b) turning circle manoeuvres.

9.3. Numerical Modelling

The free-running CFD models for this chapter were generated based on the numerical setup presented in Chapter 4, Section 4.3.

According to Section 4.3.5, the cut-off frequency of 10 rad/s was chosen for the irregular wave cases (Cases 1 and 2), which satisfies this ratio condition (f_c/f_p=2.3), as depicted in Figure 9.2. Given the cut-off frequency selected, 20 grid points for the shortest wavelength were generated in the *x* and *y* directions (ITTC, 2011). 30 grids points for the expected maximum wave height (1.2 times H_s) were generated in the *z*-direction based on CSP (2021). When it comes to the regular wave simulations (Cases 3 and 4), 80 cells per wavelength in the *x* and *y* directions and 20 cells per wave height in the *z*-direction were generated, applying a constant cell size for both *x* and *y* directions in the refined grid area for the free surface (ITTC, 2011).

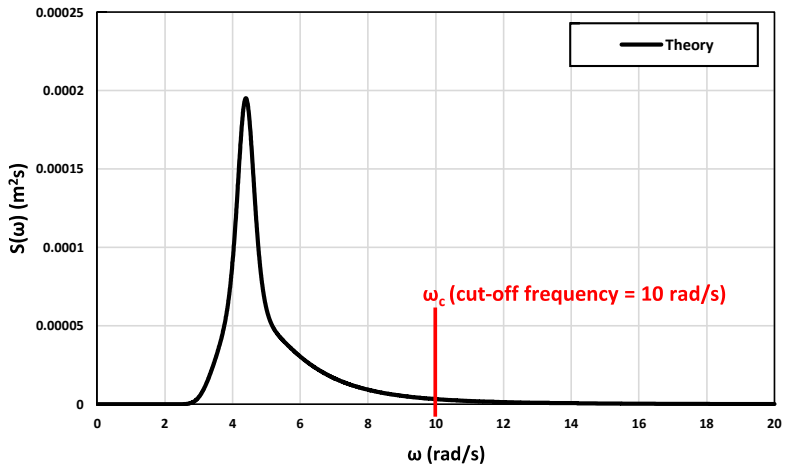

Figure 9.2 The JONSWAP wave spectrum applied in this study (sea state 6, $\mathbf{H_s}$=0.0665m and $\mathbf{T_p}$=1.43s).

Figure 9.3, as an example, presents the cross-sections of the final computational mesh obtained from Case 1 and 2 (the irregular wave condition). Three different mesh generations were applied for the free-running simulation in this chapter (Case 1 and 2 - irregular waves, Case 3 and 4 - regular waves, and Case 5 - calm water), resulting in a computation mesh of circa 14, 11, and 6 million cells in total, respectively.

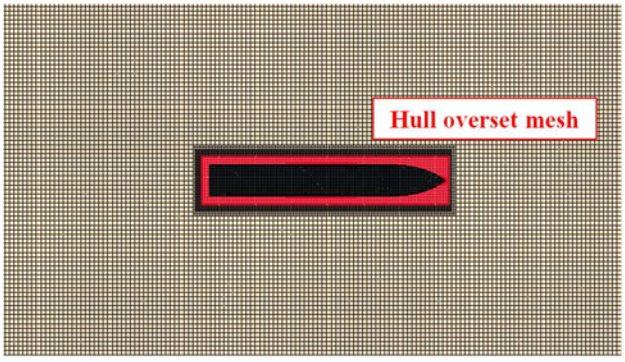

(a) Top view cross-section of the domain

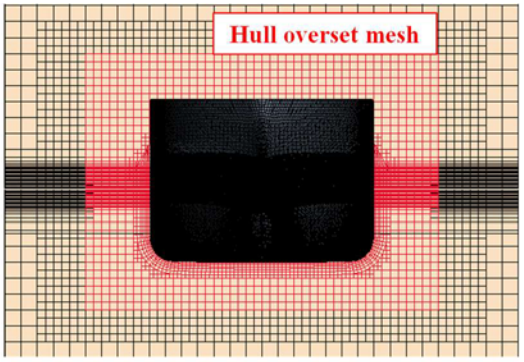

(b) Midship cross-section of the domain

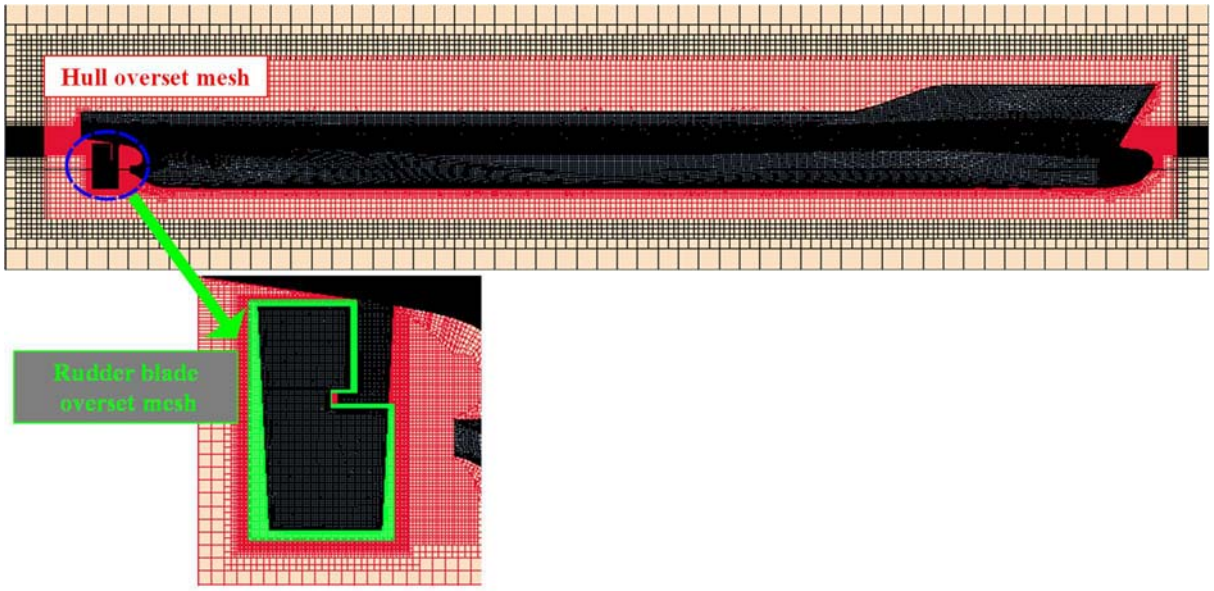

(c) Profile view cross-section of the domain

Figure 9.3 Mesh structure of the computational domain, Case 1 and 2 (Irregular wave cases).

To gain an accurate description of the wave propagation, two different time step resolutions were selected based on the flow properties of each simulation. For irregular wave simulations, ITTC (2011) recommends that a minimum of 60 time steps per period for the shortest waves should be used. Note that the shortest wave period can be estimated by determining the cut-off frequency, as previously seen in Figure 9.2. Accordingly, the time step was chosen at 2.5×10^{-3} seconds for the irregular wave cases (Cases 1 and 2), which is lower than that calculated from the recommendation of ITTC (2011). For the regular wave cases (Cases 3 and 4), the time step was determined at 5.0×10^{-3} seconds, which satisfies the guidelines of ITTC (2011) where a minimum of 100 time steps per period for regular waves should be used. The time step used in the regular wave simulations was also applied to the calm water case (Case 5).

9.4. Results

9.4.1. Wave generation

It is important to ensure that the number of waves encountered should be large enough during the computation for accurately calculating the statistical characteristics of irregular seas. ITTC (2017a) recommends that a minimum of 50 waves should be encountered for model scale tests in the presence of irregular waves, while further highlighting encountering 100 waves is preferred for the resultant values of the significant wave height and modal period. Since the selection of encountering 100 waves requires a significantly high run time, the present study complied with the minimum requirement (50 waves) for the validation of irregular wave generation to compromise the computational resources and accuracy. It is worth noting that it is technically difficult to record the wave elevation at a fixed point in the present free-running simulation because of the moving computational domain. Alternatively, an additional simulation was performed by generating the static background domain (without hull and rudder grids) with the same background grids used for the manoeuvring simulation. In the simulation,

the wave elevation was recorded using the wave probe located 1.20 LBP in front of the ship to monitor the irregular waves generated. Figure **9.4** shows the time history of the wave elevation recorded by the probe. The Fast Fourier Transform (FFT) was applied to the time series of the wave elevation displayed in the figure (a sampling frequency of 400 Hz) to produce the spectrum of the generated wave in Figure **9.5**. Once the wave spectrum is determined, all statistical wave parameters can be derived by using the spectral technique. The n^{th} order spectral moment can be written by

$$m_n = \int_0^\infty \omega^n S_J(\omega) d\omega \tag{9.1}$$

in which ω is the incident wave frequency, $S_J(\omega)$ is the JONSWAP spectrum. The square root of the zeroth spectral moment multiplied by 4, i.e., $4\sqrt{m_0}$, corresponds to the significant wave height (H_s), which describes the average height of the highest one-third of all waves measured. $2.5\sqrt{m_0}$ and $2\pi\frac{m_0}{m_1}$ represent the average wave height ($\overline{H}$) and period ($\overline{T}$).

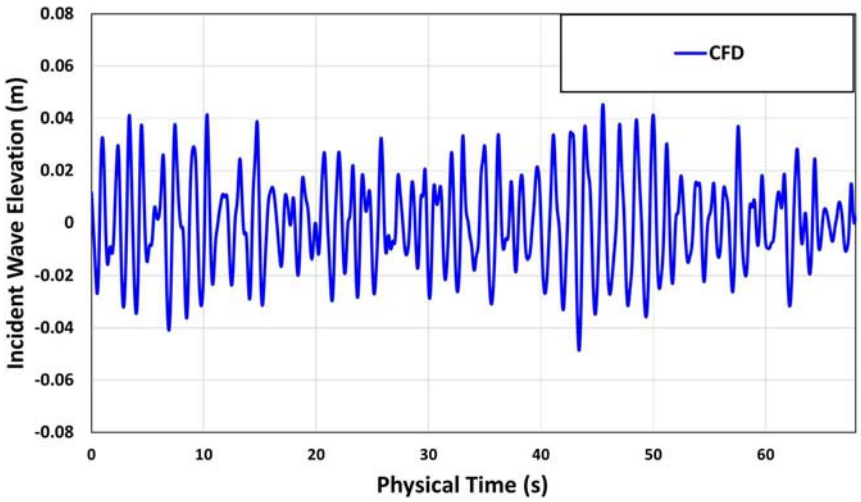

Figure 9.4 The time history of wave elevation for the irregular head sea condition at the numerical wave probe.

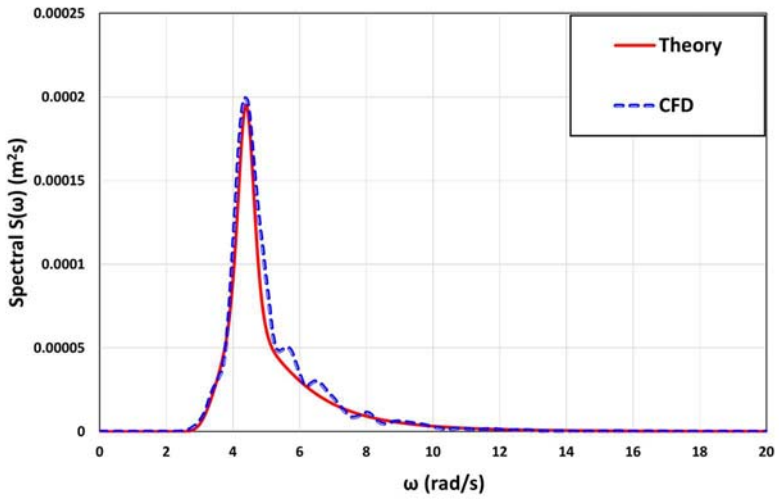

Figure 9.5 The comparison of the wave spectrum between the theoretical JONSWAP spectrum and the CFD results (concerning the irregular head sea condition) for sea state 6 ($\mathbf{H_s}$=0.0665m and $\mathbf{T_p}$=1.43s).

The critical wave characteristics obtained by the spectral analysis are given in Table **9.2** and are compared to those calculated from the theoretical JONSWAP spectrum. From Table **9.2**, it can be found that for the statistical quantities of waves, the current CFD model showed differences ranging from 1.66 – 6.63% of the theoretical values. Considering the current cell size and time step, these differences were seen to be acceptable, and the wave generation to be performed for manoeuvring simulations can be claimed to be reasonably validated.

Table 9.2 Wave characteristics in the validation study.

	Significant wave height H_s (m)	Average wave height $\overline{H}$ (m)	Average wave period $\overline{T}$ (s)
Theory (JONSWAP spectrum)	0.0665	0.0407	1.20
The Current CFD (Spectral analysis)	0.0695	0.0434	1.22
Error (% of theory)	4.51	6.63	1.66

9.4.2. Course keeping control

To evaluate the course keeping capability, the true course (the target heading angle ψ_c) was set at 000° throughout all the course keeping manoeuvres. Figure 9.6 presents the time histories of the yaw angle and rudder deflection under the course keeping manoeuvres for all cases. In agreement with the coordinate frames defined in this thesis, a positive yaw angle indicates the direction of rotation to starboard whilst a negative yaw angle refers to the direction of rotation

to port. The rudder angle is positive when turning to starboard while making the ship's heading to port, and a negative rudder angle means the rudder deflection for making the ship's heading to starboard. It can be easily seen from the figure that the rudder deflection became remarkably larger when the ship was moving forward in the irregular bow (Case 2) and regular bow seas (Case 4), i.e., oblique waves. This means that oblique incident waves make the ship's heading control more challenging. The reason for large rudder deflections is closely related to the asymmetric pressure distribution acting on the hull generated by oblique waves, resulting in a substantial yaw moment and thus the heading angle deviation from the target one. The advancing ship in the irregular bow sea experienced the randomly varying behaviour of the yaw and rudder angle during the course keeping manoeuvre, different from that identified in the regular bow sea. This is due to the irregularity in wave height and period based on the JONSWAP spectrum. The maximum rudder deflection in irregular and regular bow seas was observed to be approximately 11.5° and 5.9°, respectively.

Unlike the oblique wave conditions (Cases 2 and 4), it was found that the heading control in the irregular head (Case 1), regular head (Case 3), and calm seas (Case 5) was not an issue. In other words, very small heading deviations were observed with less than 0.5° during the course keeping manoeuvre. This mainly resulted from the symmetric pressure distribution on the hull, which hardly caused the yaw moment to make the ship turn. It is important to note that despite the irregularity in wave height and period, heading deviations rarely occurred in the irregular head sea, which implies that the wave coming from the ship's bow can be the desired environmental condition for course keeping control. It is also worth noting that in Cases 1, 3, and 5, small rudder deflections towards the port side were observed within a value of 2.5º when the ship was advancing. Such small deflections were closely correlated to the intrinsic nature of a right-handed propeller, i.e., a non-uniform flow generated by the propeller. To give an example, Figure **9**.**7** presents the snapshots of the longitudinal flow velocities around the rudder and the pressure distribution on the rudder blade during the course keeping manoeuvre. It can be noticed from the figure that the rudder surface is in the slipstream of the actuator disk model, experiencing the flow acceleration. The flow velocity on the port side of the rudder is slightly larger than that on the starboard side when the vessel was sailing forward with the neutral rudder angle. This is due to the non-uniform flow induced by the disk model, resulting in the pressure difference between the starboard side and the port side of the rudder. This uneven pressure exerted a small rudder lift force directed towards the port and thus led to the yaw moment to turn the ship's heading to the starboard side to a small extent. To counterbalance the undesirable yaw moment, the rudder blade was slightly deflected to the port side. This contribution to the ship's heading control is clearly evidenced in Figure 9.6 (a), (c), and (e).

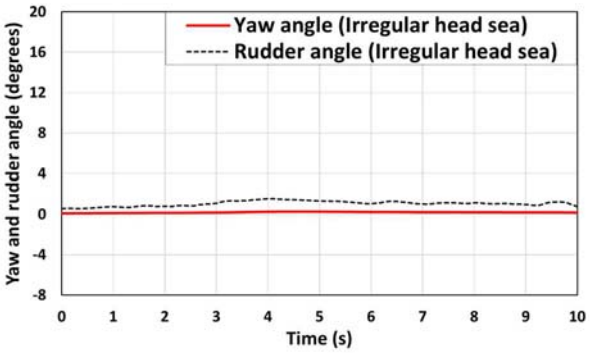

(a) Irregular head sea (Case 1)

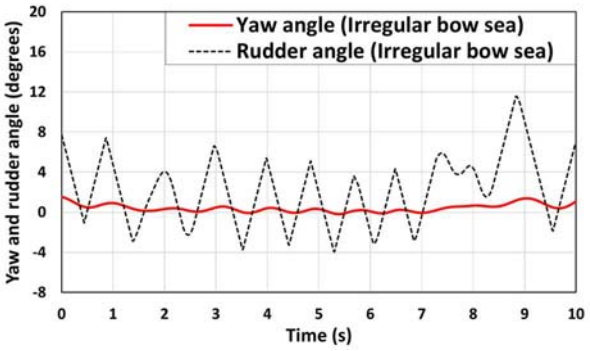

(b) Irregular bow sea (Case 2)

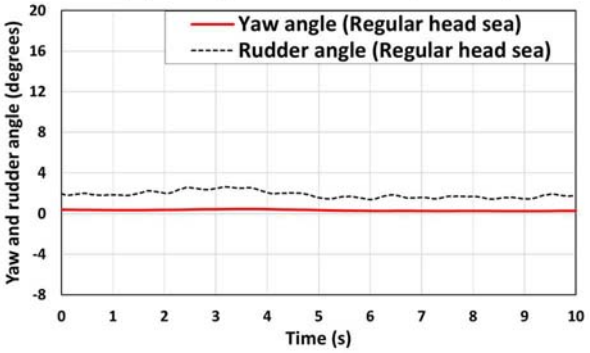

(c) Regular head sea (Case 3)

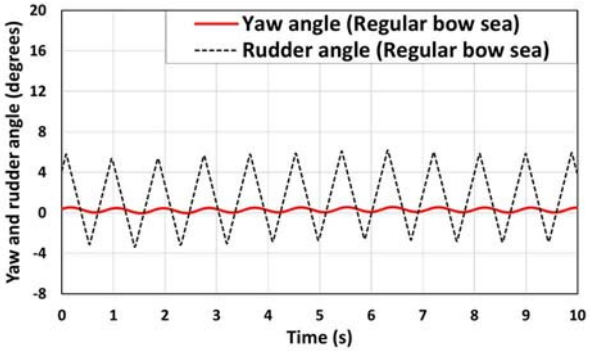

(d) Regular bow sea (Case 4)

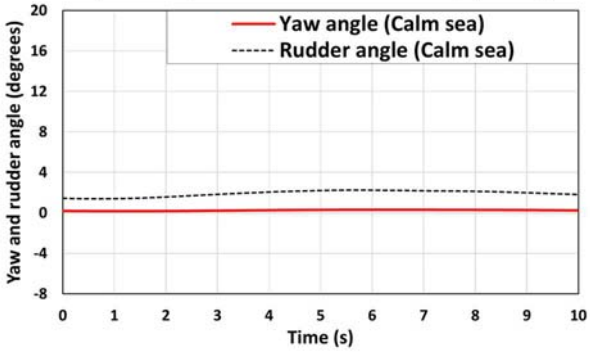

(e) Calm sea (Case 5)

Figure 9.6 The time histories of the yaw angle and rudder deflection during the course keeping manoeuvre.

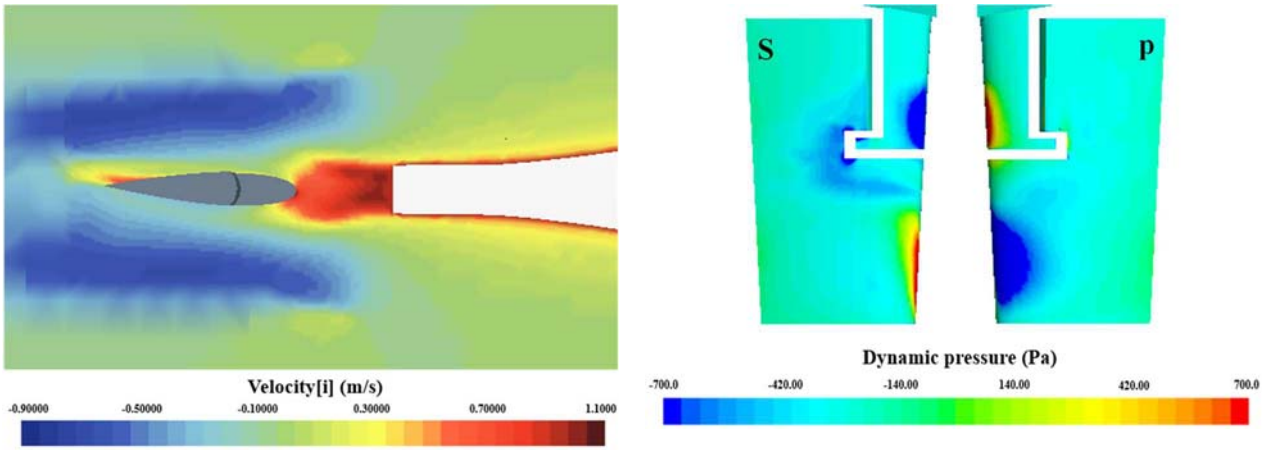

(a) Irregular head sea (Case 1)

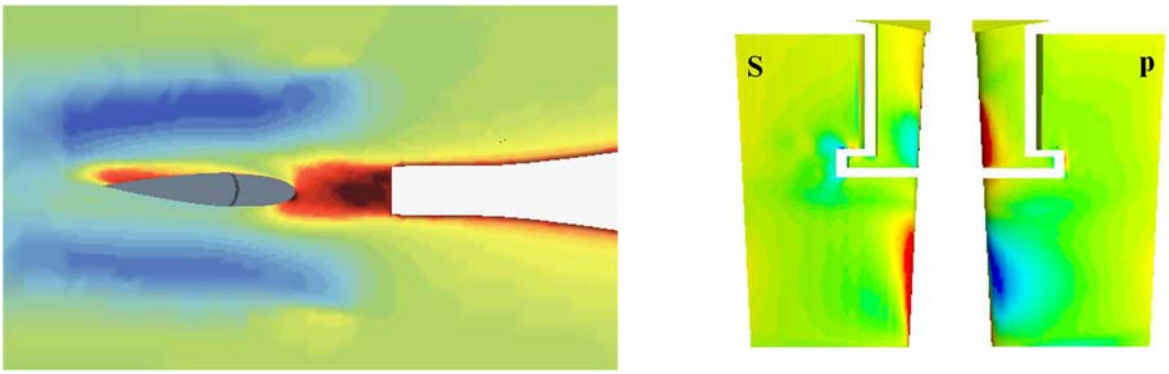

(b) Irregular bow sea (Case 2)

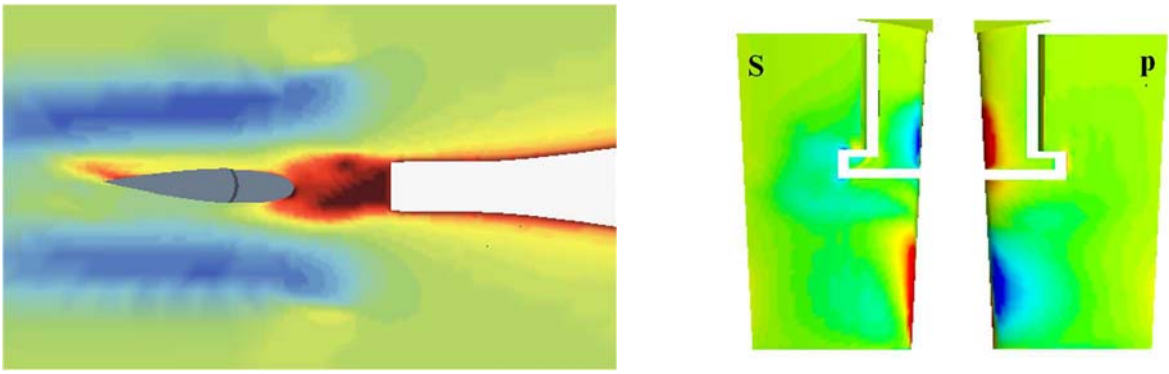

(c) Regular head sea (Case 3)

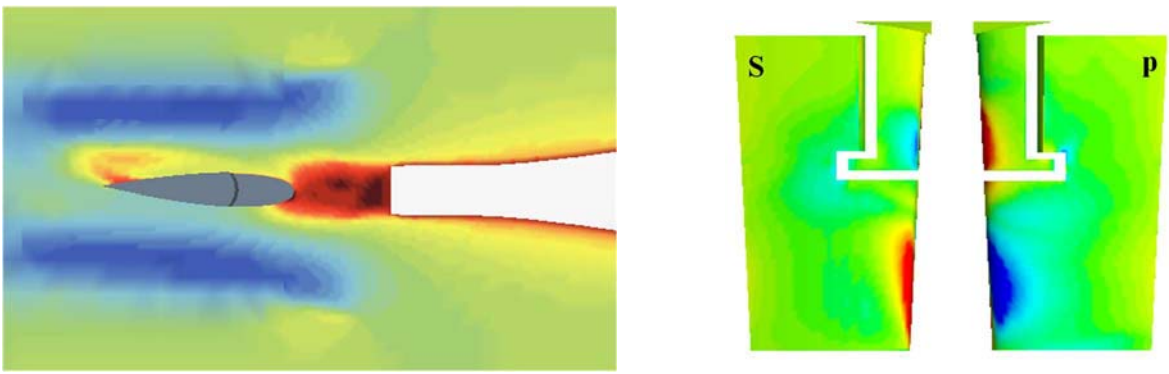

(d) Regular bow sea (Case 4)

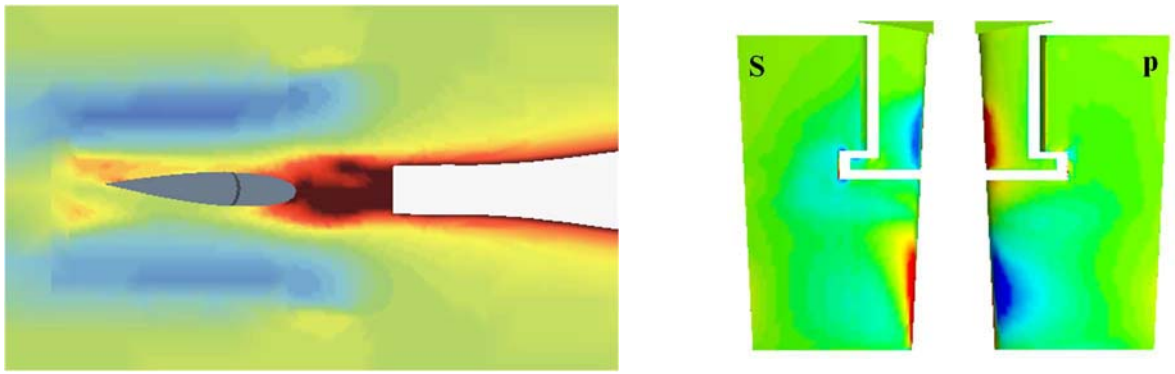

(e) Calm sea (Case 5)

Figure 9.7 The snapshots of the axial flow velocities around the rudder (left column) and the pressure distribution on the rudder (right column, S: starboard profile, P: port profile) during the course keeping manoeuvre.

The trajectories experienced by the ship during the course keeping manoeuvre are depicted in Figure **9.8**. In the figure, the origin point (0,0) represents the position where the course keeping manoeuvre started. As it can be seen, the advancing ship in the irregular and regular bow seas (Cases 2 and 4) exhibited a large deviation from the planned course, considerably biased towards the port side. This can be explained by the strong lateral force induced by the oblique waves, and the resultant paths indicated the relatively poor course keeping ability of the ship. It clearly appeared that the regular bow sea condition showed a poorer course-keeping response when compared with the irregular bow sea condition in terms of ship trajectory drifts. In other words, the difference for the trajectory drift between Case 2 and Case 4 occurred although the equivalent wave input parameters, i.e., the same average wave height and period, were applied. The possible reason for this difference may stem from the difference in the total incident wave energy (being proportional to the wave height squared) experienced by the ship during the course keeping manoeuvre. In addition, the oblique seas (i.e., the irregular and regular bow seas) commonly led to obvious oscillations for the trajectories because of the rudder behaviour with short-term oscillations (Figure 9.6 (b) and (d)). On the other hand, good course-keeping control was achieved with a very small deviation by the advancing ship in the irregular head, regular head, and calm seas. This is intimately related to the very small heading deviation caused by the non-uniform flow. It has to be pointed out that the steering capability can be further improved by applying the optimum gains to mitigate the deviation from the original course.

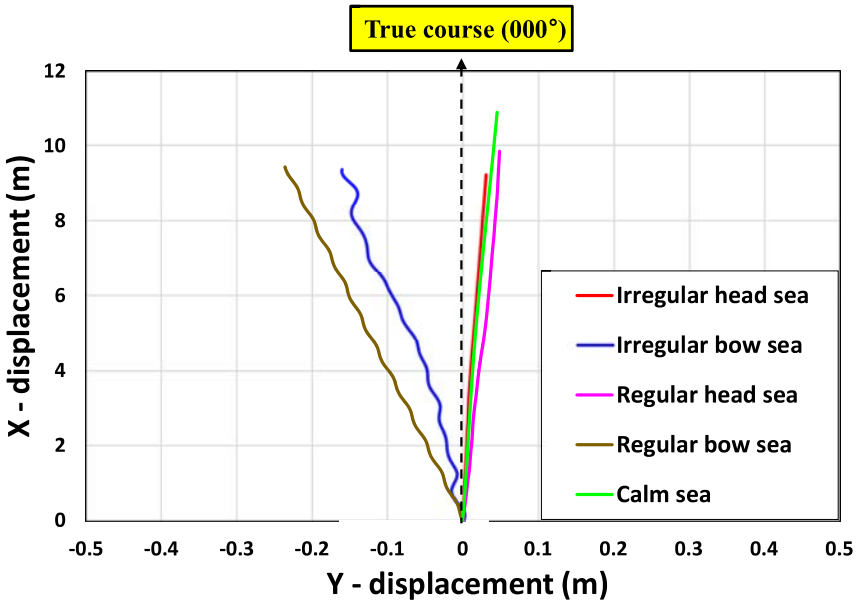

Figure 9.8 The comparison of the predicted trajectories for all cases.

In order to visualise the wave contours generated by the presence of the ship under course keeping control, the snapshots of the free surface wave elevations for all cases are presented in Figure **9.9**. It is clearly seen from the figure that asymmetric wave profiles were generated in the irregular and regular bow seas (Cases 2 and 4), which resulted in a large lateral force and yaw moment. When the ship was moving forward in the oblique waves, the free surface elevation on the starboard-bow side was higher than that on the port-bow side (Figure **9.9** (b) and (d)). As expected, symmetric wave profiles around the ship were observed for the other cases (Cases 1, 3, and 5), which can barely cause the lateral force and yaw moment.

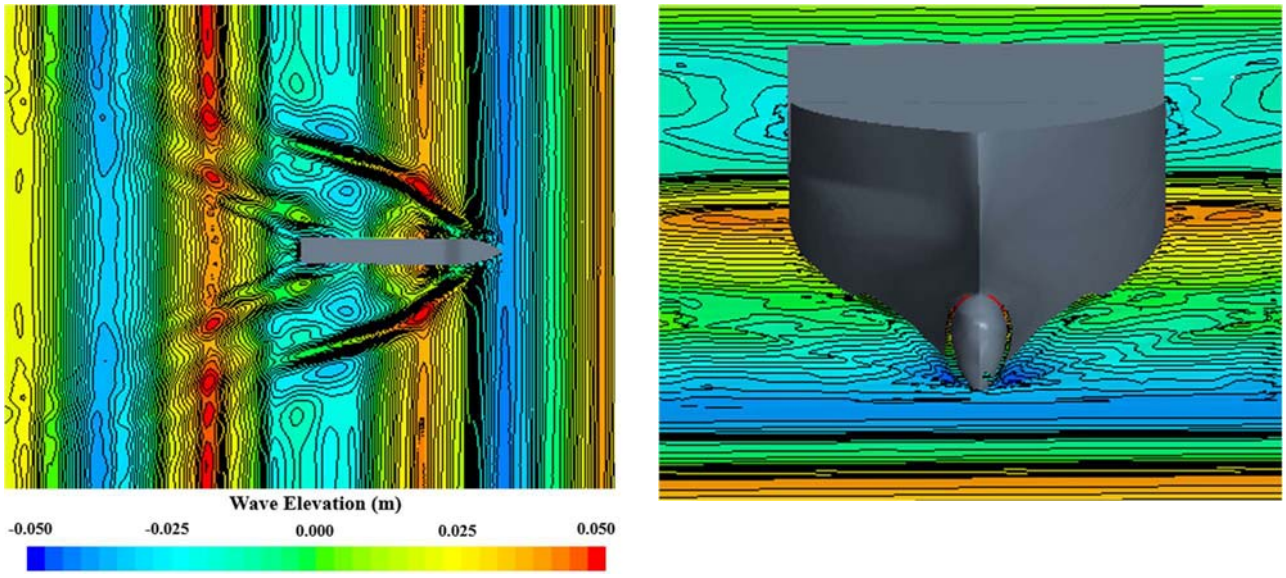

(a) Irregular head sea (Case 1)

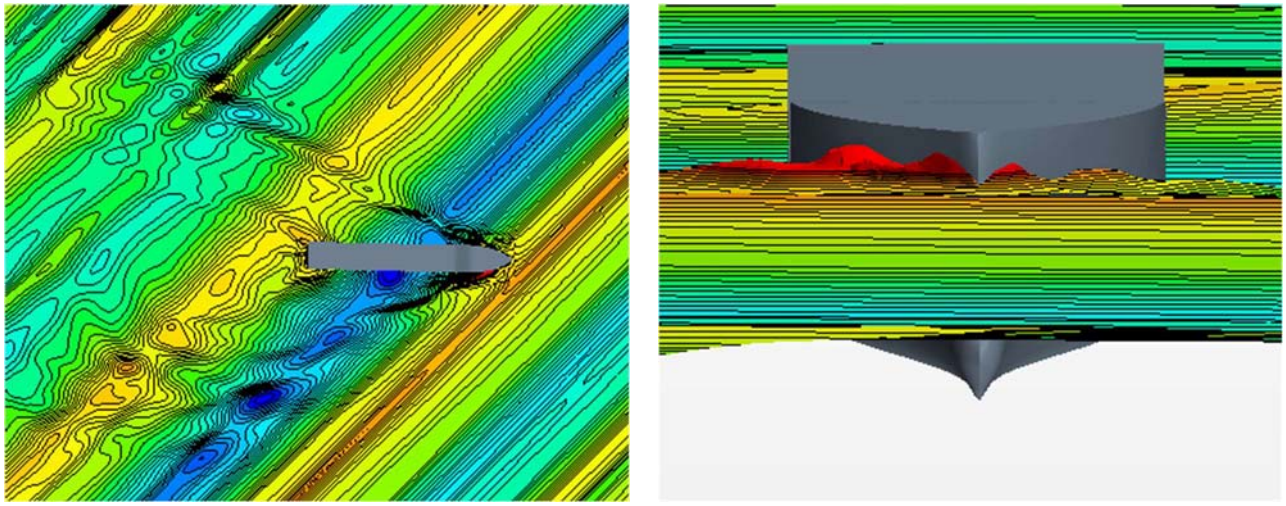

(b) Irregular bow sea (Case 2)

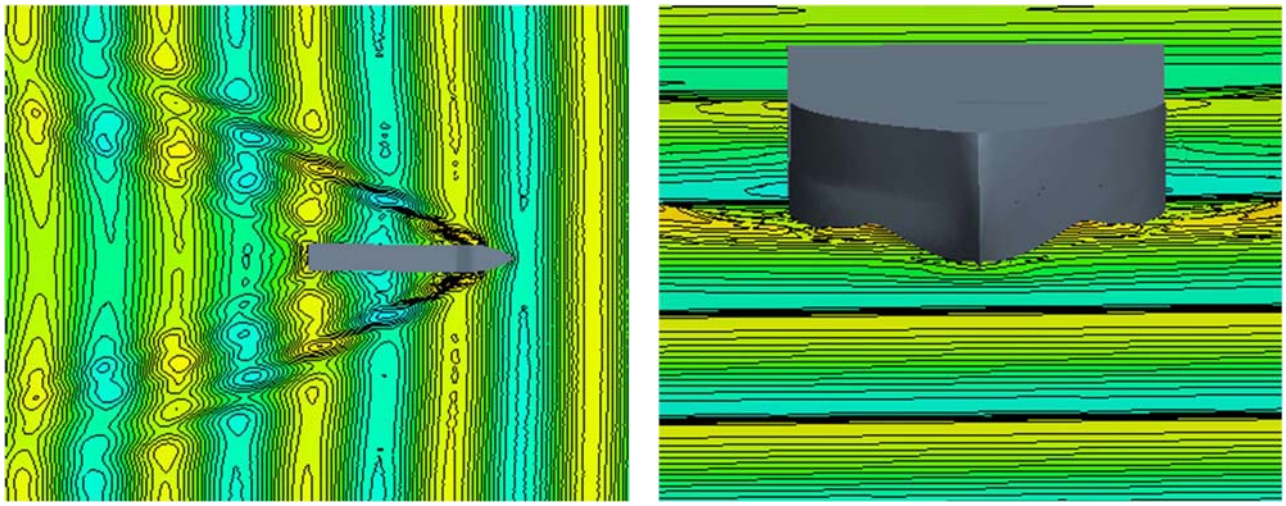

(c) Regular head sea (Case 3)

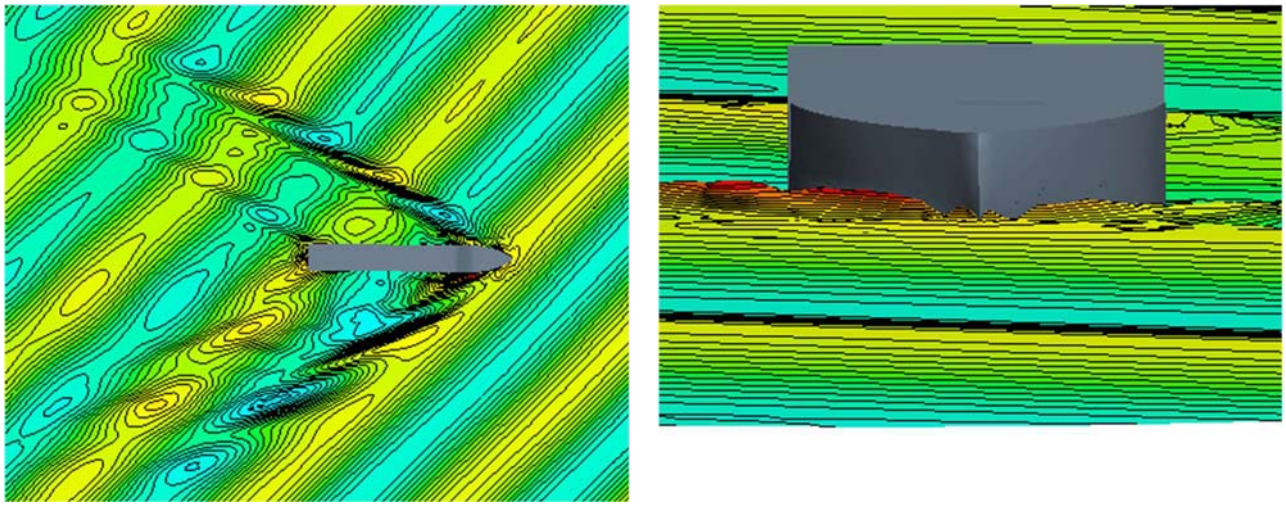

(d) Regular bow sea (Case 4)

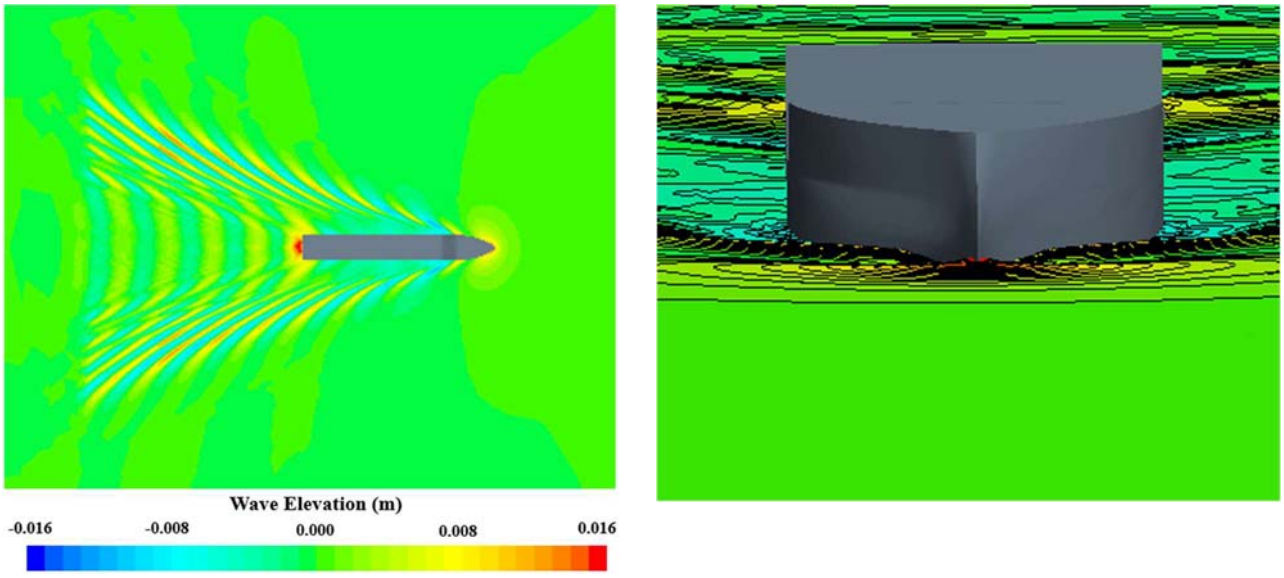

(e) Calm sea (Case 5)

Figure 9.9 Measured wave elevation around the KCS hull under course keeping control (left column: top view, right column: front view).

9.4.3. Turning circle manoeuvre

In this sub-section, the turning ability of the KCS model in each simulation will be presented in detail and the results will then be compared to each other. It has to be mentioned that this section dealt with the turning manoeuvres with only the yaw angle variation of 360° based on the guidelines (IMO, 2002). The turning circle manoeuvres were restarted from the self-propulsion conditions, deflecting the rudder blade to a maximum of 35° (towards the starboard side). The total simulation running time (to complete 360° turns) including the acceleration phase was approximately 75s for the irregular wave cases (Cases 1 and 2), 71s for the regular wave cases (Cases 3 and 4), and 100s for the calm water case (Case 5). For each irregular wave case, the time to complete the computation was around 1,500 wall clock hours and 60,000 CPU hours with 40 CPU processors. Each regular wave simulation required 14,320 CPU hours with 40 CPU processors, completed in approximately 358 wall clock hours, while the calm water simulation needed 5,700 CPU hours with 40 CPU processors to complete the computation.

9.4.3.1 Time histories during turning and turning indices

The predicted ship trajectories of the turning circle manoeuvre for all cases are presented in Figure 9.10, where each case is indicated with a different colour. In the figure, the fixed point (0,0) is the position at which the rudder blade started to be deflected for the manoeuvre. It appears from Figure 9.10 that the irregular and regular wave conditions led to substantial changes in the ship's turning capability when compared to the ship's inherent turning ability in calm water, clearly evidenced by the remarkable differences in the turning trajectory. The contribution of the wave direction to the turning trajectory was also noticed to some extent, confirming the deformation of the turning circle path compared to the trajectory in calm water (due to the wave drift forces and moments). Interestingly, in the case of the same wave direction, the overall trajectory experienced by the ship in the irregular wave was roughly similar to the one observed in the regular wave, exhibiting a similar final position at the end of the manoeuvre.

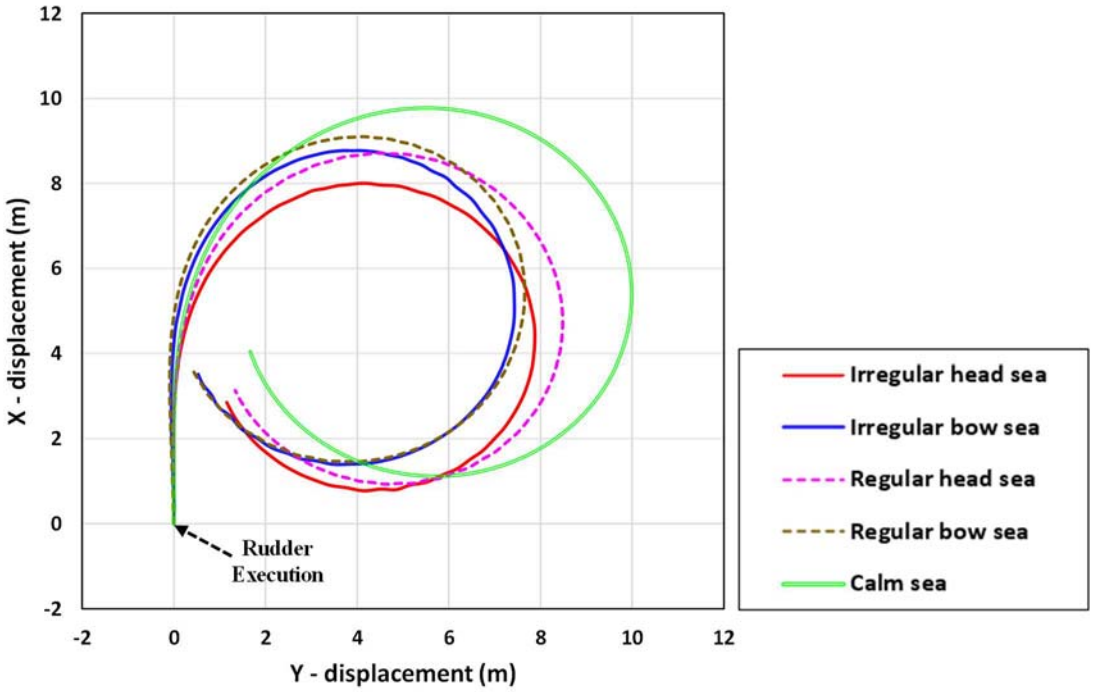

Figure 9.10 The turning circle trajectories for all cases.

The critical manoeuvring indices (i.e., the advance, the transfer, the tactical diameter, and the time to 90°/180° yaw angle change) are summarised in Table 9.3. The time histories of the predicted ship velocities, forces, and moments during the manoeuvre are shown in Figure 9.11 (surge, sway, and yaw parameters with respect to the ship-fixed coordinate and rudder normal force with respect to the rudder-fixed coordinate depicted in Figure 4.4). The critical turning parameters are highly dependent on the ship's horizontal motions, namely surge, sway, and yaw motions which are determined by the complex interactions between the hull, propeller, rudder, and environmental loads. Such ship motions have a close correlation with the ship velocities in the horizontal plane (surge, sway, and yaw velocities). In general, the greater the surge speed and the smaller the yaw velocity in the initial transient phase of the turn, the greater the ship advance can be. The maximum ship advance was found to be $3.13L_{BP}$ in calm water (Case 5), mainly due to the much larger approach speed compared to the wave cases. The advance experienced by the ship in the irregular head sea (Case 1, $2.54L_{BP}$) was predicted to be smaller than that in the irregular bow sea (Case 2, $2.80L_{BP}$) because of the relatively smaller approach speed and the shorter time taken for 90° turn. The regular bow sea condition (Case 4, $2.90L_{BP}$) showed a greater ship advance than the regular head sea condition (Case 3, $2.77L_{BP}$) due to the longer time taken for 90° turn, despite the smaller approach speed. It is worth noting that the ship manoeuvring in the irregular head sea (Case 1) achieved a shorter 90° turning time when compared to in the irregular bow sea (Case2). This may be ascribed to the wave force and moment acting on the ship during the initial transient phase, resulting in the different increasing trend of the yaw velocity after the rudder deflection (significant fluctuations were noted in the irregular bow sea. In the same manner, the regular head sea condition (Case 3) achieved a shorter 90° turning time than the regular bow sea condition (Case 4). As it can be

seen from Figure 9.10 and Table 9.3, the smaller transfer and tactical diameter were achieved by the ship performing the turning manoeuvre in the irregular bow sea condition (Case 2) compared to the irregular head sea condition (Case 1). This may be attributed to the wave drift force acting on the ship in the bow seas, and the contribution to the ship trajectory is clearly evidenced in Figure 9.10 (the trajectory drift direction was noted to be similar to the wave propagation direction). In the same way, the ship manoeuvring in the regular bow sea condition (Case 4) experienced the smaller transfer and tactical diameter than the regular head sea condition (Case 3).

Table 9.3 CFD results: turning indices in irregular, regular and calm seas.

Parameters (CFD results)	Case 1	Case 2	Case 3	Case 4	Case 5
Advance (m)	7.78 **($2.54L_{BP}$)**	8.56 **($2.80L_{BP}$)**	8.48 **($2.77L_{BP}$)**	8.86 **($2.90L_{BP}$)**	9.55 **($3.13L_{BP}$)**
Transfer (m)	2.92 **($0.95L_{BP}$)**	2.73 **($0.89L_{BP}$)**	3.26 **($1.07L_{BP}$)**	2.82 **($0.92L_{BP}$)**	4.07 **($1.33L_{BP}$)**
Time for yaw 90 degrees (s)	12.01	12.49	11.69	12.71	12.31
Tactical diameter (m)	7.64 **($2.49L_{BP}$)**	7.25 **($2.37L_{BP}$)**	8.23 **($2.69L_{BP}$)**	7.43 **($2.43L_{BP}$)**	9.82 **($3.21L_{BP}$)**
Time for yaw 180 degrees (s)	22.82	23.60	22.85	23.94	24.20

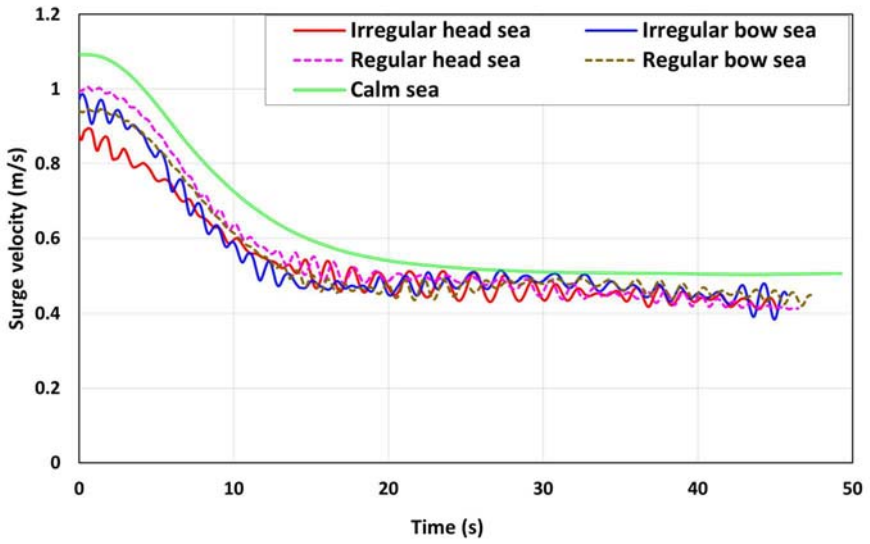

(a) Surge velocity

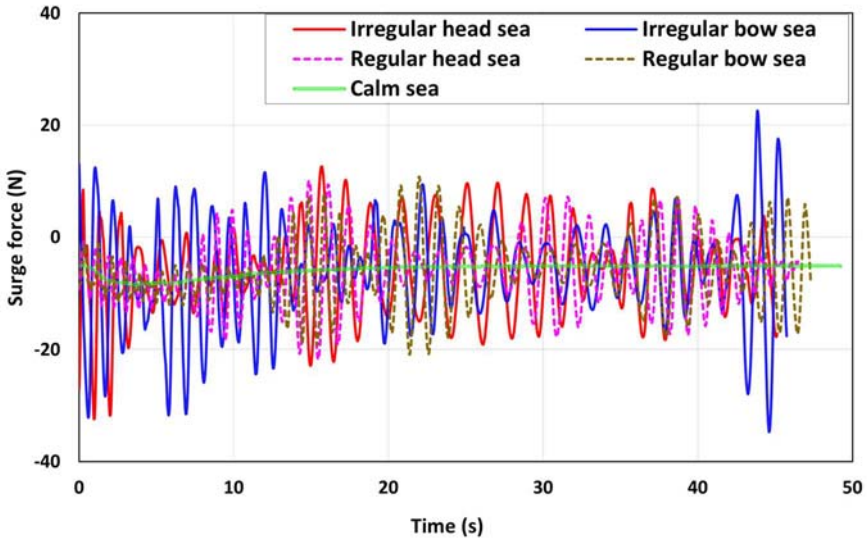

(b) Surge force

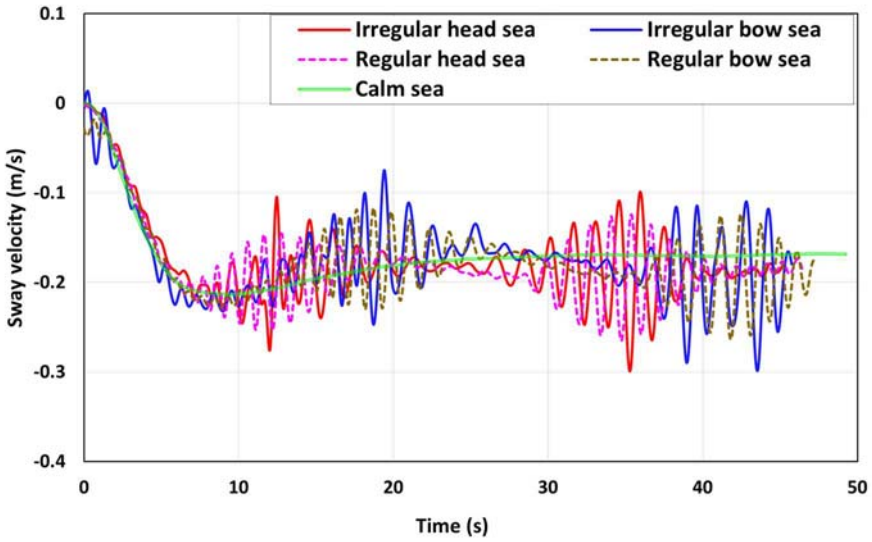

(c) Sway velocity

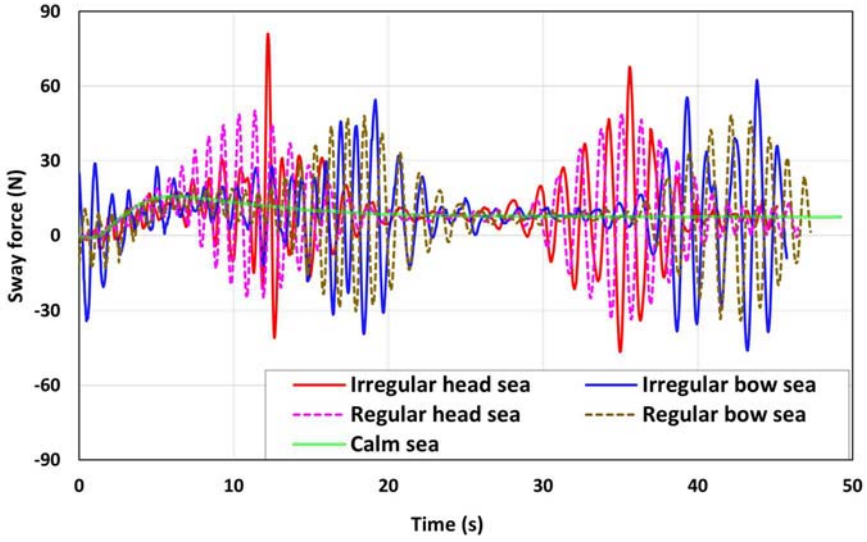

(d) Sway force

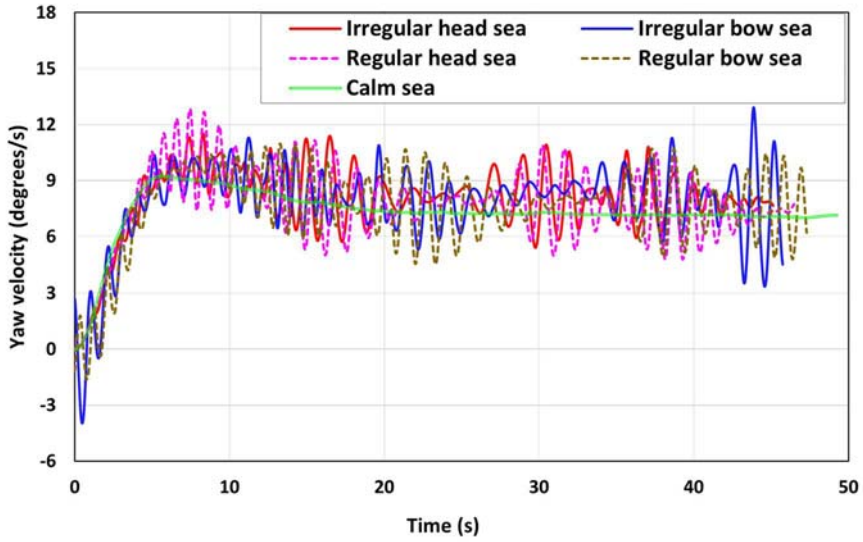

(e) Yaw velocity

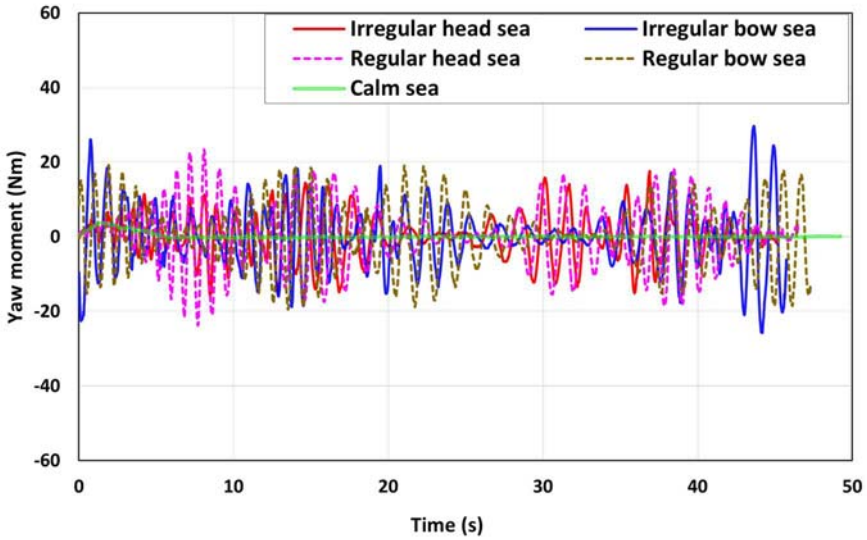

(f) Yaw moment

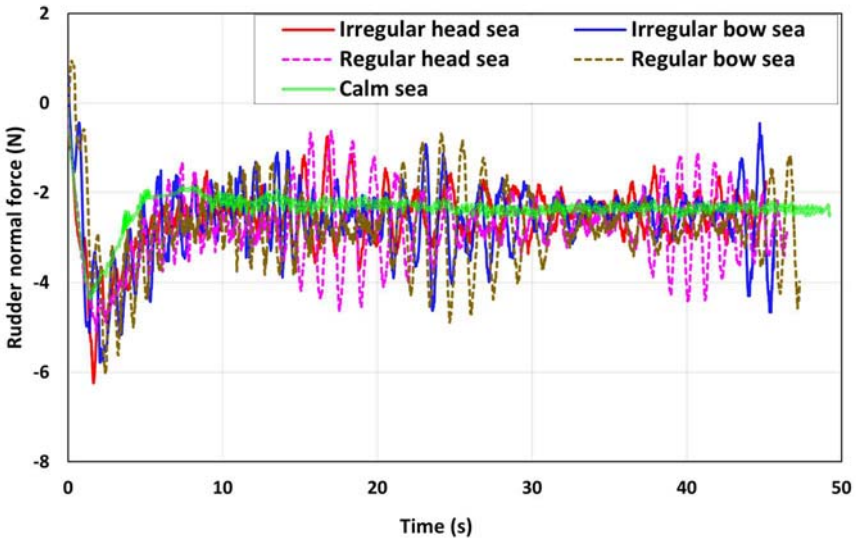

(g) Rudder normal force

Figure 9.11 The time histories of the ship velocities, forces, and moments during the ship's turning manoeuvre.

It was observed from Figure 9.11 that the rudder exerted a strong rudder normal force directed port side as it was actuated in the very early phase of the turn; this lateral force offered the positive yaw moment required to start the starboard turning manoeuvre. Figure 9.12, as an example, displays the snapshots of the axial flow velocities around the rudder and the pressure distribution of the rudder according to the rudder deflection angle in the very initial phase of the turn. The pictures are the snapshots obtained from Case 1 (the irregular head sea condition), which can present how the rudder generates the rudder normal force for the ship's turning. From the figure, it clearly appears that as the rudder deflection angle increased, the pressure difference between the starboard and the port of the rudder blade gradually increased. The uneven pressure distributions on the rudder yielded a strong lateral force towards the port side and the resulting yaw moment (positive) enabled the ship to the turning manoeuvre. From Figure 9.11, it can be found that the ship experienced an involuntary surge speed loss after the rudder was deflected to a maximum 35-degree angle. This was associated with an increase in the ship resistance caused by a large drift angle. Afterwards, some variations in the forward speed were found according to the wave-encounter condition. Under the wave conditions, a greater increase in the forward speed was obviously observed when the ship encountered the following waves whereas a greater decrease was noted in head seas during the ship's turning. The surge velocities and forces showed high-frequency fluctuations caused by the wave-induced ship motions while the ship was turning in waves, but the fluctuations significantly decreased when the ship experienced the beam waves during the turning manoeuvre. The sway velocities experienced a rapid increase until about 7s after the start of the turning manoeuvre and then showed a tendency to converge to between -0.20m/s and -0.17m/s with some fluctuations around their average value according to the environmental condition. The sway forces followed the same trend. Unlike the surge velocities and forces, the large fluctuations in the sway velocities and forces were noted when the ship experienced beam seas, whilst the fluctuations almost disappeared under the following seas. The yaw velocities and moments showed the large fluctuations when the ship experienced the oblique waves during the ship's

turning. The yaw velocities reached maximum approximately 6s after the rudder deflection. Then, they were observed to converge quickly to the values which were estimated at 7.9º/s for Case 1, 8.1º/s for Case 2, 7.3º/s for Case 3, 7.6º/s for Case 4, 7.1º/s for Case 5.

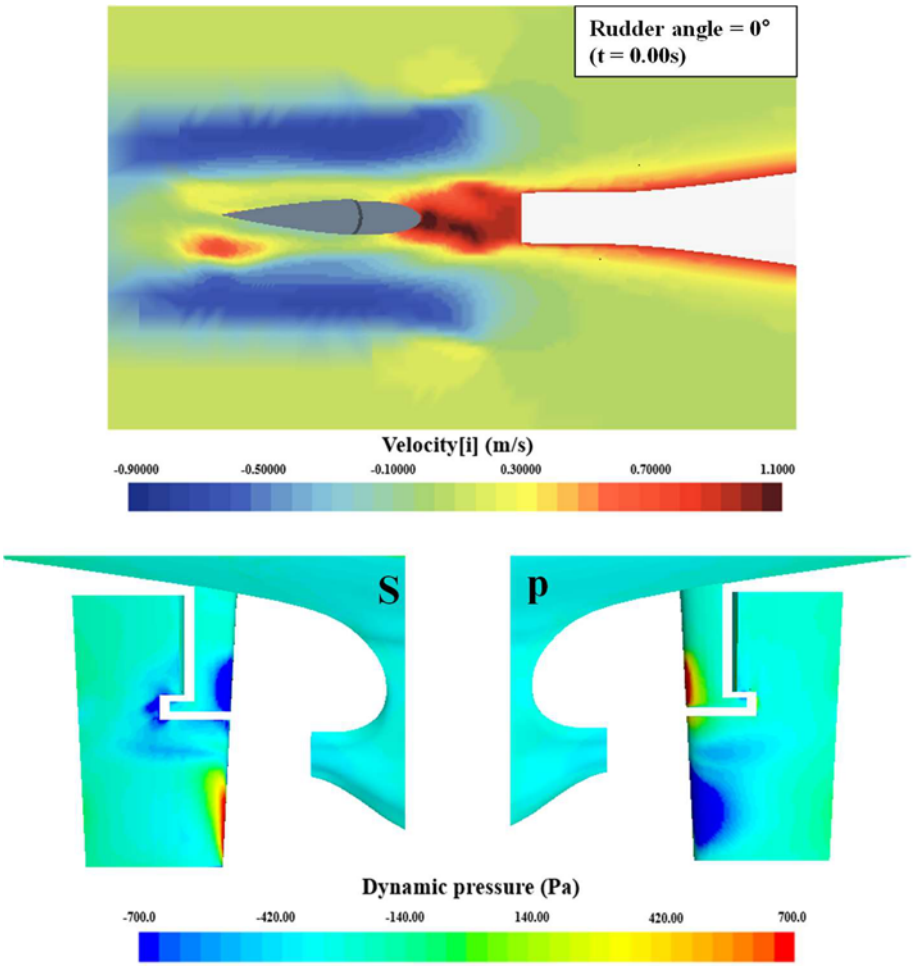

(a) Rudder angle = 0° (t= 0.00s)

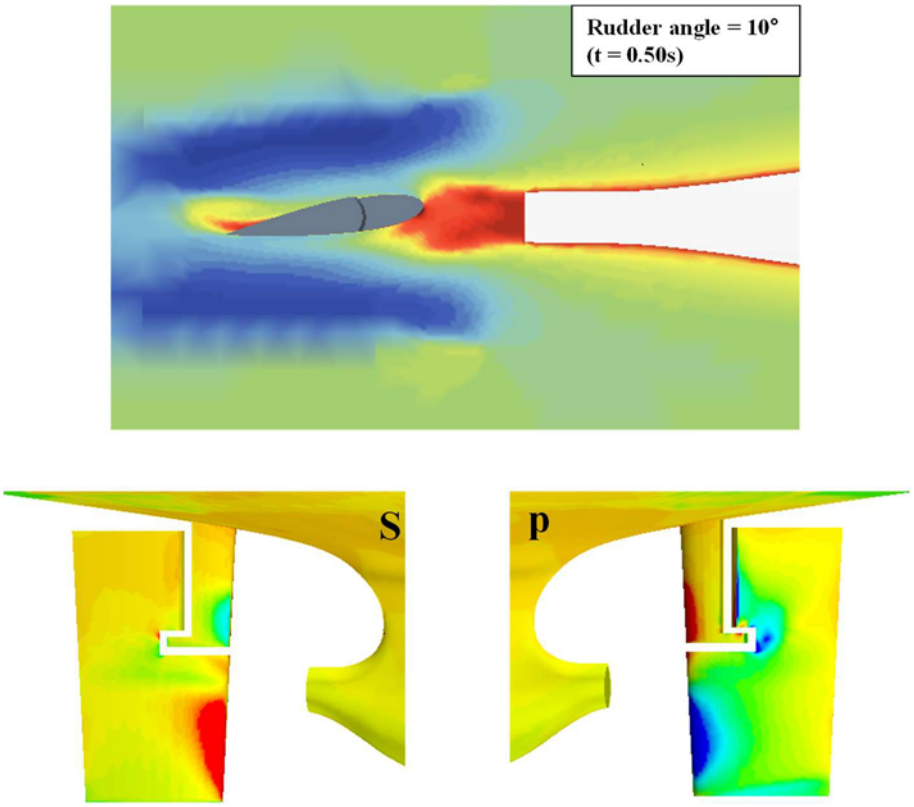

(b) Rudder angle = 10° (t= 0.50s)

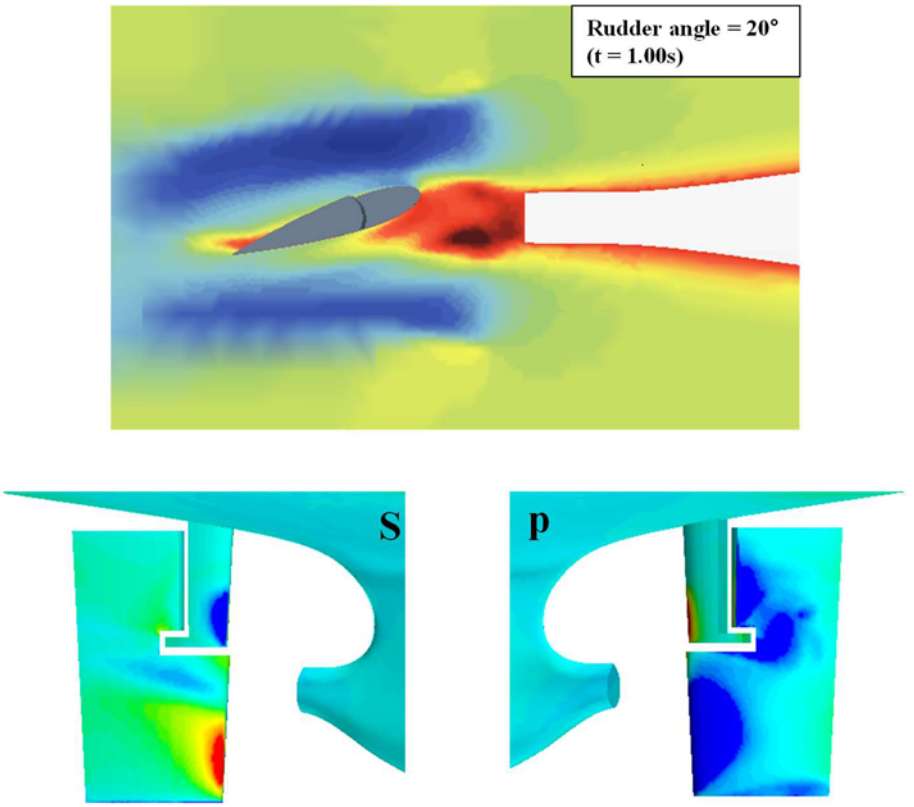

(c) Rudder angle = 20° (t= 1.00s)

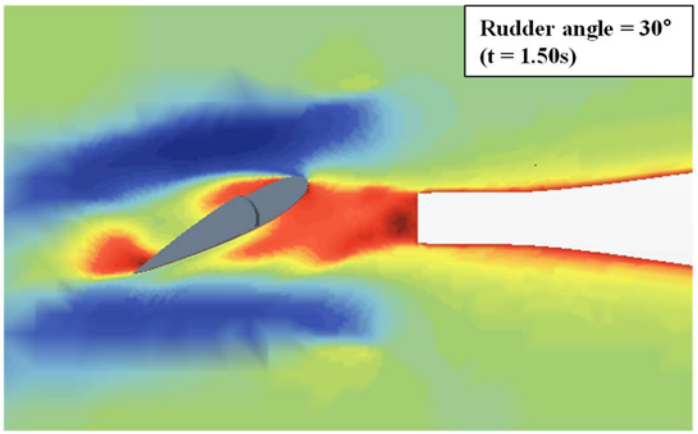

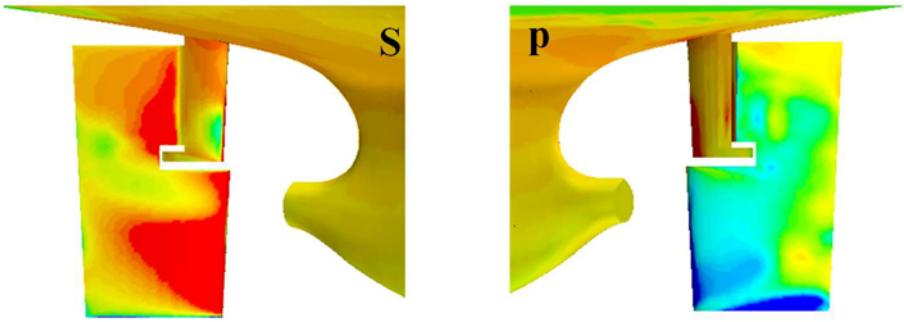

(d) Rudder angle = 30° (t= 1.50s)

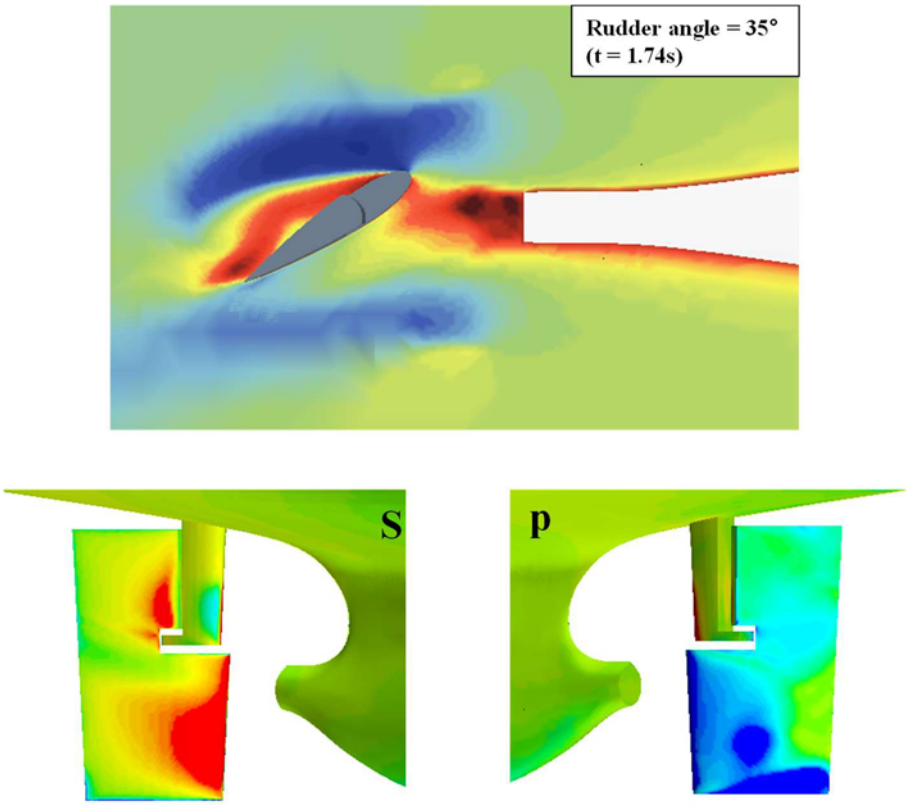

(e) Rudder angle = 35° (t= 1.74s)

Figure 9.12 The snapshots of the axial flow velocities around the rudder and the pressure distribution of the rudder (S: starboard profile, P: port profile) according to the rudder deflection angle in the initial phase of the turning manoeuvre.

Consecutive views of the free surface elevation around the ship during the turning manoeuvre are reported in Figure **9.13**. The sequence of the pictures can provide a clear description of the Kelvin waves generated by the ship performing the turning manoeuvre, closely associated with the forward speed and wave-encounter direction during the manoeuvre. The Kelvin wave generated by the ship became more visible when the ship was manoeuvring at a relatively high forward speed (the Froude number is relatively high), which can be clearly seen by the ship operating in the initial phase of the turn (yaw angle = 0° and 90°). It was also observed that the generated Kelvin wave became quite clear when the ship encountered the waves from the ship's bow during the manoeuvre. The free surface was mostly not disturbed much by the ship manoeuvring during the steady phase of the turn (yaw angle = 180°, 270°, and 360°) due to the decreased forward speed (the Froude number is relatively small).

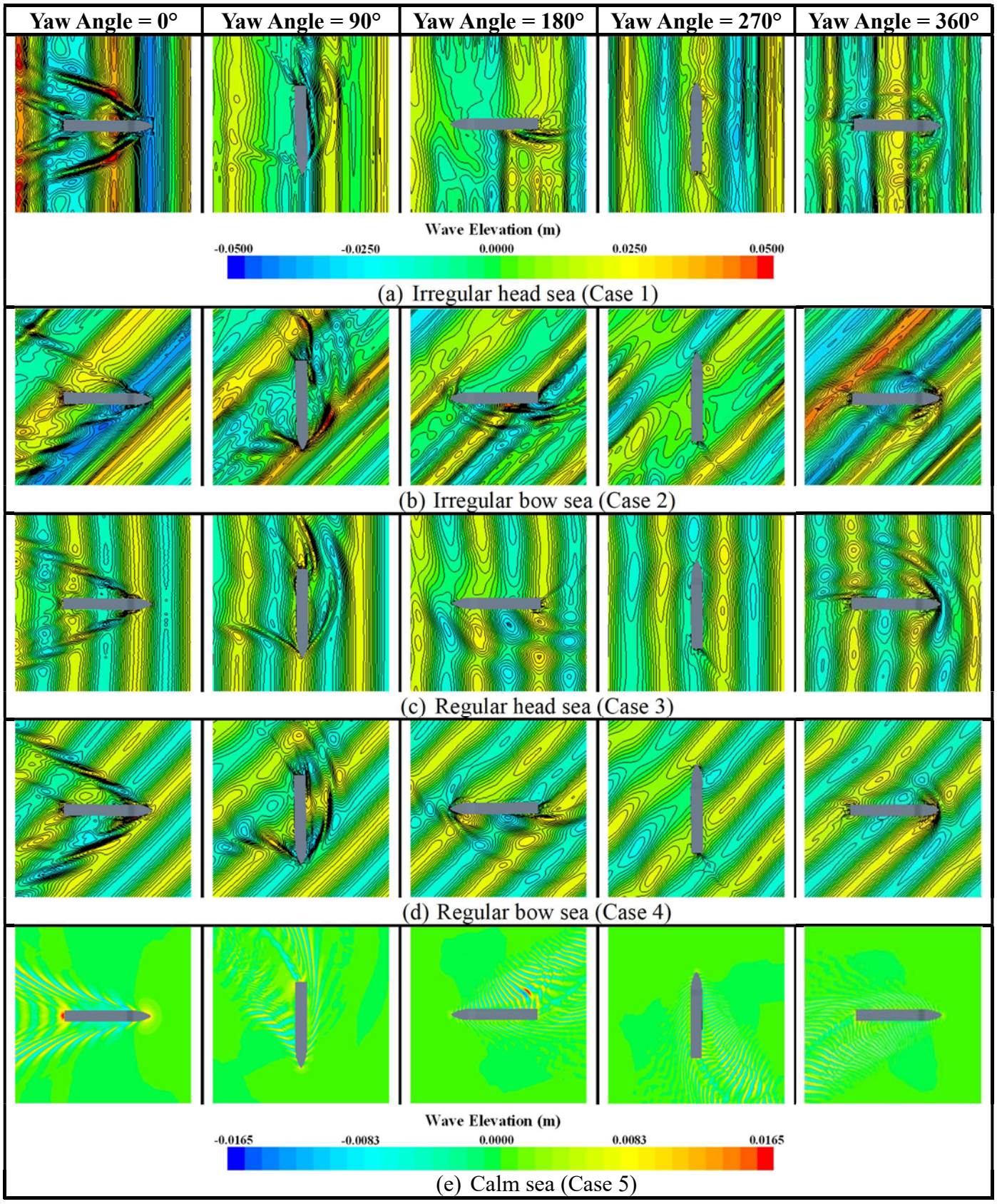

Figure 9.13 The free surface elevation during the turning manoeuvres for all cases.

9.4.3.2 Wave-induced motions during turning manoeuvre

In this sub-section, the seakeeping performance of the ship performing the standard turning manoeuvre is given in detail. The time histories of ship motions, i.e., heave, pitch, and roll as well as relevant hydrodynamic loads acting on the ship are presented in Figure 9.14, in which the forces and moments are referred to the ship-fixed coordinate system. It is apparent from the figure that the manoeuvring ship in the irregular waves (Cases 1 and 2) mostly experienced the randomly varying responses of the ship motions when compared to the regular sea conditions (Cases 3 and 4) due to the irregularity in wave height and period. In addition, instantaneous variations in the ship's velocity and wave-encounter direction during the manoeuvre also seemed to lead to the changes in the motion amplitude and frequency in the waves. For example, the ship manoeuvring in the irregular and regular head seas (Cases 1 and 3) encountered the head sea (0° turn), the port beam sea (90° turn), the following sea (180° turn), the starboard beam sea (270° turn), and the head sea (360° turn) in series after starting the starboard turning manoeuvre (the variation in the ship's heading angle is given in Figure 9.14 (g)). Given the fact that the ship motions are closely associated with the natural frequency of the motion system, it is obvious that the turning behaviour, which resulted in the continual changes in the wave-encounter frequency, can affect seakeeping performance in waves.

It is quite challenging to provide a clear description of the ship motions during the turning manoeuvre in the irregular seas since they are much more complicated than those predicted in the regular and calm seas. Possible reasons for the increase in the heave and pitch responses while the ship was turning in the irregular seas (Cases 1 and 2) include the higher incident wave height and the encounter frequency (f_e) very close to the natural frequency (f_n). Such conditions may cause relatively larger excitation forces and moments. Besides, the heave response appeared to be larger when the ship experienced the starboard or port beam seas, whereas the amplitude of the pitch was predicted to almost disappear under the beam seas (clearly evidenced in Figure 9.14 (a) and (c)). The heave and pitch responses in the regular seas (Cases 3 and 4) can be understood in a similar manner to the ship motion predictions in the irregular seas. Interestingly, it is clearly seen that during the very initial phase of the turn, the amplitudes of the heave and pitch in the regular head sea were smaller than those predicted in the regular bow sea, which is intimately related to the encountering frequency. In Figure 9.15 the time history of the encounter frequencies during the turning manoeuvre in the regular waves is presented. For the present KCS model, a study by Kim et al. (2021b) shows that the natural frequencies of the heaving and pitching system are close to $f_n \approx 0.93$ Hz. The comparison in terms of the encounter frequency confirms that the ship in the regular bow sea experienced the encounter frequency (f_e) closer to the natural frequency (f_n) at the early phase of the turn. This implies that the excitation force and moment experienced by the ship in the regular bow sea are larger than in the regular head sea. For the calm water case, only small changes in the heave and pitch responses during the manoeuvre were numerically observed due to the absence of external disturbances.

It was found that the turning manoeuvre has a significant influence on the roll response, as clearly seen in Figure 9.14 (f). As stated previously, the strong lateral force acting on the rudder

blade occurred after the rudder deflection to the hard-over angle (35°). Since the point for force application was located below the centre of mass, the rudder normal force caused the ship to heel to the starboard side (to the centre of the turning circle) right after the rudder execution. Subsequently, the ship started to heel to the port side (to the outside), which may be attributed to the hydrodynamic forces and the centrifugal force acting on the hull. Then, the amplitudes of the roll response gradually decreased and converged to between about 0 and 2 degrees with some fluctuations.

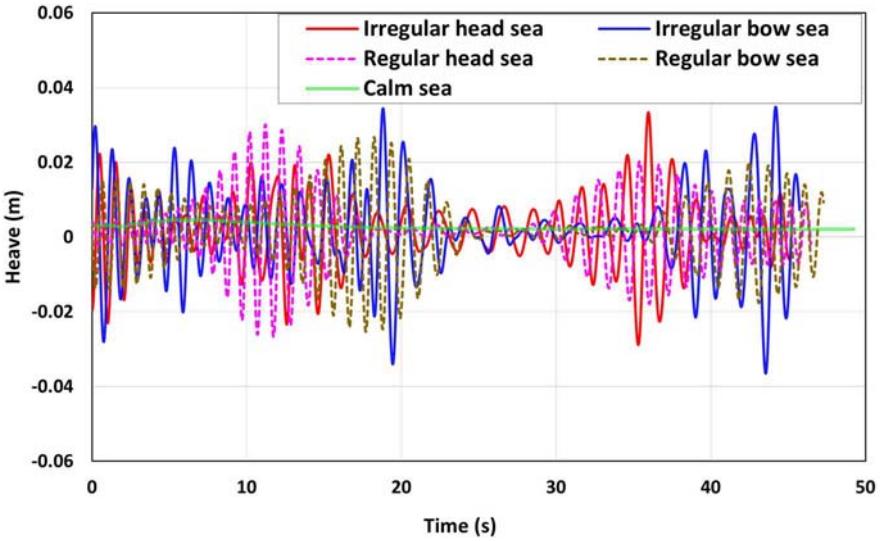

(a) Heave

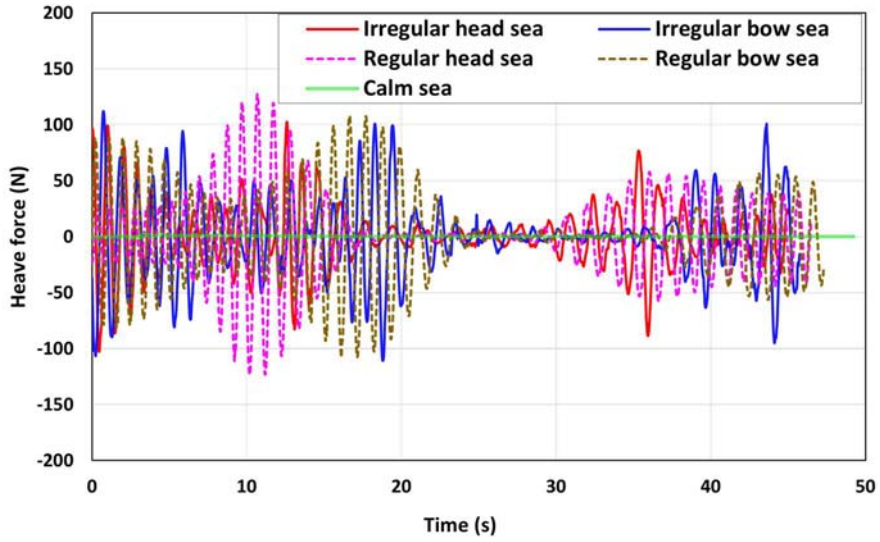

(b) Heave force

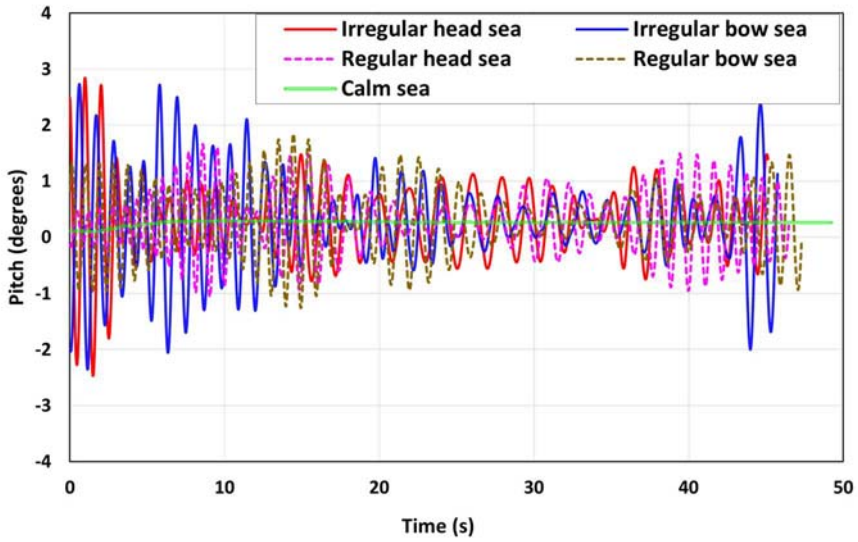

(c) Pitch

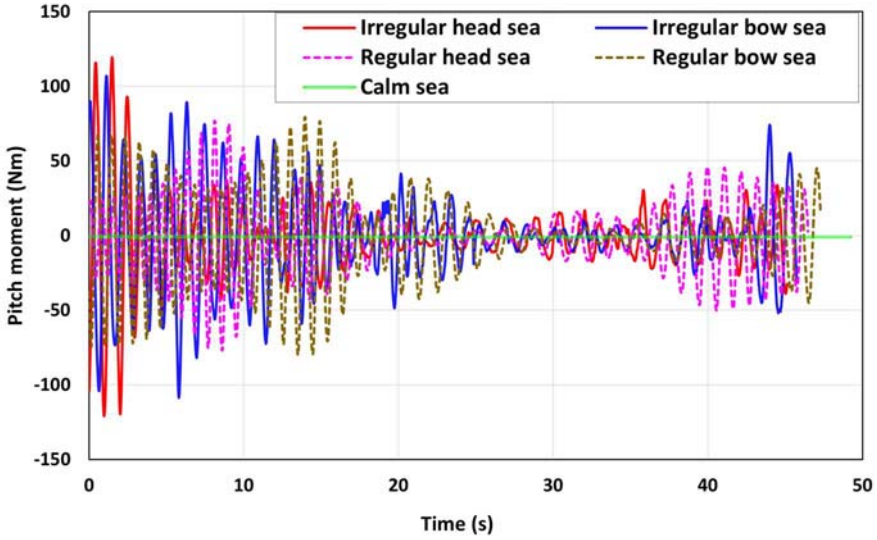

(d) Pitch moment

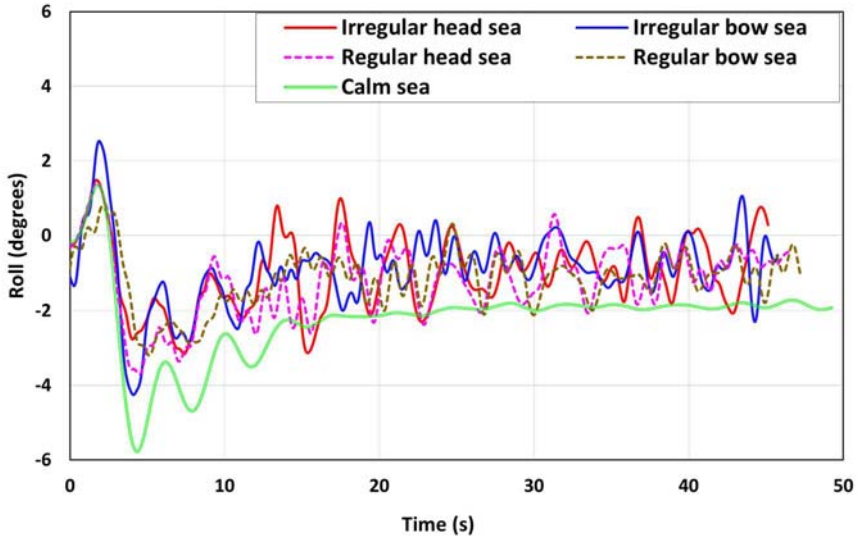

(e) Roll

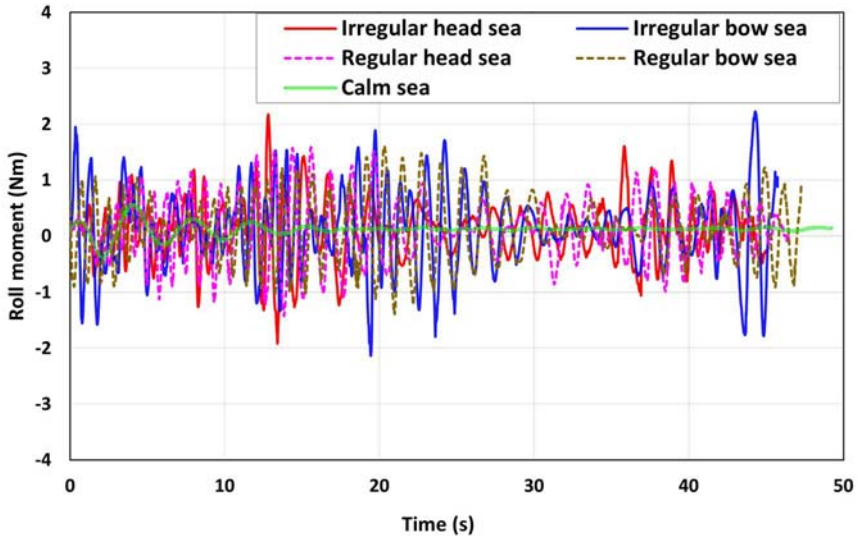

(f) Roll moment

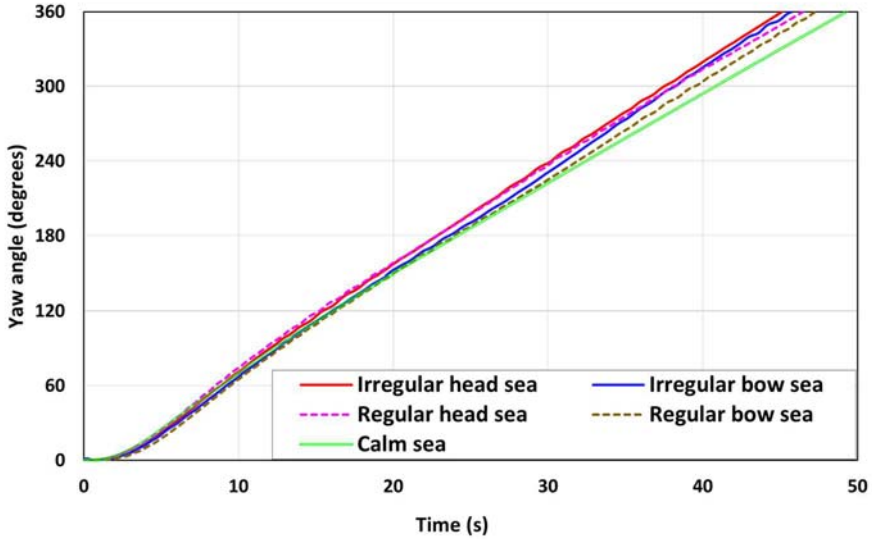

(g) Yaw angle

Figure 9.14 The time histories of ship motions, forces and moments acting on the hull during the turning manoeuvre.

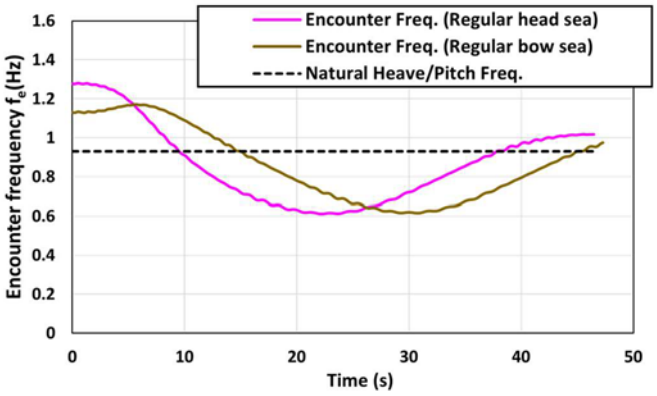

Figure 9.15 The time history of the encounter frequencies during the turning manoeuvre in the regular waves.

9.4.4. Corrected trajectory

The correction for the drift effect of waves on the turning trajectory experienced by the ship was made in this sub-section, with an aim to estimate the inherent turning trajectory in calm water by using the results measured in wave conditions. According to IMO (2002), the accurate record of the ship's trajectory, the heading angle, and the elapsed time should be made until at least a 720° turn is achieved to determine the drift velocity induced by external disturbances. To this purpose, the regular sea cases (Cases 3 and 4) were selected as representative cases to exhibit the corrected trajectory. Accordingly, additional computations were carried out for Cases 3 and 4 until the yaw angle variation of 720° was attained; in addition, the turning manoeuvres of the ship with the approach speed corresponding to Cases 3 and 4 were also performed in calm water. Based on the guideline of IMO (2002), the obtained results after the 180° change of heading were utilised to determine the magnitude and direction of the drift velocity induced by waves in the assumption that the yaw velocity is steady after the 180° turn. In Figure **9.16**, Positions (x_{1i}, y_{1i}, t_{1i}) and (x_{2i}, y_{2i}, t_{2i}) represent the positions of the ship which have a phase difference of 360°. The local drift velocity $\mathbf{V}_i$ for any two corresponding positions is defined as the follows:

$$\mathbf{V}_i = \frac{(x_{2i} - x_{1i}, y_{2i} - y_{1i})}{(t_{2i} - t_{1i})} \tag{9.2}$$

The estimated mean drift velocity can be calculated as follows:

$$\mathbf{V}_e = \frac{1}{n}\sum_{i=1}^{n} \mathbf{V}_i = \frac{1}{n}\sum_{i=1}^{n} \frac{(x_{2i} - x_{1i}, y_{2i} - y_{1i})}{(t_{2i} - t_{1i})} \tag{9.3}$$

The obtained trajectories in waves can be corrected from the following equation:

$$\mathbf{X}'(t) = \mathbf{X}(\mathrm{t}) - \mathbf{V}_e t \tag{9.4}$$

in which $\mathbf{X}(\mathrm{t})$ is the measured position vector and $\mathbf{X}'(t)$ is the corrected trajectory of the ship ($\mathbf{X}'(t) = \mathbf{X}(\mathrm{t})$ at $\mathrm{t} = 0$).

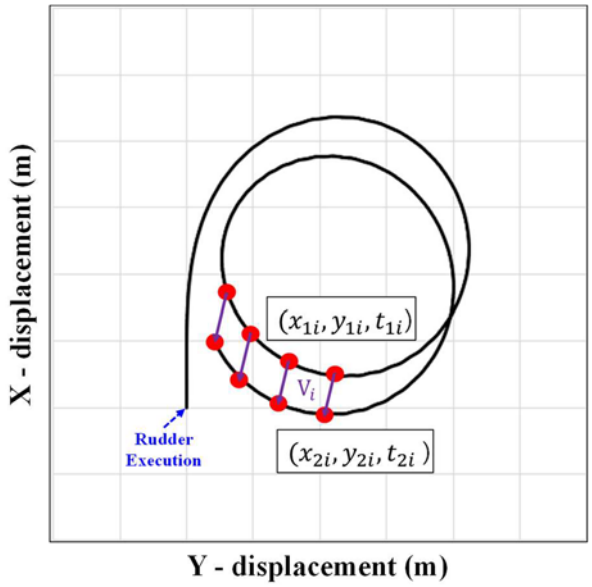

Figure 9.16 Turning trajectory in waves.

Figure 9.17 displays the corrected trajectories for Cases 3 and 4, calculated in accordance with the approach as described in the above equations. It can be noticed that the drift direction of the ship trajectory during the turning manoeuvre was similar to the wave direction of the incident wave, clearly evidenced by the uncorrected paths coloured with red. It also appeared that the ship trajectories (solid red lines) obtained from the CFD simulations were well corrected such that an exact circular shape of the path (green dashed lines) was obtained. This suggests that the drift effect of waves on the turning trajectory was eliminated for the corrected ones. However, large discrepancies were observed between the corrected trajectories (dashed green lines) and the ones (solid black lines) representing the inherent turning manoeuvrability of the ship in calm water. Possible sources of these discrepancies may mainly result from the difference in the propeller revolution rates applied to the CFD model during the manoeuvre, leading to the difference in the dynamic performance of the ship. This demonstrates the difficulty in predicting the inherent turning trajectory of the ship in calm water through the use of the results obtained in waves to calculate the corrected trajectory.

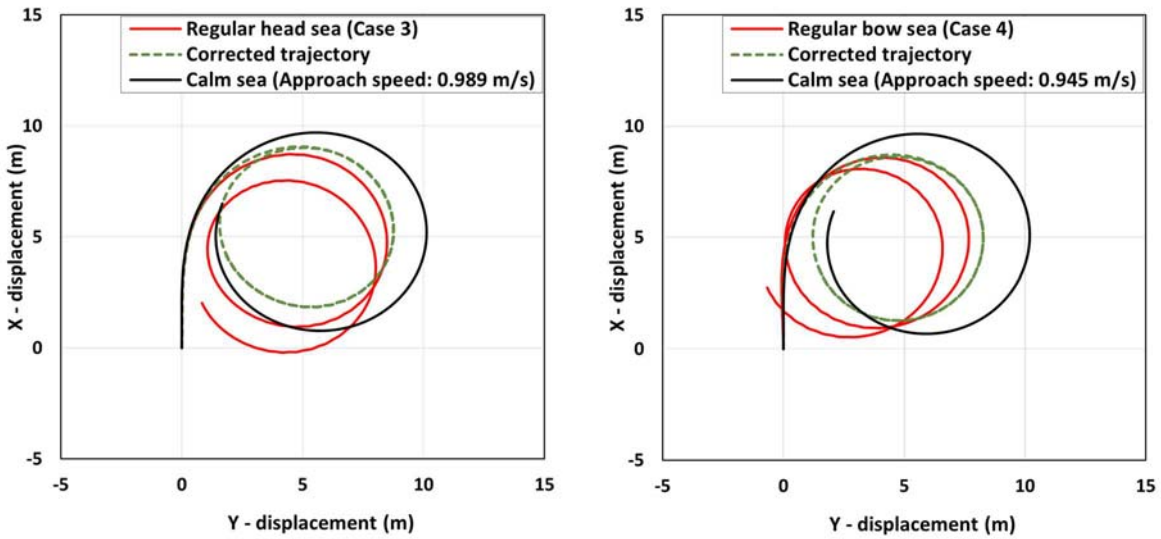

(a) Case 3 (b) Case 4

Figure 9.17 The corrected trajectories for Cases 3 and 4.

9.5. Concluding Remarks

In this chapter, free-running simulations to evaluate the course keeping and turning capabilities of a container ship model in irregular waves were performed by means of an unsteady Reynolds Averaged Navier-Stokes solver.

Before conducting the manoeuvring analyses, a simulation was performed with irregular head waves by generating the static background domain without hull and rudder girds, to monitor and record the wave elevation at the position of the wave probe. It was revealed that the waves simulated using the numerical scheme in this chapter gave fairly acceptable results, showing differences ranging from 1.66 – 6.63% of the theoretical values in terms of the statistical quantities of waves (i.e., significant wave height, average wave height, and average wave period).

Five simulation cases, which were composed of irregular, regular, and calm sea conditions, were applied to the container ship model for manoeuvring analyses. It can be noted that a detailed analysis of the course keeping and turning circle manoeuvres was carried out in this work, together with the principal properties of the flow field around the ship. In analysing the correlations between the ship manoeuvrability and the irregular waves, the findings of this study have demonstrated that the irregular waves may cause substantial changes in the course keeping capability and turning performance when compared to the inherent manoeuvring qualities in calm water. The key findings of this work can be summarised as follows:

1) For the ship's heading control in accordance with the prescribed course keeping module, it was identified that the ship operating in the irregular oblique sea experienced larger heading angle deviations than in the irregular head sea. The main reason for this lies in the asymmetric pressure distribution acting on the hull generated by the oblique wave during the course keeping manoeuvre, which resulted in a substantial yaw moment and thus the large heading angle deviation and rudder deflection. In addition, the advancing

ship in the irregular bow sea experienced the randomly varying behaviour of the yaw and rudder angle under the course keeping control, clearly different from that identified in the regular bow sea. This is because of the irregularity in wave height and period based on the JONSWAP power spectrum. Unlike the oblique sea cases, it was observed that the heading control in the irregular head, regular head, and calm seas was not an issue, showing very small heading deviations from the target one.

2) It was found that the irregular wave conditions resulted in substantial changes in the ship's turning capability when compared to the ship's inherent turning ability in calm water, showing remarkable differences in the turning trajectory. The influence of the irregular wave direction on the vessels' turning performance was also analysed; for this purpose, the waves of different directions (the irregular head and bow quartering seas) were applied for the evaluation of the ship manoeuvrability. The contribution of the wave direction to the turning trajectory was also noticed to some extent, confirming the deformation of the turning circle path compared to the trajectory in calm water (because of the wave drift forces and moments). An interesting result obtained through this study was that the overall trajectory experienced by the ship in the irregular wave was roughly similar to the one observed in the regular wave (characterised by the height and period equivalent to the average height and period of the irregular waves) in the case of the same wave direction.

10. FREE-RUNNING CFD SIMULATIONS FOR SHALLOW WATERS

10.1. Introduction

The trend of ever-increasing ship size has called for a need to understand the manoeuvring performance of a vessel in shallow water. Vessels will navigate in areas of shallow water at various times during their operational life, such as when approaching harbours or ports. As stated in Tezdogan et al. (2016), it is also true that some coastal waters and open sea areas can be regarded as shallow water regions in which the water depth is limited. According to Toxopeus et al. (2013), limited water depth has a remarkable influence on the performance of a ship, clearly demonstrated when the ratio of water depth to draft is less than 1.5. One of their key findings is that when a ship is operating at a drift angle, the forces and moments acting on the hull in shallow water increase considerably, compared to those measured in deep water. This implies that the presence of a finite water depth can lead to substantial changes in a ship's manoeuvrability when compared to deep water conditions, mainly being attributed to the strong interaction between the hull, propeller, and rudder with the sea floor.

Masters and navigation officers, who are in charge of ship handling with a high focus on navigation safety, should fully understand the manoeuvring capabilities of a ship in shallow water for proper decision-making about ship manoeuvring actions. In practice, however, they have only access to the manoeuvring information of their vessels in deep water, which is generally obtained by full-scale sea trials or model-scale experiments. This stems from the fact that evaluating the manoeuvring performance of a surface vessel in deep water practically becomes an industry standard in accordance with the International Maritime Organisation (IMO) standards for ship manoeuvrability (IMO, 2002). The IMO recommends that the water depth should exceed four times the mean draft of a ship when estimating manoeuvring behaviours. It is undeniable fact that the full-scale sea trial or model-scale experiment compliant with the IMO requirement can be informative in confirming a ship's manoeuvrability in deep unrestricted water. However, they are not able to provide a practical insight into the understanding of ship manoeuvrability in shallow water as the manoeuvring behaviour of a vessel in shallow water differs significantly from its behaviour in deep water. For this reason, this chapter aims to investigate the manoeuvring performance of a ship in shallow water, using an unsteady Reynolds-Averaged Navier Stokes (URANS) method.

So far, the previous studies have mostly focused on the evaluation of a ship's manoeuvrability in deep waters as reviewed in Chapter 3. In other words, the research devoted to investigating ship manoeuvrability in shallow water areas has been very limited in number and scope. Carrica et al. (2016), who carried out a 20/5 zigzag manoeuvre for the KCS in shallow water using CFD, only focused on case-specific analyses with a single condition of h/D=1.2, such that their findings are not able to provide the general observations on the relationship between finite depths and manoeuvring behaviours. Taking into account the lack of previous studies concerning ship manoeuvrability in shallow water, the research reported in Section 3.6 was motivated to analyse the effect of different shallow waters on the manoeuvring behaviour of a ship. In addition, as discussed in detail by Kim et al. (2021a), performing analyses of the turning

behaviour of ships is of great importance in ship navigation. A decision was therefore made to investigate the turning performance of a ship in the CFD simulations presented in this chapter.

In the present work, the turning capabilities of the KCS model in different shallow waters are investigated. Comprehensive analyses are provided for the manoeuvring indices and hydrodynamic loads closely associated with the turning behaviours, and, in order to gain more insight in understanding the turning manoeuvres, the various hydrodynamic phenomena occurring during the manoeuvre (including velocity and pressure fields) are evaluated. This study therefore may be useful to understand the comprehensive manoeuvring behaviour of a container ship model in different shallow water areas.

This chapter is organised as follows: in the next section, a list of the simulation cases to be performed in this study is illustrated. In Section 10.3, a specific description of the numerical setup for the current CFD model is presented. Next, in Section 10.4, all of the CFD results from this work, including validation studies, are demonstrated and discussed in detail. Finally, Section 10.5 briefly summarises the main results drawn from this work.

10.2. Goal and Scope

Given the scarce previous research on ship manoeuvrability in shallow water, the main goal of this chapter is to examine the shallow water effects on the manoeuvring performance of the ship by means of an unsteady RANS solver.

Seven different cases to be simulated in CFD were taken into consideration within this study, as shown in Table **10.1** and Figure **10.1** (each case indicated by their case numbers). In this study, a 20/5 modified zigzag manoeuvre (Case 0) was carried out in shallow water with water depth to draft ratio $h/D = 1.2$ for validation purposes. The experimental results of the 20/5 zigzag manoeuvre provided by MARIN (SIMMAN, 2020) were used as benchmark data for validation. In addition, two representative free-running manoeuvres (namely, course keeping and standard turning manoeuvres) were performed in different depth to draft ratios (Case 1 – 6): 1) $h/D = 1.2$, 2) $h/D = 1.5$, 3) $h/D = 2.0$, 4) $h/D = 3.0$, 5) $h/D = 4.0$, and 6) deep water. The first procedure for the free-running manoeuvres involved achieving self-propulsion at the approaching speed; the corresponding Froude and Reynolds numbers were $Fr = 0.095$ and $Re = 1.25 \times 10^6$, respectively. It should be noted that the approach speed was reached, the revolution speed of the actuator disk was kept constant at the self-propulsion value during the free-running manoeuvres to be performed. Then, the course-keeping manoeuvres were started from the stable state of the self-propulsion condition, based on a rudder controller that controls the rudder deflection angle to make the ship sail forward. Following this, the standard turning circle manoeuvres (35° starboard turns) were performed to evaluate the shallow water effects on the turning behaviour of the ship.

Table 10.1 The simulation cases to which the CFD model is applied.

Case	Surge speed U_0 (m/s)	Propeller rev. (RPS)	Depth/draft h/D	Free running simulations
0	0.518	6.75	1.20	20/5 zigzag, starting to port (**Validation case**)
1	0.518	6.75	1.20	Course keeping, 35° starboard turn
2	0.518	6.56	1.50	Course keeping, 35° starboard turn
3	0.518	6.43	2.00	Course keeping, 35° starboard turn

4	0.518	6.28	3.00	Course keeping, 35° starboard turn
5	0.518	6.24	4.00	Course keeping, 35° starboard turn
6	0.518	6.07	Deep water	Course keeping, 35° starboard turn

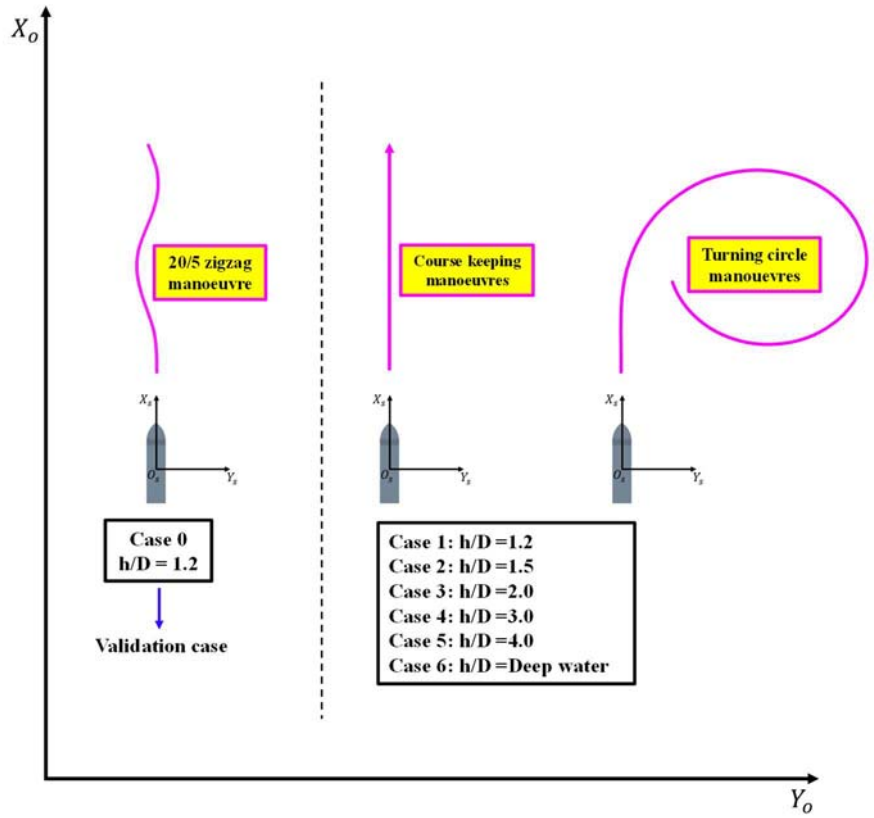

Figure 10.1 Schematic views of the simulation cases applied to this study.

10.3. Numerical Modelling

The free-running CFD model considered in this chapter were developed according to the numerical modelling scheme described in Chapter 4, Section 4.3.

In this study, six different grid generations were applied for each free-running simulation; the exact number of grids generated for each case is reported in Table 10.2. Case 0 and 1 were chosen as representative cases to display a general view of the final computational mesh for the free-running manoeuvre, as illustrated in Figure 10.2.

Table 10.2 The total cell numbers for the free-running simulations.

Case no.	Total cell number
0 (h/D=1.2)	8,854,466
1 (h/D=1.2)	8,854,466
2 (h/D=1.5)	8,968,119
3 (h/D=2.0)	9,580,662
4 (h/D=3.0)	9,950,540
5 (h/D=4.0)	10,287,254
6 (Deep water)	8,184,125

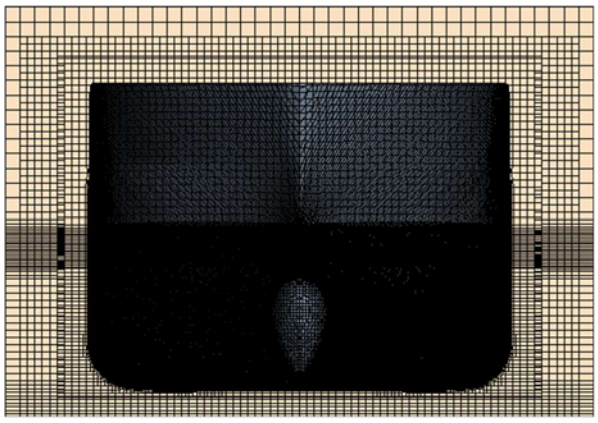

(a) Front view cross-section of the domain

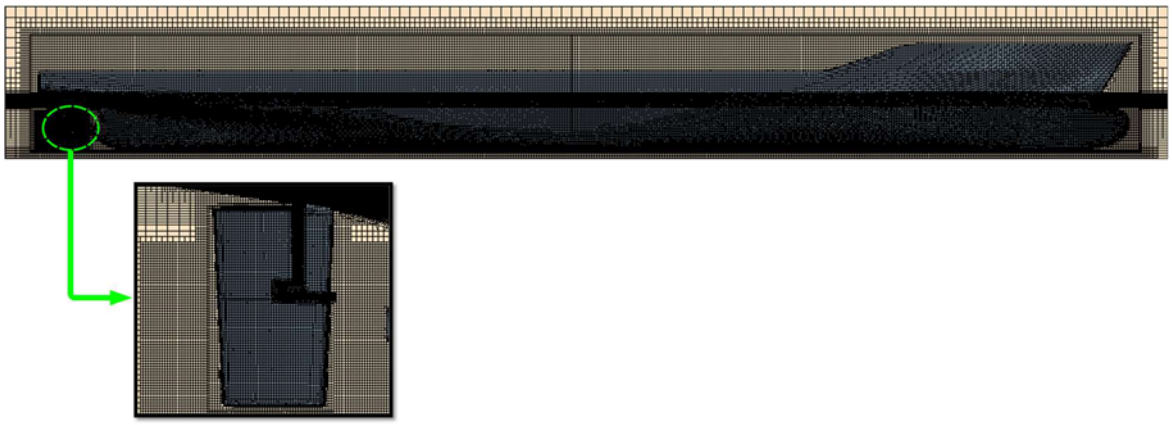

(b) Profile view cross-section of the domain

Figure 10.2 Grid structure of the computational domain (Case 0 and 1).

According to Section 4.3.6, the time step size for all the simulations in this study was set at Δt=0.005s, which is ten times lower than the value obtained from the recommendation ($\Delta t \leq 0.01 L/U$) presented by ITTC (2011) to gain a reliable level of accuracy for complex phenomena. The use of $\Delta t = 0.005$ s has been proved to be reliable in predicting the manoeuvrability of a 1/75.24 scale KCS model (which is the same model scale as that adopted in this work) by performing URANS based simulations, as evidenced in Sections 5 – 9.

10.4. Results

10.4.1. Validation study

The performance of the actuator disk model operating in open water was estimated to ensure the validity of the body force method adopted in this particular study; to this purpose, an additional simulation was carried out by using the same background grids used for the present free-running simulation (Case 6, deep water) without hull and rudder grids. In Table 10.3 and Figure 10.3, the open water characteristics (thrust coefficients K_T, torque coefficients K_Q, and efficiency η_0 for each advance ratio J) are presented and compared with the available

experimental results (SIMMAN, 2020). It can be seen from the table and figure that the agreement between the computed values of K_T, K_Q, and η_0 for the whole range of J and the values provided by the experiments is very good. K_T and K_Q were slightly underpredicted for higher propeller loads, whereas they were slightly overpredicted for lower loads (the errors remained below 6%). Given the fact that a good agreement was achieved between CFD and EFD results, it can be argued that the propeller model based on the body force method demonstrated its robust capability in predicting the propeller performance with regard to thrust and torque; thus, the successive application of this propeller model was made for all the manoeuvring simulations to represent propeller effects.

Table 10.3 Propeller open water test results.

J	CFD			Experiment (MARIN)			Error of K_T (%)	Error of K_Q (%)	Error of η_0 (%)
	K_T	$10K_Q$	η_0	K_T	$10K_Q$	η_0			
0.05	0.427	0.6345	0.053	0.454	0.6686	0.054	5.85	5.10	0.73
0.10	0.418	0.6229	0.106	0.440	0.6501	0.108	4.95	4.18	1.06
0.15	0.407	0.6092	0.159	0.424	0.6302	0.161	3.93	3.33	0.86
0.20	0.394	0.5934	0.211	0.407	0.6088	0.213	2.99	2.52	0.57
0.25	0.381	0.5757	0.263	0.389	0.586	0.264	2.05	1.75	0.25
0.30	0.365	0.5557	0.313	0.370	0.5619	0.314	1.29	1.10	0.06
0.35	0.347	0.5330	0.363	0.350	0.5364	0.364	0.74	0.63	0.25
0.40	0.328	0.5090	0.410	0.329	0.5097	0.411	0.15	0.13	0.03
0.45	0.309	0.4835	0.458	0.308	0.4817	0.457	-0.45	-0.37	-0.28
0.50	0.288	0.4563	0.502	0.285	0.4525	0.501	-1.08	-0.83	-0.28
0.55	0.265	0.4271	0.544	0.262	0.4222	0.543	-1.45	-1.16	-0.32
0.60	0.242	0.3964	0.583	0.238	0.3907	0.582	-1.84	-1.45	-0.33
0.65	0.218	0.3648	0.618	0.213	0.3581	0.617	-2.44	-1.87	-0.28
0.70	0.193	0.3317	0.649	0.188	0.3244	0.647	-2.92	-2.25	-0.44
0.75	0.168	0.2974	0.676	0.163	0.2898	0.671	-3.37	-2.62	-0.79
0.80	0.142	0.2616	0.693	0.137	0.2541	0.686	-4.01	-2.95	-1.10
0.85	0.115	0.2244	0.698	0.111	0.2175	0.688	-4.41	-3.17	-1.55
0.90	0.088	0.1858	0.680	0.084	0.1799	0.669	-5.11	-3.27	-1.75
0.95	0.060	0.1460	0.623	0.057	0.1415	0.610	-5.61	-3.18	-2.20

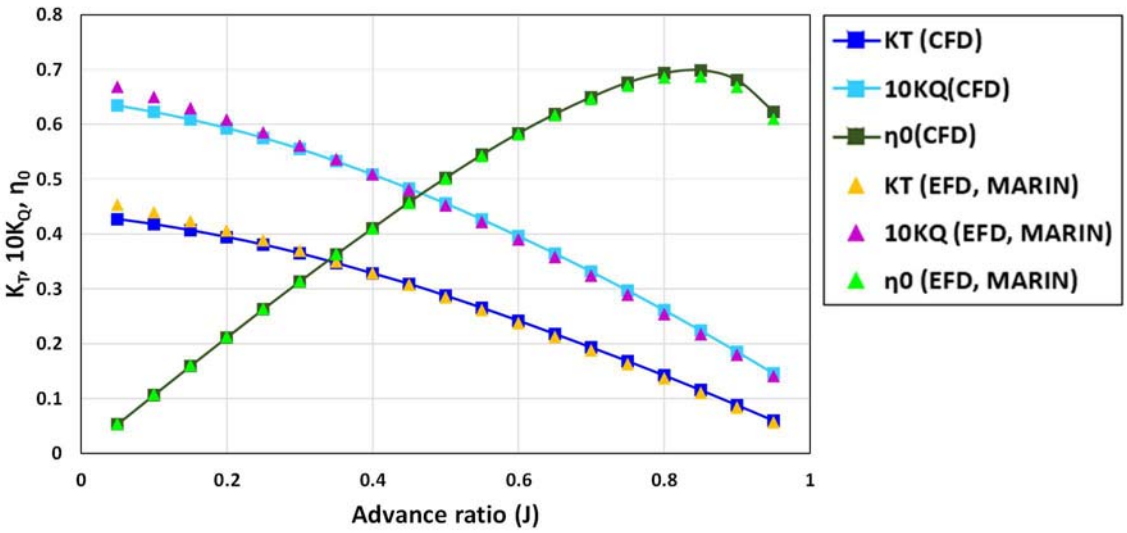

Figure 10.3 Propeller open water test results and comparison.

As was stated in Section 10.2, Case 0 was used for the validation of the present CFD model against the experimental data (SIMMAN, 2020). Figure 10.4 presents the simulated ship trajectory and time histories of the ship's speeds, yaw angle, and rudder deflection during the 20/5 modified zigzag manoeuvre in shallow water ($h/D = 1.2$), in comparison with the experimental measurements. In addition to this, the important parameters of the zigzag manoeuvre including overshoot angles were reported in Table 10.4. The CFD predictions of the trajectory experienced by the ship were found in reasonable agreement with the EFD results (Figure 10.4 (a)), with the minor discrepancy of the ship paths mainly due to the underprediction of the yaw velocity and consequent underestimation of the ship's heading angle. The comparison in terms of the kinematic parameters being composed of the ship velocities in the horizontal plane confirmed the satisfactory agreement between the CFD and EFD results (Figure 10.4 (b)-(d)). A possible reason why relatively high oscillations are observed in EFD and not in CFD regarding the sway velocity may be associated with the measurement noise during the experiment. As seen in Figure 10.4 (e) and Table 10.4, the dynamic behaviour of the ship's heading and rudder deflection was fairly well captured by the present CFD model; the CFD computation underestimated the first and second overshoot angles by 9.6% and 13.5%, respectively. Several possible sources of the discrepancies observed during the manoeuvre between the CFD and experimental results were thoroughly discussed in Carrica et al. (2016), which include variations in initial conditions for yaw angle and yaw velocity, effects of turbulence modelling, effects of neglecting the walls of the tank, the differences in the inertia characteristics between CFD and EFD, etc. Given the acceptable agreement clearly inferred from the figure and table, nevertheless, it can be stated that the validity of the present CFD model has been sufficiently demonstrated, providing a high level of confidence in dealing with the manoeuvring problems in question.

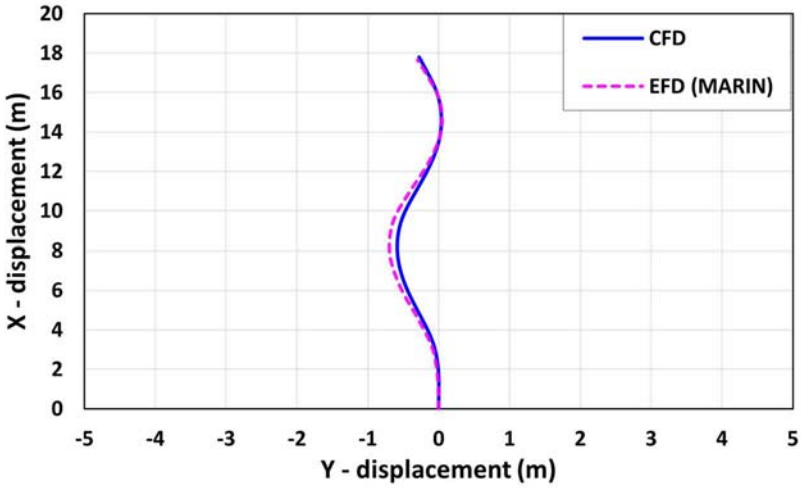

(a) Ship trajectory

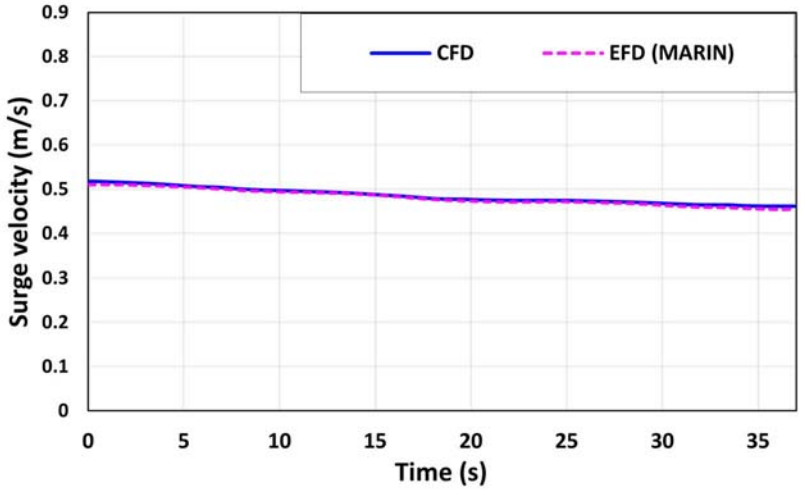

(b) Surge velocity

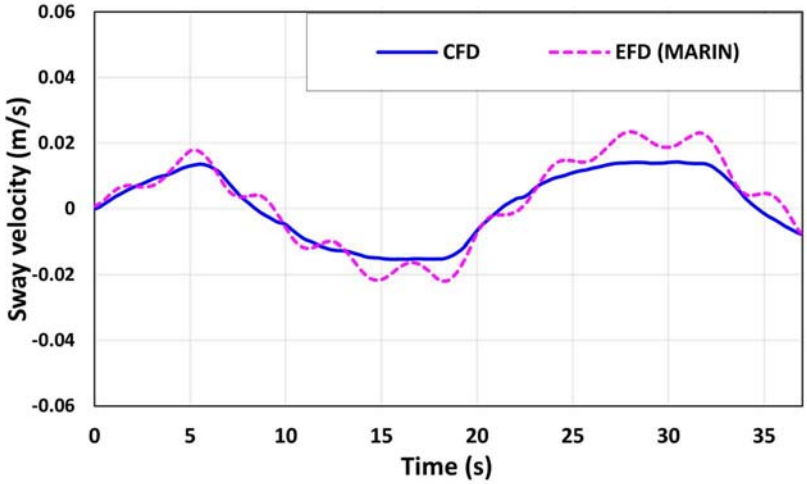

(c) Sway velocity

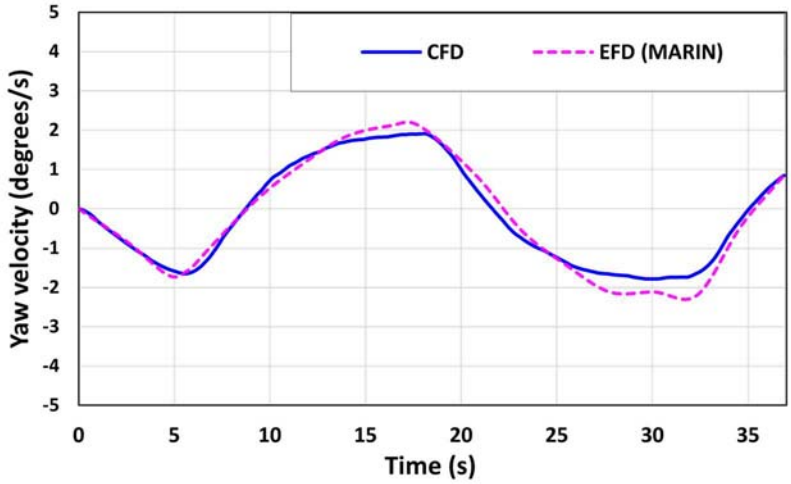

(d) Yaw velocity

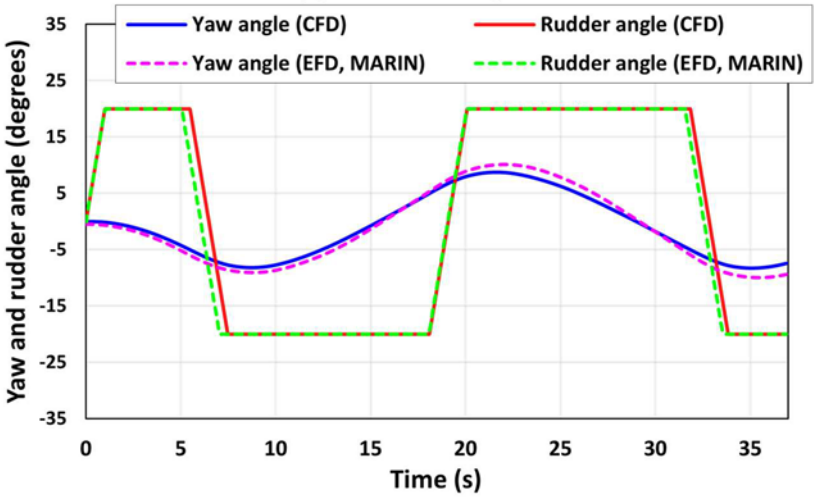

(e) Yaw angle and rudder deflection

Figure 10.4 The ship trajectory and the time histories of the yaw angle, rudder deflection, and kinematic parameters during the 20/5 modified zigzag manoeuvre in shallow water.

Table 10.4 The comparison of the main parameters of the 20/5 zigzag manoeuvre in shallow water (Case 0).

Parameters	CFD	EFD (MARIN) (SIMMAN, 2020)	Error (%)
RPS at self-propulsion point	6.75	6.28	7.48
First overshoot (degrees)	8.18	9.05	-9.61
Second overshoot (degrees)	8.75	10.12	-13.54
Time for the first overshoot (s)	8.73	8.77	-0.46
Time for the second overshoot (s)	21.64	21.99	-1.59

10.4.2. Course keeping control

From the previous validation case (Case 0), it has been demonstrated that the present free-running CFD model is fairly reliable in predicting the manoeuvring performance of the ship in shallow water, including the ship's trajectory in response to the rudder deflection (closely associated with the course keeping capability). In this sub-section, as a practical application to free-running manoeuvres, the numerical simulations of the course-keeping manoeuvre by the self-propelled ship in shallow water are illustrated.

In general, vessels operating at sea follow the navigation route consisting of different straight-line courses (determined by a master and navigation officers) except when executing ship handling actions to avoid a close-quarters situation or performing planned course alternations. This navigational property underscores the significance of understanding the straight course-keeping capability of vessels; thus, it seems necessary to assess the course keeping behaviours in different environmental conditions in which a ship is to be navigated to ensure safe navigation at sea. The same analysis, performed in Sections 5 - 9 which investigated the course keeping abilities of the KCS in different wave conditions (deep water), was here conducted for the investigation of its steering capabilities in different shallow waters (without any external disturbances).

The computed trajectories experienced by the ship under the course keeping manoeuvres are presented in Figure 10.5, in which the location (0,0) of the start of the PID control for course keeping is indicated with a grey arrow. As it can be clearly noticed, all the simulation cases attained good course-keeping control by exhibiting the ship's actual sailing directions almost consistent with the true course (000°). Given the very small deviations from the original course, it was revealed that the finite depths have practically no influence on the course keeping performance in the case of the absence of external disturbances such as winds, waves, and currents. In Figure 10.6, the time histories of the yaw angle, rudder deflection, ship resistance, and ship motions during the course keeping manoeuvre are shown. In addition, the mean values of the approach speed, resistance, heave and pitch motions during the manoeuvre are summarised in Table 10.5. As the predicted ship paths suggest, the ship's heading angles in all cases were maintained to be almost 0°, whilst the rudder deflection angles were largely predicted within a value of 2.0º (a positive rudder angle refers to the direction of rotation to port in agreement with the reference frame adopted in this study). Such small positive rudder angles resulted from an asymmetric flow field induced by the propeller model, which led to the

uneven pressure distribution on the rudder surface, as reported in Kim et al. (2021a). This contribution to the small pressure difference exerted a small positive yaw moment, i.e., it turns the ship's heading towards the starboard; as a consequence, the rudder was slightly deflected to the port side according to the PID controller. It is worth noting that the rudder deflection angle may change based on the applied control gains. The effects of the finite depths on the ship resistance were clearly shown in Figure 10.6 and Table 10.5. It was observed that the resistance experienced by the self-propelled ship remarkably increased as the ratio of water depth to draft decreased. This is mainly ascribed to the stronger hydrodynamic interaction between the bottom of the ship and the sea bed in a lower water depth. The ship resistance in shallow water with $h/D = 1.2$ was approximately 59% larger than that in deep water for the same Froude number (Fr=0.095). Regarding the ship motions, only small heave and pitch displacements during the course keeping manoeuvre were numerically observed, stemming from a low approach speed.

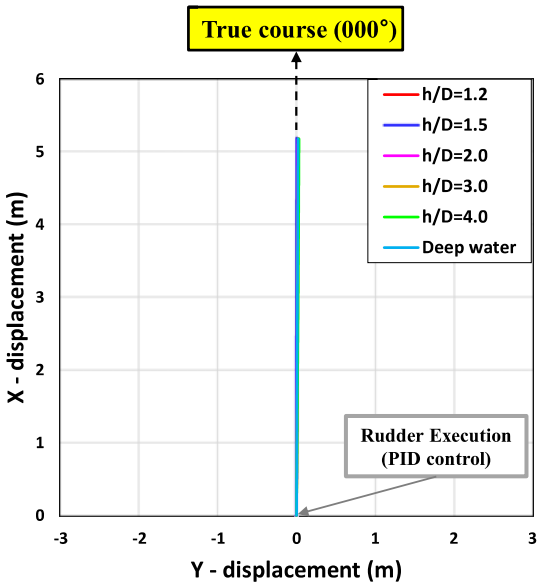

Figure 10.5 The comparison of the trajectories experienced by the ship during the course keeping manoeuvre.

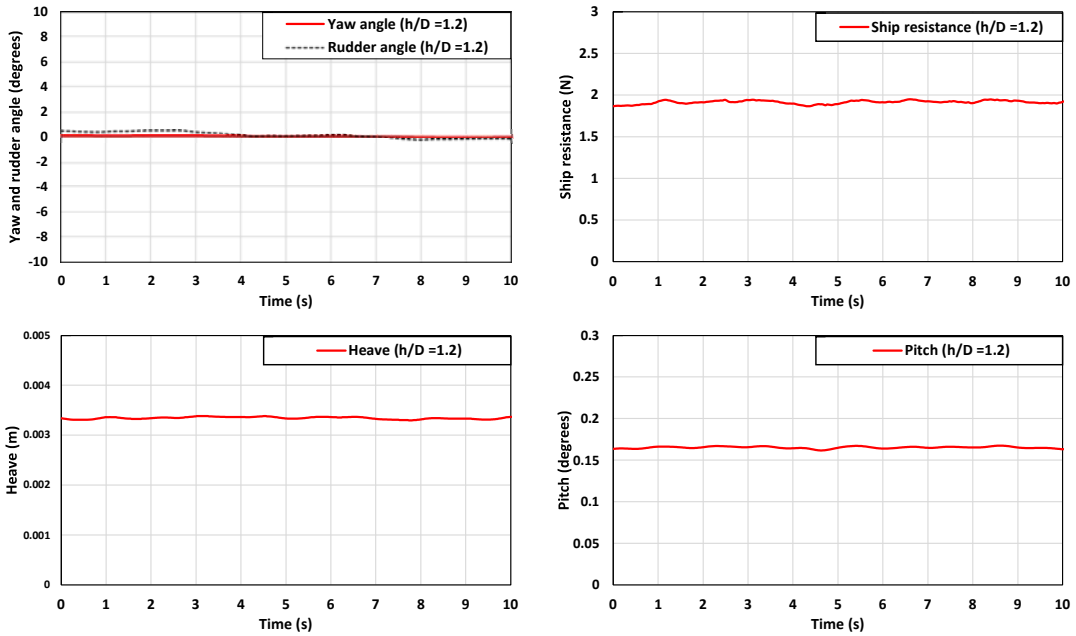

(a) Shallow water (h/D=1.2)

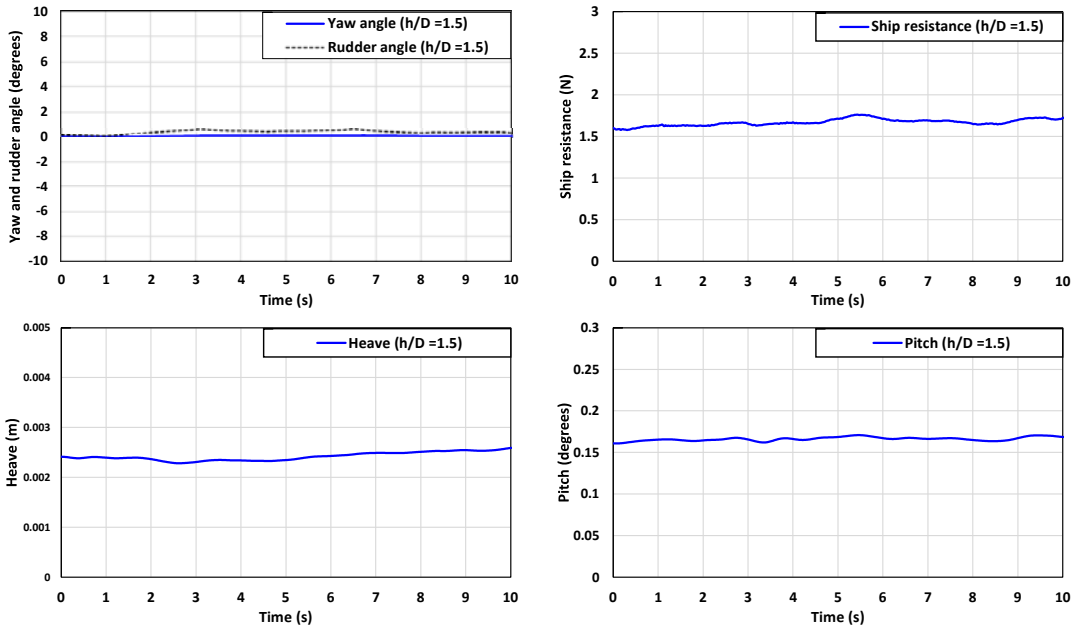

(b) Shallow water (h/D=1.5)

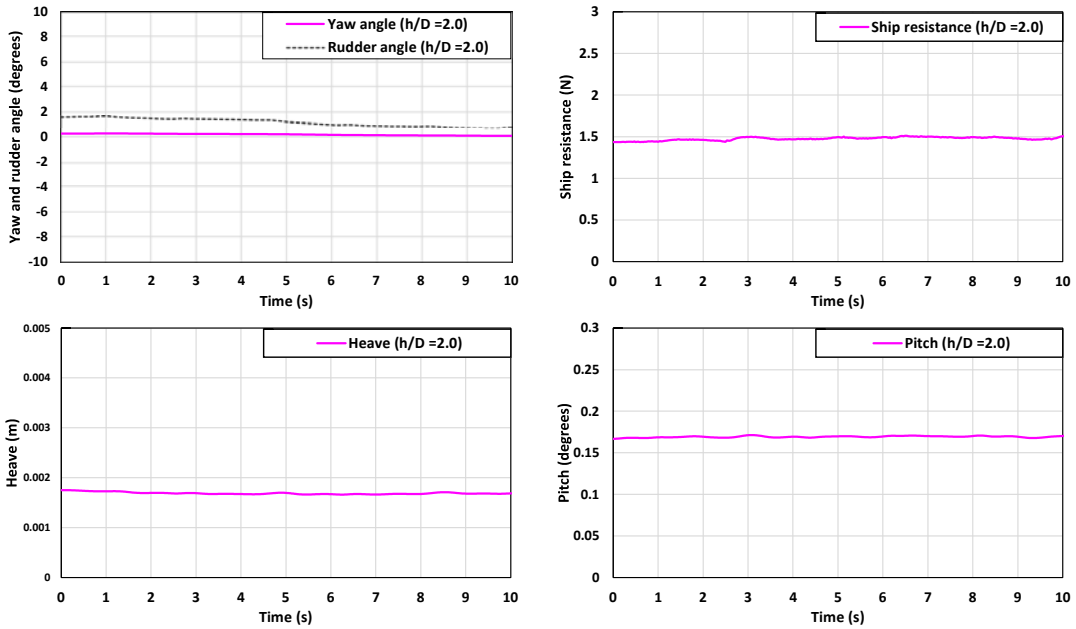

(c) Shallow water (h/D=2.0)

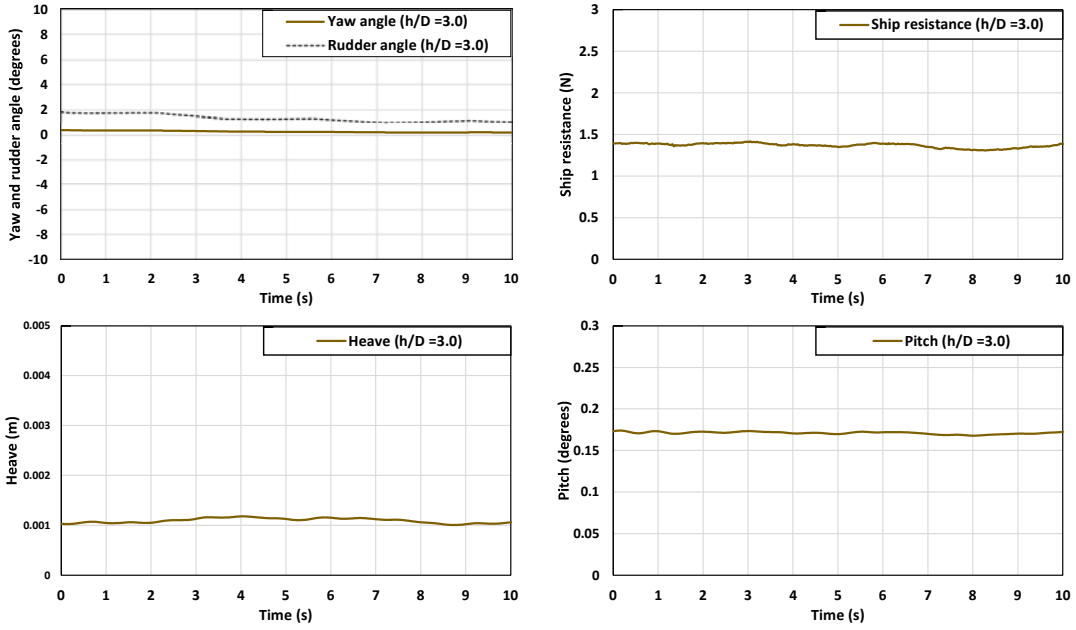

(d) Shallow water (h/D=3.0)

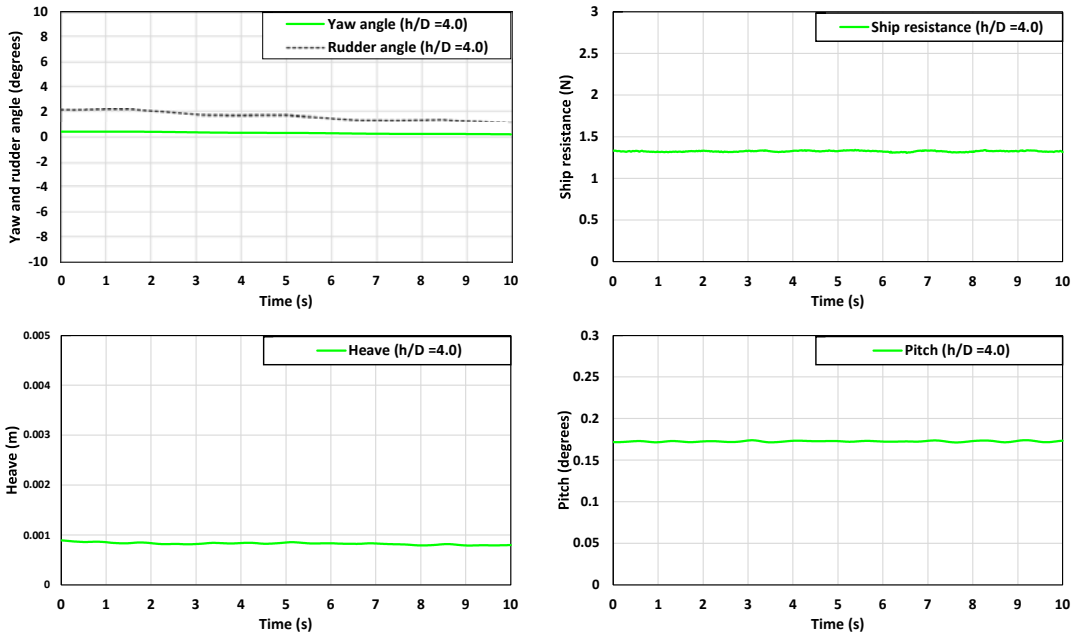

(e) Shallow water (h/D=4.0)

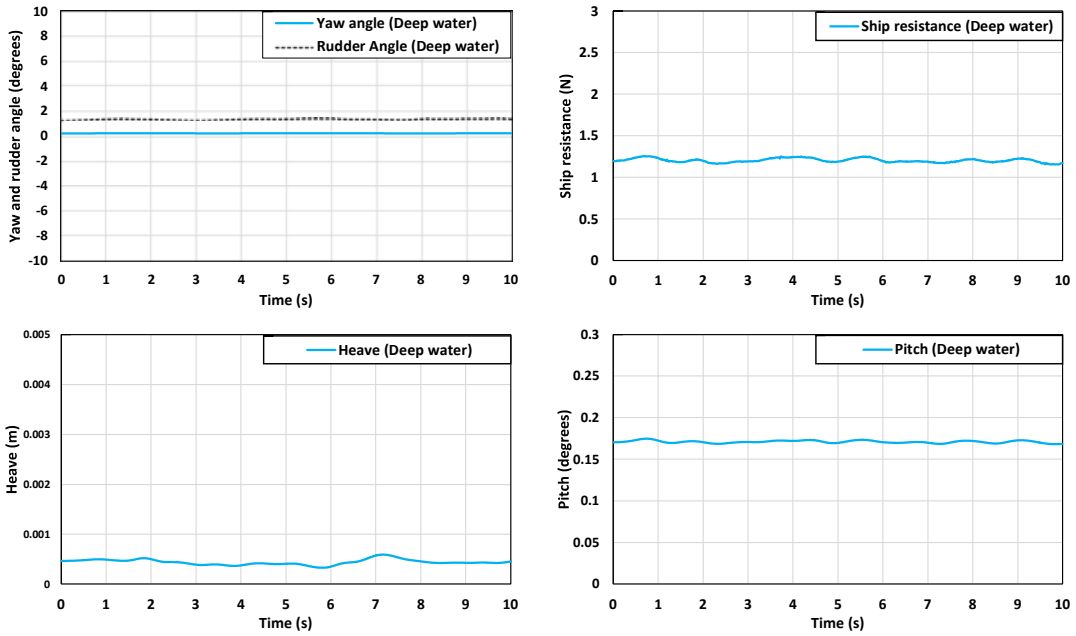

(f) Deep water

Figure 10.6 The time histories of the yaw angle, rudder deflection, ship resistance, and ship motions during the course keeping manoeuvre.

Table 10.5 The mean values of the approach speed, ship resistance, heave and pitch motions during the course keeping manoeuvre.

Case no.	Approach speed U_0 (m/s)	Resistance F_x (N)	Heave (m)	Pitch (degrees)
1 ($h/D = 1.2$)	0.518	1.913	0.0033	0.165
2 ($h/D = 1.5$)	0.518	1.669	0.0024	0.166
3 ($h/D = 2.0$)	0.518	1.474	0.0017	0.169
4 ($h/D = 3.0$)	0.518	1.367	0.0011	0.172
5 ($h/D = 4.0$)	0.518	1.323	0.0008	0.172
6 (Deep water)	0.518	1.204	0.0004	0.171

In order to visualise the pressure and velocity fields experienced by the ship advancing in shallow water, several zoomed snapshots of the dynamic pressure and longitudinal velocity contours on significant hull cross-sections (see Figure 10.7) are displayed in Figure 10.8. The sequence of the snapshots (obtained from Case 1) may provide a better insight into the flow evolution along the ship hull. These contours are from the upstream to the downstream of the ship ($-0.492 \leq X/L_{PP} \leq 0.327$). As it can be inferred from Figure 10.8, no noticeable hydrodynamic effects caused by the presence of the finite depth was observed at the bow (X/L_{PP}=0.327). At the midship section (X/L_{PP}=0.000), a negative pressure field was formed, and the flow velocity increased between the bottom of the hull and the sea floor. It was then observed that the ship boundary layer was interacted with the sea bed at X/L_{PP}=−0.327 due to the progressive evolution of the boundary layer thickness along the hull. The snapshots reported in Figure 10.8 (d) (where the flow reached the propeller, X/L_{PP}=−0.468) confirmed the disturbed flow fields because of the interaction between the turbulence produced by the boundary layer and the swirl induced by the propeller with the bottom surface. In addition, the pressure and velocity fields became more complicated at X/L_{PP}=−0.485 and −0.492 due to the inclusion of the flow around the rudder in the slipstream of the propeller.

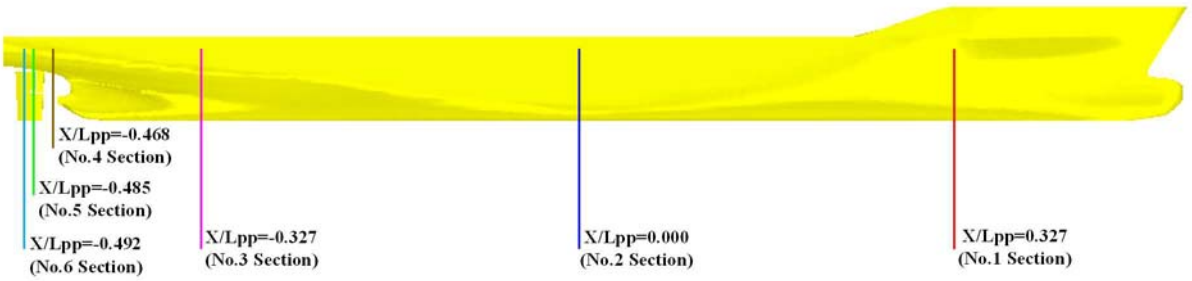

Figure 10.7 The location of the cross-sections along the ship at which pressure/velocity fields were obtained.

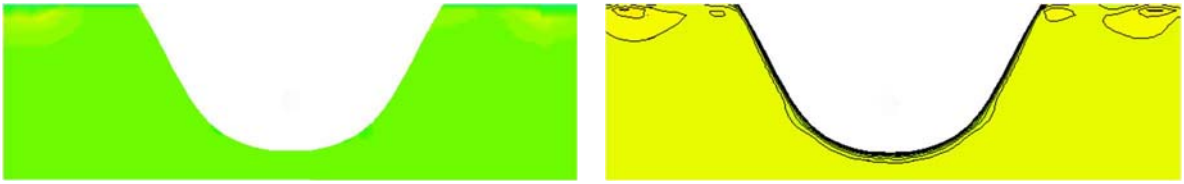

(a) X/L_{PP}=0.327 (No.1 Section)

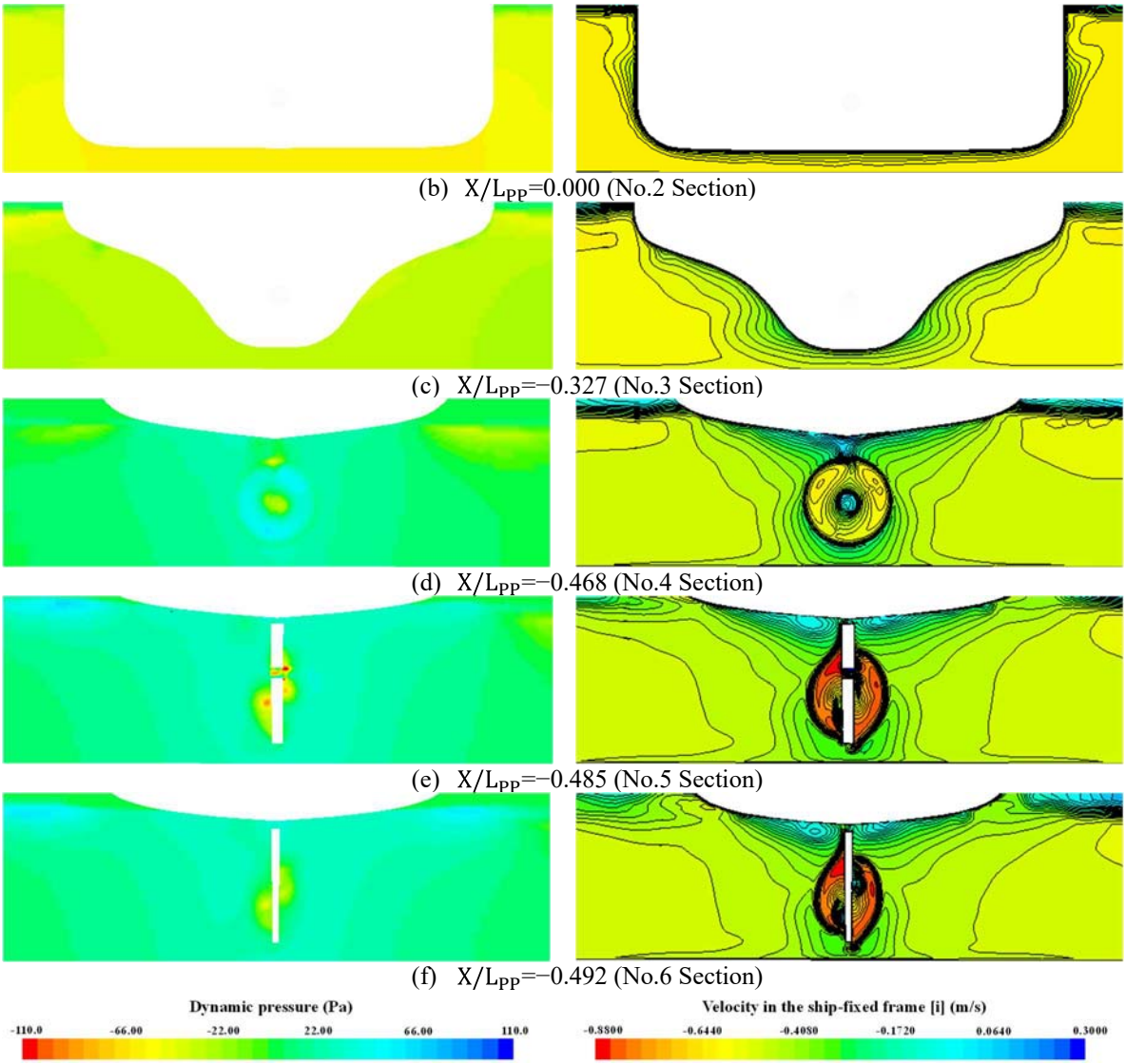

Figure 10.8 Dynamic pressure and longitudinal velocity fields during the course keeping manoeuvre on several cross-sections; left: pressure fields and right: velocity fields.

10.4.3. Turning circle manoeuvre

This sub-section will systematically investigate the turning capability of the self-propelled KCS model in different shallow waters; by comparison with the ship's inherent turning ability in deep calm water. Following this, the effects of the finite depths on the manoeuvring performance will be analysed. In the standard turning circle manoeuvre, the ship was sailing forward on a straight course at self-propulsion condition and the rudder was deflected to the hard-over angle (35°, towards the starboard side) at the maximum rudder rate (20.1°/s). Then, the ship started to turn in the starboard direction as a reaction to the rudder deflection. The free-running simulations stopped when the variation of the ship heading angle reached 360° according to the general procedure put forward by IMO (2002). The total simulation running time of each case was different due to the different yaw velocities experienced by the ship during the manoeuvre. As traditionally adopted in ship manoeuvring, the turning behaviours of the ship were assessed in terms of the turning parameters such as the ship advance, transfer,

tactical diameter as well as time to 90°/180° heading angle changes.

The predicted trajectories experienced by the ship during the turning circle manoeuvre are depicted in Figure 10.9, in which the ship paths are expressed with respect to the earth-fixed coordinate. In the figure, the origin (0,0) of the earth-fixed frame is taken as the position at which the rudder was executed for the turning manoeuvre. The results of the manoeuvring parameters are also reported in Table 10.6, with an aim to quantify the turning quality of the ship for each simulated case. The contribution of the finite depth to the turning performance of the ship can be found, as clearly evidenced by the noticeable differences in the turning trajectory. In particular, the ship performing the manoeuvre in the shallow waters with h/D=1.2, 1.5, and 2.0 exhibited poorer turning ability when compared to the ship's inherent turning performance in deep water. Despite the same approaching speed (Fr = 0.095), the ship showed significantly larger increases in the tactical diameters (Figure 10.9 and Table 10.6). This was mainly attributed to the insufficient Under Keel Clearance (UKC, the vertical distance between the bottom of the ship and the sea floor), resulting in the strong hydrodynamic interaction between the hull, propeller, and rudder with the sea bed and consequently causing substantial changes in the turning performance of the ship. It was found that when the ship performing the turning manoeuvre, the smaller the UKC, the greater the ship turning diameter can be. Interestingly, the ship manoeuvring in the shallow waters with h/D = 3.0 and 4.0 showed a similar tendency to the ship's turning performance in deep water, confirming the weakened effect of the shallow water on the ship's manoeuvrability when h/D is greater than 3.0.

Considering the fact that only small heave, pitch, and roll motions during the turning manoeuvre were observed (mainly due to the absence of waves), the ship's motions in the horizontal plane – surge, sway, and yaw motion – were found decisive for the critical turning indices. As discussed in Kim et al. (2021b), the greater the surge velocity and the longer time taken for the 90° turn, the larger the ship advance and transfer can be. In Figure 10.10, the time histories of the ship velocities, forces and moments, and drift angles during the manoeuvre were presented for all cases (each case is indicated with a different colour). It appeared from Table 10.6 that the ship advance and transfer mainly increased with the decrease in the ratio of water depth to draft (h/D) since the ship in smaller h/D ratios experienced the larger surge velocity and the smaller yaw rate during the manoeuvre (Figure 10.10). The differences in the ship advance and transfer were not significant between the h/D = 3.0, 4.0 and deep-water conditions, which may be closely associated with the weakened shallow water effects on the manoeuvrability (despite the slightly different propeller revolution rates). The tactical diameters experienced by the ship also followed the similar trend.

The lateral force of the rudder was observed to rapidly increase soon after the deflection of the rudder blade (due to the increased angle of attack of the rudder), producing a large yaw moment to turn the ship's bow towards the starboard side (Figure 10.10 (g) and (f)). Subsequently, the mean effective angle of attack of the rudder decreased as the ship started to turn, and thus the rudder normal force gradually decreased and converged to a certain value. It was found that the rudder normal force was larger in smaller h/D ratios during the steady phase of the turn, being ascribed to the shallow water effects and different propeller rotational speeds. The manoeuvring ship exhibited an involuntary speed loss in the transient phase of the turn as the ship resistance increased with an increase in the drift angle experienced by the ship (Figure

10.10 (a), (b), and (h)). The speed loss was found larger in deeper depths. The speed loss rate between the initial surge velocity and the minimum value was estimated at 57% for the h/D = 1.2, 64% for the h/D = 1.5, 68% for the h/D = 2.0, 70% for the h/D = 3.0, 71% for the h/D = 4.0, 72% for the deep-water condition. Despite the larger later force of the rudder in smaller h/D ratios, the ship experienced the smaller sway and yaw velocities during the manoeuvre, implying the poorer turning performance in shallow water (Figure 10.10 (c) and (e)). It is worth noting that the dynamic behaviours of the vessel in higher h/D ratios became progressively similar to those in deep water, mainly due to the weakened shallow water effects on the ship manoeuvrability.

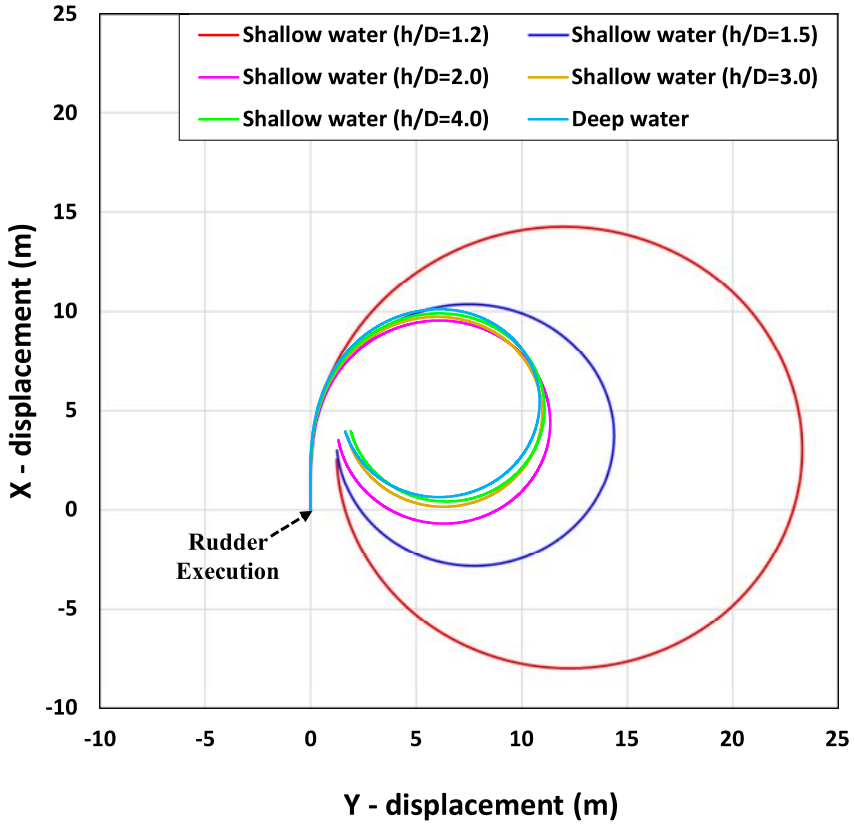

Figure 10.9 The predicted turning trajectories for all cases.

Table 10.6 CFD results: turning parameters.

Parameters (CFD results)	Case 1 (h/D=1.2)	Case 2 (h/D=1.5)	Case 3 (h/D=2.0)	Case 4 (h/D=3.0)	Case 5 (h/D=4.0)	Case 6 (Deep)
Advance (m)	14.23 **($4.66L_{BP}$)**	10.33 **($3.38L_{BP}$)**	9.45 **($3.09L_{BP}$)**	9.57 **($3.13L_{BP}$)**	9.73 **($3.18L_{BP}$)**	9.89 **($3.24L_{BP}$)**
Transfer (m)	11.56	6.82	5.16	4.80	4.80	4.65

	($3.78L_{BP}$)	**($2.23L_{BP}$)**	**($1.69L_{BP}$)**	**($1.57L_{BP}$)**	**($1.57L_{BP}$)**	**($1.52L_{BP}$)**
Time for yaw 90 degrees (s)	47.24	32.51	27.97	27.64	27.92	28.04
Tactical diameter (m)	23.28 **($7.62L_{BP}$)**	14.34 **($4.69L_{BP}$)**	11.29 **($3.69L_{BP}$)**	10.85 **($3.55L_{BP}$)**	10.94 **($3.58L_{BP}$)**	10.67 **($3.49L_{BP}$)**
Time for yaw 180 degrees (s)	93.88	64.51	55.38	54.49	54.78	55.21

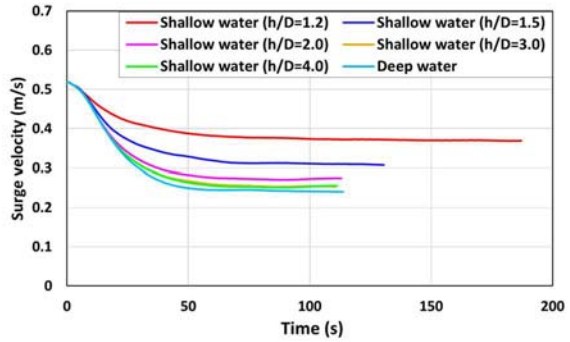

(a) Surge velocity

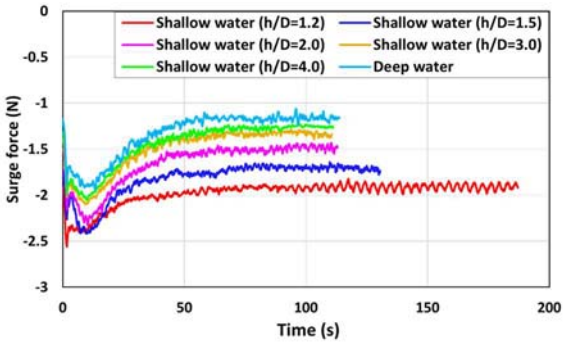

(b) Surge force

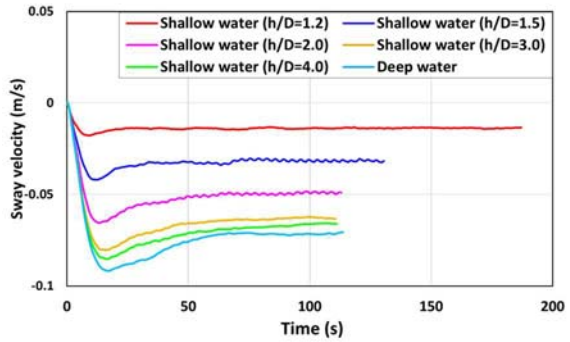

(c) Sway velocity

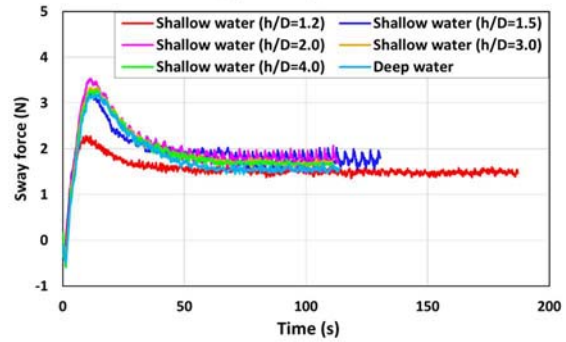

(d) Sway force

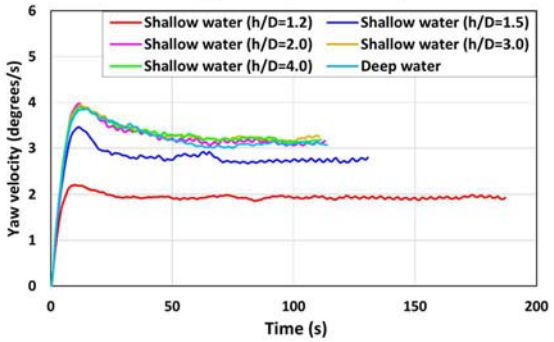

(e) Yaw velocity

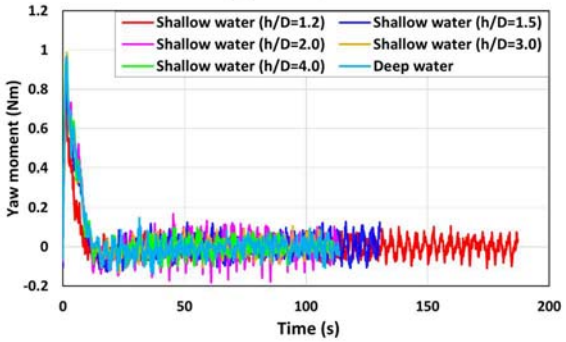

(f) Yaw moment

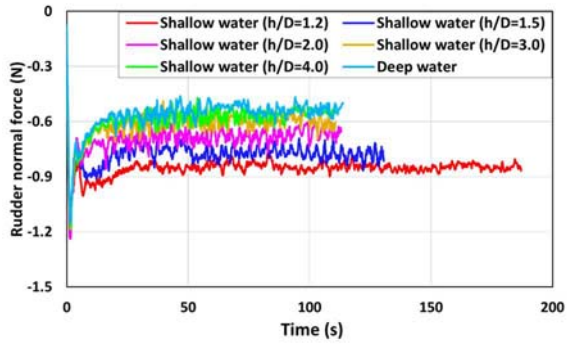

(g) Rudder normal force

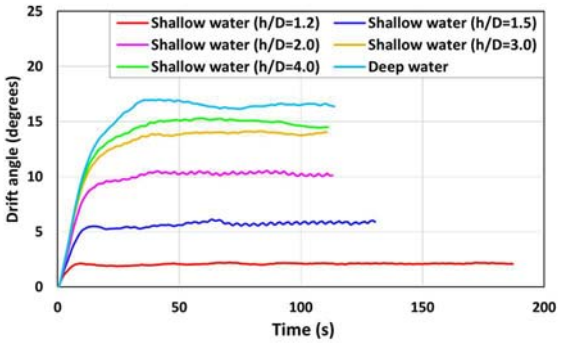

(h) Drift angle

Figure 10.10 The time histories of the ship velocities, forces and moments, and drift angles during the standard turning circle manoeuvre.

The comparison of the thrust and torque predicted by the body force method during the manoeuvre is shown in Figure 10.11. As stated previously, the performance of the propeller is highly dependent on the volume-averaged velocity over the inflow velocity plane (located upstream of the actuator disk), determined by the complicated interaction between the propeller revolution rate, the presence of the sea floor, and the wake distribution. It can be seen that right after the rudder deflection, the thrust and torque developed by the actuator disk slightly increased, being ascribed to the decrease in the advance ratio (due to the increased flow velocity in the disturbed flow region by the rudder activation). Subsequently, the thrust and torque started to decrease because of the increase of the advance coefficients caused by the rapid increases in the sway and yaw velocities experienced by the ship (Figure 10.10 (c) and (e)). After the ship experienced the peak values for the sway and yaw velocities, the advance ratio gradually decreased mainly due to the speed drops (including the surge velocity) and converged to a certain value in the steady phase of the turn. Accordingly, the propeller underwent a gradual increase in thrust (and torque) and then converged. It was also found that the propeller in smaller h/D ratios developed higher loads during the manoeuvre, closely associated with shallow water effects and different propeller revolution rates. Interestingly, the thrust and torque developed by the disk model during the steady phase of the turn for Case 1 were similar to those in the straight-ahead condition (the self-propulsion condition), whereas the propeller loads during the steady turn were larger than the self-propulsion condition for Case 2-6. This phenomenon resulted from the speed loss rate experienced by the ship during the manoeuvre.

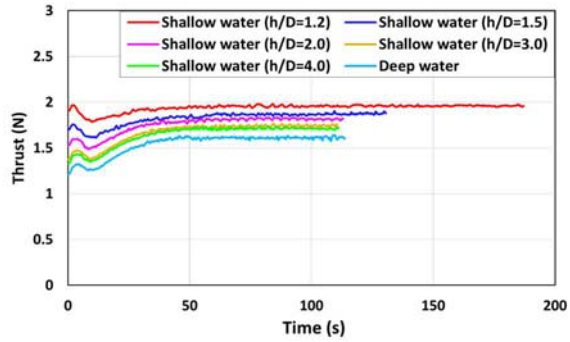

(a) Thrust

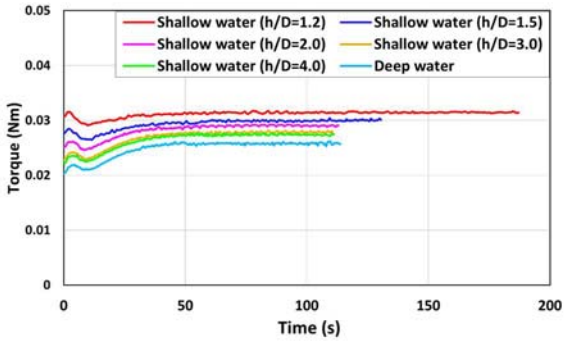

(b) Torque

Figure 10.11 The time histories of the propeller characteristics during the turning manoeuvre.

In Figure 10.12, the time histories of the heave, pitch, and roll motions experienced by the ship during the turning manoeuvre were presented. From the figure, it clearly appeared that only small ship motions were estimated during the manoeuvre mainly due to the slow approach speed and the absence of external disturbances. Given the available UKC, the predicted heave and pitch motions may not pose a significant threat to navigational safety at sea. In addition, the roll angles for all cases remained below about 1° during the manoeuvre due to a rather weak rudder normal force (compared to the design condition, Fr=0.26).

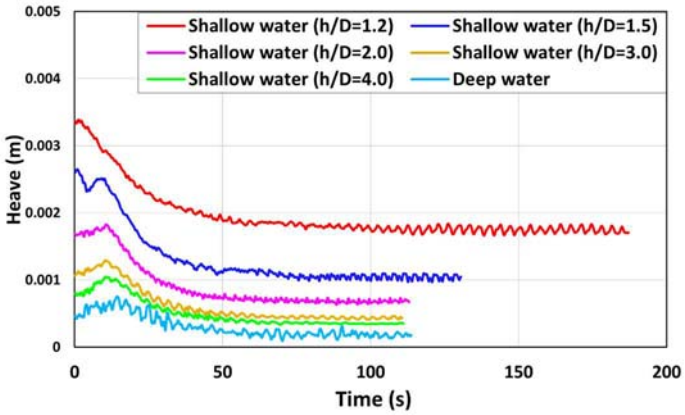

(a) Heave

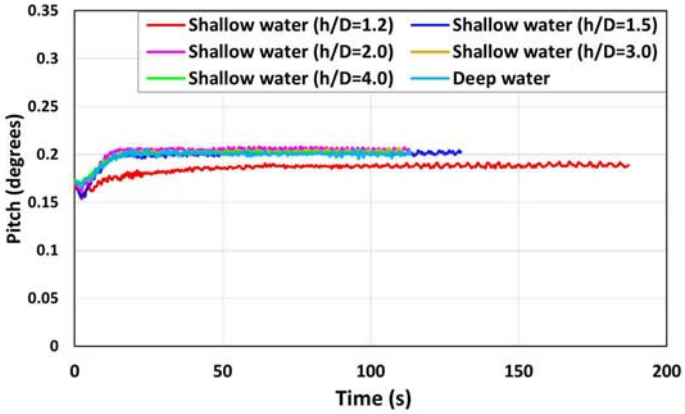

(b) Pitch

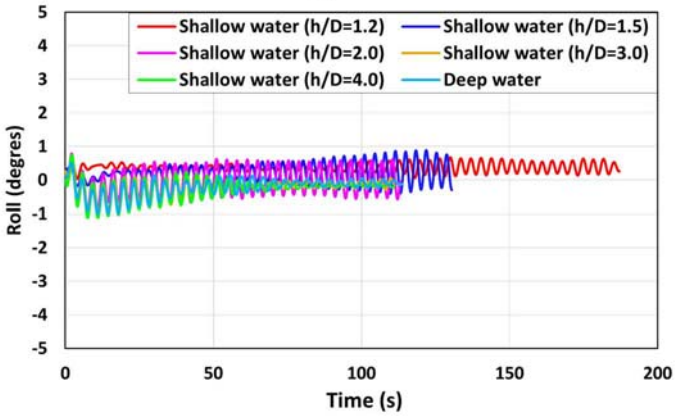

(c) Roll

Figure 10.12 The time histories of the ship motions during the turning manoeuvre.

Case 1, 2, and 3 were selected as representative cases to display pressure and velocity fields during the turning manoeuvre. Figure 10.13 shows the close-up views of dynamic pressure and longitudinal velocity fields at X/L_{PP}=−0.485 (No. 5 section) and pressure distributions on the rudder at self-propulsion, maximum yaw rate and steady yaw rate during the turning manoeuvre. It can be seen from the figure that the flow field experienced by the manoeuvring ship in shallow water was characterised by the interactions of the hull wake, boundary layer, propeller, vortex, and sea floor. As the ship started to turn, the vortex was generated by the cross-flow velocity and was convected towards the leeward side due to the yaw-drift motion (clearly evidenced in Figure 10.13, maximum yaw rate). The vortex convected away from the hull was strongly interacted with the hull boundary layer, the propeller, and the sea floor, demonstrating the complexity of the resulting flow field. It appeared that this vortex was more weakened in deeper depths. Besides, the vortex observed in the transient phase of the turn was more intense than that in the steady phase. As it can be inferred from the figure, the advancing ship at the self-propulsion condition experienced the uneven pressure distribution between the starboard and the port of the rudder blade due to the asymmetric flow (the swirl) generated by the propeller. The swirl induced by the propeller was directed from the starboard to the port at the bottom of the rudder, resulting in the pressure difference between the starboard and the port of the rudder. After the rudder deflection, the pressure differences were remarkable between the starboard and the port, causing the strong rudder lateral force to turn the ship during the manoeuvre.

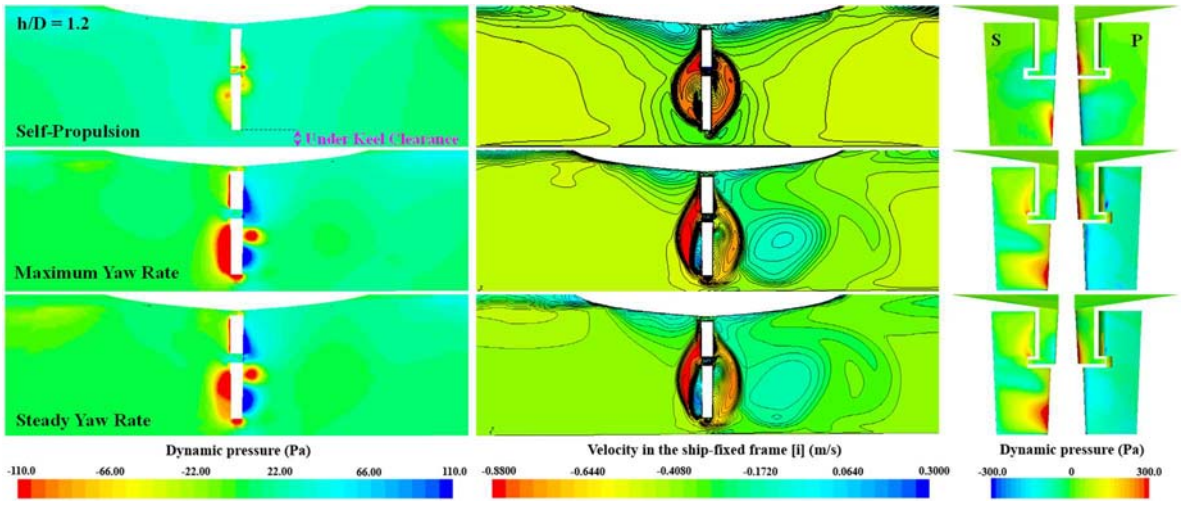

(a) Shallow water (h/D = 1.2)

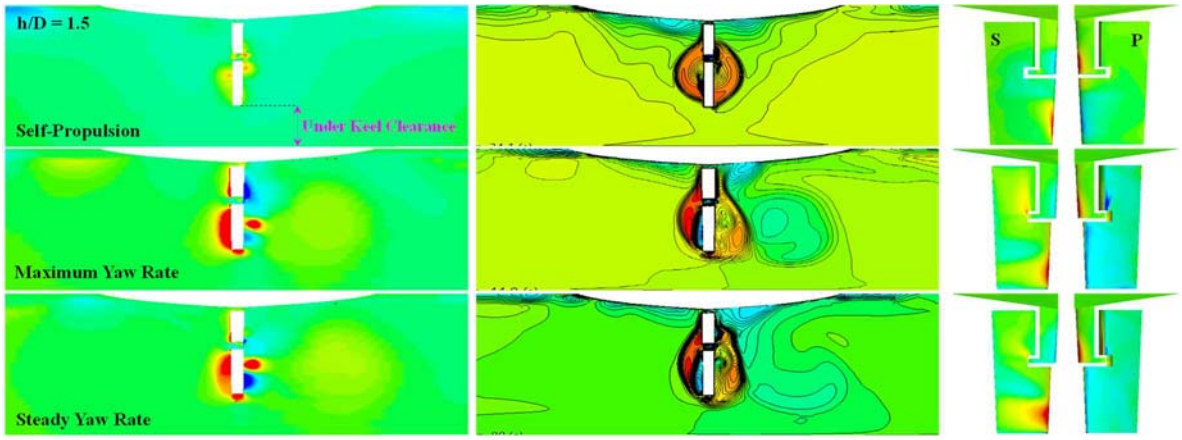

(b) Shallow water (h/D = 1.5)

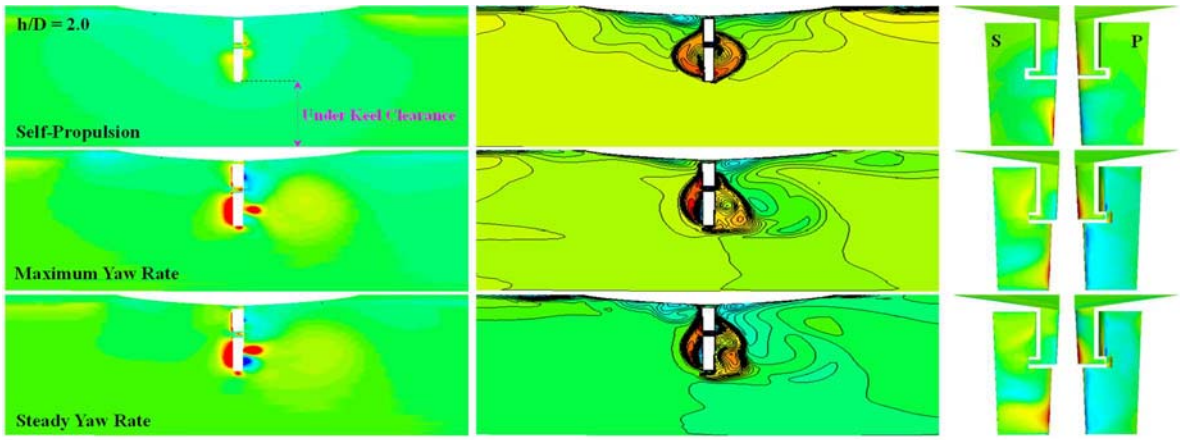

(c) Shallow water (h/D = 2.0)

Figure 10.13 The close-up views of dynamic pressure and longitudinal velocity fields at $\boldsymbol{X/L_{PP}}$=−0.485 (No. 5 section) and the pressure distributions on the rudder (S: starboard profile, P: port profile) at self-propulsion (top), maximum yaw rate (centre) and steady yaw rate (bottom) during the turning manoeuvre (obtained from Case1, 2 and 3).

10.5. Concluding Remarks

In this chapter, the shallow water effects on the manoeuvring performance of a container ship (the KCS model) have been thoroughly investigated. To this purpose, the free-running model for the prediction of ship manoeuvrability in shallow water has been developed by means of an unsteady Reynolds Averaged Navier-Stokes solver. The proposed CFD model has demonstrated an acceptable level of accuracy and reliability in estimating the manoeuvring behaviour of the ship in shallow water. The comparisons with the available free-running model experiments have been satisfactory in terms of both kinematic and trajectory parameters (Case 0). In addition, this model has allowed to analyse the different manoeuvring properties of the ship in question, i.e., course-keeping and turning circle manoeuvres. Although the results obtained from this study are for a specific benchmarking ship, the results could be applicable to a conventional container vessel of similar type and dimensions. The key findings of this study can be summarised as follows:

1) As long as the course keeping capability of the ship is concerned, the manoeuvring ship

in different shallow waters attained good course-keeping control as supported by the ship's actual sailing directions consistent with the true course. This aspect underscores that the finite depths have practically no influence on the course keeping ability in the case of the absence of external loads.

2) Regarding the turning manoeuvre, the contribution of the finite depth to the turning behaviour of the ship has been emphasised in comparison with the critical turning parameters and hydrodynamic quantities in relation to h/D ratios. It was revealed that the ship advance, transfer, and tactical diameter mainly increased with the decrease in the ratio of water depth to draft. The predicted transfer and tactical diameter for the h/D = 1.2 are more than twice as large as those for the deep-water condition, for the same approach speed (Fr = 0.095). It has to be pointed out that the differences in the turning parameters were not significant between the h/D = 3.0, 4.0, and the deep-water condition, which may stem from the negligible contribution of shallow water to the manoeuvring performance of the ship in these particular water depths.

3) The involuntary speed loss in the transient phase of the turn was found larger in deeper depths as the ship resistance increased with an increase in the drift angle experienced by the ship. The speed loss rate between the initial surge velocity and the minimum value was predicted at 57% for the h/D = 1.2, 64% for the h/D = 1.5, 68% for the h/D = 2.0, 70% for the h/D = 3.0, 71% for the h/D = 4.0, 72% for the deep-water condition.

11. FREE-RUNNING CFD SIMULATIONS FOR CURRENTS

11.1. Introduction

An accurate prediction of ship manoeuvrability under realistic environmental conditions is a prerequisite for the development and use of remote-controlled ships or maritime autonomous surface ships (MASS). These ships should be capable of performing path following and collision avoidance manoeuvres within an acceptable level of safety and reliability. Given that the reliable estimation of ship manoeuvrability can be decisive for the execution of such safe autonomous operations, it is critical to accurately predict the manoeuvring performance of a ship under external disturbances (waves, winds, and currents) in which the ship is to be operated. As the prediction of ship manoeuvrability in waves have already been studied in Chapters 5 – 9, this chapter aims to comprehensively analyse the manoeuvring behaviour of a ship in different ocean currents.

Ships sailing in open seas and coastal waters are mostly exposed to ocean currents. According to the National Oceanic and Atmospheric Administration (NOAA), ocean currents (characterised by the horizontal movement of water) are generally driven by the rise and fall of the tides, wind, and thermohaline circulation (density differences in water due to temperature). It has to be highlighted that the tidal currents can travel much faster than the currents driven by wind or thermohaline circulation, indicating top daily speeds of eight knots or more in a specific sea area. For example, the Kurushima Kaikyo of the Japan inland sea can be regarded as strong tidal current waters with up to 10 knots of current (monitored by its VTS centre to ensure navigational safety). The presence of currents will lead to substantial changes in a ship's manoeuvring behaviour when compared to its inherent behaviour in calm water without current, due to the hydrodynamic effects induced by currents. In this regard, it is believed that a better understanding of ship manoeuvrability in currents may contribute to proper decision making for ship handling actions and thus safe ship operation at sea.

Although numerous attempts have been made to investigate the manoeuvring behaviour of a ship in calm water and waves (as reviewed in Chapter 3), there has been a notable lack of research into the effect of currents on ship manoeuvrability. It has been observed in real operations that vessels experience currents of different velocities and directions depending on the area the ship is to be navigated through. The importance of potential current effects and the lack of previous studies support the main argument of this chapter: the analysis of the relationship between ocean currents and ship manoeuvrability is necessary. In this context, this chapter was motivated to investigate the impact of currents on the manoeuvring capability of the well-known benchmarking KCS which has been widely used in the fields of ship hydrodynamics. In this particular study, all manoeuvring analyses were performed by means of URANS simulations.

In the present work, the turning capability of a container ship was investigated with a complete analysis of the turning indices and hydrodynamic loads experienced by the manoeuvring ship in different current conditions to obtain a deeper insight into the ship manoeuvrability. It will

be shown that the numerical results can confirm the critical contribution of current effects on the manoeuvring performance of the ship in terms of the ship advance, transfer, and tactical diameter. It is believed that this study will provide a clear and detailed description of ship manoeuvrability in ocean currents and may give a significant contribution to navigational safety at sea.

This chapter is organised as follows: The CFD simulation cases designed in this study are provided in Section 11.2. Following this, a specific presentation of the numerical modelling for the current CFD model is described in Section 11.3. Then, the obtained CFD results are illustrated in Section 11.4, including validation studies for the present CFD model. Finally, concluding remarks wrap up this chapter in Section 11.5.

11.2. Goal and Scope

The main goal of this chapter is to examine the effects of ocean currents on the manoeuvrability of the KCS with particular emphasis on the turning capability, performing free-running CFD simulations.

The present study considered nine different simulation cases for which the free-running CFD model was applied, as reported in Table 11.1. For the sake of clarity, the schematic representation of the cases is also depicted in Figure 11.1. As a validation case for the CFD approach used in this study, a standard turning circle manoeuvre (35° starboard turn) in deep water without a current (Case 0) was performed. The experimental results of the turning circle manoeuvre produced by Hiroshima University (SIMMAN, 2020) were utilised as benchmark data for validation purposes. After the validation study, a series of numerical simulations for turning manoeuvres were carried out in different current speed to ship speed ratios (Case 1 - 8): 1) $V_c/U_0 = -0.138$, 2) $V_c/U_0 = -0.276$, 3) $V_c/U_0 = -0.414$, 4) $V_c/U_0 = -0.552$, 5) $V_c/U_0 = +0.138$, 6) $V_c/U_0 = +0.276$, 7) $V_c/U_0 = +0.414$, 8) $V_c/U_0 = +0.552$ (with indicating V_c and U_0 the current speed and ship speed, respectively). A negative sign indicates ahead currents, whereas a positive sign means following currents. It can be estimated from the ratios that the currents applied in this study ranged between -8 knots and +8 knots in full scale, in correspondence to the speed of strong currents identified by NOAA. The simulation cases cover a significant range of ocean current conditions experienced by a ship in real navigation. The approach speed of the ship in all cases was chosen to be 0.86 m/s (corresponding to 14.5 knots in full scale) in a similar manner to the experiments of Hiroshima University. The corresponding Froude and Reynolds numbers were $Fr = 0.157$ and $Re = 2.07 \times 10^6$ in model scale, respectively. It has to be mentioned that all the manoeuvring analyses were conducted using deep water conditions.

Table 11.1 The simulation cases to which the CFD model is applied.

Case	Approach speed U_0 (m/s)	Current speed/ Ship speed V_c/U_0	Free running manoeuvres
0	0.860	0.000 (without a current)	35° starboard turn **(Validation case)**
1	0.860	−0.138 (ahead current)	35° starboard turn
2	0.860	−0.276 (ahead current)	35° starboard turn
3	0.860	−0.414 (ahead current)	35° starboard turn
4	0.860	−0.552 (ahead current)	35° starboard turn
5	0.860	+0.138 (following current)	35° starboard turn
6	0.860	+0.276 (following current)	35° starboard turn
7	0.860	+0.414 (following current)	35° starboard turn
8	0.860	+0.552 (following current)	35° starboard turn

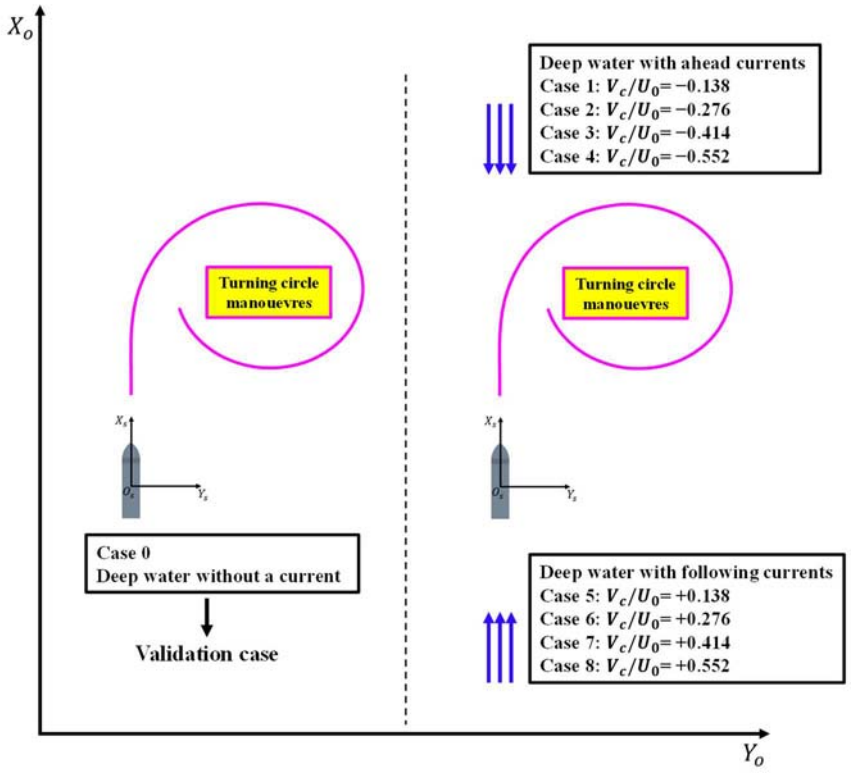

Figure 11.1 The schematic view of the simulation cases applied to this study.

11.3. Numerical Modelling

It has to be mentioned that the current CFD model was developed in accordance with the numerical setup explained in detail in Chapter 4, Section 4.3.

Computational grids were generated by means of the automatic meshing facility in Star-CCM+, leading to the total number of grid cells being about 6.2 million. Two views of the final computational mesh of the CFD model are shown in Figure 11.2.

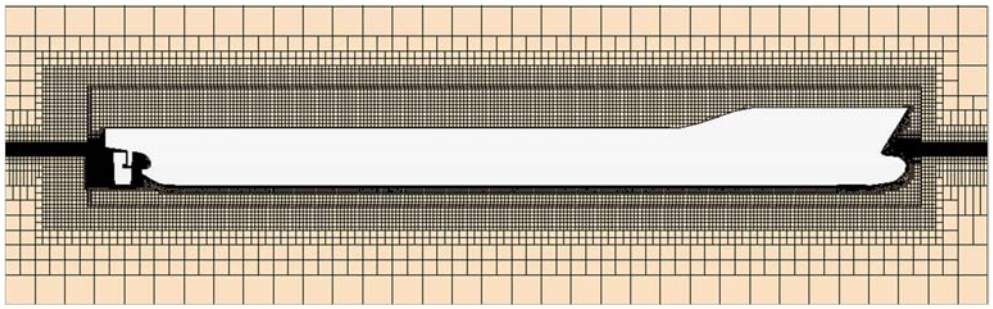

(a) Profile view cross-section of the domain

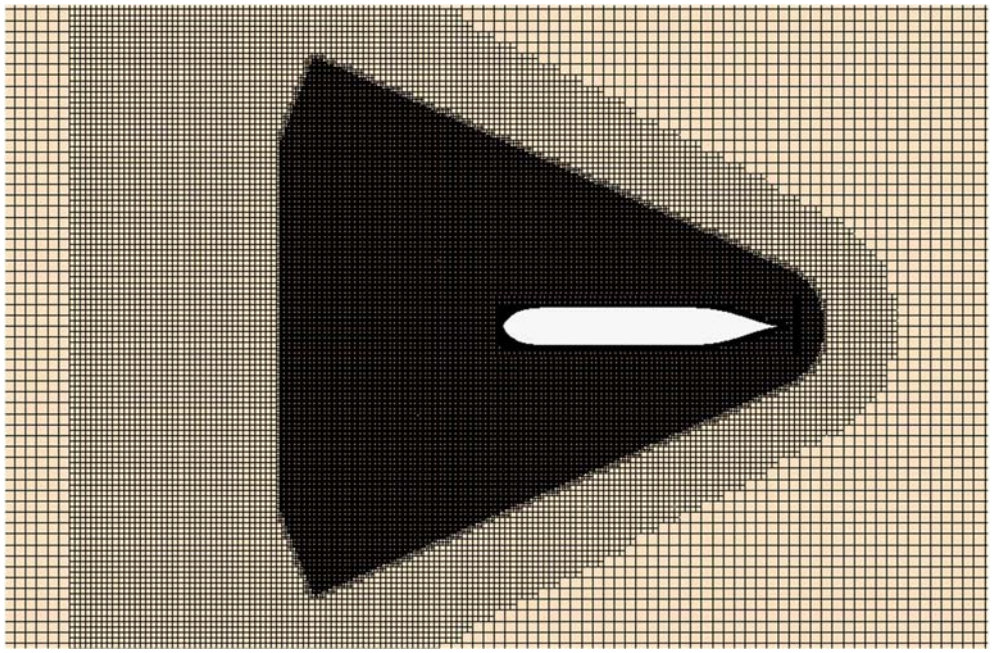

(b) Top view cross-section of the domain

Figure 11.2 Mesh structure of the computational domain.

The time-step size of the simulations in this work was selected to be $\Delta t = 0.005$s, ensuring the Courant-Friedrichs-Lewy (CFL) number is less than unity during the computations to avoid numerical instabilities. The chosen time step also satisfied the recommendation for the time-step condition of $\Delta t \leq 0.01L/U$ put forward by ITTC (2011), in which L and U denote ship length and ship speed, respectively. $\Delta t = 0.005$s is even seven times lower than the value calculated from the recommendation by ITTC (2011). It has been already demonstrated that the use of $\Delta t = 0.005$s is sufficiently appropriate when performing free-running simulations of the 1/75.24 scale KCS model in Chapters 5 and 10, yielding reliable numerical results.

11.4. Results

11.4.1. Validation study

As outlined in Section 11.2, Case 0 (deep water without a current) was used for the validation of the present CFD model against the experiment (a free-running model test) performed by Hiroshima University (SIMMAN, 2020). It has to be pointed out that there are no available

experimental results for the KCS's manoeuvrability in currents in the literature so that the validation study concerning the current conditions (Case 1 – 8) could not be conducted in this work. Figure **11.3** presents a comparison of the time histories of the kinematic parameters, motions, and propeller characteristics and the trajectory experienced by the ship during the turning manoeuvre in deep water without a current between this study's CFD model and the experiment. In the presented results, t = 0 is the time at which the rudder blade started to be deflected for the turning manoeuvre. The numerical simulation stopped when the ship's heading angle variation reached 360° based on the general procedure by IMO (2002). The comparison in terms of the ship's velocity in the horizontal plane consisting of the surge, sway, and yaw velocities confirmed the satisfactory agreement between CFD and Experimental Fluid Dynamics (EFD) (Figure 11.3 (a) - (c)); a slight overprediction of the sway velocity was observed during the steady phase of the turn. Regarding the ship's roll motion, an error of approximately 3° was observed during the turning manoeuvre (Figure 11.3 (d)). The underestimation of the roll angle can be attributed to the limitation of the present disk model that cannot take into account the side force of the propeller during the manoeuvre. As expected, only small pitch and heave motions were observed both numerically and experimentally due to the absence of external disturbances, showing a reasonable agreement between the CFD and EFD results (Figure 11.3 (e) and (f)). The CFD results for the thrust and torque experienced by the ship during the manoeuvre were found in good agreement with the experimental data; the predicted trend qualitatively and quantitatively corresponded well with the experiment (Figure 11.3 (g) and (h)). It can be seen that the predicted trajectory experienced by the manoeuvring ship was fairly well consistent with the experiment (Figure 11.3 (i)).

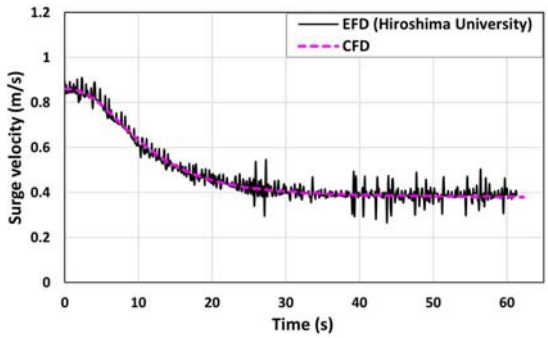

(a) Surge velocity

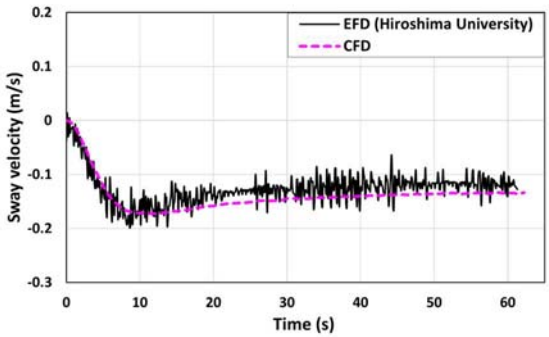

(b) Sway velocity

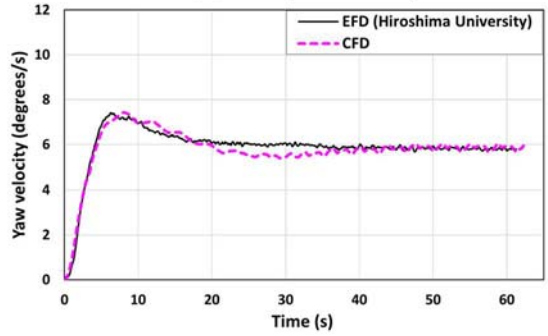

(c) Yaw velocity

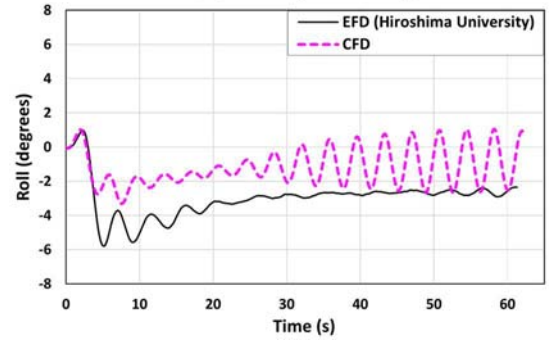

(d) Roll displacement

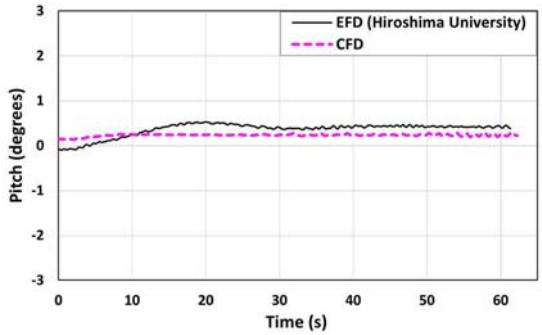

(e) Pitch displacement

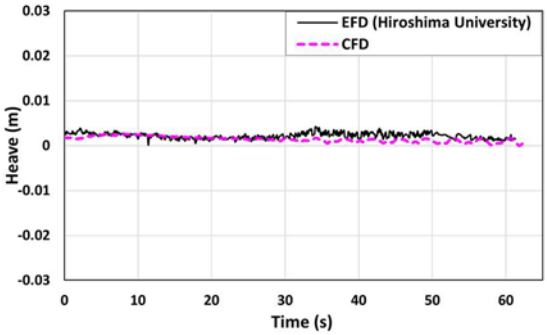

(f) Heave displacement

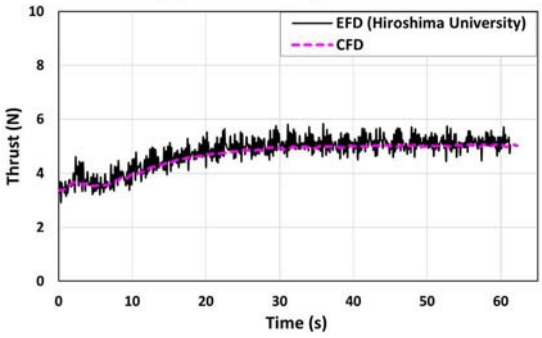

(g) Thrust

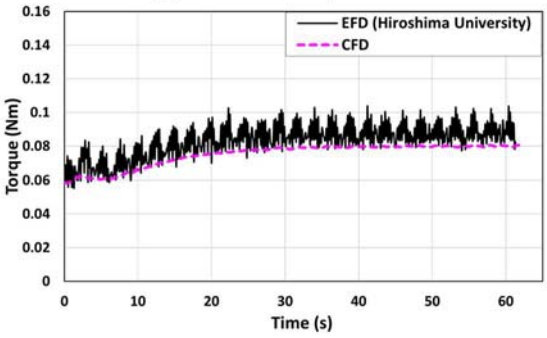

(h) Torque

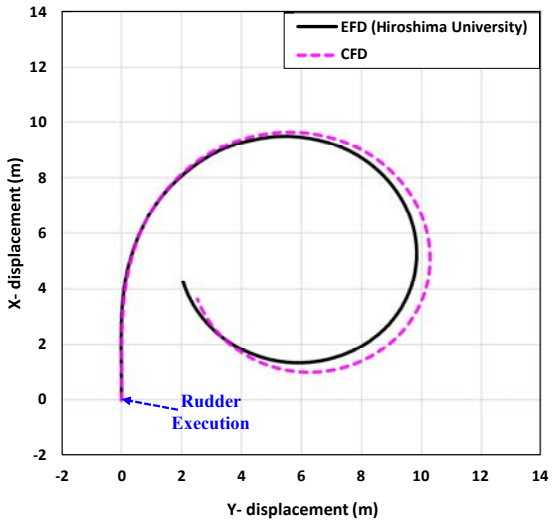

(i) Ship trajectory

Figure 11.3 The comparisons of the kinematic parameters, motions, propeller characteristics, and trajectory experienced by the ship during the turning manoeuvre in deep water without a current (Case 0).

In addition, Table 11.2 presents a comparative analysis in terms of the ship advance, transfer, tactical diameter, time to 90°/180° yaw angle change, and kinematic parameters in the steady phase of the turn. In the table, the discrepancies between the numerical and experimental results are reported as well. The free-running CFD model has shown good agreement with respect to the trajectory and kinematic parameters against the experiment. It can be seen from Table 11.2 that the largest error was observed for the tactical diameter; however, the error remained below 4%. In light of the acceptable agreement evidenced from Figure 11.3 and Table 11.2, it can be

claimed that the present CFD model enables the reliable estimation of the manoeuvring performance of the ship in question.

Table 11.2 The comparison of the trajectory and kinematic parameters (Case 0).

Parameters	CFD	EFD (SIMMAN, 2020)	Error (%)
RPS at self-propulsion point	10.56	10.40	1.58
Advance (m)	9.38	9.29	0.97
Transfer (m)	4.07	4.16	–2.16
Time for yaw 90 degrees (s)	15.46	15.64	–1.15
Tactical diameter (m)	10.02	9.66	3.72
Time for yaw 180 degrees (s)	31.12	30.50	2.03
Speed loss (m/s)	0.476	0.472	0.85
Yaw velocity (degrees/s, steady phase)	5.84	5.83	0.17

11.4.2. Self-propulsion

The self-propulsion computations were first conducted to obtain the approach speed (0.86 m/s), allowing the ship to move in full 6DOF with the moving rudder controlled by a Proportional-Integral-Derivative (PID) controller for course-keeping control before the turning manoeuvre (as described in Chapter 4, Section 4.3.9).

The average values of the ship resistance and the propeller revolution rates at the self-propulsion condition are reported in Table 11.3. As can be seen, the presence of the current was found to result in noticeable changes in the ship resistance experienced by the advancing ship at self-propulsion when compared to Case 0 (the deep water without a current condition). For the ahead current conditions (Case 1 - 4), the increase of the current velocity led to a substantial increase in the ship resistance with consequent demand for the additional propulsion power to achieve the same approach speed. For the following current conditions (Case 5 – 8), on the other hand, the ship resistance was found to gradually decrease with the decrease in the current velocity. It has to be noticed that the propeller revolution rate to reach the same approaching speed was remarkably different from each case due to the different current contributions to the ship resistance. In this sub-section, the effects of currents on the ship motions at self-propulsion were not discussed since only small amplitudes of the ship motions (i.e., roll, heave, and pitch) were numerically observed, mainly due to the absence of incident waves in this work.

Table 11.3 The mean value of the ship resistance and the propeller revolution rate at self-propulsion in model scale.

	Case 0	Case 1	Case 2	Case 3	Case 4	Case 5	Case 6	Case 7	Case 8
Ship resistance (N)	3.35	4.16	5.19	6.45	7.87	2.61	1.99	1.63	0.99
Propeller rev. (RPS)	10.56	12.00	13.42	15.05	16.60	9.25	8.25	7.10	5.50

A zoomed view of the instantaneous free surface elevation around the ship at self-propulsion is depicted in Figure **11.4**. The markedly different wave patterns around the KCS can be clearly seen from the figure, despite the same approaching speed (Fr = 0.157). This may be mainly attributed to the strong interaction between the Kelvin waves generated by the ship and the current. The effects of the different propeller revolution rates on the stern waves were also

clearly shown, evidenced by the different free surface elevations at the stern region.

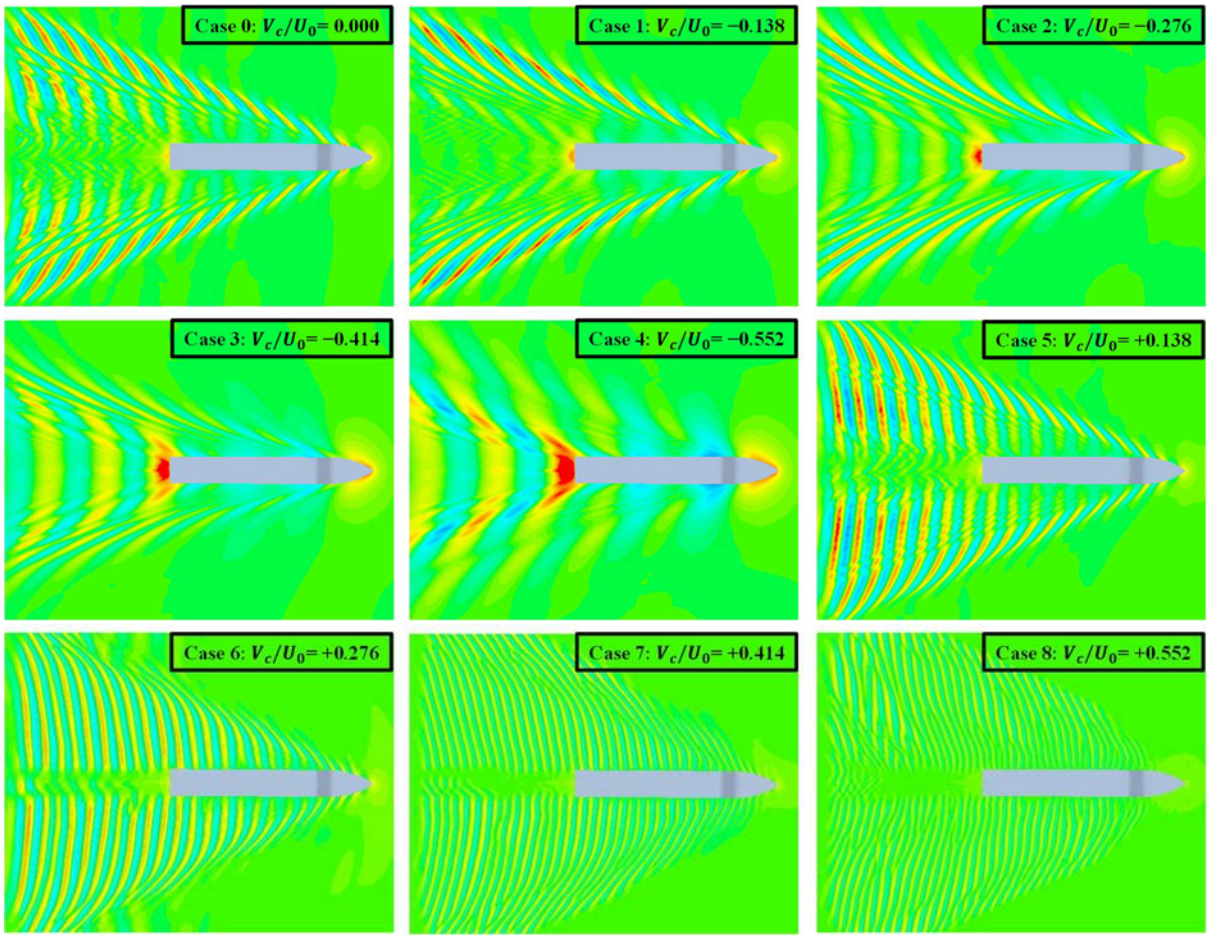

Figure 11.4 Measured wave pattern around the advancing ship at self-propulsion (Fr = 0.157).

11.4.3. Turning circle manoeuvre

11.4.3.1 Turning indices and time histories during the turning manoeuvre

This sub-section will provide the details of the numerical results for the free-running manoeuvres with particular emphasis on the turning performance of the ship operating in different currents (such as ahead and following current conditions). The contribution of different currents to the ship's turning behaviour was analysed in detail by comparison with its inherent behaviour in deep water without a current (Case 0). The results presented in this sub-section addressed the turning manoeuvres with only yaw angle variation up to 360° as implemented in the validation study. It is expected that the manoeuvring ship in the currents (Case 1 - 8) may experience substantial changes in the turning capability when compared to that observed in deep water without a current, attributed to the hydrodynamic effects caused by the presence of the current.

The ship trajectories predicted by the free-running CFD model performing the turning manoeuvre in accordance with the control mechanism (given by Equation (4.21)) are displayed in Figure 11.5, expressed with respect to the earth-fixed reference frame. In the figure, all the rudder activation points were shifted to the origin (0,0) of the reference frame for the sake of

the correct comparisons of the ship paths. The turning indices for each case are also reported in Table 11.4, which can be determined from the obtained trajectories as defined in ITTC (2021b). It was evident that the inclusion of the current noticeably affects the ship trajectory and its turning parameters, clearly evidenced in the figure and table. The ship's heading angle continued to change while turning, leading to continual changes in the current-encounter direction during the manoeuvre. As a result, the acceleration and deceleration phenomena of the ship's speed occurred with the variation of the current-encounter direction. For example, a ship advancing in the ahead currents (Case 1 - 4) encountered the current from the bow direction (0° turn), from the port beam (90° turn), from the stern (180° turn), from the starboard beam (270° turn), and again from the bow (360° turn) in series after starting the starboard turning manoeuvre. The ship's velocity was decelerated by the ahead currents (from the bow) or accelerated by the following currents (from the stern) during the manoeuvre, consequently leading to substantial changes in the turning behaviour of the ship. It is confirmed that the presence of the current caused the drift of the path towards the current propagation direction, such that the turning trajectories were significantly deformed under stronger current conditions when compared to Case 0. When the ship was manoeuvring in the ahead current conditions (Case 1 - 4), it was revealed that the greater current velocity led to the smaller ship advance. On the contrary, the ship showed an opposite tendency in the following current conditions (Case 5 - 8). Unlike the remarkable changes in the advance, the ship experienced a slight change in the transfer and tactical diameter for both the ahead and following current conditions. Different propeller revolution rates applied to the CFD model (to obtain the same approach speed at a given condition) resulted in noticeable differences in the time taken for the 90°/180° turn. The greater propeller thrust led to the shorter 90°/180° turning time, generating the larger rudder normal force when the rudder blade was deflected. It seems difficult to sufficiently characterise the trajectories experienced by the ship operating in strong currents by means of the turning indices, as can be inferred from Figure 11.5 and Table 11.4.

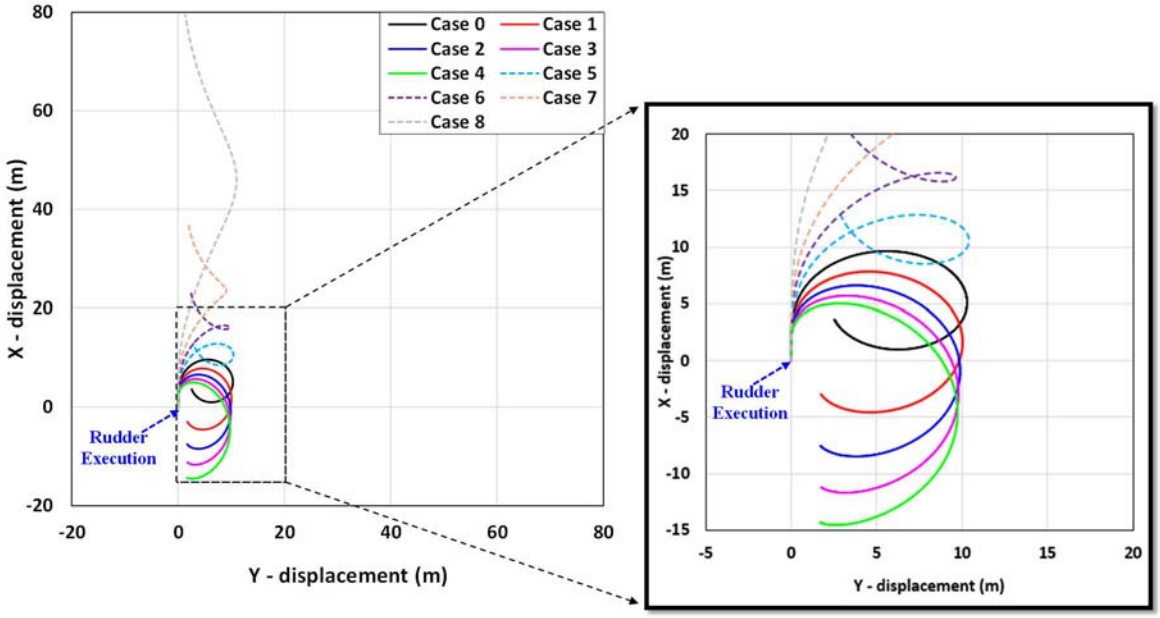

Figure 11.5 The predicted turning trajectories for all cases.

Table 11.4 CFD results: turning parameters.

Parameters (CFD results)	Case 0	Case 1	Case 2	Case 3	Case 4
			Ahead current conditions		
Advance (m)	9.38 **($3.07L_{BP}$)**	7.81 **($2.55L_{BP}$)**	6.60 **($2.16L_{BP}$)**	5.63 **($1.84L_{BP}$)**	4.86 **($1.59L_{BP}$)**
Transfer (m)	4.07 **($1.33L_{BP}$)**	4.02 **($1.32L_{BP}$)**	4.00 **($1.31L_{BP}$)**	3.98 **($1.30L_{BP}$)**	3.96 **($1.29L_{BP}$)**
Time for yaw 90 degrees (s)	15.46	13.58	12.17	10.99	10.13
Tactical diameter (m)	10.02 **($3.28L_{BP}$)**	9.78 **($3.20L_{BP}$)**	9.66 **($3.16L_{BP}$)**	9.56 **($3.13L_{BP}$)**	9.51 **($3.11L_{BP}$)**
Time for yaw 180 degrees (s)	31.12	27.03	23.92	21.33	19.53

Parameters (CFD results)	Case 5	Case 6	Case 7	Case 8
		Following current conditions		
Advance (m)	11.90 **($3.89L_{BP}$)**	14.14 **($4.63L_{BP}$)**	16.90 **($5.53L_{BP}$)**	24.27 **($7.94L_{BP}$)**
Transfer (m)	4.26 **($1.39L_{BP}$)**	3.95 **($1.29L_{BP}$)**	3.59 **($1.17L_{BP}$)**	3.51 **($1.15L_{BP}$)**
Time for yaw 90 degrees (s)	18.74	20.91	23.72	33.28
Tactical diameter (m)	10.15 **($3.32L_{BP}$)**	9.39 **($3.07L_{BP}$)**	8.84 **($2.89L_{BP}$)**	10.46 **($3.42L_{BP}$)**
Time for yaw 180 degrees (s)	36.85	40.72	47.09	76.5

The time histories of the velocities, forces and moments, and drift angles experienced by the ship during the turning manoeuvre are displayed in Figure 11.6, where each case is indicated with a different colour. It was observed for all cases that the ship started to turn towards the starboard side immediately after the execution of the rudder due to the increased rudder normal force (Figure 11.6 (g)). After the rudder completed its deflection (35°), the ship experienced the peak value for the rudder normal force. The ship operating in the ahead currents (Case 1 - 4) led to a larger rudder normal force peak (mainly attributed to the relatively large propeller revolution rate) than the following current conditions (Case 5 - 8), consequently, caused larger yaw moment and yaw velocity peaks (Figure 11.6 (e) and (f)). Then, the rudder normal force exhibited a gradual decrease (because of the decrease in the mean effective angle of attack of the rudder) and finally stabilised. The trends observed for the yaw velocity and yaw moment were similar to the behaviour of the rudder force. From Figure 11.6 (a) and (c), it clearly appeared that the differences were remarkable in terms of the surge and sway velocities experienced by the ship in the currents (Case 1 – 8), characterised by the acceleration and deceleration phenomena due to the current. Such perceptible differences in the surge and sway velocities are the main contributions to the differences in the predicted ship trajectories, as evidenced in Figure 11.5. The surge and sway velocities finally converged to a steady value for Case 0, whereas they showed a changing trend that continued to decrease and increase during

the turn for Case 1 - 8 (stemming from the presence of the current). In this regard, the drift angle β' experienced by the ship in the currents (Case 1 - 8) also followed a similar trend, showing continuous changes in the drift angle during the manoeuvre (the drift angle β' is expressed by $\sin\beta' = -\frac{Sway\ velocity}{Absolute\ velocity}$) (Figure 11.6 (h)).

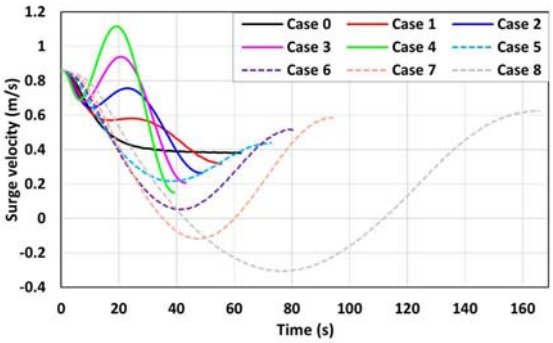

(a) Surge velocity

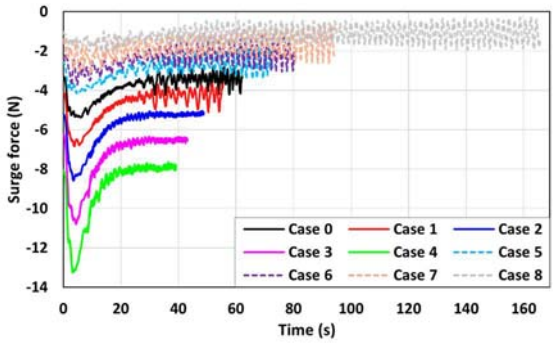

(b) Surge force

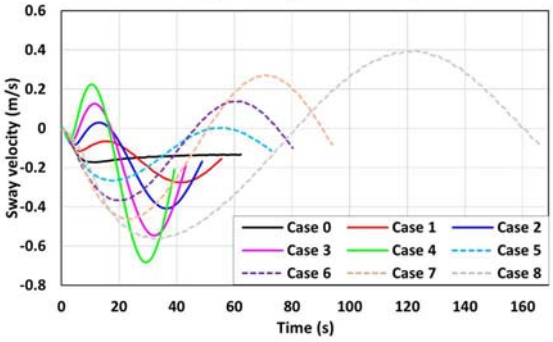

(c) Sway velocity

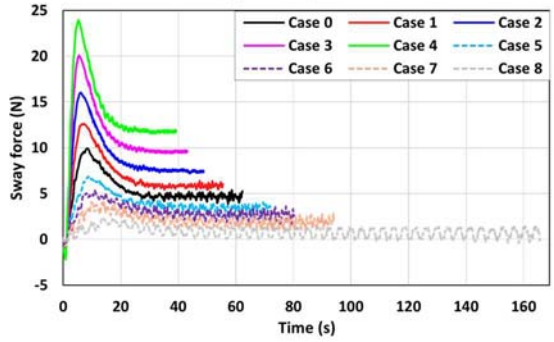

(d) Sway force

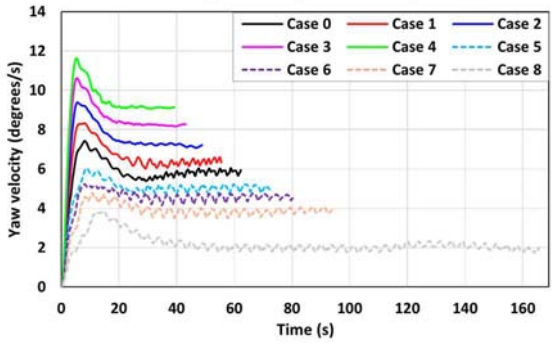

(e) Yaw velocity

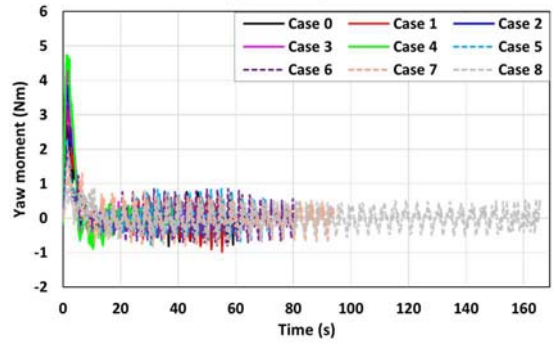

(f) Yaw moment

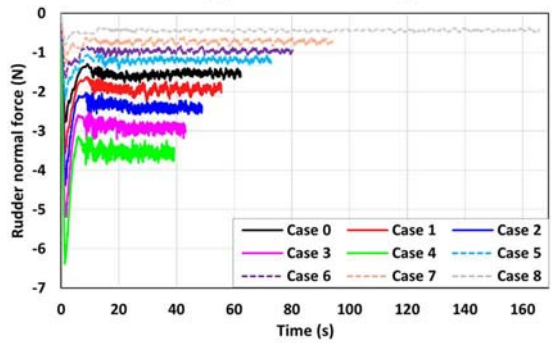

(g) Rudder normal force

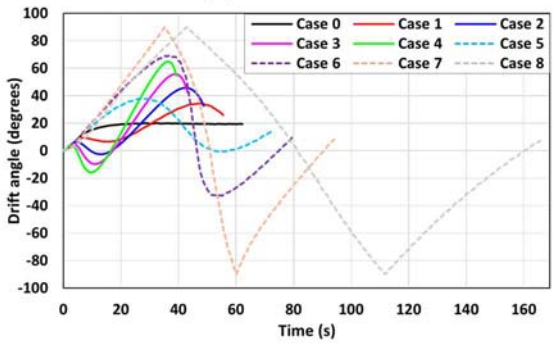

(h) Drift angle

Figure 11.6 The time histories of the ship velocities, forces and moments, and drift angles during the turning circle manoeuvre.

In Figure 11.7, the different characteristics of the propeller in the currents during the turning manoeuvre can be appreciated in terms of the thrust and torque. A larger increase in the thrust was observed after the rudder deflection for the ahead currents (Case 1 - 4), whereas a relatively small increase was noted for the following currents (Case 4 - 8). The behaviour of the torque was similar to the thrust. As mentioned previously, the volume-averaged velocity over the inflow velocity plane was an important factor in the determination of the performance of the propeller, which was dependent on the complicated interaction between the propeller revolution rate, the presence of the current, and the propeller wake velocity field.

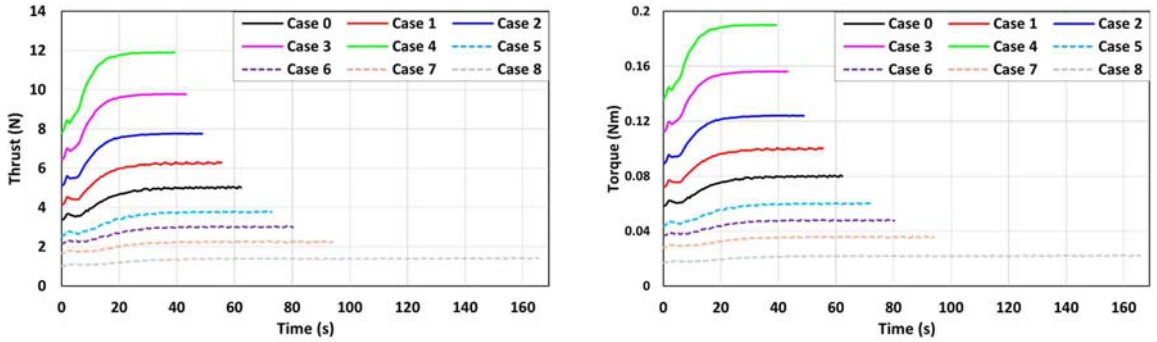

(a) Thrust (b) Torque

Figure 11.7 The time histories of the propeller characteristics during the turning manoeuvre.

Figure 11.8 shows the time histories of the heave, pitch, and roll motions during the turning manoeuvres. A rapid increase in the pitch and heave displacements was observed during the beginning of the turn, and, after a peak, they converged to a certain value after approximately two-quarters of the turn. The self-propelled ship performing the turning manoeuvre can be characterised by the trim by stern condition (the condition in which a vessel inclines aft). The ship operating in the ahead currents (Case 1 - 4) experienced a relatively large roll angle during the manoeuvre, attributed to the strong lateral force acting on the rudder (related to the initial peak roll angle) and the hydrodynamic forces and the centrifugal force acting on the hull (associated with the second peak). The ship with the maximum propeller rate exhibited the maximum roll angle of 10 degrees (i.e., under the maximum velocity of the current condition, Case 4). Relatively small roll angles of less than two degrees were observed for the following current conditions (Case 5 – 8).

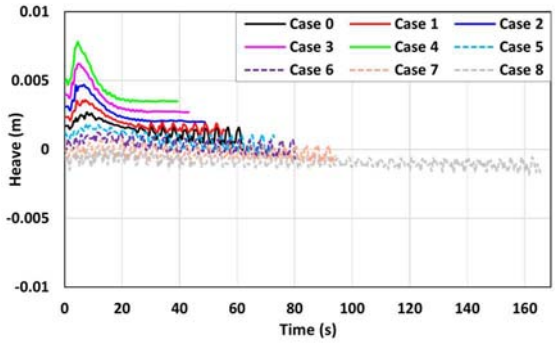

(a) Heave

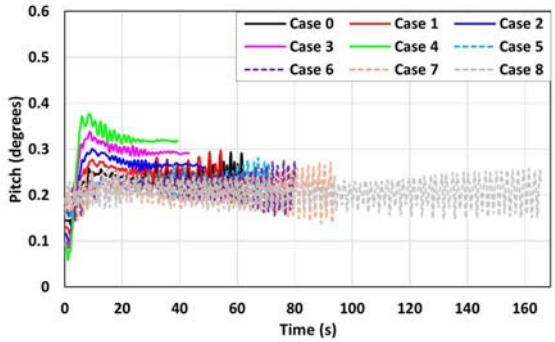

(b) Pitch

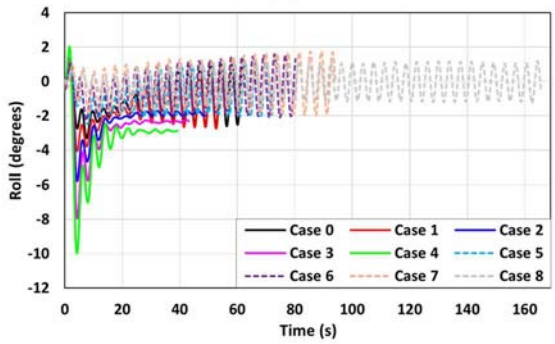

(c) Roll

Figure 11.8 The time histories of the ship motions during the turning manoeuvre.

Understanding the speed through water (STW) experienced by a manoeuvring ship in navigation practice is critical for making proper decisions on collision avoidance. STW is the speed of the vessel relative to the water, which is required to be used in ARPA (automatic radar plotting aids) radars to provide an accurate estimate of the target's aspect (for radar collision avoidance). It is worth noting that Figure 11.6 (a) and (b) represent the speed over ground (SOG) which is the speed of the vessel relative to the surface of the earth (closely associated with the trajectory experienced by the ship). Figure 11.9 presents the time histories of the ship surge and sway velocities with respect to STW during the turning manoeuvres. The differences were remarkable between the speeds over ground (Figure 11.6 (a) and (b)) and the speeds through water (Figure 11.9 (a) and (b)), demonstrating that currents are the main factor responsible for the difference between SOG and STW. It was observed that all the speeds through water showed a similar trend to the speeds experienced by the ship in deep water without a current. STW is totally consistent with SOG when the ship operates in water without a current (for example, Case 0). The speeds through water were noted to be relatively large when the ship was performing the turning manoeuvre at the relatively large propeller revolution rate.

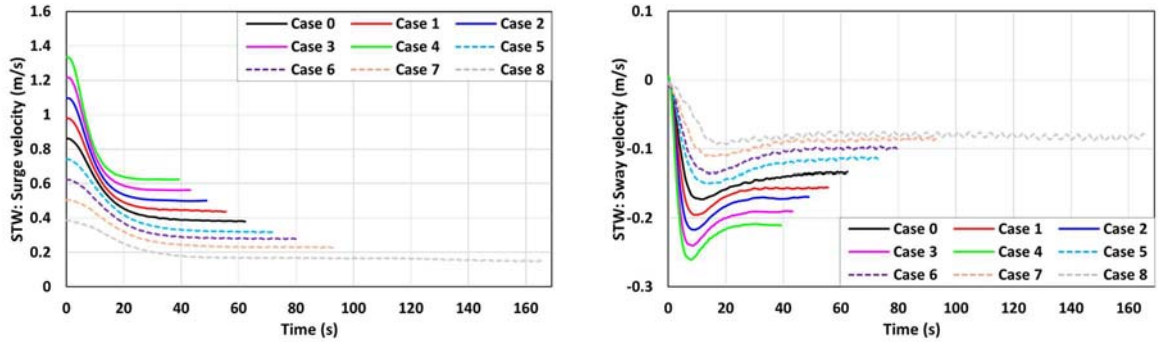

(a) STW: Surge velocity (b) STW: Sway velocity

Figure 11.9 The time histories of the ship velocities with respect to the speed through water (STW) during the turning manoeuvre.

11.4.3.2 Corrected trajectories

IMO (2002) states that the turning trajectory of a ship in calm water (i.e., the inherent turning capability) can be obtained by the correction for the drift effect of external disturbances on the ship's turning trajectory measured in currents, winds, and waves. As the present study only considered the current effects on the ship's manoeuvrability, the attention was devoted to the correction for the drift effect of currents on the trajectory in this sub-section. According to the guidelines of IMO (2002), the ship's trajectory, the heading angle, and the elapsed time should be recorded at least until the ship's heading variation reaches 720° to determine the local surface current velocity experienced by the ship. Based on this, additional computations were performed for Cases 1, 2, 5, and 6 (which were selected as representative cases to present the corrected trajectory) until a 720° change of heading angle was achieved. The obtained results after the ship's heading variation of 180° were used to estimate the magnitude and direction of the current in the assumption that the yaw velocity is steady after 180° turn. Positions (x_{1i}, y_{1i}, t_{1i}) and (x_{2i}, y_{2i}, t_{2i}) in Figure 11.10 indicate the positions of the ship which have a phase difference of 360°. The local current velocity $\mathbf{V}_i$ for any two corresponding positions is defined as the follows:

$$\mathbf{V}_i = \frac{(x_{2i} - x_{1i}, y_{2i} - y_{1i})}{(t_{2i} - t_{1i})} \tag{11.1}$$

The estimated mean current velocity can be obtained from the following equation:

$$\mathbf{V}_e = \frac{1}{n}\sum_{i=1}^{n} \mathbf{V}_i = \frac{1}{n}\sum_{i=1}^{n} \frac{(x_{2i} - x_{1i}, y_{2i} - y_{1i})}{(t_{2i} - t_{1i})} \tag{11.2}$$

The obtained trajectories in the currents can be corrected as follows:

$$\mathbf{X}'(t) = \mathbf{X}(\mathrm{t}) - \mathbf{V}_e t \tag{11.3}$$

in which $\mathbf{X}(\mathrm{t})$ is the measured position vector and $\mathbf{X}'(t)$ is the corrected trajectory of the ship ($\mathbf{X}'(t) = \mathbf{X}(\mathrm{t})$ at $\mathrm{t} = 0$).

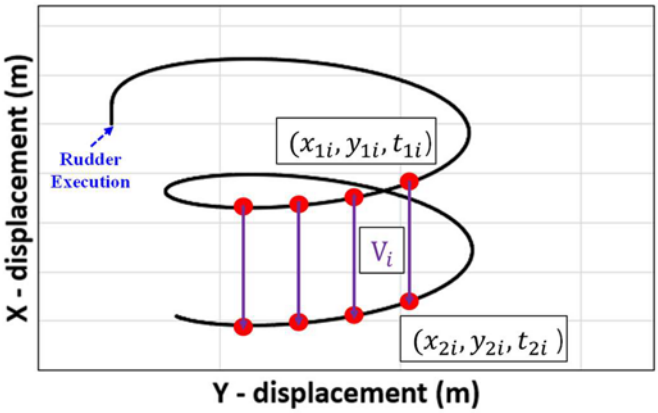

Figure 11.10 Turning trajectory in a current.

The corrected trajectories (for Case 1, 2, 5, and 6) calculated by the above equations are depicted in Figure 11.11. In the figure, the uncorrected results (indicated with red colour) and the inherent turning trajectory (Case 0, black line) are also presented for comparison purposes. As can be seen from the figure, some discrepancies between the corrected trajectories and Case 0 were observed for all cases. The possible reason for such discrepancies may be related to the non-uniformity of $\mathbf{V}_i$ caused by the assumption that yaw rate is stabilised. It is confirmed that the discrepancies are much more pronounced in stronger currents. This implies that the accurate estimation of the inherent turning trajectory is challenging, especially when using the results measured in strong currents to calculate the corrected trajectory.

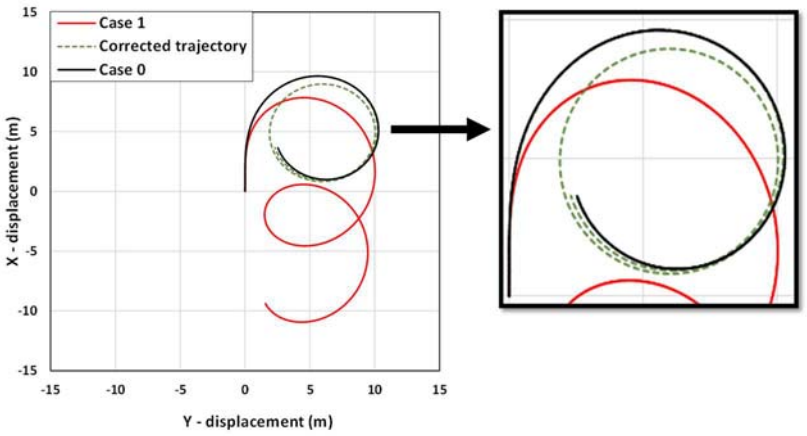

(a) Case 1

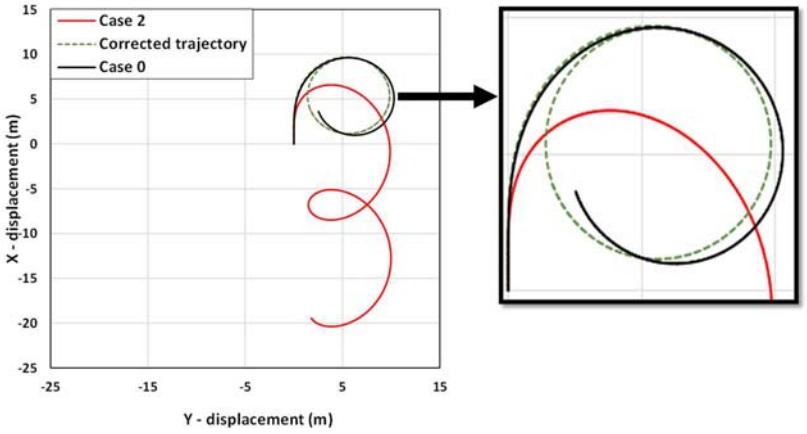

(b) Case 2

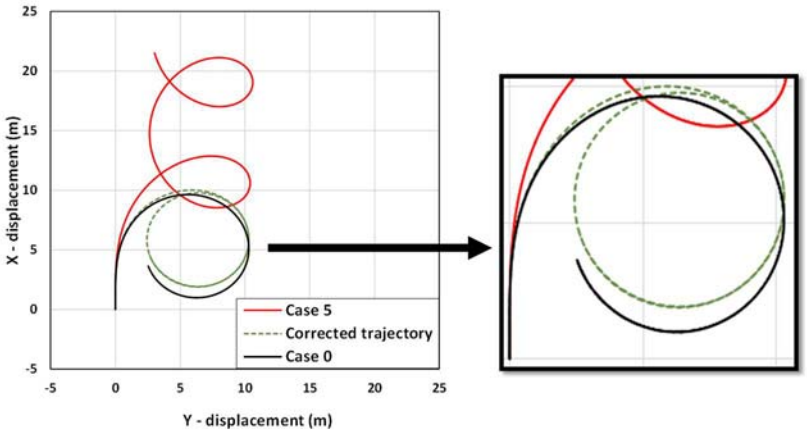

(c) Case 5

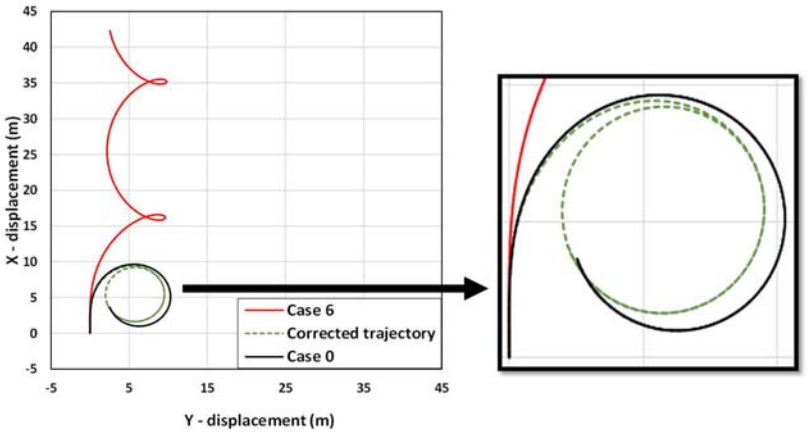

(d) Case 6

Figure 11.11 The corrected trajectories for Cases 1, 2, 5, and 6.

11.5. Concluding Remarks

In this chapter free-running CFD simulations to predict the turning capability of a container ship (the KCS model) in different current conditions have been carried out, along with comparisons with the inherent ship manoeuvrability in deep water without a current.

First, a validation study was carried out to assess the validity of the CFD model by comparison with the available experimental results from a free-running test. In turning indices predictions, it was revealed that the present CFD model predicted the ship advance, transfer, and tactical diameter with a range of –2.16 - 3.72% of the EFD data. In addition, the CFD results for the kinematic parameters, ship motions, and propeller parameters during the manoeuvre were found in good agreement with the experiment. The acceptable agreement between CFD and EFD demonstrated the reliability of the current CFD model when dealing with manoeuvring problems.

Following this, a series of turning manoeuvres (eight simulation cases) in deep waters with current speed to ship speed ratios varying between −0.552 and −0.138 / +0.138 and +0.552 were carried out using the present CFD model. The results were combined and plotted in form of graphs in order to enable the current effect on the ship manoeuvrability to be presented clearly. The main results drawn from this study can be summarised as follows:

1) It was found that the presence of the current resulted in noticeable changes in the resistance experienced by the advancing ship to achieve the self-propulsion condition when compared to that in deep water without a current. When it comes to the ahead current conditions, as expected, the increase of the current velocity caused a substantial increase in the ship resistance with consequent demand for the additional propulsion power to reach the same approach speed (Fr = 0.157). For the following current conditions, on the contrary, the ship resistance exhibited a gradual decrease with the decrease in the current velocity.

2) It can be concluded that the inclusion of the current has a remarkable influence on the turning performance of the ship, leading to significant changes in the ship trajectory and its turning parameters (compared to the inherent ship manoeuvrability, Case 0). When the ship started the standard turning manoeuvre in the ahead currents (Case 1 - 4), the ship advance became remarkably smaller with an increase in the current velocity. On the other hand, in the following currents (Case 5 - 8), a larger increase was observed in the advance as the current velocity increased. Unlike the marked changes in the ship advance, slight changes in the transfer and tactical diameter for both ahead and following currents were observed.

3) It was revealed that the differences were remarkable in terms of the surge and sway velocities experienced by the manoeuvring ship in the currents (Case 1 - 8), characterised by the acceleration and deceleration phenomena due to the current. Given that the ship's velocities in the horizontal plane may be decisive for the ship trajectory and its parameters, such perceptible differences in the surge and sway velocities can be considered as the main contributions to the differences in the predicted ship trajectories. It was observed that only small heave and pitch displacements occurred during the manoeuvre for all cases. The ship experienced a relatively large roll motion (up to 10 degrees) when starting the turn in the ahead currents, whereas a small roll motion of less than two degrees was observed for the following currents.

12. CONCLUSIONS AND DISCUSSION

12.1. Introduction

This chapter will summarise the main findings of the respective chapters, with a clear description of how the research aim and objectives have been achieved. Then, a comprehensive discussion on free-running CFD simulations will be provided. Finally, future recommendations will be given based on the findings of the thesis.

12.2. Conclusions

This thesis investigated a variety of subjects within the field of ship manoeuvrability by means of a fully nonlinear unsteady RANS solver. Each main chapter provided a comprehensive analysis, designed to offer a practical insight into the underlying phenomena.

The first research objective listed in Chapter 2 was as follows:

- ✓ *To examine the shortcomings of the current standards, existing practices, and studies on ship manoeuvrability based on the critical review of the literature and to identify open research questions*

The 'Literature Review' in Chapter 3 dealt with this through a broad survey of the literature on the previous studies in the field of ship manoeuvrability, together with the investigation of related existing standards and prediction methods. A discussion was also provided on the strengths and weaknesses of each prediction method. This chapter also presented a survey of the literature on specific fields, such as manoeuvring problems in deep unrestricted water, unified manoeuvring and seakeeping analyses in waves, and the prediction of ship manoeuvrability in shallow water. Finally, the research gaps identified during the literature review were reported in the concluding remarks of Chapter 3. It was also stated that the main chapters of this thesis (Chapter 5 - 11) were designed to fill the research gaps listed in the conclusion of Chapter 3.

The following objective reported in Chapter 2 was achieved in Chapter 4:

- ✓ *To develop a general framework for the analysis of ship manoeuvrability using CFD, with particular focus on the numerical modelling for free-running CFD model*

A general methodology to estimate the manoeuvrability of a ship using an unsteady RANS solver was presented in Chapter 4, with a detailed description of each individual stage of the numerical setup for free-running CFD simulations. The principal characteristics of the KCS model considered in this thesis were also provided. It should be emphasised that the numerical modelling approach (such as grid generation, boundary conditions, and control mechanism) depends on the environmental conditions applied to the CFD model and on the type of standard manoeuvres considered. Five different environmental conditions to be applied in the manoeuvring analyses were chosen in this thesis: 1) Deep unrestricted water, 2) regular waves, 3) irregular waves, 4) shallow water, and 4) deep water with a current. In addition, four representative manoeuvres were taken into consideration as follows: 1) course keeping control, 2) turning manoeuvre, 3) zigzag manoeuvre and 4) propulsion failure. In line with the

methodology provided, this thesis carried out the free-running simulations designed in the main chapters of the thesis.

The next research objective to be tackled was discussed in Chapters 5:

- ✓ *To investigate the effects of wave directions on the manoeuvring performance of a ship by means of an unsteady RANS solver*

The research reported in Chapter 5 (Task 3) addressed fully nonlinear unsteady RANS simulations to predict the manoeuvring behaviour of the KRISO Container Ship (KCS) model in regular waves of different directions. Course keeping and turning manoeuvres were performed based on the control mechanism embedded in the simulation. Before providing the CFD results, validation and verification studies were carried out to quantify the numerical uncertainties of the CFD model. The overall agreement between available experimental data and numerical results were satisfactory, which demonstrates that CFD is a reliable approach to estimate ship manoeuvrability in waves. Then, the effects of wave travelling directions on the manoeuvring performance of the ship were comprehensively investigated from the obtained results. The numerical results clearly demonstrated that wave directions lead to substantial changes in the ship's manoeuvring behaviours, compared to those observed in deep unrestricted water. An important point to note is that oblique incident waves make the ship's heading control more challenging, which means that the rudder angle deflection became large to make the ship straight in oblique seas.

The next research objective was achieved in Chapter 6:

- ✓ *To evaluate the contributions of wave lengths to the course-keeping and turning capabilities of a ship performing fully nonlinear unsteady RANS simulations*

The study performed in Chapter 6 (Task 4) presented a numerical study of ship manoeuvrability in regular waves of different wavelengths by means of a fully nonlinear unsteady RANS solver. The manoeuvring analyses were carried out in bow waves covering a range of important wavelength-to-ship-length ratios for constant wave height. Two representative free-running manoeuvres were conducted, namely, course keeping control, and standard turning circle manoeuvres. For the course keeping manoeuvres in waves, similar large rudder deflections were predicted approximately 7º in all bow waves, regardless of the wavelength. However, the steering frequency was found to vary significantly depending on the wavelength. It was also identified that the critical manoeuvring turning quantities were strongly affected by the wavelength and thus lead to significant changes in the turning trajectories.

The following research objective was achieved in Chapter 7:

- ✓ *To examine the correlations between a ship's manoeuvrability and wave heights using a CFD-based RANS solver*

A numerical study on free-running CFD simulations to estimate the manoeuvrability of the KCS under various wave height conditions were carried out in Chapter 7 (Task 5). Two types of manoeuvres were simulated with the free-running KCS model appended with an actuator disk and a moving semi-balanced horn rudder using a dynamic overset technique: course

keeping control and turning circle manoeuvres. Manoeuvring analyses were carried out in the bow quartering waves of a range of wave heights for constant wavelength, as coupled with the fifth-order Stokes wave model. The results clearly revealed that wave heights have a strong effect on the manoeuvring behaviour of the KCS, including ship's speeds, seakeeping behaviour, and critical turning indices through comparative analyses under different wave height conditions. One important finding is the standard manoeuvring parameters in waves, which would help navigation officers in decision-making for manoeuvring actions in waves.

The following research objective was achieved in Chapter 8:

- ✓ *To introduce a CFD-based unsteady RANS simulation model to assess the effects of a propulsion failure on the manoeuvrability of a ship in waves*

The first attempt to evaluate the effects of a propulsion failure on the manoeuvrability of the KRISO Container Ship (KCS) in waves was made in Chapter 8 (Task 6) using a fully nonlinear URANS model, which is capable of resolving complex fluid-structure interactions with high accuracy. A speed controller was embedded in the actuator disk to represent the failure condition of the ship propulsion system during the manoeuvres. A series of case studies were carried out to compare the ship performances of both the normal and propulsion loss condition, especially for the course keeping and turning circle manoeuvres. The results explicitly revealed that the propulsion failure has a strong influence on the ship manoeuvrability, implying the importance of sufficient propulsion power when vessels are underway.

The next research objective was achieved in Chapter 9:

- ✓ *To analyse the effects of irregular waves on the course-keeping and turning capabilities of a ship using a fully nonlinear unsteady RANS model*

In Chapter 9 (Task 7), the manoeuvrability of a well-known benchmarking ship in an irregular sea state was investigated using a fully nonlinear unsteady RANS model. The JONSWAP spectrum was used to generate long-crested irregular seas with a significant wave height of 5m and a peak period of 12.4s in full scale, representing sea state 6. Comparisons with the ship manoeuvrability in both calm and regular seas were also made with a view to identifying the changes in the manoeuvring characteristics of the ship. The generated regular waves were characterised by the height and period equivalent to the average height and period of the irregular waves applied in this work. In analysing the correlations between the ship manoeuvrability and the irregular waves, the findings of this study have demonstrated that the irregular waves may cause substantial changes in the course keeping capability and turning performance when compared to the inherent manoeuvring qualities in calm water. It is expected that the results of this work can provide a deeper insight into ship manoeuvrability in irregular waves as well as help masters and navigation officers in decision-making for ship handling actions in real sea states.

The following research objective was achieved in Chapter 10:

- ✓ *To predict the shallow water effects on the manoeuvring performance of a ship by employing an unsteady RANS solver*

In Chapter 10 (Task 8), the manoeuvrability of the KRISO Container Ship (KCS) model in different shallow water conditions was comprehensively analysed by means of the unsteady Reynolds-Averaged Navier-Stokes (URANS) computations coupled with the equations of rigid body motion with full six degrees of freedom (6DOF). A series of manoeuvring simulations were performed in shallow waters with water depth to draft ratios varying between 1.2 and 4.0, and partially validated with the available experimental data from a free running test. The numerical results revealed that the ship advance, transfer, and tactical diameter mainly increased with the decrease in the ratio of water depth to draft, closely associated with the complicated interactions between the hull wake, boundary layer, propeller, vortex, and sea floor.

The following research objective was achieved in Chapter 11:

- ✓ *To evaluate the effects of ocean currents on the manoeuvrability of a ship with particular emphasis on the turning capability, performing free-running CFD simulations*

A numerical study of ship manoeuvrability in different currents was performed in Chapter 11 (Task 9) by means of an unsteady RANS solver. Firstly, a model-scale container ship (the KRISO Container Ship) was used to develop the Computational Fluid Dynamics (CFD) model capable of performing a self-propelled free manoeuvre. Then, a validation study was carried out to assess the validity of the CFD model by comparison with the available experimental results from a free-running test. Following this, a series of manoeuvring simulations (i.e., standard turning manoeuvres) in deep waters with current speed to ship speed ratios varying between −0.552 and −0.138 / +0.138 and +0.552 were conducted using the present CFD model. The numerical results demonstrated that the inclusion of the current has a remarkable influence on the turning performance of the ship, leading to significant changes in the ship trajectory and its turning parameters when compared to the inherent ship manoeuvrability in deep water without a current.

12.3. Discussion

It is important to note that the task of ship navigation is to operate the ship from one destination to another as safely as possible in real sea states where the ship is to be navigated. Masters and navigation officers, who are responsible for the navigational operation, are required to fully understand the manoeuvring performance of the ship in a real seaway to ensure navigational safety. It should be borne in mind that inadequate manoeuvring actions by them can result in navigational casualties such as collision, contact, and grounding incidents. There is, however, only limited information available on the ship manoeuvrability under calm water conditions, which is generally measured from full-scale sea trials or model-scale tests; not able to predict a wide range of real sea conditions. Given that the fact that such data may be inconclusive on the effects of critical factors (such as waves, finite depths, and ocean currents) on the manoeuvring performance of a ship, it is expected that the studies reported in Chapters 5 – 11 will provide navigators with a deeper insight into the ship manoeuvrability in real sea states as well as support them in proper decision-making for ship handling actions to avoid collision. When vessels in sight of one another involve the risk of collision, navigators should take proper

and effective action to avoid collision according to COLREGs (International Regulations for Preventing Collisions at Sea) established by the IMO (2001). COLREGs also states that making a large course alteration may be the most effective action to avoid a close-quarters situation, which obviously leads to the ship's turning behaviour. Thus, it is paramount to fully understand the ship's turning performance when taking action to avoid collision, especially the advance, the transfer, and the time to 90° yaw angle change addressed in detail in this thesis.

The research tackled in Chapter 8, has furnished a very useful starting point for analyses of ship performances under the propulsion failure condition, especially course keeping and turning manoeuvres. COLREGs (International Regulations for Preventing Collisions at Sea, IMO (2001)) state that "the term 'vessel not under command' means a vessel which through some exceptional circumstance is unable to manoeuvre as required by these Rules and is, therefore, unable to keep out of the way of another vessel" in rule 3(f). For this reason, ships suffering from propulsion failure could be regarded as a vessel not under command as they have poor ship manoeuvrability. In general, a vessel in the normal operating conditions should, if the circumstances of the case admit, avoid impeding the safe passage of a vessel not under command to prevent collision, due to the better controllability. Nevertheless, navigators, in charge of handling a vessel suffering from propulsion loss, should fully understand the ship's manoeuvrability to determine proper decision-making for ship-handling actions. For example, an emergency anchor operation can be carried out in areas of narrow waterways or shallow water, taking into consideration the poor ship manoeuvrability. In this regard, the manoeuvring results obtained from this particular study would be helpful for navigators to have a practical insight into the ship manoeuvrability concerning the propulsion failure condition.

In connection with a rapidly growing interest in autonomous navigation, the importance has been stressed of the correct prediction of ship manoeuvrability in a real seaway (i.e., course keeping and turning capabilities). Autonomous or remote-controlled ships should be capable of operating independently based on an autonomous navigation system that adequately controls the rudder and propeller with an aim to maintain its intended course or avoid collision. Safe autonomous operation can be achieved through the accurate prediction of the manoeuvring performance of a ship, enabling the ship to maintain its desired trajectory during a given operation. With this point of view, the CFD-based ship manoeuvring analyses adopted in this thesis could offer a comprehensive and detailed insight into ship manoeuvrability in various environmental conditions, providing a valuable contribution to the improvement of autonomous navigation systems.

This author believes that this thesis has demonstrated the effectiveness and applicability of the CFD model to analyse the course keeping, turning circle, and zigzag manoeuvres of a ship under various environmental conditions, using the state-of-the-art unsteady RANS approach. The free-running CFD model was successful in providing an understanding of the manoeuvring behaviour of the KCS in different environmental conditions. With the provision of time history data regarding the critical manoeuvring quantities, the simulation results were able to directly indicate the correlations between the ship's manoeuvrability and critical factors such as waves, finite depths, and ocean currents, which confirmed the impact of them on the manoeuvring performance of the ship. An unsteady RANS approach will also be expected to be an alternative tool to the conventional experiments investigating ship manoeuvring in a real seaway with the

advance of computational resources, making a leap forward in the field of ship manoeuvrability.

12.4. Recommendations for Future Research

Recommendations for future work pertaining to the studies tackled in this thesis are given in this section.

1. The research tackled in Chapters 5 - 7 has provided a practical starting point for the examination of a ship's manoeuvring behaviour in regular waves using an unsteady RANS method. Especially, the combined seakeeping and manoeuvring performance of a ship in waves of different directions/lengths/heights were observed. In addition to this, the impact of various combinations of wave characteristics such as wave height, length, and directions on the manoeuvrability of a ship should be investigated. It has already been noted in real operations that a ship can experience diverse wave conditions in a real seaway. Therefore, a piece of future work may be the prediction of the ship manoeuvre in waves with different combinations of wave properties using the free-running CFD model developed in this thesis. This will help in improving understanding of a ship's manoeuvres in waves and hence improve navigational safety at sea.

2. The study presented in Chapter 8 has furnished a very useful starting point for analyses of ship performances under the propulsion failure condition, especially course keeping and turning manoeuvres in regular waves. Given that incident waves have a remarkable effect on ship behaviour and performance, irregular waves are believed to cause substantial changes in the ship manoeuvrability, specifically under the propulsion loss. In this context, this study could further add values by investigating the impacts of the irregular wave on the manoeuvring performance under both the normal and propulsion loss conditions as a next step.

3. The study performed in Chapter 9 can further be extended for zigzag manoeuvres in irregular waves, where significant changes in the yaw checking ability of a ship are expected to be observed.

4. According to the European funded Project SHOPERA (Sprenger et al., 2016), it was revealed that finite depths have a notable effect on propagating wave properties. Given this, the research in Chapter 10 should be extended to incorporate different wave conditions as ship manoeuvrability will be strongly dependent on not only shallow water effects but also incident wave conditions. With the Stokes wave model, further study into the manoeuvring performance of the ship in waves with shallow water could be made.

5. In Chapter 11, free-running CFD simulations to predict the turning capability of the KCS model in different current conditions have been carried out. This particular study could be extended by merging Chapters 5 - 9. In other words, this research could further add values by taking into account the presence of waves together with currents, as these will also have a remarkable influence on the manoeuvring behaviour of a ship. Using the methodology presented in Chapter 4, further studies into ship manoeuvrability in waves with currents could be made.

6. The research performed in this thesis can also be extended to investigate the effect of hull roughness on ship manoeuvrability, as the added resistance due to hull roughness will also have a remarkable effect on the manoeuvring behaviour of a ship. The roughness effect can be estimated by using modified wall functions available in CFD software as successfully shown in Song et al. (2020a); Song et al. (2020b).
7. The CFD model developed in this thesis can easily be combined with a path-following algorithm for autonomous or remote-controlled vehicles. The free-running CFD simulations of path-following control are currently being performed as a piece of future work, with particular attention to the contribution of waves to path-following operation.

References

Abkowitz, M.A., 1964. Lectures on ship hydrodynamics--Steering and manoeuvrability.

Balagopalan, A., Tiwari, K., Rameesha, T., Krishnankutty, P., 2020. Manoeuvring prediction of a container ship using the numerical PMM test and experimental validation using the free running model test. Ships and Offshore Structures 15 (8), 852-865.

Broglia, R., Dubbioso, G., Durante, D., Di Mascio, A., 2013. Simulation of turning circle by CFD: analysis of different propeller models and their effect on manoeuvring prediction. Applied Ocean Research 39, 1-10.

Broglia, R., Dubbioso, G., Durante, D., Di Mascio, A., 2015. Turning ability analysis of a fully appended twin screw vessel by CFD. Part I: Single rudder configuration. Ocean Engineering 105, 275-286.

Carrica, P.M., Fu, H., Stern, F., 2011. Computations of self-propulsion free to sink and trim and of motions in head waves of the KRISO Container Ship (KCS) model. Applied Ocean Research 33 (4), 309-320.

Carrica, P.M., Mofidi, A., Eloot, K., Delefortrie, G., 2016. Direct simulation and experimental study of zigzag maneuver of KCS in shallow water. Ocean Engineering 112, 117-133.

Celik, I.B., Ghia, U., Roache, P.J., Freitas, C.J., 2008. Procedure for estimation and reporting of uncertainty due to discretization in CFD applications. Journal of fluids Engineering-Transactions of the ASME 130 (7).

Cepeda, M.A.F.-s., Pereira, N.N., Kahn, S., Caprace, J.-D., 2019. A review of the use of LNG versus HFO in maritime industry. Marine Systems & Ocean Technology 14 (2), 75-84.

CSP, C.-A., 2021. Personal Corrospondents, Customer Support Portal.

Date, J., Turnock, S., 1999. A study into the techniques needed to accurately predict skin friction using RANS solvers with validation against Froude's historical flat plate experimental data. University of Southampton, Department of Ship Science.

Di Mascio, A., Broglia, R., Muscari, R., 2007. On the application of the single-phase level set method to naval hydrodynamic flows. Computers & fluids 36 (5), 868-886.

Dubbioso, G., Durante, D., Di Mascio, A., Broglia, R., 2016. Turning ability analysis of a fully appended twin screw vessel by CFD. Part II: Single vs. twin rudder configuration. Ocean Engineering 117, 259-271.

el Moctar, O., Sprenger, F., Schellin, T.E., Papanikolaou, A., 2016. Numerical and experimental investigations of ship maneuvers in waves, Proceedings 35th International Conference on Ocean, Offshore and Arctic Engineering, OMAE2016 - 54847, Busan, South Korea, 19-24 June 2016.

EMSA, 2020. Annual Overview of Marine Casualties and Incidents 2020.

Fenton, J.D., 1985. A fifth-order Stokes theory for steady waves. Journal of waterway, port, coastal, and ocean engineering 111 (2), 216-234.

Ferziger, J.H., Peric, M., 2020. Computational Methods for Fluid Dynamics.

Fossen, T.I., 2005. A nonlinear unified state-space model for ship maneuvering and control in a seaway. International Journal of Bifurcation and Chaos 15 (09), 2717-2746.

Franceschi, A., Piaggio, B., Tonelli, R., Villa, D., Viviani, M., 2021. Assessment of the Manoeuvrability Characteristics of a Twin Shaft Naval Vessel Using an Open-Source CFD Code. Journal of Marine Science and Engineering 9 (6), 665.

Guedes, D.d.L., Kleine, F.A.d.S., de Castro, F.S., Carvalho, D., Dozzi Dantas, J.L., 2018. Maneuverability Towing Tank Experiments With Manifold Models: Part II—PMM Oscillation Tests, International conference on offshore mechanics and arctic engineering. American Society of Mechanical Engineers, p. V001T001A068.

Guo, H.-p., Zou, Z.-j., 2017. System-based investigation on 4-DOF ship maneuvering with hydrodynamic derivatives determined by RANS simulation of captive model tests. Applied Ocean Research 68, 11-25.

Guo, H.-p., Zou, Z.-j., Liu, Y., Wang, F., 2018. Investigation on hull-propeller-rudder interaction by RANS simulation of captive model tests for a twin-screw ship. Ocean Engineering 162, 259-273.

Hajivand, A., Mousavizadegan, S.H., 2015a. Virtual maneuvering test in CFD media in presence of free surface. International journal of naval architecture and ocean engineering 7 (3), 540-558.

Hajivand, A., Mousavizadegan, S.H., 2015b. Virtual simulation of maneuvering captive tests for a surface vessel. International journal of naval architecture and ocean engineering 7 (5), 848-872.

Hasanvand, A., Hajivand, A., 2019. Investigating the effect of rudder profile on 6DOF ship turning performance. Applied Ocean Research 92, 101918.

Hasnan, M., Yasukawa, H., Hirata, N., Terada, D., Matsuda, A., 2019. Study of ship turning in irregular waves. Journal of Marine Science and Technology, 1-20.

Hasselmann, K.F., Barnett, T.P., Bouws, E., Carlson, H., Cartwright, D.E., Eake, K., Euring, J., Gicnapp, A., Hasselmann, D., Kruseman, P., 1973. Measurements of wind-wave growth and swell decay during the Joint North Sea Wave Project (JONSWAP). Ergaenzungsheft zur Deutschen Hydrographischen Zeitschrift, Reihe A.

He, S., Kellett, P., Yuan, Z., Incecik, A., Turan, O., Boulougouris, E., 2016. Manoeuvring prediction based on

CFD generated derivatives. Journal of Hydrodynamics 28 (2), 284-292.
IMO, 2001. International Regulations for Preventing Collisions at Sea (COLREGs) 1972.
IMO, 2002. Explanatory Notes to the standards for ship manoeuvrability.
IMO, 2014. 2013 Interim Guidelines for determining minimum propulsion power to maintain the manoeuvrability of ships in adverse conditions.
IMO, 2020. PROCEDURES FOR PORT STATE CONTROL, 2019.
IMO, 2021. Guidelines for determining minimum propulsion power to maintain the manoeuvrability of ships in adverse conditions.
Inoue, S., Hirano, M., Kijima, K., 1981a. Hydrodynamic derivatives on ship manoeuvring. International Shipbuilding Progress 28 (321), 112-125.
Inoue, S., Hirano, M., Kijima, K., Takashina, J., 1981b. A practical calculation method of ship maneuvering motion. International Shipbuilding Progress 28 (325), 207-222.
ITTC, 2011. ITTC - Recommended Procedures and Guidelines : Practical Guidelines for Ship CFD Applications.
ITTC, 2017a. Recommended Procedures and Guidelines - Seakeeping Experiments.
ITTC, 2017b. Tasks and structure of 29th ITTC technical committees and groups (version 4).
ITTC, 2021a. ITTC - Recommended Procedures and Guidelines : Captive Model Test.
ITTC, 2021b. ITTC - Recommended Procedures and Guidelines: Full Scale Manoeuvring Trials.
ITTC, 2021c. The Manoeuvring Committee Final Report and Recommendations to the 29th ITTC.
Kavli, H.P., Oguz, E., Tezdogan, T., 2017. A comparative study on the design of an environmentally friendly RoPax ferry using CFD. Ocean Engineering 137, 22-37.
Kim, D., Song, S., Jeong, B., Tezdogan, T., Incecik, A., 2021a. Unsteady RANS CFD simulations of ship manoeuvrability and course keeping control under various wave height conditions. Applied Ocean Research 117, 102940.
Kim, D., Song, S., Tezdogan, T., 2021b. Free running CFD simulations to investigate ship manoeuvrability in waves. Ocean Engineering 236, 109567.
Kim, D.J., Choi, H., Yun, K., Yeo, D.J., Kim, Y.G., 2022. Experimental study on turning characteristics of KVLCC2 tanker in long-crested irregular waves. Ocean Engineering 244, 110362.
Kim, D.J., Yun, K., Park, J.-Y., Yeo, D.J., Kim, Y.G., 2019. Experimental investigation on turning characteristics of KVLCC2 tanker in regular waves. Ocean Engineering 175, 197-206.
Kim, I.-T., Kim, C., Kim, S.-H., Ko, D., Moon, S.-H., Park, H., Kwon, J., Jin, B., 2021c. Estimation of the manoeuvrability of the KVLCC2 in calm water using free running simulation based on CFD. International journal of naval architecture and ocean engineering.
Kleine, F.A.d.S., Guedes, D.d.L., de Castro, F.S., Carvalho, D., Dozzi Dantas, J.L., 2018. Maneuverability Towing Tank Experiments With Manifold Models: Part I—Static Tests, International conference on offshore mechanics and arctic engineering. American Society of Mechanical Engineers, p. V001T001A057.
Lee, S., Hong, C., 2017. Study on the course stability of very large vessels in shallow water using CFD. Ocean Engineering 145, 395-405.
Liu, C., Wang, J., Wan, D., 2020. CFD Simulations of Self-Propulsion and Turning Circle Maneuver up to 90° of Ship in Waves. Journal of Ship Research, 1-14.
Liu, H., Ma, N., Gu, X., 2015. Maneuvering prediction of a VLCC model based on CFD simulation for PMM tests by using a circulating water channel, International Conference on Offshore Mechanics and Arctic Engineering. American Society of Mechanical Engineers, p. V002T008A041.
Liu, Y., Zou, L., Zou, Z., Guo, H., 2018. Predictions of ship maneuverability based on virtual captive model tests. Engineering Applications of Computational Fluid Mechanics 12 (1), 334-353.
Liu, Y., Zou, Z., Zou, L., Fan, S., 2019. CFD-based numerical simulation of pure sway tests in shallow water towing tank. Ocean Engineering 189, 106311.
Maimun, A., Priyanto, A., Muhammad, A., Scully, C., Awal, Z., 2011. Manoeuvring prediction of pusher barge in deep and shallow water. Ocean Engineering 38 (11-12), 1291-1299.
Menter, F.R., 1994. Two-equation eddy-viscosity turbulence models for engineering applications. AIAA journal 32 (8), 1598-1605.
Mofidi, A., Carrica, P.M., 2014. Simulations of zigzag maneuvers for a container ship with direct moving rudder and propeller. Computers & fluids 96, 191-203.
Muscari, R., Broglia, R., Di Mascio, A., 2008. Trajectory prediction of a self-propelled hull by unsteady RANS computations., In: Proceedings of the 27th ONR Sym- posium on Naval Hydrodynamics. Seoul, Korea.
Ohkusu, M., Wen, G., 1998. Radiation and diffraction waves of a ship at forward speed, Proc. of 21st Symposium on Naval Hydrodynamics, pp. 29-44.
Papanikolaou, A., Fournarakis, N., Chroni, D., Liu, S., Plessas, T., Sprenger, F., 2016. Simulation of the

maneuvering behavior of ships in adverse weather conditions, Proc. 31st Symposium on Naval Hydrodynamics, Monterey, California, 11-16 September 2016, pp. 11-16.
Papanikolaou, A., Zaraphonitis, G., Bitner-Gregersen, E., Shigunov, V., El Moctar, O., Soares, C.G., Reddy, D.N., Sprenger, F., 2015. Energy efficient safe ship operation (SHOPERA), Proc. 6th European Transport Research Conference, Transport Research Arena - TRA 2016, Warsaw, 18-21 April, 2016.
Paroka, D., Muhammad, A.H., Asri, S., 2017. Prediction of ship turning maneuvers in constant wind and regular waves. Int J Technol 8 (3), 387-397.
Perić, R., Abdel-Maksoud, M., 2018. Analytical prediction of reflection coefficients for wave absorbing layers in flow simulations of regular free-surface waves. Ocean Engineering 147, 132-147.
Richardson, L.F., 1911. IX. The approximate arithmetical solution by finite differences of physical problems involving differential equations, with an application to the stresses in a masonry dam. Philosophical Transactions of the Royal Society of London. Series A, Containing Papers of a Mathematical or Physical Character 210 (459-470), 307-357.
Romanowski, A., Tezdogan, T., Turan, O., 2019. Development of a CFD methodology for the numerical simulation of irregular sea-states. Ocean Engineering 192, 106530.
Sanada, Y., Elshiekh, H., Toda, Y., Stern, F., 2019. ONR Tumblehome course keeping and maneuvering in calm water and waves. Journal of Marine Science and Technology 24 (3), 948-967.
Seo, M.-G., Kim, Y., 2011. Numerical analysis on ship maneuvering coupled with ship motion in waves. Ocean Engineering 38 (17-18), 1934-1945.
Shen, Z., Wan, D., Carrica, P.M., 2015. Dynamic overset grids in OpenFOAM with application to KCS self-propulsion and maneuvering. Ocean Engineering 108, 287-306.
Shin, H.-K., Choi, S.-H., 2011. Prediction of Maneuverability of KCS Using Captive Model Test. Journal of the Society of Naval Architects of Korea 48 (5), 465-472.
Siemens, 2020. Simcenter STAR-CCM+ Documentation.
SIMMAN, 2020. Workshop on Verification and Validation of Ship Manoeuvring Simulation Methods.
Simonsen, C.D., Otzen, J.F., Klimt, C., Larsen, N.L., Stern, F., 2012. Maneuvering predictions in the early design phase using CFD generated PMM data, 29th symposium on naval hydrodynamics, pp. 26-31.
Skejic, R., Faltinsen, O.M., 2008. A unified seakeeping and maneuvering analysis of ships in regular waves. Journal of Marine Science and Technology 13 (4), 371-394.
Skjetne, R., Smogeli, Ø.N., Fossen, T.I., 2004. A nonlinear ship manoeuvering model: Identification and adaptive control with experiments for a model ship.
Son, K., Nomoto, K., 1981. On the coupled motion of steering and rolling of a high speed container ship. Journal of the Society of Naval Architects of Japan 1981 (150), 232-244.
Song, S., Demirel, Y.K., Atlar, M., Shi, W., 2020a. Prediction of the fouling penalty on the tidal turbine performance and development of its mitigation measures. Applied Energy 276, 115498.
Song, S., Demirel, Y.K., Muscat-Fenech, C.D.M., Tezdogan, T., Atlar, M., 2020b. Fouling effect on the resistance of different ship types. Ocean Engineering 216, 107736.
Sprenger, F., Maron, A., Delefortrie, G., Cura-Hochbaum, A., Papanikolaou, A., 2016. Experimental studies on seakeeping and manoeuvrability in adverse weather conditions. Journal of Ship Research, SNAME Publ.
Stern, F., Agdraup, K., Kim, S., Hochbaum, A., Rhee, K., Quadvlieg, F., Perdon, P., Hino, T., Broglia, R., Gorski, J., 2011. Experience from SIMMAN 2008—the first workshop on verification and validation of ship maneuvering simulation methods. Journal of Ship Research 55 (02), 135-147.
Subramanian, R., Beck, R.F., 2015. A time-domain strip theory approach to maneuvering in a seaway. Ocean Engineering 104, 107-118.
Sung, Y.J., Park, S.-H., 2015. Prediction of ship manoeuvring performance based on virtual captive model tests. Journal of the Society of Naval Architects of Korea 52 (5), 407-417.
Terziev, M., Tezdogan, T., Incecik, A., 2019. A geosim analysis of ship resistance decomposition and scale effects with the aid of CFD. Applied Ocean Research 92, 101930.
Terziev, M., Tezdogan, T., Incecik, A., 2020. Application of eddy-viscosity turbulence models to problems in ship hydrodynamics. Ships and Offshore Structures 15 (5), 511-534.
Tezdogan, T., Demirel, Y.K., Kellett, P., Khorasanchi, M., Incecik, A., Turan, O., 2015. Full-scale unsteady RANS CFD simulations of ship behaviour and performance in head seas due to slow steaming. Ocean Engineering 97, 186-206.
Tezdogan, T., Incecik, A., Turan, O., 2016. Full-scale unsteady RANS simulations of vertical ship motions in shallow water. Ocean Engineering 123, 131-145.
Toffoli, A., Bitner-Gregersen, E.M., 2017. Types of ocean surface waves, wave classification. Encyclopedia of Maritime and Offshore Engineering, 1-8.

Toxopeus, S., Simonsen, C., Guilmineau, E., Visonneau, M., Xing, T., Stern, F., 2013. Investigation of water depth and basin wall effects on KVLCC2 in manoeuvring motion using viscous-flow calculations. Journal of Marine Science and Technology 18 (4), 471-496.
Ventikos, N., Papanikolaou, A., Louzis, K., Koimtzoglou, A., 2018. Statistical analysis and critical review of navigational accidents in adverse weather conditions. Ocean Engineering 163, 502-517.
Wang, J., Wan, D., 2018. CFD investigations of ship maneuvering in waves using naoe-FOAM-SJTU Solver. Journal of Marine Science and Application 17 (3), 443-458.
Wang, J., Zhao, W., Wan, D., 2016. Free maneuvering simulation of ONR Tumblehome using overset grid method in naoe-FOAM-SJTU solver, 31th Symposium on Naval Hydrodynamics, Monterey, USA.
Wang, J., Zou, L., Wan, D., 2017. CFD simulations of free running ship under course keeping control. Ocean Engineering 141, 450-464.
Wang, J., Zou, L., Wan, D., 2018. Numerical simulations of zigzag maneuver of free running ship in waves by RANS-Overset grid method. Ocean Engineering 162, 55-79.
Yan, Z., Zhang, X., Zhu, H., Li, Z., 2020. Course-keeping control for ships with nonlinear feedback and zero-order holder component. Ocean Engineering 209, 107461.
Yasukawa, H., Hasnan, M., Matsuda, A., 2021. Validation of 6-DOF motion simulations for ship turning in regular waves. Journal of Marine Science and Technology, 1-16.
Yasukawa, H., Yoshimura, Y., 2015. Introduction of MMG standard method for ship maneuvering predictions. Journal of Marine Science and Technology 20 (1), 37-52.
Zhang, W., Zou, Z., 2016. Time domain simulations of the wave-induced motions of ships in maneuvering condition. Journal of Marine Science and Technology 21 (1), 154-166.
Zhang, Z., Li, X.-M., 2017. Global ship accidents and ocean swell-related sea states. Natural Hazards and Earth System Sciences 17 (11), 2041-2051.

Publications

The following papers have been published for publication. All of the papers listed below have been drawn from this thesis.

Journal papers:

1. Kim, D., Song, S., Tezdogan, T., 2021. Free running CFD simulations to investigate ship manoeuvrability in waves. Ocean Engineering 236, 109567.
2. Kim, D., Song, S., Jeong, B., Tezdogan, T., 2021. Numerical evaluation of a ship's manoeuvrability and course keeping control under various wave conditions using CFD. Ocean Engineering 237, 109615.
3. Kim, D., Song, S., Jeong, B., Tezdogan, T., Incecik, A., 2021. Unsteady RANS CFD simulations of ship manoeuvrability and course keeping control under various wave height conditions. Applied Ocean Research 117, 102940.
4. Kim, D., Song, S., Sant, T., Demirel, Y.K., Tezdogan, T., 2022. Nonlinear URANS model for evaluating course keeping and turning capabilities of a vessel with propulsion system failure in waves. International journal of naval architecture and ocean engineering 14, 100425.
5. Kim, D., Tezdogan, T., 2022. CFD-based hydrodynamic analyses of ship course keeping control and turning performance in irregular waves. Ocean Engineering 248, 110808.

6. Kim, D., Tezdogan, T., Incecik, A., 2022. Hydrodynamic analysis of ship manoeuvrability in shallow water using high-fidelity URANS computations. Applied Ocean Research 123, 103176.

7. Kim, D., Tezdogan, T., Incecik, A., 2022. A high-fidelity CFD-based model for the prediction of ship manoeuvrability in currents. Ocean Engineering 256, 111492.